MIXED-MODE CRACK PROPAGATION IN FUNCTIONALLY GRADED MATERIALS

BY

JEONG-HO KIM

B.S., Hanyang University, 1996
M.S., University of Illinois at Urbana-Champaign, 2000

THESIS

Submitted in partial fulfillment of the requirements
for the degree of Doctor of Philosophy in Department of Civil and Environmental Engineering
in the Graduate College of the
University of Illinois at Urbana-Champaign, 2003

Urbana, Illinois

UMI Number: 3101883

UMI®

CERTIFICATE OF COMMITTEE APPROVAL

University of Illinois at Urbana-Champaign
Graduate College

September 2, 2003

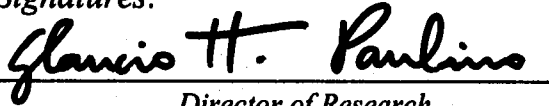We hereby recommend that the thesis by:

JEONG-HO KIM

Entitled:

**MIXED-MODE CRACK PROPAGATION
IN FUNCTIONALLY GRADED MATERIALS**

Be accepted in partial fulfillment of the requirements for the degree of:

Doctor of Philosophy

Signatures:

_____
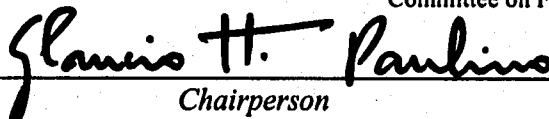Director of Research

_____
Head of Department

Committee on Final Examination*

_____
Chairperson

_____
Committee Member

_____
Committee Member

_____
Committee Member

_____
Committee Member

* Required for doctoral degree but not for master's degree

Abstract

The fracture parameters characterizing the crack tip fields in functionally graded materials (FGMs) include stress intensity factors (SIFs) and T-stress (non-singular stress). These fracture parameters are important for determining the behavior of a crack under mixed-mode loading conditions in brittle FGMs (e.g. ceramic/ceramic such as TiC/SiC). The mixed-mode SIFs and T-stress in isotropic and orthotropic FGMs are evaluated by means of the interaction integral method, in the form of an equivalent domain integral, in combination with the finite element method, and are compared with available reference solutions. Mixed-mode crack propagation in homogeneous and graded materials is performed by means of a remeshing algorithm of the finite element method considering general mixed-mode loadings. Each step of crack growth simulation consists of calculation of mixed-mode SIFs, determination of crack growth based on fracture criteria, and local automatic remeshing along the crack path. Crack trajectories obtained by the present numerical simulation are compared with available experimental results. The history of the load and SIFs versus crack extension are also provided for better understanding of fracture behavior of FGMs.

For the glory of God

Acknowledgments

Table of Contents

List of Tables

List of Figures

Chapter 1

Introduction

Functionally graded materials (FGMs) are a new class of composites in which the volume fractions of constituent materials vary smoothly, giving a nonuniform microstructure with continuously graded macroproperties [58, 113]. FGMs possess the distinguishing feature of nonhomogeneity with regard to thermomechanical and strength related properties including yield strength, fracture toughness, and fatigue and creep behavior. These multifunctional materials were introduced to take advantage of ideal behavior of its constituents, e.g. heat and corrosion resistance of ceramics together with mechanical strength and toughness of metals. Although the initial emphasis for FGMs focused on the synthesis of thermal barrier coatings for space-type applications [59], subsequent investigations have addressed a wide variety of applications [88, 58, 134]. These include the potential use of FGMs in nuclear fusion and fast breeder reactors as first-wall composite materials [67]; in electronic and magnetic applications as piezoelectric and thermoelectric devices, and as high density magnetic recording media and position measuring devices [135, 60, 107, 142]; in optical applications, e.g. graded refractive index materials in audio-video disks [87]; in thermionic applications, e.g. thermionic converters [30]; in biomaterials, e.g. dental and other implants [143, 106]; and in other applications, e.g. the development of fire retardant doors [44].

Knowledge of the behavior of cracks in FGMs is important for assessing and enhancing their structural integrity. Thus this thesis focuses on the evaluation of fracture parameters (i.e. stress intensity factors (SIFs) and T-stress) in FGMs within the framework of linear elasticity, and simulates crack growth in FGMs by means of a remeshing algorithm of the displacement-based finite element method considering mechanical and mixed-mode loadings. Moreover, the FEM results for such fracture parameters and crack trajectories obtained by the present work are compared with

1

available semi-analytical and experimental results.

1.1 Crack-tip fields in functionally graded materials

Eischen [34] extended the eigenfunction expansion technique of Williams [147], and derived the general form of the crack-tip stress and displacement fields in a nonhomogeneous material by assuming that the material properties are *continuous, differentiable and bounded* (see Figure 1.1).

(a) admissible   (b) inadmissible
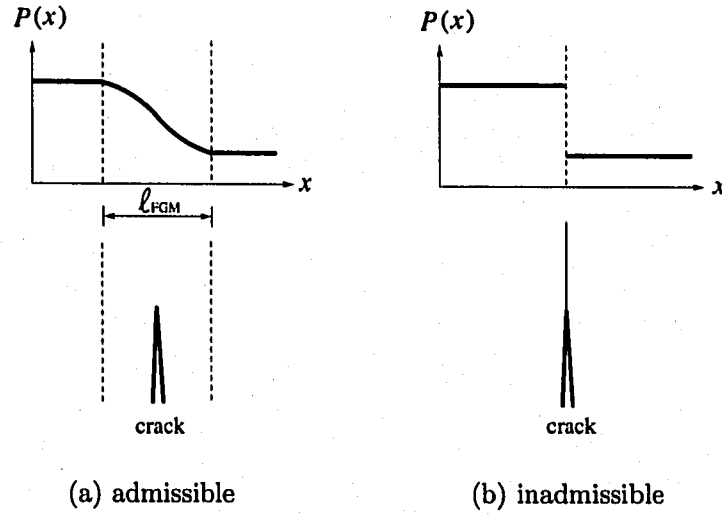
Figure 1.1: Admissible and inadmissible material variations. The notation $P(x)$ denotes a generic material property and ℓ_{FGM} refers to the length over which the property varies.

Figure 1.2 shows a crack in a two dimensional FGM elastic body with prescribed tractions and displacements on the boundary. The asymptotic crack-tip stresses are given by [34]

$$\sigma_{ij} = \frac{K_I}{\sqrt{2\pi r}} f_{ij}^I(\theta) + \frac{K_{II}}{\sqrt{2\pi r}} f_{ij}^{II}(\theta) + T\delta_{i1}\delta_{j1} + O(r^{1/2}) \tag{1.1}$$

and the corresponding near-tip displacements are [34]

$$u_i = \frac{K_I}{\mu_{\text{tip}}} \sqrt{\frac{r}{2\pi}} g_i^I(\theta) + \frac{K_{II}}{\mu_{\text{tip}}} \sqrt{\frac{r}{2\pi}} g_i^{II}(\theta) + O(r) \tag{1.2}$$

where K_I and K_{II} are the mode I and mode II stress intensity factors (SIFs), respectively, T is the T-stress, δ_{ij} is the Kronecker delta, $f_{ij}(\theta)$ $(i, j = 1, 2)$ is the standard angular function for the

2

stresses, and $g_i(\theta)$ $(i = 1, 2)$ is the standard angular function for the displacements, which can be found in many references, e.g. [33]. Notice that the material property appears in Eq.(1.2), and the shear modulus $\mu \equiv \mu(x)$ is sampled at the crack tip location, i.e. μ_{tip}.
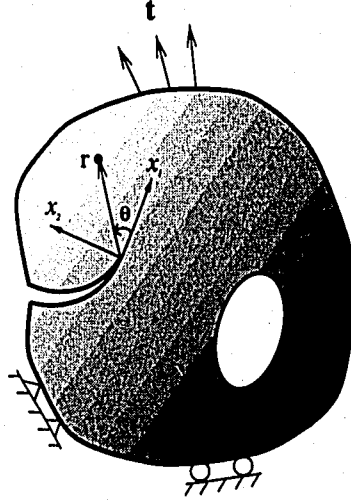
Figure 1.2: Cartesian (x_1, x_2) and polar (r, θ) coordinates originating from the crack tip in FGMs under traction (t) and displacement boundary conditions.

As inferred by Eischen [34], the order of stress singularity, i.e. $r^{-1/2}$, of an FGM is the same as for conventional homogeneous materials. Moreover, the standard angular functions $f_{ij}(\theta)$ and $g_i(\theta)$ of an FGM are the same as those for a homogeneous material. However, the material nonhomogeneity will influence the SIFs and the T-stress. Moreover, the angular functions for the terms $O(r^{1/2})$ and higher for the stresses, and for the terms $O(r^{3/2})$ and higher for the displacements do change due to material nonhomogeneity [34]. For instance, recently, Parameswaran and Shukla [111] have derived the crack-tip fields up to the order of r^2 for stresses considering an exponentially-graded material, which varies along the line of a crack in the form

$$E(x) = E_0 e^{\beta x} \tag{1.3}$$

and constant Poisson's ratio. In Eq.(1.3), E_0 denotes the modulus of elasticity at the crack tip, and $1/\beta$ denotes the length-scale of material nonhomogeneity. The correspondence of the crack-tip behavior between homogeneous and FGMs provides a basis for *local homogenization* near the

crack tip [34] (see Figure 1.3).
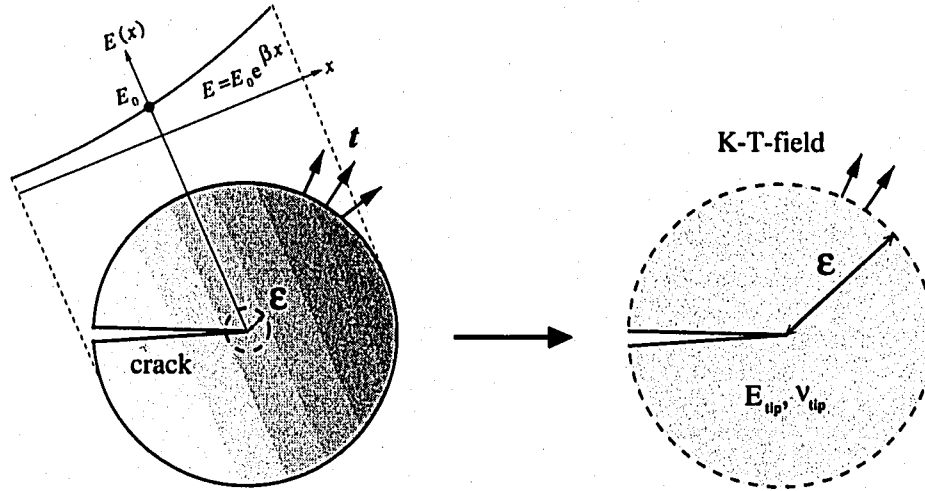
Figure 1.3: Description of local homogenization near the crack tip in an arbitrary FGM. The radius ε is the geometric length-scale over which local homogenization is valid, and it is related to the length-scale of material nonhomogeneity, e.g. $1/\beta$ for exponentially graded materials. A locally homogenized region ($\varepsilon \to 0$) is subjected to the K-T-field (K_I, K_{II}, T) of the crack in FGMs.

This thesis assumes that material properties are *continuous, differentiable and bounded*, and the graded material is locally homogeneous near the crack tip. Based on these assumptions, this thesis establishes the relationship between asymptotically defined line M-integral and SIFs (or T-stress), converts the line M-integral to a final form of equivalent domain integral (EDI) using auxiliary fields adopted from those for a homogeneous material, and calculates SIFs and T-stress using a finite domain.

1.1.1 Stress intensity factors

Extensive studies have been carried out on fracture mechanics under mechanical [28, 37, 108, 109] or thermal [104, 69, 38, 68, 70] loading in FGMs. Mixed-mode fracture of FGMs under mechanical loadings has been investigated primarily by evaluating mixed-mode SIFs of a stationary crack. Eischen [34] has investigated the J_k^*-integral in the form of line integral for mixed-mode cracks in nonhomogeneous materials using the finite element method (FEM). Kim and Paulino [76] have also evaluated mixed-mode SIFs in FGMs by means of the path-independent J_k^*-integral using the equivalent domain integral (EDI) and the FEM. Honein and Herrmann [61] have studied

4

the path-independent J-integral based on conservation laws for elastic nonhomogeneous materials. Gu *et al.* [50] have proposed a simplified method based on the standard J-integral [120] to evaluate SIFs in FGMs using the EDI and the FEM. They considered material properties at the Gauss integration points and selected very small domains to avoid the effect of the extra term in the domain integral due to nonhomogeneity. Anlas *et al.* [7] have evaluated SIFs in FGMs by the FEM where the material property variation was discretized by assigning different homogeneous elastic properties to each element. Chen *et al.* [23] have presented a modified J-integral for FGMs using the element-free Galerkin method. Gu *et al.* [50], Anlas *et al.* [7], and Chen *et al.* [23] have considered a pure Mode I crack where the crack is parallel to the material gradation. Marur and Tippur [99] have considered a crack normal to the elastic gradient and have performed FEM analysis along with experiments. Bao and Wang [9] have studied multiple cracking in functionally graded ceramic/metal coatings using the FEM. Bao and Cai [8] have investigated delamination cracking and buckling in a functionally graded ceramic/metal substrate under mechanical and thermal loads using the FEM.

Yau *et al.* [151] proposed the interaction integral method for evaluating SIFs in homogeneous isotropic solids. The method is based on conservation laws of elasticity and fracture mechanics concepts. It makes use of a conservation integral for two admissible states of an elastic solid: actual and auxiliary (see also the paper by Haber and Koh [52]). Wang *et al.* [140] extended the method to homogeneous orthotropic solids. Yau [150] also used the method for bimaterial interface problems. Recently, the interaction integral method has emerged as an accurate and robust scheme for evaluating SIFs in FGMs [31, 117, 79]. For instance, Dolbow and Gosz [31] considered the plane problem of an arbitrarily oriented crack and used the extended finite element method (X-FEM), Rao and Rahman [117] used the element-free Galerkin (EFG) method, and Kim and Paulino [79, 82] used the FEM to investigate FGMs with multiple cracks and material properties determined by means of either continuum functions (e.g. exponentially graded materials) or micromechanics models. All of the above papers are concerned with isotropic FGMs.

In practice, the nature of processing techniques of some FGMs may lead to loss of isotropy. For example, graded materials processed by a *plasma spray* technique generally have a lamellar structure [124], where flattened splats and relatively weak splat boundaries create an oriented ma-

terial with higher stiffness and weak cleavage planes parallel to the boundary (see Figure 1.4(a)).

Furthermore, graded materials processed by the *electron beam physical vapor deposition* technique can have a columnar structure [74], which leads to a higher stiffness in the thickness direction and weak fracture planes perpendicular to the boundary (see Figure 1.4(b)). Thus, such materials would be orthotropic with preferential material directions that are perpendicular to each other. Gu and Asaro [49] studied orthotropic FGMs considering a four-point bending specimen with varying Young's modulus and varying Poisson's ratio. Ozturk and Erdogan [108, 109] used integral equations to investigate Mode I and mixed-mode crack problems in an infinite nonhomogeneous orthotropic medium with a crack aligned with one of the principal material directions considering constant Poisson's ratio. Kim and Paulino [78, 81] evaluated mixed-mode SIFs for cracks arbitrarily oriented in orthotropic FGMs using the modified crack closure (MCC) method and the path-independent J_k^*-integral, respectively. Recently, Kim and Paulino [80, 84] extended the interaction integral method to orthotropic FGMs, and evaluated SIFs with high accuracy. Because of the accuracy and robustness, the interaction integral method is used for this work.

(a)   (b)
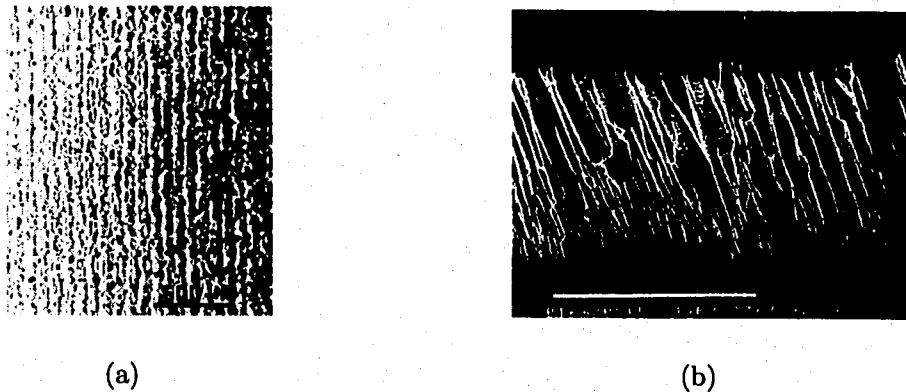
Figure 1.4: Cross-section microscopy of FGMs: (a) lamellar NiCrAlY-PSZ FGM processed by plasma spray technique (Sampath *et al.* [124]); (b) columnar $ZrO_2 - Y_2O_3$ thermal barrier coating with graded porosity processed by electron beam physical vapor deposition (Kaysser and Ilschner [74]).

1.1.2 T-stress

Although SIFs are well-known fracture parameters, T-stress is less understood, and thus its implications in fracture of FGMs need to be investigated further. For homogeneous materials, T-stress

has a significant influence on crack growth under mixed-mode loading [146, 138, 133] and crack path stability in mode I loading considering a small imperfection [27]. T-stress has a significant influence on crack-tip constraint and toughness [32, 105]. Because of the importance of T-stress in fracture, investigations of T-stress have been extensively performed for homogeneous materials. Larsson and Carlsson [92] investigated T-stress in mode I loading and found that it affects the size and shape of the plastic zone. Leevers and Radon [94] used a variational formulation to evaluate T-stress. Afterwards, Cardew *et al.* [16] and Kfouri [75] used the path-independent J-integral in conjunction with the interaction integral to calculate T-stress in mode I crack problems. Sladek *et al.* [132] used another type of path-independent integral, based on Betti-Rayleigh reciprocal theorem, for evaluating T-stress in mixed-mode loading. Recently Chen *et al.* [22] investigated T-stress under mode I loading by means of both the Betti-Rayleigh reciprocal theorem and Eshelby's energy momentum tensor (i.e. path-independent J-integral) using the p-version finite element method, and addressed the accuracy of numerical computations.

For brittle FGMs (e.g. $MoSi_2/SiC$ [18], TiC/SiC [70]), T-stress has a significant influence in crack initiation angle [82] and crack stability. However, it is worth mentioning that the present analysis is **not** analogous to the influence of T-stress in changing "constraint", as discussed in many references [32, 105, 92, 5]. Considerations of "constraint" are **not** applicable to the analysis of ideal linearly elastic brittle materials (cf. [133]). Recent work in the field of FGMs include that by Becker *et al.* [72] who have investigated T-stress and finite crack kinking by using a hyperbolic-tangent material gradation with steep gradient of Young's modulus. They found that T-stress in FGMs is affected by both the far-field loading and the far-field phase angle, and that the magnitude of T-stress in FGMs is, on average, greater than that for homogeneous materials with identical geometry. They calculated T-stress using the stress difference along $\theta = 0$, i.e. $\sigma_{xx} - \sigma_{yy}$. On the other hand, Kim and Paulino [82], and Paulino and Kim [114] evaluated T-stress in FGMs using the interaction integral in conjunction with the FEM, and obtained quite accurate results. All of the papers given in this paragraph are concerned with isotropic FGMs.

For anisotropic linearly elastic homogeneous solids, Gao and Chiu [43] investigated slightly curved or kinked cracks under mode I loading in orthotropic elastic solids by means of perturbation analysis, which is based on complex variable representations in the Stroh formalism. They also

7

investigated the effects of mode-mixity, material orthotropy, and T-stress on the behavior of a nearly symmetric crack. Yang and Yuan [148] evaluated the elastic T-stress and higher-order coefficients in the crack tip fields in an anisotropic elastic solid by means of path-independent integrals (J-integral and Betti-Rayleigh reciprocal theorem) and the Stroh formalism. Yang and Yuan [149] also investigated a kinked crack in an anisotropic elastic solid, and evaluated T-stress, stress intensity factors and energy release rates at the main and kinked crack tips by using the integral equation method and the Stroh formalism. All of the above papers in this paragraph are concerned with homogeneous materials. For orthotropic FGMs, Kim and Paulino [85, 84] extended the interaction integral method to evaluating T-stress with reasonable accuracy, and used the Lekhnitskii and Stroh formalisms.

1.2 On a boundary layer model for FGMs

A boundary layer model is presented for FGMs. Marur and Tippur [99] investigated crack-tip stress fields of FGMs using the FEM, and compared numerically obtained angular stress distribution with the asymptotic stress fields for homogeneous materials. This section investigates the behavior of crack-tip fields of exponentially graded materials by means of a boundary layer model, and focuses on the evaluation of auxiliary fields for FGMs.

Figure 1.5(a) illustrates the boundary layer model (e.g. see [5]) for FGMs. Figure 1.5(b) shows the FEM mesh discretization which consists of total 1764 elements with 1728 Q8 elements and 36 T6 elements, e.g. 36 elements in the hoop direction and 49 elements in the radial direction. Young's modulus varies exponentially as given by (see Figure 1.5(a))

$$E(x_1) \;=\; E_0 \exp{(\delta x_1)} \;=\; E_0 \exp{(\beta X_1 + \gamma X_2)}, \qquad (1.4)$$

$$\nu \;=\; \text{constant} = 0.3, \qquad (1.5)$$

where $E_0 = 1$, $\mathbf{X} = (X_1, X_2)$ refers to a global coordinate system, x_1 is the direction of material gradation (inclined by θ_m with respect to the X_1 coordinate), and the nonhomogeneity parameters

8

δ, β, and γ are related by

$$\beta = \delta \cos \theta_m, \quad \gamma = \delta \sin \theta_m. \tag{1.6}$$
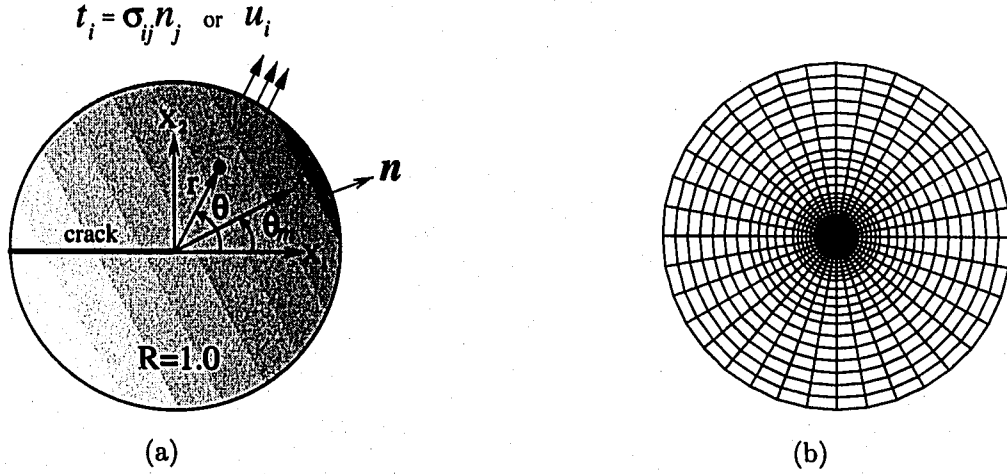
Figure 1.5: Boundary layer model for FGMs: (a) boundary layer model subjected to traction $(t_i = \sigma_{ij} n_j)$ or displacement (u_i) loading. Material properties vary along the x_1 direction inclined by θ_m; (b) the complete finite element mesh using quadratic (Q8 and T6) elements.

The loads can be applied along the outer boundary considering either tractions $(t_i = \sigma_{ij} n_j)$ corresponding to the asymptotic stresses for a homogeneous material given by [34, 147]

$$\sigma_{ij} = \frac{K_I}{\sqrt{2\pi r}} f_{ij}^I(\theta) + \frac{K_{II}}{\sqrt{2\pi r}} f_{ij}^{II}(\theta), \tag{1.7}$$

or corresponding near-tip displacements given by [34, 147]

$$u_i = \frac{K_I}{\mu_{\text{tip}}} \sqrt{\frac{r}{2\pi}} g_i^I(\theta) + \frac{K_{II}}{\mu_{\text{tip}}} \sqrt{\frac{r}{2\pi}} g_i^{II}(\theta). \tag{1.8}$$

The alternative expressions for the asymptotic stresses have been derived by Erdogan [35] for exponentially graded materials with constant Poisson's ratio, and the stress fields are given by [35]

$$\sigma_{ij}(r, \theta) = \exp[r(\beta \cos \theta + \gamma \sin \theta)] \left[\frac{K_I}{\sqrt{2\pi r}} f_{ij}^I(\theta) + \frac{K_{II}}{\sqrt{2\pi r}} f_{ij}^{II}(\theta) \right]. \tag{1.9}$$

A study of the region of dominance of stresses given by Eqs.(1.6) and (1.8) was presented by Anlas

et al. [6].

Figure 1.6 shows FEM results for stresses obtained considering *Mode I* displacement loading, i.e. Eq.(1.7) with $K_{II} = 0$, and material gradation in the X_1 direction and $\beta = 1.0$. The range of Young's modulus $[E(X_1=-1) \; E(X_1=+1)] = [0.367 \; 2.718]$. As expected, due to material gradation, the angular functions for stresses vary with the distance r, however, this behavior is not observed for a homogeneous material. Notice that the shear stress σ_{12}, obtained numerically, is almost zero at $\theta = 0°$. The normal stresses σ_{11} and σ_{22} for the angle $-180° \leq \theta \leq 0°$ are symmetric along the $\theta = 0°$ line, and the shear stress σ_{12} are anti-symmetric along the $\theta = 0°$ line.

Figure 1.7 shows FEM results for stresses obtained considering *Mode II* displacement loading, i.e. Eq.(1.7) with $K_I = 0$, and material gradation in the X_1 direction and $\beta = 1.0$. Again, due to material gradation, the angular functions for stresses vary with the distance r. Notice that the normal stress σ_{22}, obtained numerically, is almost zero at $\theta = 0°$. The shear stress σ_{12} for the angle $-180° \leq \theta \leq 0°$ is symmetric along the $\theta = 0°$ line, and the normal stresses σ_{11} and σ_{22} are anti-symmetric along the $\theta = 0°$ line.
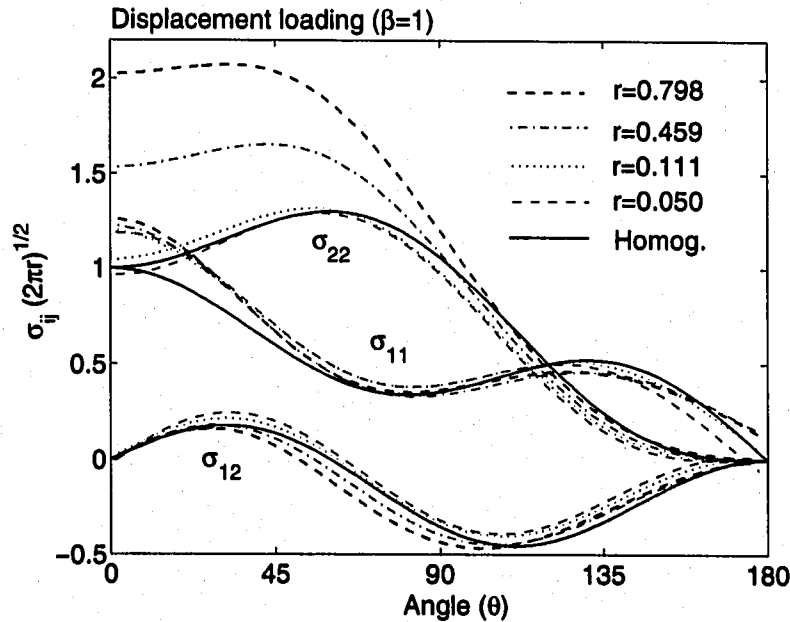
Figure 1.6: FEM results for stresses obtained considering *Mode I* displacement loading and $E(X_1) = E_0 \exp^{\beta X_1}$ with $\beta = 1.0$. The range of Young's modulus $[E(X_1=-1), \; E(X_1=+1)] = [0.367, 2.718]$.

The displacements, strains, and stresses obtained for an exponential material gradation parallel
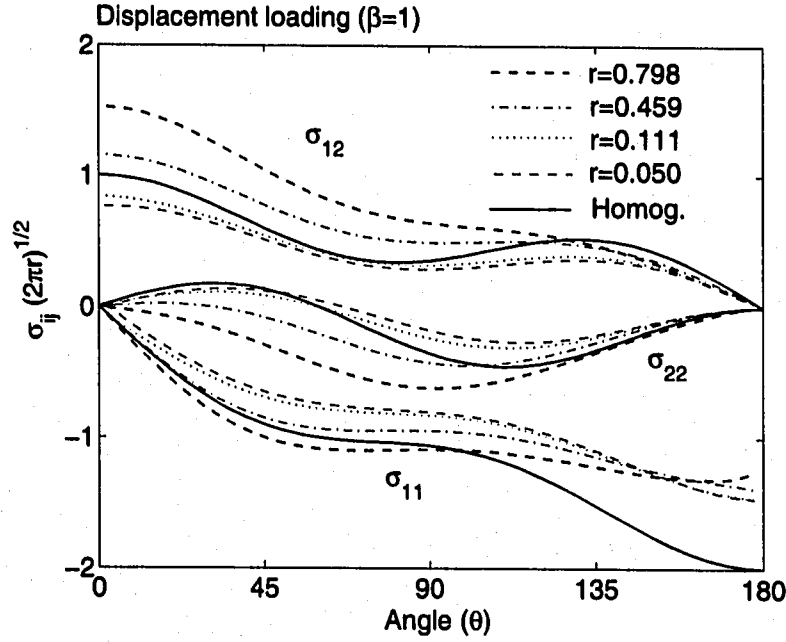
Figure 1.7: FEM results for stresses obtained considering *Mode II* displacement loading and $E(X_1) = E_0 \exp^{\beta X_1}$ with $\beta = 1.0$. The range of Young's modulus $[E(X_1=-1),\ E(X_1=+1)] = [0.367, 2.718]$.

to the crack line satisfy three relations of mechanics, i.e. equilibrium, compatibility, and constitutive relations, and they can be used as auxiliary fields for the interaction integral method in such a specific case. However, the type of material gradation is not restricted to the above case, and the fields for a general type of material gradation, e.g. micromechanics models, can be obtained in a similar manner.

Figure 1.8 shows FEM results for stresses obtained considering *Mode I* displacement loading and material gradation in the x_1 direction inclined by $\theta_m = 45°$ and $\delta = 1.0$. Even under the mode I loading, due to material gradation in the inclined direction, the angular functions for stresses are *not symmetric* along the $\theta = 0°$ line, and they vary with the distance r. Notice that the shear stress σ_{12} is non-zero at $\theta = 0°$, i.e. $K_{II} \neq 0$.

Figure 1.9 shows FEM results for stresses obtained considering *Mode I* displacement loading and material gradation in the X_2 direction inclined by $\theta_m = 90°$ and $\gamma = 1.0$. Again, the angular functions for stresses are *not symmetric* along the $\theta = 0°$ line, and they vary with the distance r. Notice that, again, the shear stress σ_{12} is non-zero at $\theta = 0°$, i.e. $K_{II} \neq 0$.

11
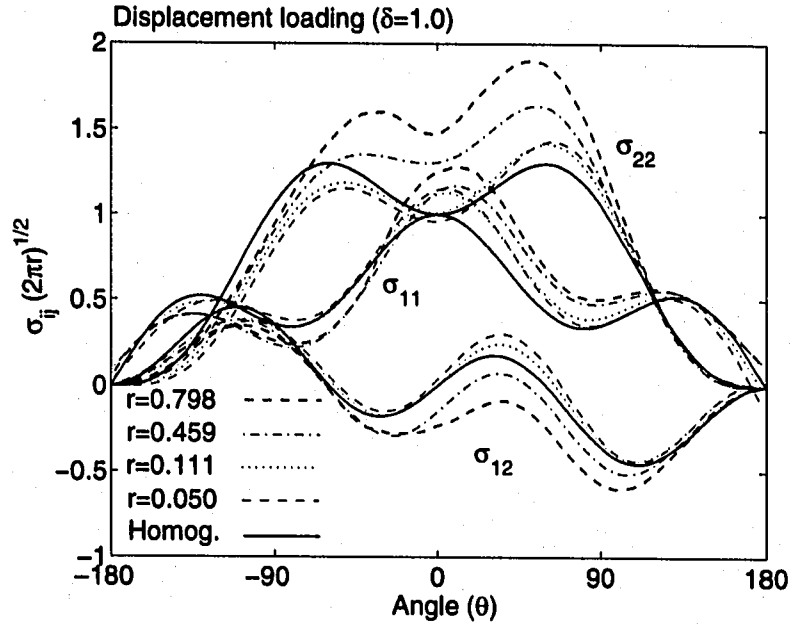
Figure 1.8: FEM results for stresses obtained considering mode I displacement loading and material gradation in the x_1 direction inclined by $\theta_m = 45°$, i.e. $E(x_1) = E_0 \exp^{\delta x_1}$ with $\delta = 1.0$. The range of Young's modulus $[E(x_1{=}{-}1), E(x_1{=}{+}1)] = [0.367, 2.718]$.

1.3   Crack growth in functionally graded materials

Stress intensity factors (SIFs) are important for determining the crack growth direction under mixed-mode loading conditions in brittle FGMs (e.g. ceramic/ceramic such as TiC/SiC). The mixed-mode SIFs in FGMs are functions of material gradients, external loading and geometry. The material gradients do not affect the order of singularity and the angular functions of the singular crack tip fields, but do affect the SIFs. Thus, as explained in the introduction the singular crack-tip fields of FGMs take the same forms as those for homogeneous materials. Here we also consider the local homogenization argument discussed by Gu and Asaro [48] (cf. Figure 1.3).

Assuming the local homogenization crack initiation angles can be predicted by using the same fracture criteria as for a homogeneous material. For instance, these criteria include maximum hoop stress [36], maximum energy release rate [66, 110], minimum strain energy density [130], $K_{II} = 0$ [27], and W-criterion [141, 46]. Recently, Bouchard et $al.$ [13] investigated crack propagation in homogeneous materials, and compared various criteria in terms of crack path prediction. In

12
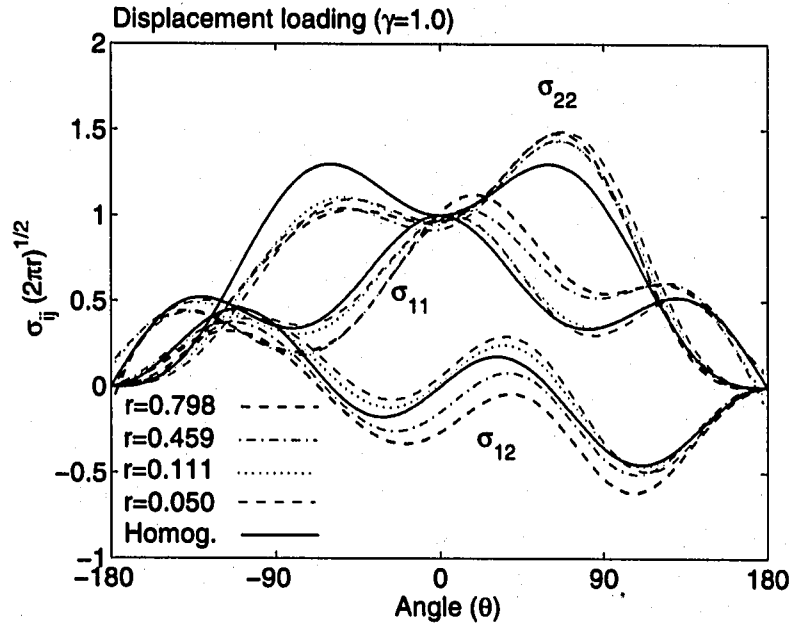
Figure 1.9: FEM results for stresses obtained considering mode I displacement loading and material gradation in the X_2 direction ($\theta_m = 90°$), i.e. $E(X_2) = E_0 \exp^{\gamma X_2}$ with $\gamma = 1.0$. The range of Young's modulus $[E(X_2 = -1), E(X_2 = +1)] = [0.367, 2.718]$.

this thesis, the maximum hoop stress [36] and maximum energy release rate [66] criteria are used to determine crack initiation angles and to check crack growth stability. In addition to crack initiation angle, crack increment is also important to determine crack trajectory. The present approach uses a user-defined crack increment, which needs to be provided at the beginning of each step. For homogeneous materials, Hori and Vaikuntan [62] proposed a formulation to determine the curvature and length of a small crack extension. Thorough investigation on crack increment in FGMs is needed, but it is out of the scope of the present work.

Gu and Asaro [48] investigated crack deflection in brittle FGMs by considering exponential gradation perpendicular to the crack, and used $K_{II} = 0$ criterion [27]. They investigated the effect of material nonhomogeneity on kink angles for three-point bending, double cantilever, four-point bending, and center-cracked specimens. Becker et $al.$ [72] investigated finite crack kinking by considering a hyperbolic-tangent material gradation with steep gradient of Young's modulus. They used the maximum energy release rate [110] and $K_{II} = 0$ [27] criteria. On the other hand, there are an increasing number of fracture experiments on crack growth in FGMs in the literature.

Lin *et al.* [96] investigated mode I fracture of aluminium alloy 2124/SiC FGMs where a crack is parallel to material gradation. Moon *et al.* [101] investigated crack growth resistance (R-curve) behavior of multilayer graded alumina-zirconia FGMs considering a crack parallel to the material gradation. Carpenter *et al.* [17] performed fracture testing and analysis of a layered functionally graded Ti/TiB beam subjected to three-point bending. Rousseau and Tippur [123] performed experimental and numerical investigations on crack kink angles and crack growth for a crack normal to the material gradient in an FGM beam, made of solid A-glass spheres dispersed within a slow curing epoxy matrix, subjected to four-point bending. Lambros *et al.* [91] and Abanto-Bueno and Lambros [1] investigated mode I crack growth for an edge crack in FGMs subjected to fixed-grip loading. The FGMs are fabricated using a polyethylene 1% carbon monoxide co-polymer (ECO) which is subjected to controlled ultraviolet (UV) irradiation time throughout the specimen.

The main focuses of this thesis consist of the accurate evaluation of mixed-mode SIFs using the interaction integral method, the use of selected fracture criteria for crack initiation angles, and the simulation of mixed-mode crack propagation in homogeneous and nonhomogeneous materials. The current approach is mainly concerned with brittle materials, which is characterized by stress intensity factors in linear elastic crack-tip fields.

Chapter 2

Graded finite elements for nonhomogeneous materials

2.1 Introduction

Graded finite elements are presented to model and discretize nonhomogeneous materials. Such elements possess a spatially varying material property field, e.g. Young's modulus (E) and Poisson's ratio (ν) for isotropic materials; and principal Young's moduli (E_{11}, E_{22}), in-plane shear modulus (G_{12}), and Poisson's ratio (ν_{12}) for orthotropic materials. This chapter verifies the formulation of graded finite element, and investigates the behavior of graded and conventional homogeneous elements considering various loading conditions in both isotropic and orthotropic nonhomogeneous materials with respect to available analytical solutions. Figure 2.1 compares the graded elements with conventional homogeneous elements. The graded element incorporates the material property gradient at the size scale of the element, while the homogeneous element produces a step-wise constant approximation to a continuous material property field. The framework described here can serve as the basis for further investigations such as thermal and dynamic problems in functionally graded materials.

2.2 Basic finite element formulation

Displacements for an isoparametric finite element can be written as

$$u^e = \sum_{i=1}^{m} N_i \, u_i^e,$$ (2.1)
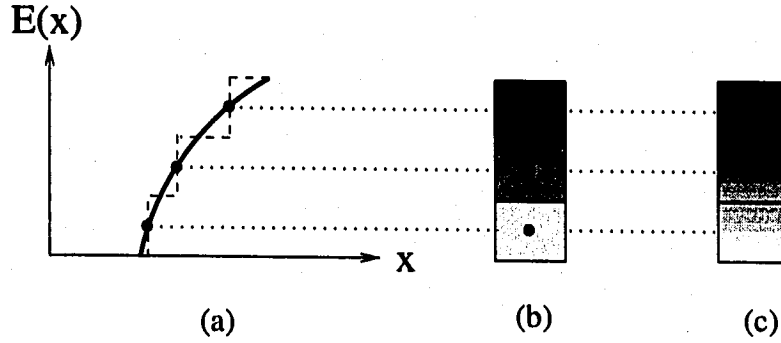
Figure 2.1: Homogeneous versus graded finite elements. (a) Property variation along one coordinate axis; (b) homogeneous elements; (c) graded elements. Notice that the property of the homogeneous element corresponds to the property at the centroid of the graded element.

where N_i are shape functions, u_i^e is the nodal displacements corresponding to node i, and m is the number of nodes in the element. For example, for a Q4 element, the standard shape functions are

$$N_i = (1 + \xi\xi_i)(1 + \eta\eta_i)/4, \qquad i = 1, ..., 4 \tag{2.2}$$

where (ξ, η) denote intrinsic coordinates in the interval $[-1, 1]$ and (ξ_i, η_i) denote the local coordinates of node i. Strains are obtained by differentiating displacements as

$$\varepsilon^e = B^e \, u^e, \tag{2.3}$$

where B^e is the strain-displacement matrix of shape function derivatives. The strain-stress relations are given by

$$\sigma^e = D^e(x) \, \varepsilon^e, \tag{2.4}$$

where $D^e(x)$ is the constitutive matrix, which is a function of spatial position, i.e. $D^e(x) = D^e(x, y)$. For example, for plane stress,

$$D^e(x) = \frac{E(x)}{1 - \nu^2(x)} \begin{bmatrix} 1 & \nu(x) & 0 \\ \nu(x) & 1 & 0 \\ 0 & 0 & \frac{1 - \nu(x)}{2} \end{bmatrix} \tag{2.5}$$

16

and, for plane strain,

$$D^e(x) = \frac{E(x)}{(1 + \nu(x))(1 - 2\nu(x))} \begin{bmatrix} 1 - \nu(x) & \nu(x) & 0 \\ \nu(x) & 1 - \nu(x) & 0 \\ 0 & 0 & \frac{1 - 2\nu(x)}{2} \end{bmatrix}. \qquad (2.6)$$

The principle of virtual work yields the following finite element stiffness equations [65]

$$k^e \ u^e \ = \ f^e \quad , \quad k^e \ = \ \int_{\Omega_e} B^{e^T} \ D^e(x) \ B^e \ d\Omega_e \qquad (2.7)$$

where f^e is the load vector, k^e is the element stiffness matrix, and Ω_e is the domain of element (e). A system of algebraic equations is assembled such that

$$K \ u \ = \ F \quad , \quad K_{ij} = \sum k_{ij}^e \quad , \quad F_i = \sum f_i^e . \qquad (2.8)$$

The linear system and the derivatives (e.g. strains and stresses) are recovered using standard procedures.

2.2.1 Generalized isoparametric formulation

Material properties (e.g. at each Gaussian integration point) can be interpolated from the nodal material properties of the element using isoparametric shape functions which are the same for spatial coordinates (x, y):

$$x = \sum_{i=1}^{m} N_i \ x_i, \qquad y = \sum_{i=1}^{m} N_i \ y_i \qquad (2.9)$$

and displacements (u, v):

$$u = \sum_{i=1}^{m} N_i \ u_i, \qquad v = \sum_{i=1}^{m} N_i \ v_i. \qquad (2.10)$$

Thus, by generalization of the isoparametric concept, the Young's modulus $E = E(x)$ and Poisson's ratio $\nu = \nu(x)$ are interpolated as

$$E = \sum_{i=1}^{m} N_i \ E_i, \qquad \nu = \sum_{i=1}^{m} N_i \ \nu_i, \qquad (2.11)$$

respectively, as illustrated by Figure 2.2(a).

<center>(a)</center>   <center>(b)</center>
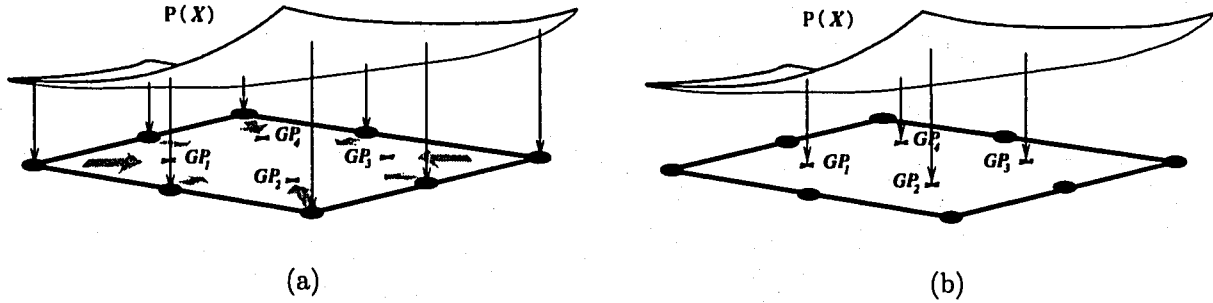
Figure 2.2: Graded finite elements: (a) Generalized isoparametric formulation (GIF); (b) Direct Gaussian integration formulation. The above figure illustrates a graded Q8 element and $P(x)$ denotes a generic material property, e.g. Young's moduli, shear modulus, or the Poisson's ratio. The material properties at the Gauss points (P_{GP}) are either interpolated from nodal material properties (P_i) by $P_{GP} = \sum N_i P_i$ where N are element shape functions or directly sampled.

Similar expansions can also be made to two-dimensional orthotropic materials where the four independent engineering elastic parameters are the principal Young's moduli, $E_{11} \equiv E_{11}(x)$, $E_{22} \equiv E_{22}(x)$, in-plane shear modulus $G_{12} \equiv G_{12}(x)$; and Poisson's ratio $\nu_{12} = \nu_{12}(x)$, i.e.

$$E_{11} = \sum_{i=1}^{m} N_i \, (E_{11})_i, \qquad E_{22} = \sum_{i=1}^{m} N_i \, (E_{22})_i,$$

$$G_{12} = \sum_{i=1}^{m} N_i \, (G_{12})_i, \qquad \nu_{12} = \sum_{i=1}^{m} N_i \, (\nu_{12})_i. \tag{2.12}$$

Unlike the isoparametric formulation, the polynomial order of interpolation functions can be independently selected for displacements and material properties. The characteristics of such non-isoparametric formulations can be explored based on those for conventional subparametric and superparametric elements in the FEM [10, 26].

2.2.2 Direct Gaussian integration formulation

The integral of Eq.(2.7) is evaluated by Gaussian quadrature, and the matrix $D^e(x)$ can be directly specified employing the Young's modulus and the Poisson's ratio at each Gaussian integration point (see Figure 2.2(b)). Thus, for 2D problems, the resulting integral becomes

$$k^e = \sum_i \sum_j B^{e^T} \, D^e(\xi) \, B^e \, t \, J \, W_i \, W_j, \tag{2.13}$$

<center>18</center>

where i and j indicates the corresponding Gauss sampling points in the element, $\boldsymbol{\xi}=(\xi, \eta)$, J is the determinant of the Jacobian matrix, i.e $J=\det(\boldsymbol{J})$, and W_i is the weight corresponding to each Gauss point.

2.3   Mechanics models for nonhomogeneous materials

Mechanics models for FGMs include continuum models and micromechanics-based models. Continuum models are expressed in the form of explicit functions for material properties (i.e. exponentially graded materials). On the other hand, micromechanics-based models involve discrete material properties in terms of volume fractions. For instance, such material models may be given in terms of the volume fraction (V) of a material phase, "p", e.g. the metal phase in a ceramic/metal FGM [71]. In this case, the generalized isoparametric formulation approximates V^p by the standard interpolation

$$V^p = \sum_{i=1}^{m} N_i \, V_i^p, \tag{2.14}$$

where V_i^p $(i = 1, 2, ..., m)$ are the values of V^p at the nodal points. This approach offers a convenient framework to couple the FEM with micromechanics-based models, e.g. self-consistent method. The details on several micromechanics models are given in Appendix A.1.

The above framework allows development of a fully isoparametric formulation in the sense that the same shape functions are used to interpolate the unknown displacements, the geometry, and the material properties. Thus, the actual variation of the material properties may be approximated by the element interpolation functions (e.g. a certain degree of polynomial functions).

2.4   Exact solutions for nonhomogeneous elasticity

Exact solutions for both isotropic and orthotropic FGMs will be used as reference solutions for the numerical examples that follow. Let's consider an *orthotropic* functionally graded plate of infinite length and finite width subjected to various loading conditions such as remote fixed grip, tension, and bending, as shown in Figure 2.3. Both exponential and linear material variations are considered. First, analytical solutions for stresses and displacements are developed for orthotropic

FGMs and, afterwards, they are particularized (e.g. in the limit) for isotropic FGMs. The analytical solutions for exponentially graded isotropic FGMs coincide with those of Erdogan and Wu [39]. The analytical solutions for linearly graded isotropic and orthotropic FGMs are derived in the paper by Kim and Paulino [77].

2.4.1 Exponential material variation

Let's consider a plate under plane stress conditions (see Figure 2.3) made of a nonhomogeneous orthotropic material. Assume the Poisson's ratio (ν_{12}) constant, and the Young's moduli and in-plane shear modulus with variations given by the following expressions:

$$
\begin{aligned}
E_{11}(x) &= E_{11}^0 \, e^{\beta_{11} \, x}, \\
E_{22}(x) &= E_{22}^0 \, e^{\beta_{22} \, x}, \\
G_{12}(x) &= G_{12}^0 \, e^{\beta_{12} \, x}, \\
\nu_{12}(x) &= \text{constant},
\end{aligned}
\tag{2.15}
$$

where $E_{11}^0 = E_{11}(0)$, $E_{22}^0 = E_{22}(0)$, and $G_{12}^0 = G_{12}(0)$ are the material properties at the $x = 0$ line (see Figure 2.3(a)), and the coefficients β_{ij} above are independent nonhomogeneity parameters characterized by

$$
\begin{aligned}
\beta_{11} &= \frac{1}{W} \log \left[\frac{E_{11}(W)}{E_{11}(0)} \right], \\
\beta_{22} &= \frac{1}{W} \log \left[\frac{E_{22}(W)}{E_{22}(0)} \right], \\
\beta_{12} &= \frac{1}{W} \log \left[\frac{G_{12}(W)}{G_{12}(0)} \right],
\end{aligned}
\tag{2.16}
$$

where W is the width of the FGM plate as shown in Figure 2.3. Notice that in this case the β_{ij} parameters have units $[Length]^{-1}$.

For a corresponding nonhomogeneous isotropic material ($E=E_{11}=E_{22}$, $\nu_{12}=\nu$), the Poisson's

ratio is assumed constant and Young's modulus varies exponentially, i.e.

$$E(x) = E^0 e^{\beta x}$$

$$\nu(x) = \text{constant} \tag{2.17}$$

where $E^0 = E(0)$. The nonhomogeneity parameter β is given by

$$\beta = \frac{1}{W} \log \left[\frac{E(W)}{E(0)} \right], \tag{2.18}$$

which has units $[Length]^{-1}$.

(a)   (b)   (c)   (d)
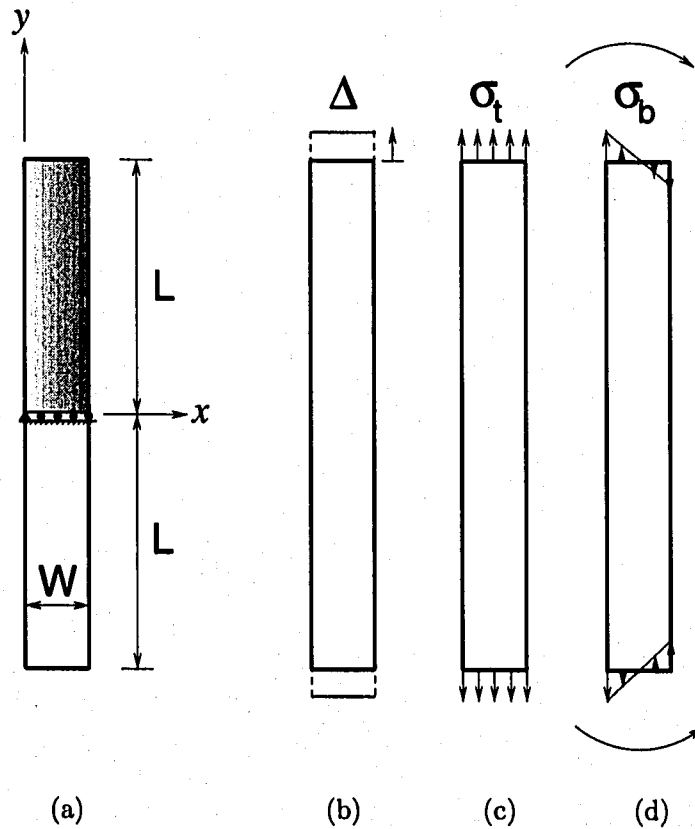
Figure 2.3: A graded plate: (a) geometry – the shaded region indicates the symmetric region of the plate used in the present FEM analyses; (b) fixed-grip loading; (c) tension; (d) bending. The displacement boundary conditions shown in (a) remain the same for all the three loading conditions.

Fixed-grip loading

For fixed grip loading (see Figure 2.3(b)) with $\varepsilon_{yy}(x, y) = \varepsilon_0$, the stress distribution becomes

$$\sigma_{yy}(x) = E_{22}^0 \, \varepsilon_0 \, e^{\beta_{22} \, x}. \tag{2.19}$$

Using strain-displacement relations and the boundary conditions

$$u_x(0, 0) = 0 \quad , \quad u_y(x, 0) = 0, \tag{2.20}$$

one obtains the displacements [77]

$$
\begin{aligned}
u_x(x, y) &= -\nu_{12} \, \varepsilon_0 \frac{E_{22}^0}{E_{11}^0} \, \frac{1}{\beta_{22} - \beta_{11}} \left[e^{(\beta_{22} - \beta_{11})x} - 1 \right] \\
u_y(x, y) &= \varepsilon_0 \, y.
\end{aligned}
\tag{2.21}
$$

Notice that for isotropic materials ($E = E_{11} = E_{22}$, $\nu_{12} = \nu$), the stress distribution Eq.(2.19) becomes [39]

$$\sigma_{yy}(x) = E^0 \, \varepsilon_0 \, e^{\beta x}, \tag{2.22}$$

and the displacements are obtained in the limit of Eq.(2.21) as $(\beta_{22} - \beta_{11}) \rightarrow 0$. Thus

$$
\begin{aligned}
u_x(x, y) &= -\nu \, \varepsilon_0 \, x \\
u_y(x, y) &= \varepsilon_0 \, y.
\end{aligned}
\tag{2.23}
$$

Tension and bending

For tension and bending loads (see Figures 2.3(c) and 2.3(d), respectively), the applied stresses are defined by

$$N = \sigma_t \, W \quad , \quad M = \frac{\sigma_b W^2}{6}, \tag{2.24}$$

where N is a membrane resultant along the $x = W/2$ line (see Figure 2.3(a)), and M is the bending moment. For these two loading cases, the compatibility condition $\partial^2 \varepsilon_{yy} / \partial x^2 = 0$ gives

22

$\varepsilon_{yy} = Ax + B$, and thus

$$\sigma_{yy}(x) = E_{22}^0 \, e^{\beta_{22}x} \, (Ax + B) \tag{2.25}$$

where the constants A (with unit $[Length]^{-1}$) and B (dimensionless) are determined from

$$\int_0^W \sigma_{yy}(x) \, dx = N \quad , \quad \int_0^W \sigma_{yy}(x)x \, dx = M \tag{2.26}$$

by considering

$$M = NW/2 \quad \text{for tension}$$
$$N = 0 \qquad \text{for bending.} \tag{2.27}$$

Thus, for tension load, the stress distribution is given by Eq.(2.25) with [77]

$$A = \frac{\beta_{22}N}{2E_{22}^0} \left(\frac{W\beta_{22}^2 e^{\beta_{22}W} - 2\beta_{22}e^{\beta_{22}W} + W\beta_{22}^2 + 2\beta_{22}}{e^{\beta_{22}W}\beta_{22}^2 W^2 - e^{2\beta_{22}W} + 2e^{\beta_{22}W} - 1} \right), \tag{2.28}$$

$$B = \frac{\beta_{22}N}{2E_{22}^0} \left(\frac{-W^2\beta_{22}^2 e^{\beta_{22}W} + 3W\beta_{22}e^{\beta_{22}W} - 4We^{\beta_{22}W} + W\beta_{22} + 4}{e^{\beta_{22}W}\beta_{22}^2 W^2 - e^{2\beta_{22}W} + 2e^{\beta_{22}W} - 1} \right).$$

For bending load, the stress distribution is also given by Eq.(2.25), however, the coefficients A and B for this case are [77]

$$A = \frac{\beta_{22}^2 M}{E_{22}^0} \left(\frac{\beta_{22} \left(1 - e^{\beta_{22}W}\right)}{e^{\beta_{22}W}\beta_{22}^2 W^2 - e^{2\beta_{22}W} + 2e^{\beta_{22}W} - 1} \right),$$

$$B = \frac{\beta_{22}^2 M}{E_{22}^0} \left(\frac{\beta_{22}We^{\beta_{22}W} - e^{\beta_{22}W} + 1}{e^{\beta_{22}W}\beta_{22}^2 W^2 - e^{2\beta_{22}W} + 2e^{\beta_{22}W} - 1} \right), \tag{2.29}$$

respectively. For both tension and bending loads, using the strain-displacement relations and the boundary conditions (2.20), one obtains the displacements [77]

$$u_x(x,y) = -\nu_{12} \frac{E_{22}^0}{E_{11}^0} \left\{ \frac{\left(Ax - \frac{A}{\beta_{22}-\beta_{11}} + B\right)}{\beta_{22} - \beta_{11}} e^{(\beta_{22}-\beta_{11})x} + \frac{A - B(\beta_{22} - \beta_{11})}{(\beta_{22} - \beta_{11})^2} \right\} - \frac{A}{2}y^2$$

$$u_y(x,y) = (Ax + B)\, y. \tag{2.30}$$

The constants A and B refer to the appropriate loading case above, either tension (Eq.(2.28)) or bending (Eq.(2.29)).

For the isotropic case ($E=E_{11}=E_{22}$, $\nu_{12}=\nu$), the stress distribution is obtained by Eqs.(2.28) and (2.29) (for tension and bending loads, respectively) with β_{22} replaced by β, which agree with Erdogan and Wu's [39] solution. The displacements are obtained in the limit of Eq.(2.30) as $(\beta_{22} - \beta_{11}) \rightarrow 0$. Thus

$$
\begin{aligned}
u_x(x,y) &= -\nu \left(\frac{A}{2}x^2 + Bx \right) - \frac{A}{2}y^2 \\
u_y(x,y) &= (Ax + B)\, y.
\end{aligned}
\tag{2.31}
$$

2.4.2 Linear material variation

For a plate under plane stress conditions, as illustrated by Figure 2.3, let's assume the Poisson's ratio (ν_{12}) is constant, and the Young's moduli and in-plane shear modulus with variations given by the following expressions:

$$
\begin{aligned}
E_{11}(x) &= E_{11}^0 + \gamma_{11}x, \\
E_{22}(x) &= E_{22}^0 + \gamma_{22}x, \\
G_{12}(x) &= G_{12}^0 + \gamma_{12}x, \\
\nu_{12}(x) &= \text{constant},
\end{aligned}
\tag{2.32}
$$

where $E_{11}^0 = E_{11}(0)$, $E_{22}^0 = E_{22}(0)$, and $G_{12}^0 = G_{12}(0)$ are the material properties at the $x = 0$ line (see Figure 2.3(a)) and the coefficients γ_{ij} are independent nonhomogeneity parameters characterized by

$$
\begin{aligned}
\gamma_{11} &= \frac{E_{11}(W) - E_{11}(0)}{W}, \\
\gamma_{22} &= \frac{E_{22}(W) - E_{22}(0)}{W}, \\
\gamma_{12} &= \frac{G_{12}(W) - G_{12}(0)}{W}.
\end{aligned}
\tag{2.33}
$$

Notice that in this case the γ_{ij} parameters have units $[Force]/[Length]^3$.

24

For a corresponding nonhomogeneous isotropic material ($E=E_{11}=E_{22}$, $\nu_{12}=\nu$), the Poisson's ratio is assumed constant and the Young's modulus varies linearly, i.e.

$$
\begin{aligned}
E(x) &= E^0 + \gamma x, \\
\nu(x) &= \text{constant},
\end{aligned}
\tag{2.34}
$$

where $E^0 = E(0)$. The nonhomogeneity parameter γ is given by

$$
\gamma = \frac{E(W) - E(0)}{W}
\tag{2.35}
$$

which has units $[Force]/[Length]^3$.

Fixed-grip loading

For fixed grip loading (see Figure 2.3(b)) with $\varepsilon_{yy}(x,y) = \varepsilon_0$, the stress distribution becomes

$$
\sigma_{yy}(x) = \varepsilon_0 \ (E_{22}^0 + \gamma_{22} x).
\tag{2.36}
$$

Using strain-displacement relations and the boundary conditions given by Eq.(2.20), one obtains the displacements [77]

$$
\begin{aligned}
u_x(x,y) &= -\nu_{12}\,\varepsilon_0\ \left\{ \frac{\gamma_{22}}{\gamma_{11}}x + \frac{E_{22}^0\,\ln(E_{11}^0 + \gamma_{22}x)}{\gamma_{11}} - \frac{\gamma_{22}E_{11}^0\,\ln(E_{11}^0 + \gamma_{11}x)}{\gamma_{11}^2} \right. \\
&\quad \left. - \left(\frac{E_{22}^0}{\gamma_{11}} - \frac{\gamma_{22}E_{11}^0}{\gamma_{11}^2} \right)\ \ln(E_{11}^0) \right\}, \\
u_y(x,y) &= \varepsilon_0\,y.
\end{aligned}
\tag{2.37}
$$

For isotropic materials ($E = E_{11} = E_{22}$, $\nu_{12} = \nu$), the stress distribution (2.36) becomes

$$
\sigma_{yy}(x) = \varepsilon_0 \ (E^0 + \gamma x),
\tag{2.38}
$$

and the displacements are obtained from Eq.(2.37) as

$$u_x(x, y) = -\nu \, \varepsilon_0 \, x,$$

$$u_y(x, y) = \varepsilon_0 \, y. \tag{2.39}$$

Tension and bending

For tension and bending loads (see Figures 2.3(c) and 2.3(d), respectively), the applied stresses are defined by Eq.(2.24). For these two loading cases, the compatibility condition $\partial^2 \varepsilon_{yy}/\partial x^2 = 0$ gives $\varepsilon_{yy} = Ax + B$ and thus

$$\sigma_{yy}(x) = (E_{22}^0 + \gamma_{22}x) \, (Ax + B), \tag{2.40}$$

where the constants A (with unit $[Length]^{-1}$) and B (dimensionless) are determined from Eq.(2.26). Thus, for tension load, the stress distribution is given by Eq.(2.40) with [77]

$$A = \frac{-\gamma_{22}N}{\frac{1}{6}\gamma_{22}^2 W^3 + \gamma_{22}E_{22}^0 W^2 + (E_{22}^0)^2 W}, \quad B = \frac{N(E_{22}^0 + \gamma_{22}W)}{\frac{1}{6}\gamma_{22}^2 W^3 + \gamma_{22}E_{22}^0 W^2 + (E_{22}^0)^2 W}. \tag{2.41}$$

For bending load, the stress distribution is also given by Eq.(2.40) with [77]

$$A = \frac{-36M \, (2E_{22}^0 + \gamma_{22}W)}{\gamma_{22}^2 W^5 + 6E_{22}^0 \gamma_{22} W^4 + 6(E_{22}^0)^2 W^3}, \quad B = \frac{36M(2E_{22}^0 + \gamma_{22}W) \frac{3\gamma_{22}W^2 + 3E_{22}^0 W}{2\gamma_{22}W + 6E_{22}^0}}{\gamma_{22}^2 W^5 + 6E_{22}^0 \gamma_{22} W^4 + 6(E_{22}^0)^2 W^3}. \tag{2.42}$$

For both tension and bending loads, using the strain-displacement relations and the boundary conditions given by Eq.(2.20), one obtains the displacements as [77]

$$
\begin{aligned}
u_x(x, y) = -\nu_{12} &\left\{ -\left(\frac{E_{11}^0 \gamma_{22} A}{\gamma_{11}^2} - \frac{\gamma_{22}B}{\gamma_{11}} - \frac{E_{22}^0 A}{\gamma_{11}} \right) x \right. \\
&+ \frac{\gamma_{22}A}{2\gamma_{11}}x^2 + \left(\frac{E_{22}^0 B}{\gamma_{11}} - \frac{E_{11}^0 \gamma_{22} B}{\gamma_{11}^2} - \frac{E_{11}^0 E_{22}^0 A}{\gamma_{11}^2} + \frac{(E_{11}^0)^2 \gamma_{22} A}{\gamma_{11}^3} \right) \ln(\gamma_{11}x + E_{11}^0) \\
&\left. - \left(\frac{E_{22}^0 B\gamma_{11}^2 - E_{11}^0 \gamma_{11}\gamma_{22}B - E_{11}^0 E_{22}^0 \gamma_{11} A + (E_{11}^0)^2 \gamma_{22} A}{\gamma_{11}^3} \right) \ln(E_{11}^0) \right\} - \frac{A}{2}y^2, \\
u_y(x, y) = &\ (Ax + B) \, y. \tag{2.43}
\end{aligned}
$$

For the isotropic case ($E = E_{11} = E_{22}$, $\nu_{12} = \nu$), the stress distribution is obtained by Eqs.(2.41) and (2.42) (for tension and bending loads, respectively) with γ_{22} and E_{22}^0, replaced by γ and E^0,

26

respectively. The displacements are obtained from Eq.(2.43) as

$$
\begin{aligned}
u_x(x,y) &= -\nu \left(\frac{A}{2}x^2 + Bx \right) - \frac{A}{2}y^2, \\
u_y(x,y) &= (Ax + B)\, y.
\end{aligned}
\tag{2.44}
$$

Notice that the form of the exact solutions for displacements in orthotropic FGMs differs significantly from that for isotropic FGMs because the former case depend on two principal Young's moduli, while in the latter case the explicit moduli dependence is absent.

2.5 Numerical examples

Although the FEM offers a lot of flexibility in terms of modeling material property variation, the actual choice of properties and boundary value problems in this section was dictated by the analytical solutions derived in Section 2.4 for the plate configuration of Figure 2.3. Here the analytical solutions are compared with the numerical ones.

To verify the present formulation, the boundary conditions of the FEM models are identical to those for the exact solutions. The exact solutions are obtained considering an infinitely long strip for the tension and bending loads, and finite length for the fixed-grip loading. Thus, for the tension and bending cases, the boundary conditions are satisfied by applying the analytical stress distributions (i.e. Eq.(2.25)) on the top edge of the finite plate.

The first example serves as verification, and it considers a finite plate subjected to the analytical stress distributions corresponding to the far-field tension. The second example investigates the performance of graded finite elements using finite length. The numerical results obtained for a *finite* plate under tension or bending loads (not analytical stress distributions) may not reach the exact solutions with a certain accuracy level because of the mismatch of the boundary conditions, but can be approximation to the exact solutions.

2.5.1 Verification example

This example is presented for the verification of the formulation of graded finite elements in the context of element stiffness matrix. Figure 2.4 shows geometry and BCs for a finite FGM plate

27

subjected to the analytical stress distributions corresponding to the far-field tension.

Figure 2.4: Verification example: a finite FGM plate subjected to the exact stress distributions corresponding to far-field tension.

Young's modulus varies exponentially as given by Eq.(2.17) with

$$E_1 = E^0 = E(0) = 1 \quad \text{and} \quad E_2 = E(W) = 5, \qquad (2.45)$$

and Poisson's ratio is constant, i.e. $\nu = 0.3$.

The discretization error can be quantified by the error in the energy norm $||e||$ defined as [153, 115]

$$||e|| = \left(\int_\Omega (\varepsilon - \varepsilon_{FE})^T D(x)(\varepsilon - \varepsilon_{FE}) \, d\Omega \right)^{1/2}, \qquad (2.46)$$

where ε and ε_{FE} are the exact and finite element strain fields, $D(x)$ is the constitutive matrix of FGMs, and Ω is the domain of the problem. Figure 2.5 shows the error in the energy norm $||e||$ calculated considering the whole plate, and also gives useful information on the convergence rate. The notation h denotes the size of the square element. This figure ensures the correct evaluation of the element stiffness matrix of graded finite elements. The 8-node (Q8) quadrilateral elements with 3×3 and 2×2 Gauss quadrature provides higher accuracy and convergence rate than those for 4-node (Q4) quadrilateral elements.
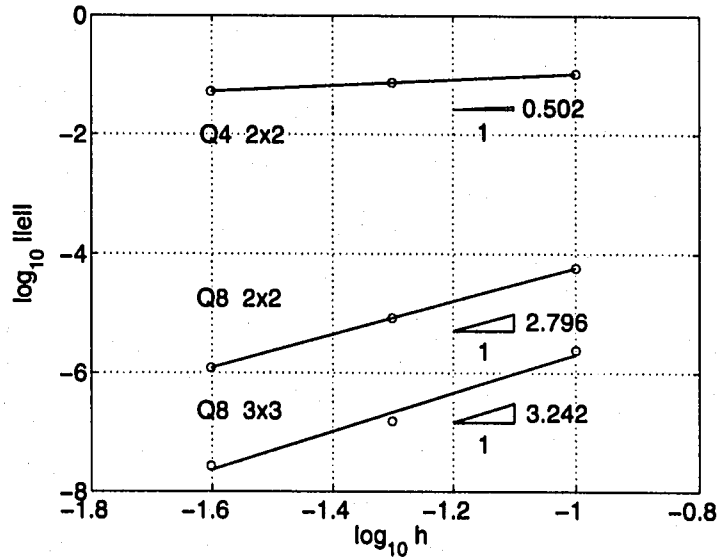
Figure 2.5: Error in the energy norm $\|e\|$ of the problem. The slopes indicate convergence rates.

2.5.2 Plate under far-field loadings

This example is divided into two groups:

1. Isotropic FGM plate

2. Orthotropic FGM plate

For each group, two material variations along the Cartesian direction x are examined:

1. Exponentially graded materials

2. Linearly graded materials

and also the following loading conditions are considered:

1. Fixed grip

2. Tension loading

3. Bending loading

For fixed grip loading (see Figure 2.3(b)), the stress σ_{yy} is considered. For tension applied parallel to the material gradation, the stress σ_{xx} is the quantity of interest, while for tension and bending loads applied perpendicular to the material gradation (see Figures 2.3(c) and 2.3(d), respectively), the stress σ_{yy} is the quantity of interest. Moreover, for a few of the examples, the displacements computed numerically are also compared with the analytical solutions.

The finite element meshes consist of square elements (Q4 or Q8) with edges of unit length. For all the examples, 2×2 Gauss quadrature was employed. All the numerical stress values reported here are nodal values extrapolated directly from the Gauss points and without any averaging. The finite element program developed in this work was implemented in a simple code using MATLAB.

Isotropic FGM plate

Figure 2.6 illustrates an isotropic FGM plate with material variation in the Cartesian direction x subjected to various loading conditions. Figure 2.6(a) shows the basic geometry, boundary conditions and properties. The FEM mesh consists of 9×9 Q4 or Q8 elements (either graded or homogeneous) as illustrated in Figures 2.6(b) to 2.6(d).
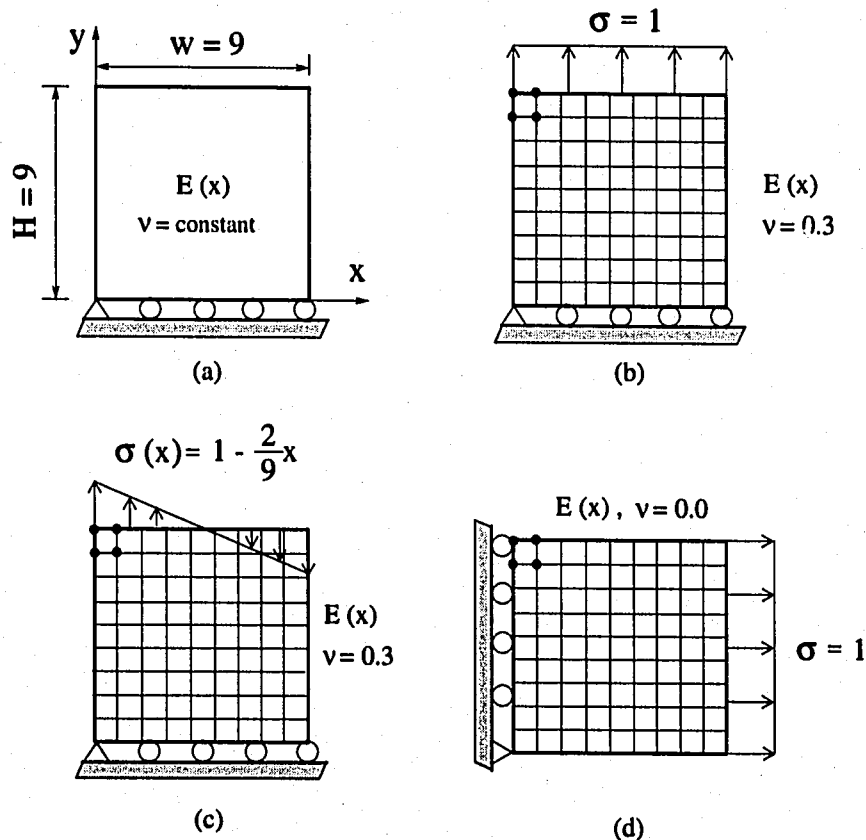
Figure 2.6: Isotropic FGM plate with material variation in the x direction: (a) geometry, boundary conditions and material properties; (b) tension load perpendicular to material gradation; (c) bending load; (d) tension load parallel to material gradation. The finite element mesh (9 × 9 quads: either Q4 or Q8) is illustrated in parts (b) through (d) with a representative Q4 element at the upper left hand corner.

The Young's modulus varies from

$$E_1 = E^0 = E(0) \quad \text{to} \quad E_2 = E(W) \tag{2.47}$$

either exponentially as given by Eq.(2.17) or linearly as given by Eq.(2.34) with E_1=1.0 and E_2=8.0. The independent nonhomogeneity parameters are given by Eqs.(2.18) and (2.35) for the exponential and linear material variations, respectively, with

$$\beta = (\ln(8/1))/9 \quad \text{and} \quad \gamma = 7/9. \tag{2.48}$$

Consistent units are employed here. The Poisson's ratio is constant and it is selected as follows:

$\nu = 0.3$ for tension and bending applied perpendicular to material gradation

(Figures 2.6(b) and 2.6(c), respectively)

$\nu = 0.0$ for tension load parallel to material gradation (Figure 2.6(d)).

The behavior of the elements (homogeneous versus graded) is as follows. Figures 2.7 and 2.8 show the stress σ_{yy} and displacements versus x for an exponentially graded isotropic plate subjected to a uniform displacement in the y direction with $\varepsilon_0 = \Delta/H$. According to Eq.(2.22), the stress σ_{yy} is uniform in the y direction and thus the graph of Figure 2.7 is applicable to the entire range of y coordinates, i.e. $0 \leq y \leq H$ (see Figure 2.6(a)). In this case, the solutions obtained with graded Q4 elements matches the exact solution well. Figure 2.7 also shows that the stress obtained with homogeneous Q4 elements is piecewise constant due to the fact that these elements have a single value for each material property, which leads to a piecewise constant material property approximation as illustrated by Figure 2.1. Therefore such homogeneous elements tend to predict the actual stress values only at their centroids where the properties match the material gradation. Moreover, the amplitude of the nodal stress jumps for homogeneous Q4 elements increases with the coordinate x in a nearly exponential fashion, as illustrated by Figure 2.7. These observations are consistent with those by Santare and Lambros [125]. Of course, the accuracy of the solutions is improved with higher-order graded elements, e.g. Q8 (cf. Figure 2.5). The homogeneous Q8

31

elements also lead to a piecewise constant nodal stress profile with the stress at the midnode location along the x direction matching the exact stress value, which occurs because the material properties at the mid-nodes match the actual material properties.
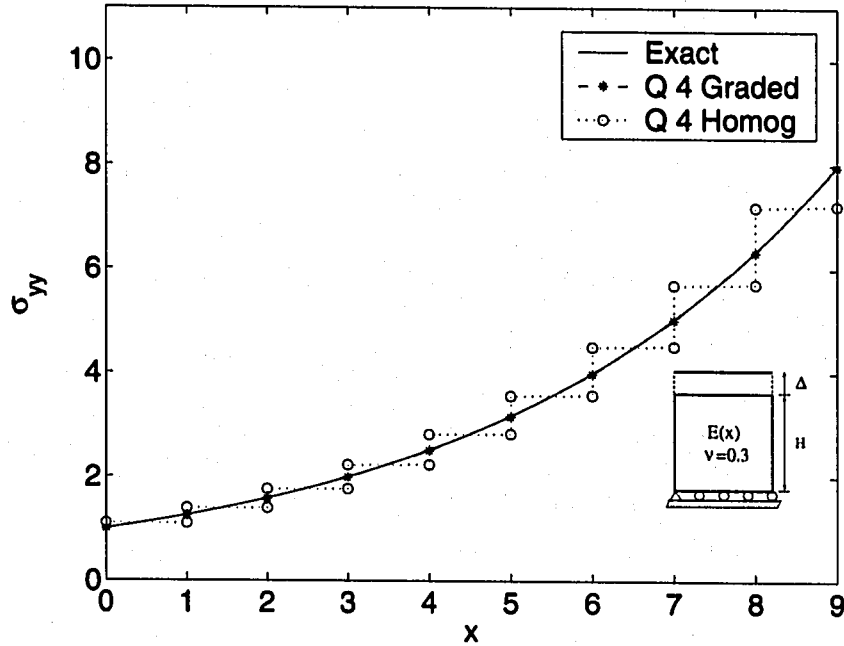
Figure 2.7: Stress distribution (σ_{yy}) using Q4 elements for *fixed grip* $(\varepsilon_0 = \Delta/H)$ load applied perpendicular to the *exponential* material gradation.

Figures 2.9 and 2.10 compare nodal stresses σ_{yy} interpolated from stresses at Gauss integration points using graded and homogeneous Q4 and Q8 elements, respectively, which are subjected to tension loading applied perpendicular to the material gradation. Figures 2.11 and 2.12 show such comparison considering linear material variation. On the left side of the domain in Figures 2.9 to 2.12, the exact solution shows an increasing trend of σ_{yy} with x, while the homogeneous elements (either Q4 or Q8) give σ_{yy} as a decreasing function of x in each individual element. Notice that this problem does not occur with the graded elements.

In this case, the exact solution for displacements is quadratic (see Eqs.(2.31) and (2.44) for exponential and linear material variations, respectively), which coincides with the order of interpolation for the Q8 element. Moreover, the material variation for the linear case is captured by the element shape functions. The stress results for the Q8 element considering exponential and linear material variations are shown in Figures 2.10 and 2.12, respectively. As expected, the homogeneous
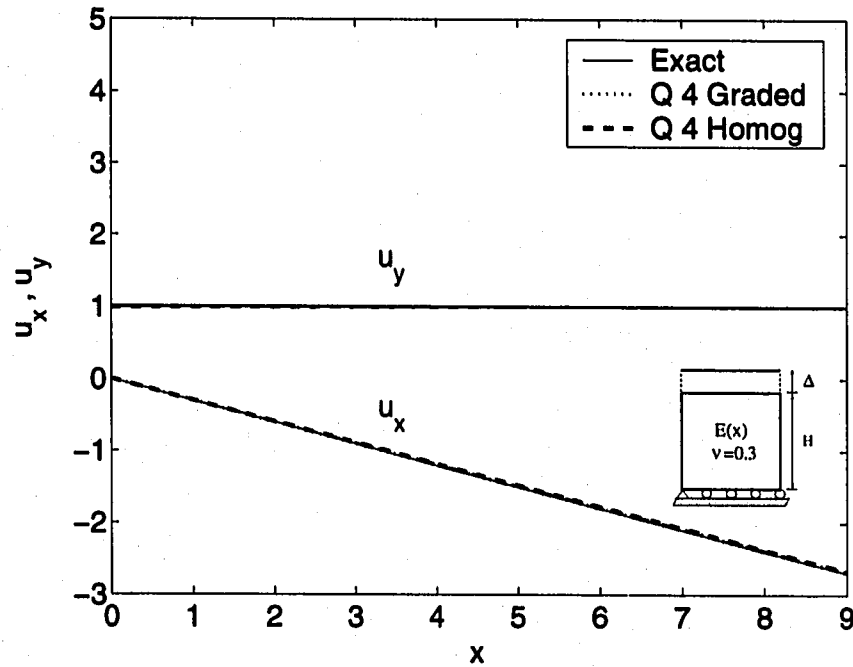
Figure 2.8: Displacements (u_x and u_y) using Q4 elements for *fixed grip* load applied perpendicular to the *exponential* material gradation in isotropic FGMs.

Q8 element shows piecewise variation while the graded Q8 element approaches the analytical solution quite well. The relatively small differences observed between the analytical and graded Q8 solutions may be attributed to the finite plate length (length/width = 1 as shown in Figure 2.6) utilized in the numerical calculation - the analytical solution was derived for an *infinitely long* plate of finite width.

A similar comparison is also made for a different loading case consisting of bending applied perpendicular to the material gradation. Figures 2.13 and 2.14 show the behavior of the Q4 and Q8 elements, respectively, for the exponential variation. Figures 2.15 and 2.16 show such comparison for the bending case considering linear material variation. The stress results for the Q8 element considering exponential and linear material variations are shown in Figures 2.14 and 2.16, respectively. Similar comments to those made comparing the Q8 (homogeneous versus graded) and analytical solutions for the tension load case also hold for the present bending load case.

The above results lead to the following observations. The variation of stress with position x is larger for linear than with exponential material variations (cf. Figures 2.9 and 2.11, 2.10
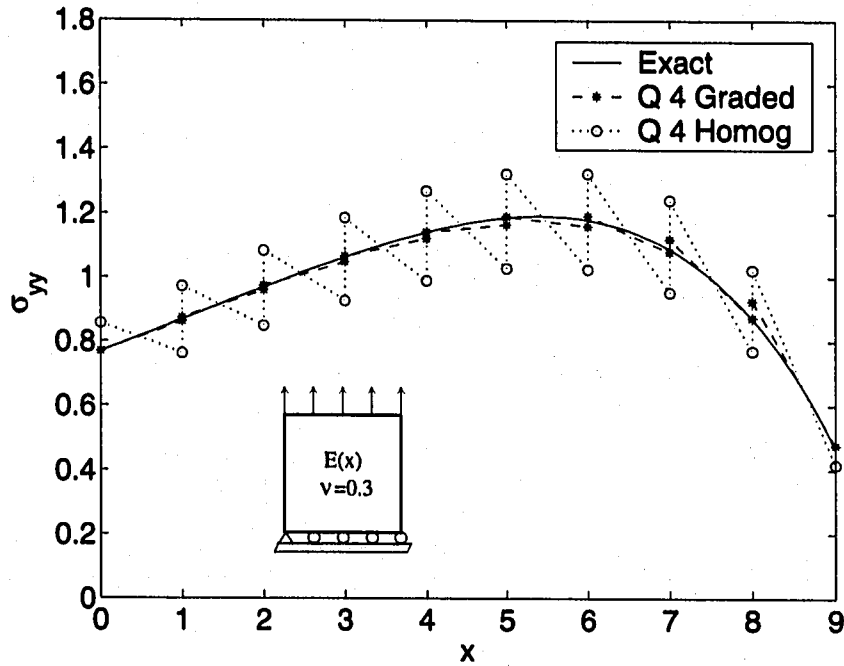
Figure 2.9: Stress distribution (σ_{yy}) using Q4 elements for *tension* load applied perpendicular to the *exponential* material gradation.
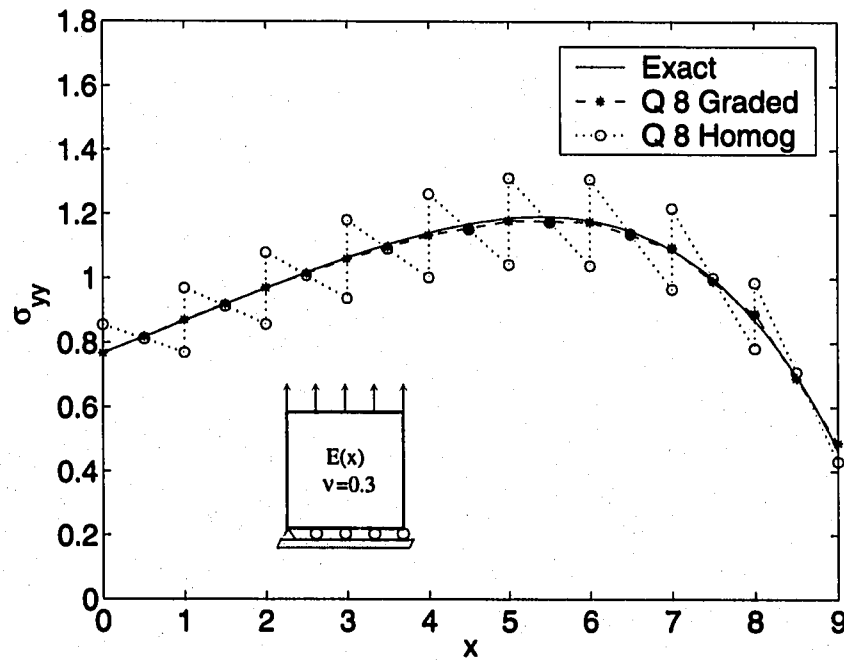
Figure 2.10: Stress distribution (σ_{yy}) using Q8 elements for *tension* load applied perpendicular to the *exponential* material gradation.

34
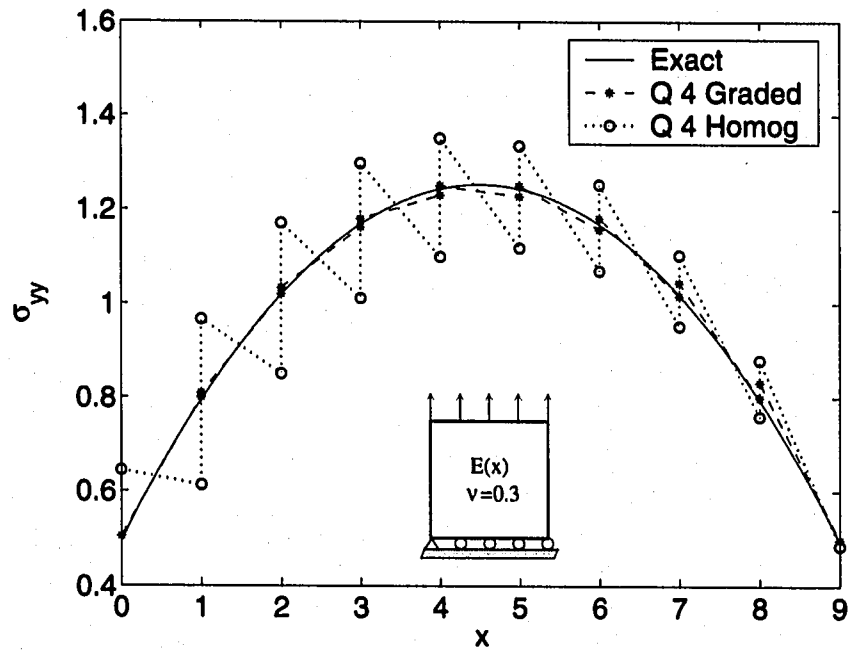
Figure 2.11: Stress distribution (σ_{yy}) using Q4 elements for *tension* loading applied perpendicular to the *linear* material gradation.
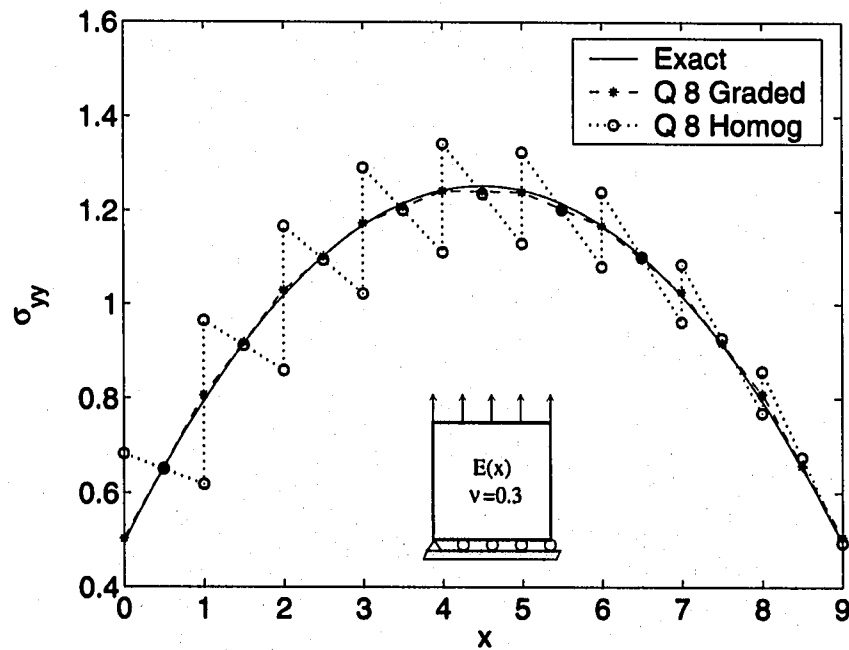
Figure 2.12: Stress distribution (σ_{yy}) using Q8 elements for *tension* load applied perpendicular to the *linear* material gradation.
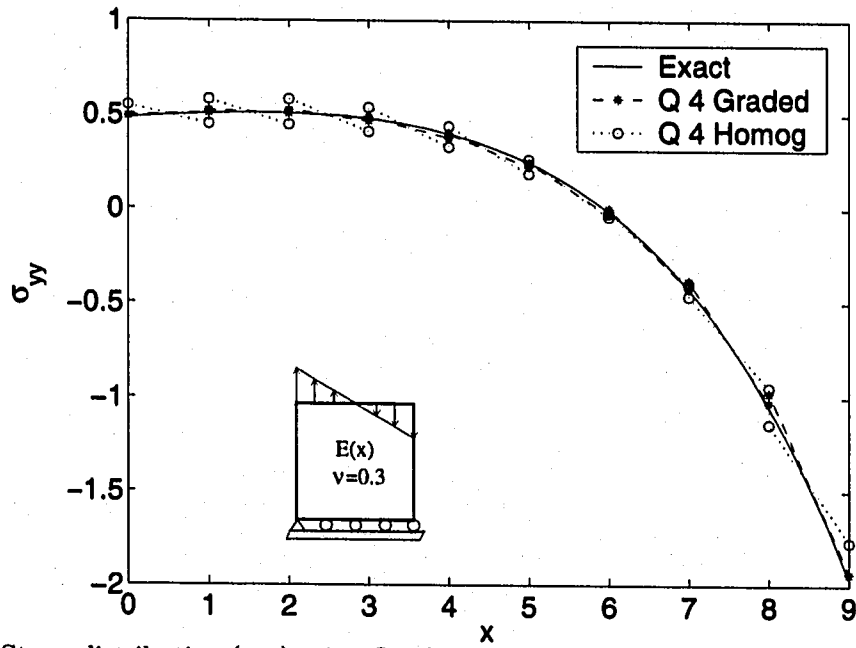
Figure 2.13: Stress distribution (σ_{yy}) using Q4 elements for *bending* load applied perpendicular to the *exponential* material gradation.
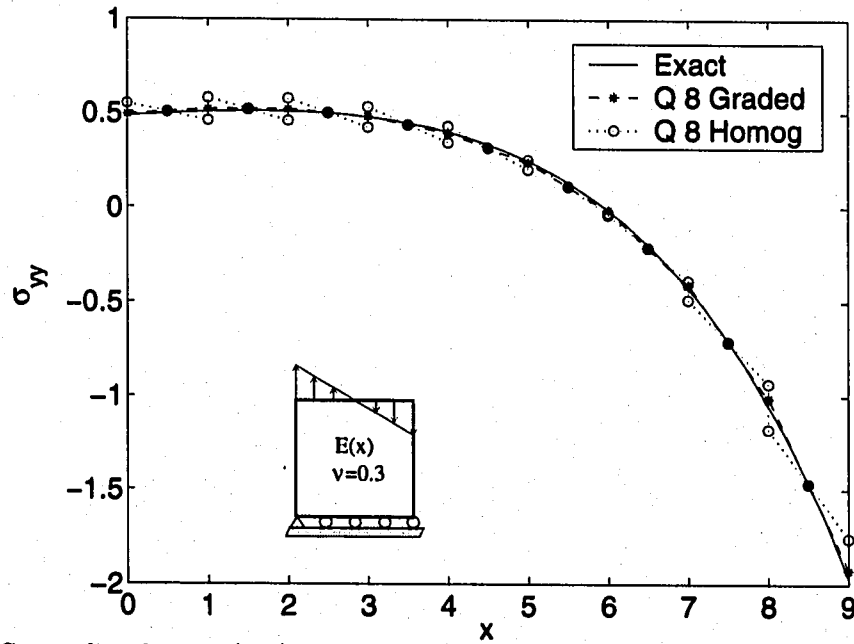
Figure 2.14: Stress distribution (σ_{yy}) using Q8 elements for *bending* load applied perpendicular to the *exponential* material gradation.

and 2.12, 2.13 and 2.15, and 2.14 and 2.16). In general, the amplitude of stress jumps between Q4 elements is larger than between Q8 elements, especially for conventional homogeneous elements (cf.
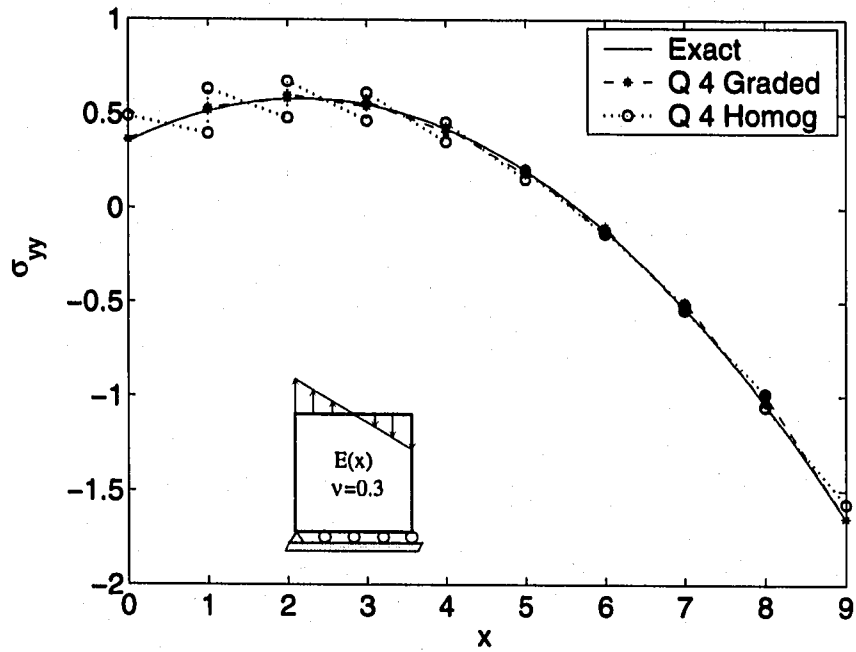
Figure 2.15: Stress distribution (σ_{yy}) using Q4 elements for *bending* load applied perpendicular to the *linear* material gradation.
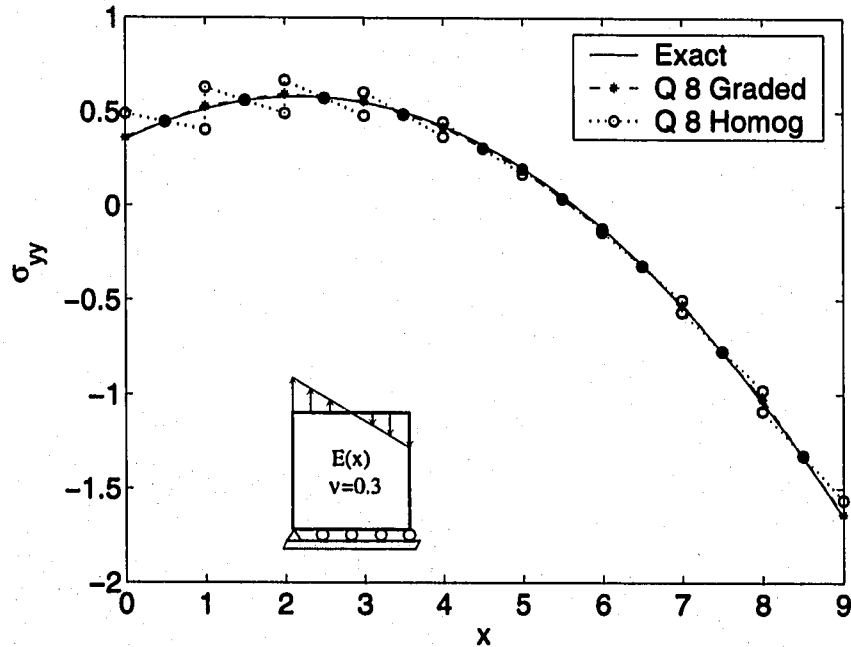
Figure 2.16: Stress distribution (σ_{yy}) using Q8 elements for *bending* load applied perpendicular to the *linear* material gradation.

Figures 2.9 and 2.10, 2.11 and 2.12, 2.13 and 2.14, and 2.15 and 2.16). As expected, the graded elements show superior performance to homogeneous elements, i.e. the graded elements provide a

better approximation to the exact solution in every element. Essentially, the graded elements show good performance in terms of actual (i.e. no averaging) nodal stress (σ_{yy}) along the $y = 0$ line and the homogeneous elements behave well in terms of the averaged nodal stresses.

Figures 2.17 and 2.18 compare nodal stresses of graded versus homogeneous Q4 and Q8 elements (9×9 mesh), respectively, which are subjected to tension applied parallel to the material gradation (see Figure 2.6(d)). The exact solution is $\sigma_{xx} = 1.0$. Different from the observation above, it is interesting to observe in Figure 2.17 that the Q4 graded element shows poor performance when compared to Q4 homogeneous elements for both material variations (i.e. exponential and linear). Although mesh refinement (for a fixed material gradient) increases the accuracy of the solution, the same trend of Figure 2.17 is observed for a finer mesh, e.g. 18×18. Figure 2.17 shows that the Q4 graded elements provide piecewise continuous solutions to the nodal stresses (σ_{xx}), while the homogeneous Q4 elements do recover the exact solution. This is the reverse of the effect seen in the previous load cases. However, a higher order element such as Q8 (either graded or homogeneous) is able to capture the exact solution in this case, as shown in Figure 2.18.
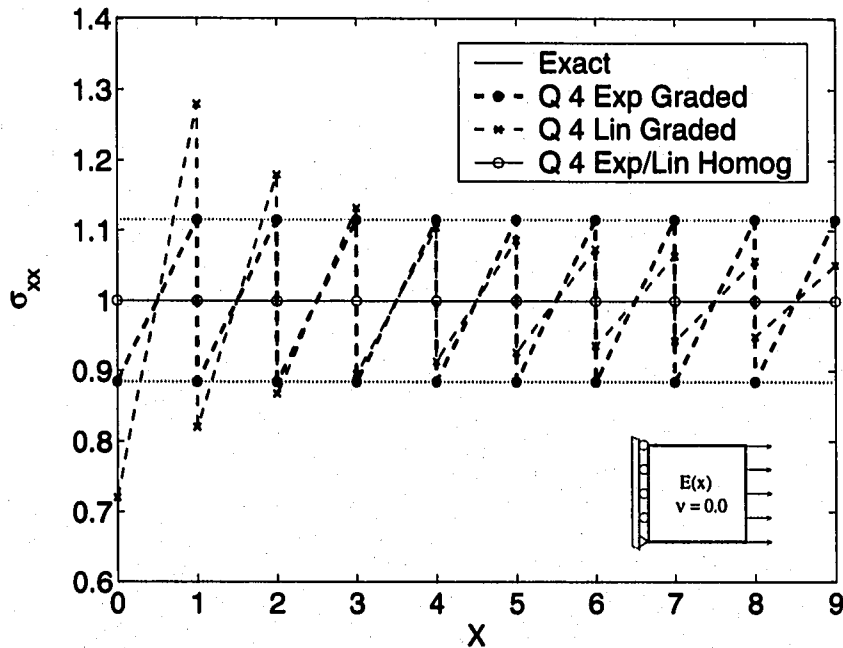
Figure 2.17: Stress distribution (σ_{xx}) using Q4 elements (9×9 mesh) for *tension* load applied parallel to the *exponential* or *linear* material gradation.

A few additional remarks, regarding the behavior of Q4 elements observed in Figure 2.17, are
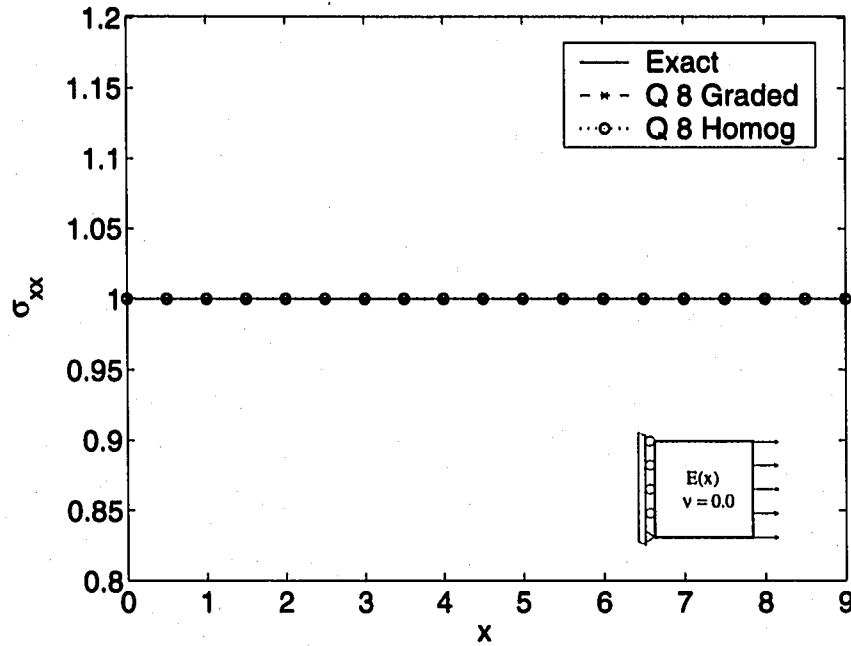
Figure 2.18: Stress distribution (σ_{xx}) using Q8 elements (9 × 9 mesh) for *tension* load applied parallel to the *material* gradation.

in order. Both graded and homogeneous elements lead to the same displacements at all nodes and the same constant strains for each element. Notice that along the $y = 0$ line, the nodal stress range has constant amplitude for the exponential material case, while it has decreasing amplitude for the linear material case (see Figure 2.17). The reason for this behavior is illustrated by Figure 2.19 by investigating the strain distribution for two mesh discretizations (9 × 9 and 18 × 18 meshes). For instance, for the exponential material case, the nodal strains decrease exponentially while the Young's modulus increase exponentially. Thus the multiplication of these two factors cancel each other to give a constant stress amplitude at the nodal points, as shown in Figure 2.17.

Orthotropic FGM plate

Figure 2.20 shows orthotropic FGM plates, with material variation in the Cartesian direction x, subjected to various loading conditions. Figure 2.20(a) shows the basic geometry, boundary conditions and material property variation. The two principal Young's moduli and in-plane shear modulus vary proportionally either with an exponential function of x as given by Eq.(2.15) or with a linear function of x as given by Eq.(2.32). The independent nonhomogeneity parameters

39
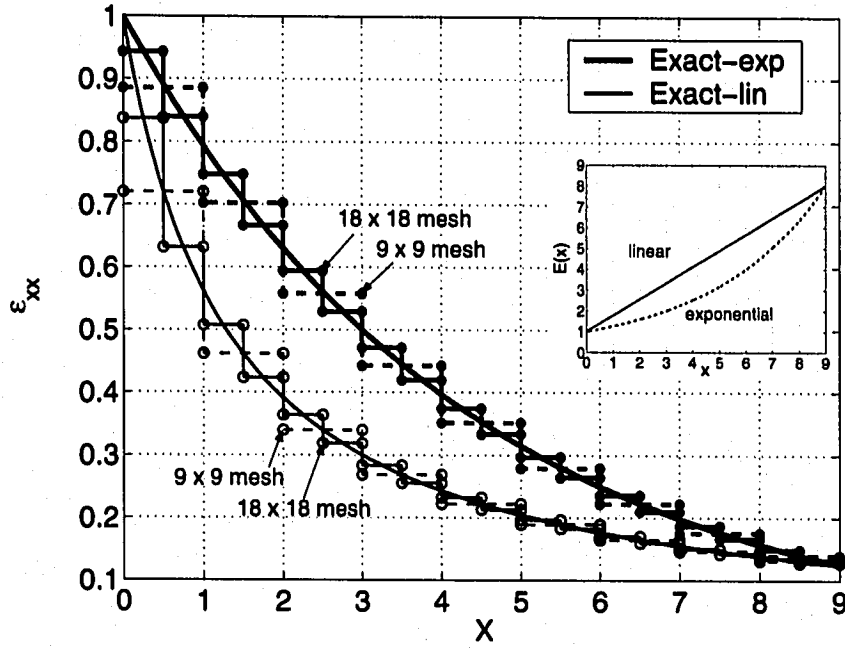
Figure 2.19: Strain distribution (ε_{xx}) using Q4 elements (either 9×9 and 18×18) for *tension* load applied parallel to the material gradation (either exponential or linear).

(β_{ij} and γ_{ij}) are given by Eqs.(2.16) and (2.33) for the exponential and linear material variations, respectively. The Poisson's ratio is assumed constant.

For the examples in Figure 2.20, the FEM mesh consists of either Q4 or Q8 (graded or homogeneous) elements under plane stress. The FEM mesh for the geometry of Figures 2.20(b) and 2.20(c) consists of 9×18 elements. For the sake of completeness, all the properties used in the numerical analyses are given as follows. For the fixed grip, for tension and bending perpendicular to the material gradation, the following data are used for the finite element analysis:

$$E_{11}^0 = 1, \quad E_{22}^0 = 0.1, \quad G_{12}^0 = 0.5, \quad \nu_{12} = 0.3 \tag{2.49}$$

in which consistent units are employed. For tension parallel to the material gradation, the following data are used for the finite element analysis:

$$E_{11}^0 = 1, \quad E_{22}^0 = 0.1, \quad G_{12}^0 = 0.5, \quad \nu_{12} = 0.0. \tag{2.50}$$

40
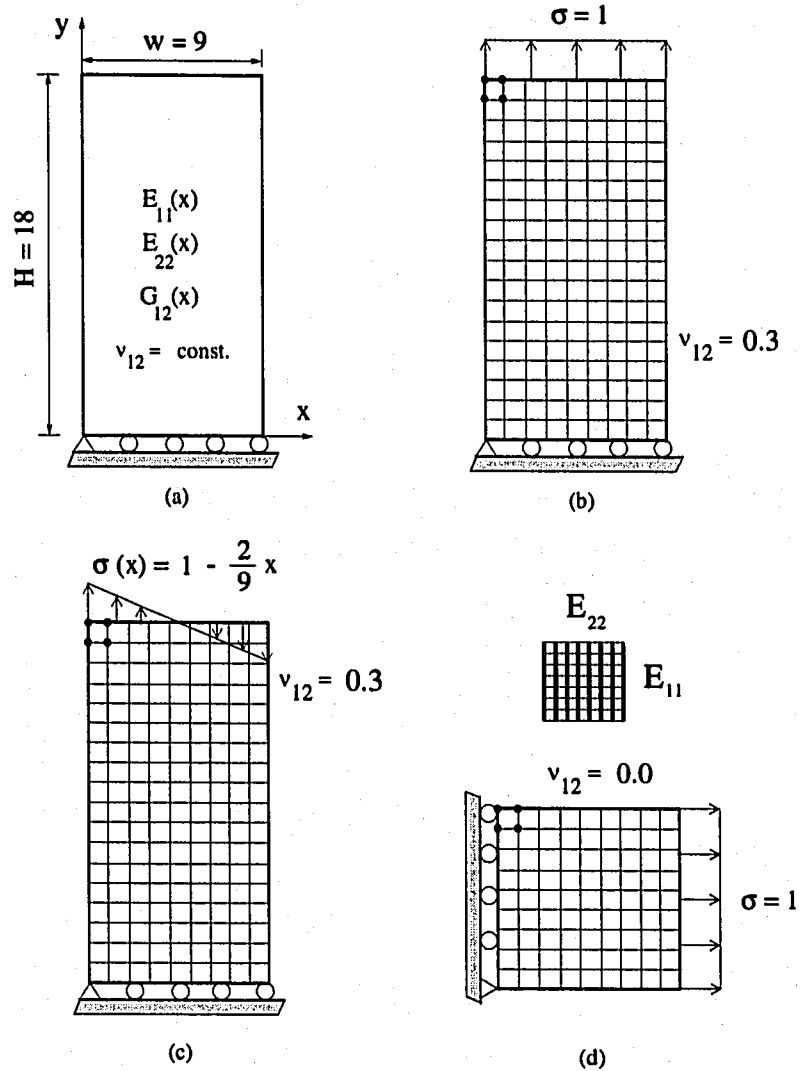
Figure 2.20: Orthotropic FGM plate with material variation in the x direction: (a) geometry, boundary conditions and material properties; (b) tension load perpendicular to material gradation; (c) bending load; (d) tension load parallel to the material gradation. The finite element mesh (Q4 or Q8 elements) is illustrated in parts (b) through (d) with a representative Q4 element at the upper left hand corner.

For the single case of fixed grip loading, only exponential material variation was considered. In this case, the β_{ij} parameters are

$$\beta_{22} = (\ln 8)/9 = \beta, \quad \beta_{11} = \beta/2, \quad \beta_{12} = \beta/3 \tag{2.51}$$

41

so that the range of properties is the following

$$E_{11} = [1, 2.828], \quad E_{22} = [0.1, 0.8], \quad G_{12} = [0.5, 1.0]. \tag{2.52}$$

For all other loading cases (i.e. tension and bending perpendicular to the material gradation, and tension parallel to the material gradation), the β_{ij} parameters, characteristic of exponential material variation, are chosen so that the variations of E_{11}, E_{22}, and G_{12} are proportional [108, 109], i.e.

$$\beta_{11} = \beta_{22} = \beta_{12} = (\ln 8)/9 = \beta, \tag{2.53}$$

and the γ_{ij} parameters, characteristic of linear material variation, are given by

$$\gamma_{11} = 7/9 = \gamma, \quad \gamma_{22} = 0.7/9, \quad \gamma_{12} = 3.5/9 \tag{2.54}$$

so that the range of properties is the following

$$E_{11} = [1.0, 8.0], \quad E_{22} = [0.1, 0.8], \quad G_{12} = [0.5, 4.0]. \tag{2.55}$$

Regarding the element behavior (homogeneous versus graded), several of the observations made for isotropic materials in the previous section also hold for orthotropic materials. Thus rather than repeating those common observations, this section focuses on new observations and insights. Moreover, the analytical solutions of Section 2.4 show that, for exponential material gradation (Section 2.4.1), the relevant stress quantity only depends on the nonhomogeneous parameter β_{22}, and the displacements depend on both β_{11} and β_{22}. For linear material gradation (Section 2.4.2), the relevant stress depends on γ_{22}, and the displacements depend on both γ_{11} and γ_{22}. This information will be helpful to understand the examples reported below.

Figure 2.21 shows the stress σ_{yy} versus x for a nonhomogeneous orthotropic plate, subjected to a uniform displacement in the y direction, with the material properties given by Eqs.(2.49), (2.51), and (2.52). According to Eq.(2.19), the stress σ_{yy} is uniform in the y direction and thus this graph is applicable to the entire range of y coordinates, i.e. $0 \leq y \leq H$ (see Figure 2.20(a)). In this case, the solution obtained with graded Q4 elements agrees with the exact solution within plotting

accuracy. Figure 2.21 also shows that the solution with homogeneous Q4 elements is piecewise constant, which occurs because these conventional elements have a single value for each material property, which leads to a piecewise constant material property approximation as illustrated by Figure 2.1. Therefore such elements predict the actual stress values only at their centroids where the properties match the material gradient functions.
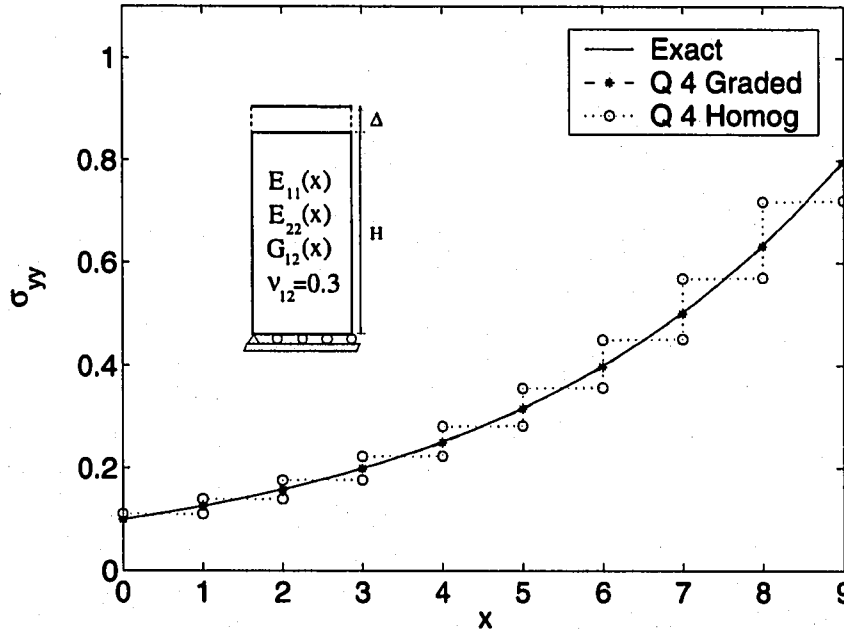
Figure 2.21: Stress distribution (σ_{yy}) using Q4 elements for *fixed grip* loading applied perpendicular to the *exponential* material gradation in orthotropic FGMs ($E_{11}^0 = 1$, $E_{22}^0 = 0.1$, $G_{12}^0 = 0.5$, $\nu_{12} = 0.3$).

Figure 2.22 shows a comparison of the displacements u_x and u_y obtained numerically with those calculated by means of Eq.(2.21). Notice that the nonlinear behavior of u_x is captured quite well by the FEM solution. Obviously, the accuracy of the solutions is also improved with higher-order graded elements, e.g. Q8. Moreover, the homogeneous Q8 elements also lead to a piecewise constant nodal stress profile with the stress at the midnode location along the x direction matching the actual stress values which occurs because the material properties at the mid-nodes match the actual properties.

The example above (Figures 2.21 and 2.22) addressed the orthotropic FGM plate considering nonproportional material properties (see Eq.(2.51)). For proportional variation of material properties (see Eq.(2.53)), the change of u_x with x is linear (rather than the nonlinear function

43
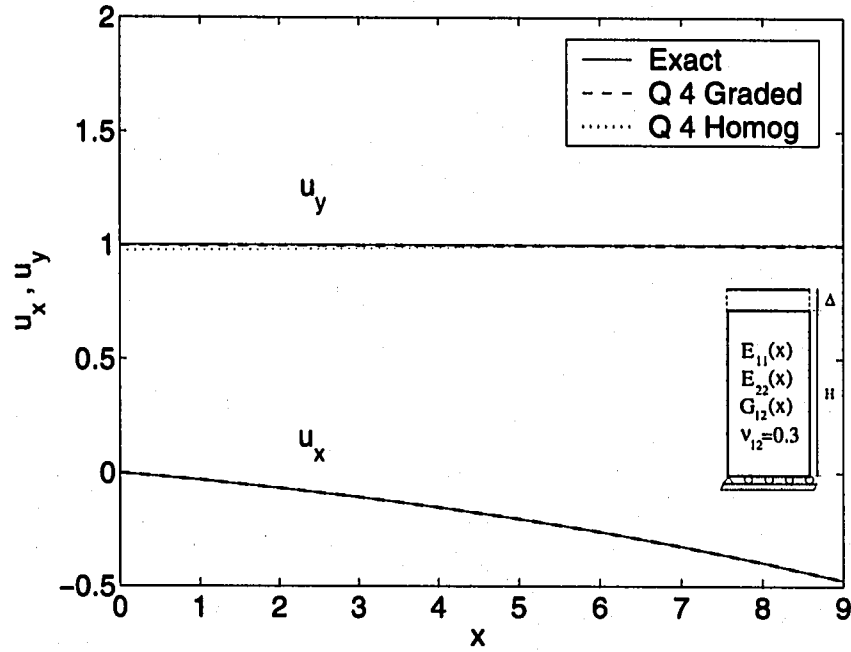
Figure 2.22: Displacements (u_x and u_y) along $y=1$ using Q4 elements for *fixed grip* load applied perpendicular to the *exponential* material gradation in orthotropic FGMs ($E_{11}^0 = 1$, $E_{22}^0 = 0.1$, $G_{12}^0 = 0.5$, $\nu_{12} = 0.3$).

of Eq.(2.21)), which is similar to the behavior of the isotropic plate under the same boundary conditions, i.e. fixed grip (see Figure 2.8). This behavior can be seen by the following limit

$$\lim_{(\beta_{22}-\beta_{11})\to 0} u_x = \lim_{(\beta_{22}-\beta_{11})\to 0} \left\{ -\nu_{12} \, \varepsilon_0 \, \frac{E_{22}^0}{E_{11}^0} \frac{1}{\beta_{22}-\beta_{11}} \left[e^{(\beta_{22}-\beta_{11})} - 1 \right] \right\} = -\nu_{12} \, \varepsilon_0 \, \frac{E_{22}^0}{E_{11}^0} \, x. \quad (2.56)$$

Figures 2.23 and 2.24 compare nodal stresses interpolated from stresses at Gauss points using graded and homogeneous Q4 and Q8 elements, respectively, which are subjected to tension load applied perpendicular to the exponential material gradation. Figure 2.25 shows a comparison of the displacements (u_x and u_y) computed numerically with those obtained by means of Eq.(2.30) for all the element types investigated in the present loading case. The curves for u_y indicate that the best elements in terms of matching the analytical solution (Eq.(2.30)) are Q8 graded, Q8 homogeneous, Q4 graded and Q4 homogeneous, which is somehow expected. Figures 2.26 and 2.27 show the nodal stress plots considering linear material variation. Qualitatively, the nodal stress plots considering linear material variation are somewhat similar to those of Figures 2.23 and 2.24.

44
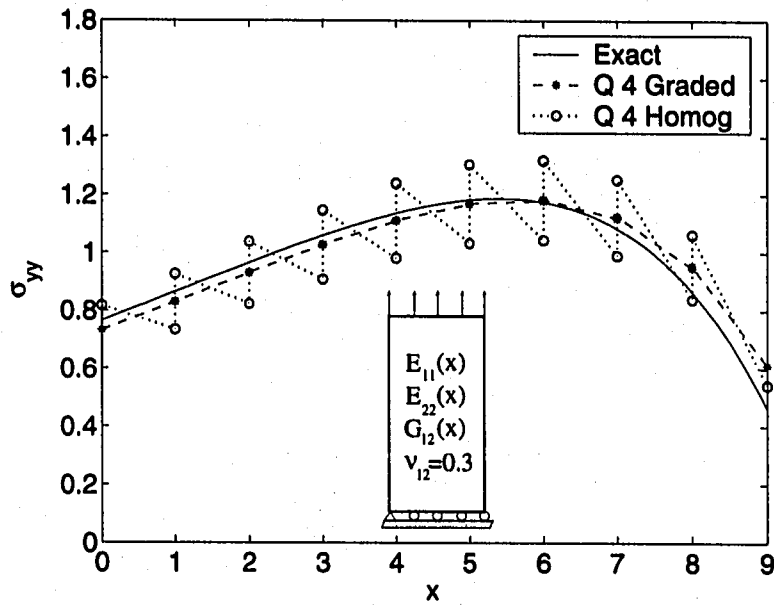
Figure 2.23: Stress distribution (σ_{yy}) using Q4 elements for *tension* loading applied perpendicular to the *exponential* material gradation in orthotropic FGMs ($E_{11}^0 = 1$, $E_{22}^0 = 0.1$, $G_{12}^0 = 0.5$, $\nu_{12} = 0.3$).
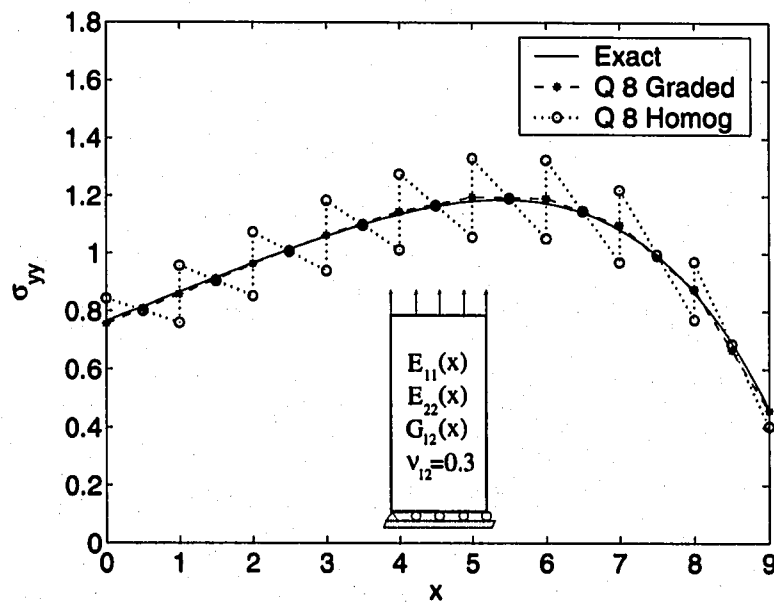
Figure 2.24: Stress distribution (σ_{yy}) using Q8 elements for *tension* loading applied perpendicular to the *exponential* material gradation in orthotropic FGMs ($E_{11}^0 = 1$, $E_{22}^0 = 0.1$, $G_{12}^0 = 0.5$, $\nu_{12} = 0.3$).
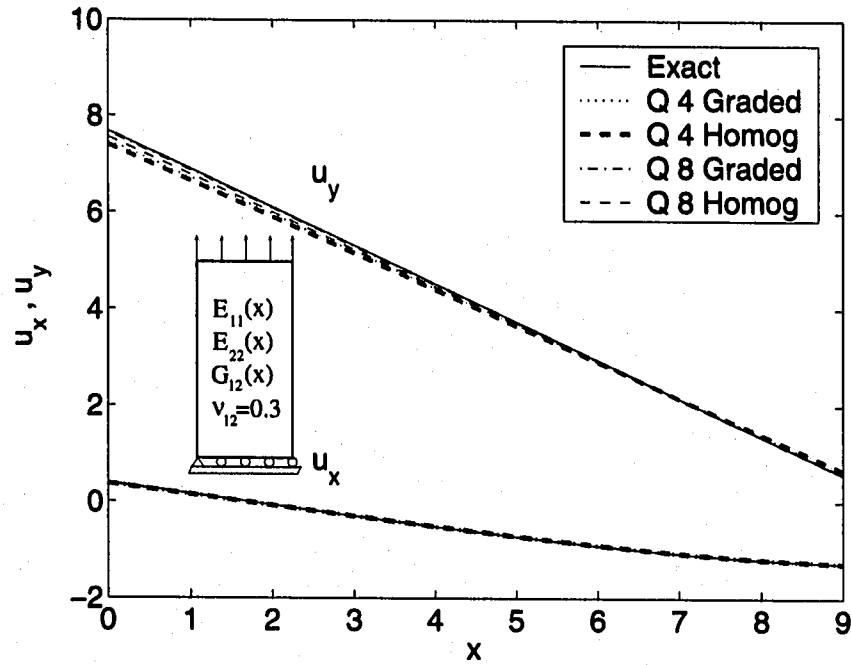
Figure 2.25: Displacements (u_x and u_y) along $y{=}1$ using Q4 and Q8 elements for *tension* load applied perpendicular to the *exponential* material gradation in orthotropic FGMs ($E_{11}^0 = 1$, $E_{22}^0 = 0.1$, $G_{12}^0 = 0.5$, $\nu_{12} = 0.3$).

A similar comparison is also made for a different loading case consisting of bending applied perpendicular to the material gradation. Figures 2.28 and 2.29 present the behavior Q4 and Q8 elements, respectively, for the exponential material variation. Figure 2.30 shows a comparison of the displacements (u_x and u_y) computed numerically with those obtained by Eq.(2.30) for all the element types investigated in the present loading case. As expected, the Q8 elements capture the analytical solution (Eq.(2.30)) for u_y better than the Q4 elements. Figures 2.31 and 2.32 show the nodal stress plots for the bending case considering linear material variation.
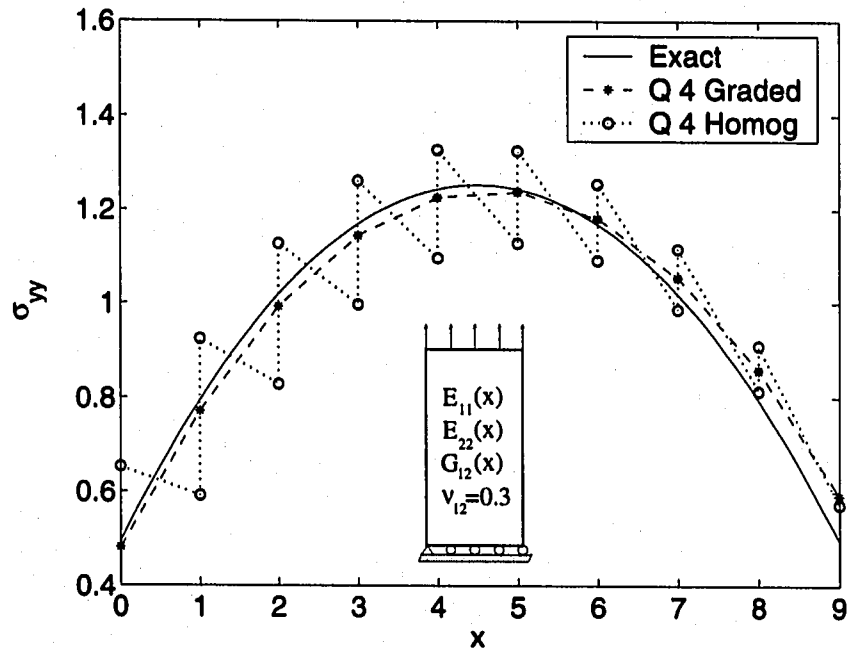
Figure 2.26: Stress distribution (σ_{yy}) using Q4 elements for *tension* loading applied perpendicular to the *linear* material gradation in orthotropic FGMs ($E_{11}^0 = 1$, $E_{22}^0 = 0.1$, $G_{12}^0 = 0.5$, $\nu_{12} = 0.3$).
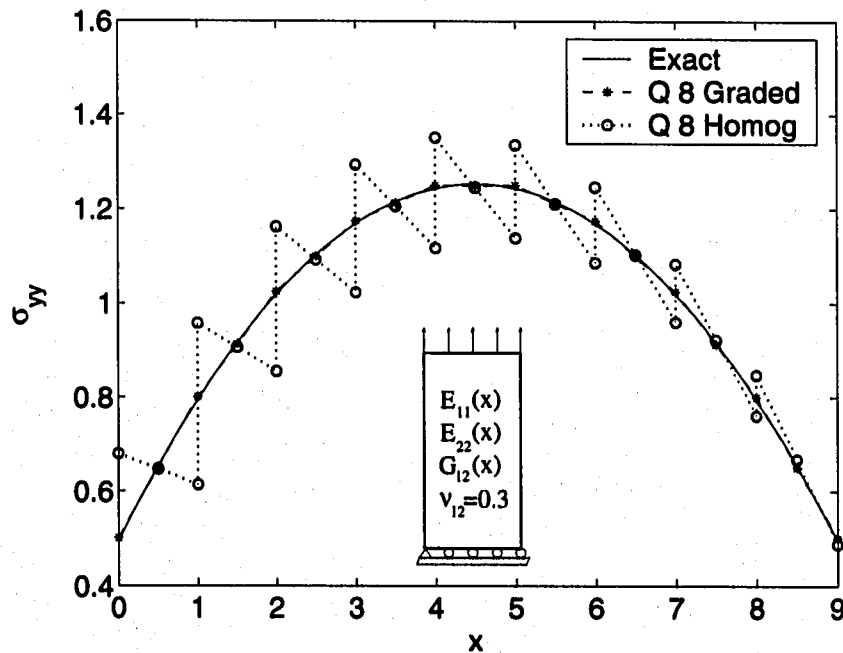
Figure 2.27: Stress distribution (σ_{yy}) using Q8 elements for *tension* load applied perpendicular to the *linear* material gradation in orthotropic FGMs ($E_{11}^0 = 1$, $E_{22}^0 = 0.1$, $G_{12}^0 = 0.5$, $\nu_{12} = 0.3$).
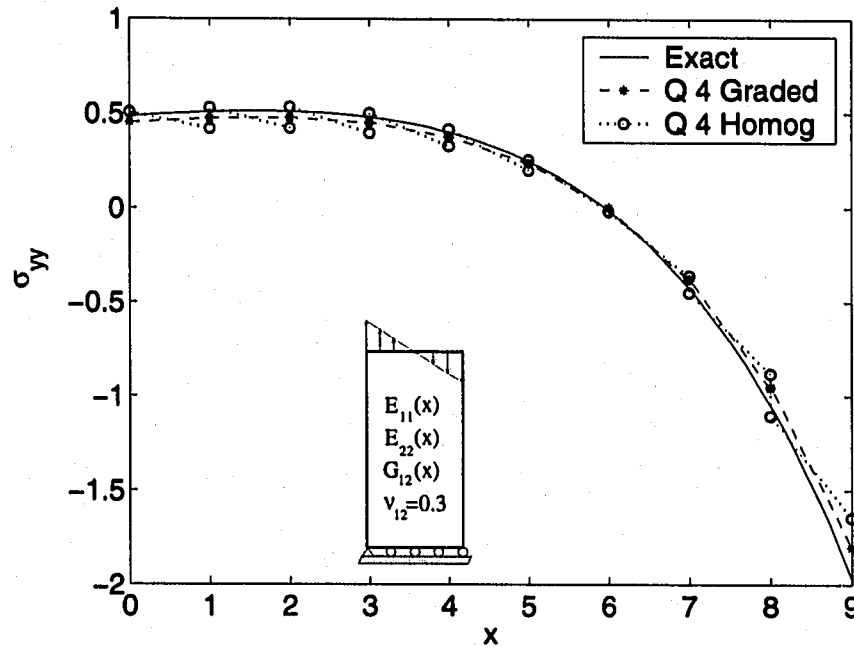
Figure 2.28: Stress distribution (σ_{yy}) using Q4 elements for *bending* load applied perpendicular to the *exponential* material gradation in orthotropic FGMs ($E_{11}^0 = 1$, $E_{22}^0 = 0.1$, $G_{12}^0 = 0.5$, $\nu_{12} = 0.3$).
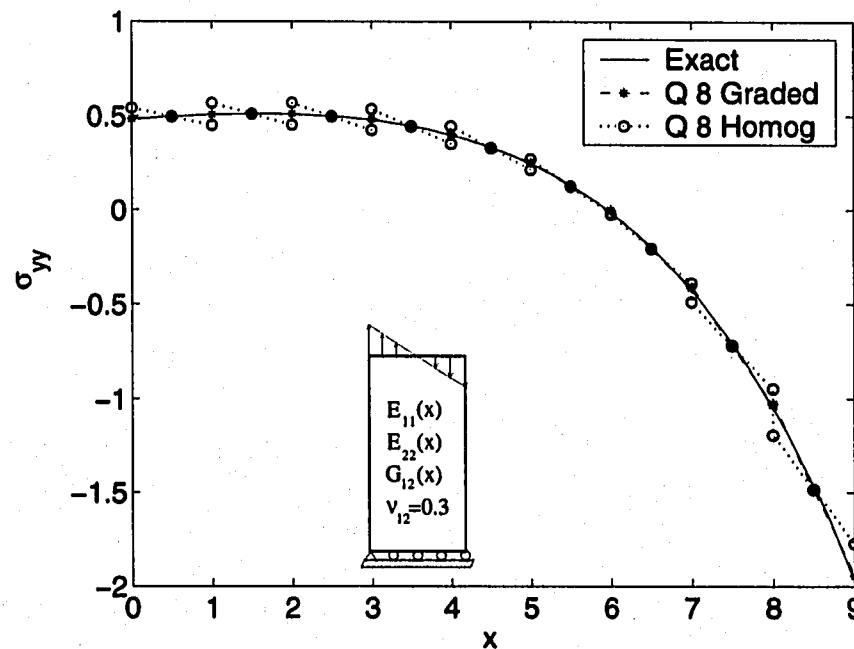
Figure 2.29: Stress distribution (σ_{yy}) using Q8 elements for *bending* load applied perpendicular to the *exponential* material gradation in orthotropic FGMs ($E_{11}^0 = 1$, $E_{22}^0 = 0.1$, $G_{12}^0 = 0.5$, $\nu_{12} = 0.3$).
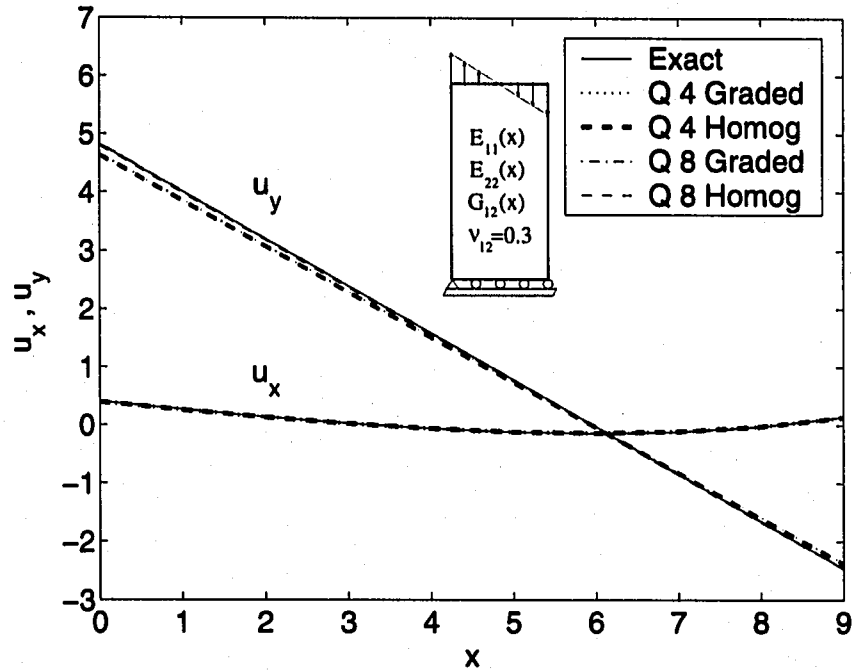
Figure 2.30: Displacements (u_x and u_y) along $y{=}1$ using Q4 and Q8 elements for *bending* load applied perpendicular to the *exponential* material gradation in orthotropic FGMs ($E_{11}^0 = 1$, $E_{22}^0 = 0.1$, $G_{12}^0 = 0.5$, $\nu_{12} = 0.3$).
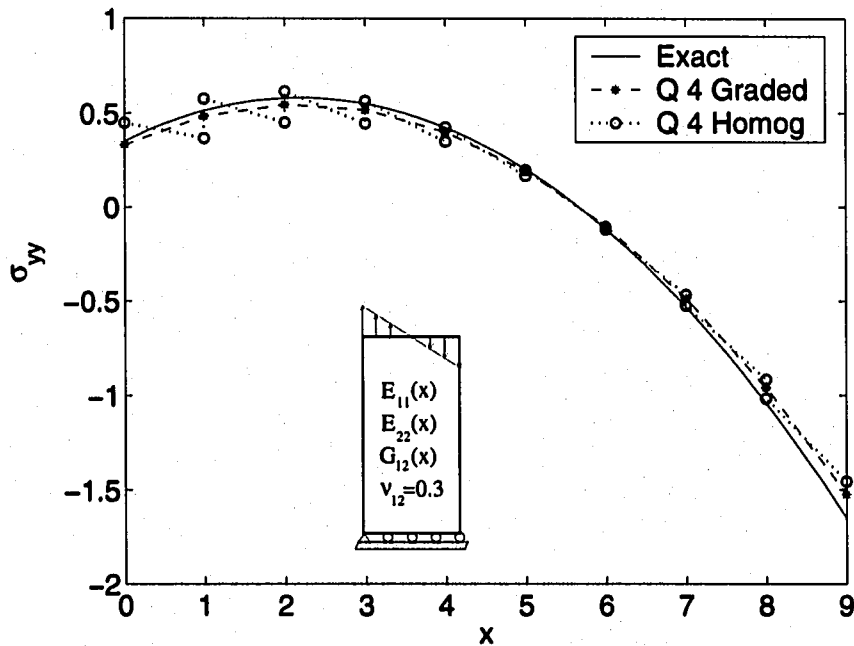
Figure 2.31: Stress distribution (σ_{yy}) using Q4 elements for *bending* load applied perpendicular to the *linear* material gradation in orthotropic FGMs ($E_{11}^0 = 1$, $E_{22}^0 = 0.1$, $G_{12}^0 = 0.5$, $\nu_{12} = 0.3$).

49
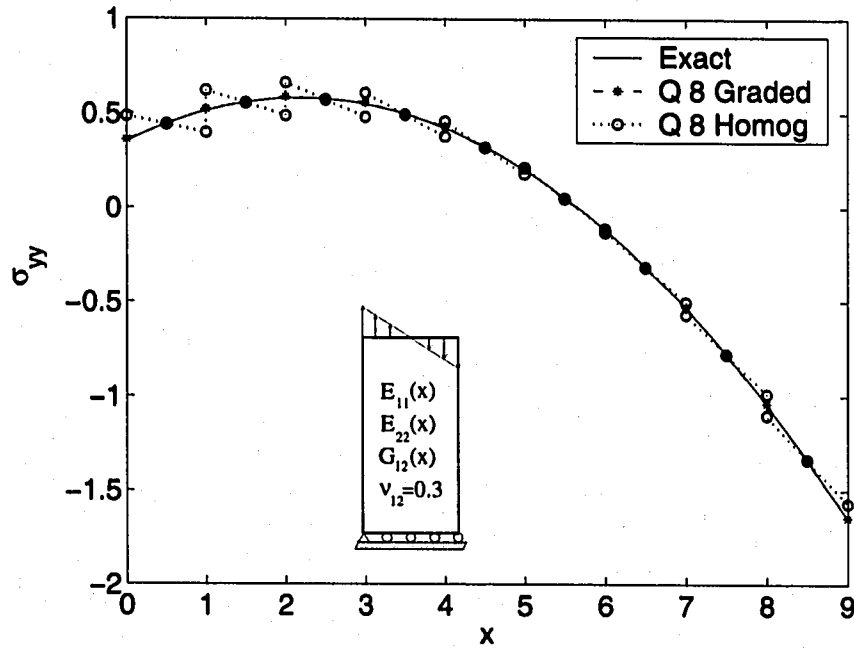
Figure 2.32: Stress distribution (σ_{yy}) using Q8 elements for *bending* load applied perpendicular to the *linear* material gradation in orthotropic FGMs ($E_{11}^0 = 1$, $E_{22}^0 = 0.1$, $G_{12}^0 = 0.5$, $\nu_{12} = 0.3$).

Finally, a few comments regarding the case of tension loading applied parallel to the material gradation in orthotropic FGMs (Figure 2.20(d)) are in order. Qualitatively, the counter-intuitive behavior of homogeneous versus graded Q4 elements is similar to the case involving isotropic non-homogeneous materials illustrated by Figures 2.17 and 2.18. Thus, for orthotropic case, the Q4 graded element also shows poor performance when compared to the Q4 homogeneous elements for both material variations (i.e. exponential or linear). The reasons for such behavior are given in the last two paragraphs of the previous section and are not repeated here. This is the reverse of the effect seen in the previous load cases for graded orthotropic materials where the graded elements show superior behavior to the corresponding homogeneous elements. Similarly to the isotropic case, a higher-order element such as Q8 (either graded or homogeneous) with 2 × 2 Gauss quadrature is able to capture the exact solution for this loading case.

2.5.3 Discussion

This study leads to the following remarks. The formulation of graded finite elements are verified against analytical solutions.

50

The isotropic FGM plate (see Figure 2.6) has length to width ratio equal to 1 and the orthotropic FGM plate (see Figure 2.20) has ratio 2 (for tension and bending loading cases). Because the analytical solution (Section 2.4) was derived for an infinitely long plate, the higher the aspect ratio (within limits) the better the numerical solution (with respect to the analytical one). For some load cases, e.g. tension and bending perpendicular to the material gradation, the *homogeneous elements* give σ_{yy} as a decreasing function of x in each individual element on the left side of the domain, while the exact solution shows an increasing trend of σ_{yy} with x for this portion of the domain. However, the *graded elements* show the same trend as the exact solution in each element (see, for example, Figures 2.11 and 2.12). The stress plots show that the graded Q8 element gives a smoother stress profile than the graded Q4 element (cf. Figures 2.9, 2.10, 2.31, and 2.32). For each loading case, the numerical values of the stress components other than the relevant normal stress quantity should approach zero. Thus the remainder of this paragraph focus on the maximum magnitude of these stress values (obtained numerically) which are theoretically zero. In general, these stress magnitudes are lower with Q8 than with Q4 elements.

For tension parallel to the material gradation, the numerical values of the stress σ_{xy} and σ_{yy} are exactly zero for all cases investigated. For the fixed grip case, the largest magnitude of σ_{xy} is $O(10^{-2})$ and occurs for the orthotropic plate with Q4 elements. The largest magnitude of σ_{xx} and σ_{xy} is $O(10^{-3})$ or less for all other analyses for this loading case. For tension and bending perpendicular to the exponential material gradation, the Q4 element leads to spurious shear stresses of $O(10^{0})$ for the orthotropic plate and of $O(10^{-1})$ for the isotropic plate. Smaller magnitudes for the maximum shear stresses are obtained considering linear material gradation. The stress σ_{xx} is of $O(10^{-2})$ or less for all the analyses involving these two loading cases.

2.6 Concluding remarks

Graded finite elements, which incorporate the material property gradient at the size scale of the element, are presented using a generalized isoparametric formulation, and have been verified against analytical solutions. Both linear (Q4) and quadratic (Q8) quadrilateral elements are investigated in detail. To address the influence of material property variation, both exponential and linear gradation have been considered and compared. Several plates with continuously nonhomo-

51

geneous isotropic and orthotropic materials were considered under fixed grip, tension and bending conditions. The performance of graded elements was compared to that of conventional elements with respect to analytical solutions.

Higher-order graded elements (e.g. quadratic and higher) are superior to conventional homogeneous elements based on the same shape functions. One should be careful when using graded elements with linear shape functions (e.g. Q4) as it may lose accuracy in certain situations such as uniform traction parallel to the material gradient direction. When using this element, it is recommended to average the nodal properties of the element, which would convert it to a regular homogeneous element. Thus the value of material properties at the integration points used to compute stresses depend on whether first-order or higher-order elements are used. This simple procedure leads to a more robust element. A similar procedure is used in the FEM code ABAQUS [55] for heat transfer analysis and also in the WARP3D code [51].

Chapter 3

The interaction integral method for fracture of FGMs

3.1 Introduction

The interaction integral method provides a unified framework for evaluating fracture parameters (e.g. stress intensity factors and T-stress) in functionally graded materials (FGMs). The method is based on a conservation integral involving auxiliary fields, which have the following three relations of solid mechanics problems:

- *equilibrium*

- *compatibility*

- *constitutive*

To determine fracture parameters, e.g. stress intensity factors (SIFs) and T-stress, by means of the interaction integral (M-integral[1]) method, *auxiliary fields* such as displacements (u^{aux}), strains (ε^{aux}), and stresses (σ^{aux}) are needed. In fracture of FGMs, the use of the auxiliary fields developed for homogeneous materials results in non-satisfaction of one of the three relations above, which leads to three independent formulations (see Figure 3.1): non-equilibrium, incompatibility, and constant-constitutive-tensor formulations. Each formulation leads to a different final form of the resulting M-integral, and for *consistency*, extra terms are added to account for the difference in response

---
[1]Here, the so-called M-integral should not be confused with the M-integral of Knowles and Sternberg [86], Budiansky and Rice [15], and Chang and Chien [20]. Also, see the book by Kanninen and Popelar [73] for a review of conservation integrals in fracture mechanics.

between homogeneous and nonhomogeneous materials. The extra terms arise from the complete derivative expressions, and should not be dropped. Table 3.1 illustrates the auxiliary fields corresponding to each formulation. Notice that the non-equilibrium formulation satisfies compatibility ($\varepsilon^{aux}=(\text{sym}\nabla)u^{aux}$) and the constitutive relations ($\sigma^{aux} = C(x)\varepsilon^{aux}$), but violates equilibrium ($\nabla \cdot \sigma^{aux} \neq 0$ with no body forces). The incompatibility formulation satisfies equilibrium and the constitutive relations, but violates compatibility conditions ($\varepsilon^{aux} \neq (\text{sym}\nabla)u^{aux}$). The constant-constitutive-tensor formulation satisfies equilibrium and compatibility conditions, but violates the constitutive relations ($\sigma^{aux} = C_{tip}\varepsilon^{aux}$ with $C_{tip} \neq C(x)$). Conservation integrals based on these three consistent formulations are the focus of this chapter.
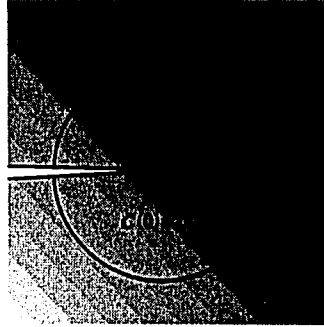
Figure 3.1: Motivation for development of alternative consistent formulations. Notice that $C(x) \neq C_{tip}$ for $x \neq 0$. The area A denotes a representative region around the crack tip.

Table 3.1: Comparison of alternative formulations.

Non-equilibrium formulation	Incompatibility formulation	Constant-constitutive-tensor formulation
u^{aux}	u^{aux}	u^{aux}
ε^{aux}	σ^{aux}	ε^{aux}
$\sigma^{aux} = C(x)\varepsilon^{aux}$	$\varepsilon^{aux} = S(x)\sigma^{aux}$	$\sigma^{aux} = C_{tip}\varepsilon^{aux}$
$\nabla \cdot \sigma^{aux} \neq 0$	$\varepsilon^{aux} \neq (sym\nabla)u^{aux}$	$C(x) \neq C_{tip}$

3.2 Auxiliary fields

The interaction integral makes use of auxiliary fields, such as displacements (u^{aux}), strains (ε^{aux}), and stresses (σ^{aux}). These auxiliary fields have to be suitably defined in order to evaluate mixed-

mode SIFs and T-stress. There are various choices for the auxiliary fields. The fields developed for FGMs, which satisfy all three relations of mechanics can be used as auxiliary fields. For instance, the numerical approximate solutions can be independently obtained for a specific material gradation. In this case, the extra terms will vanish in the final M-integral. Here we adopt fields originally developed for homogeneous materials. For each formulation (non-equilibrium, incompatibility, constant-constitutive-tensor), the selection of auxiliary fields is done according to Table 3.1. The auxiliary fields adopted are described below.

3.2.1 Fields for SIFs

For evaluating mixed-mode SIFs, the auxiliary displacement, strain, and stress fields are selected from the crack-tip asymptotic fields (i.e. $O(r^{1/2})$ for the displacements and $O(r^{-1/2})$ for the strains and stresses) with the material properties sampled at the crack-tip location (e.g. [34]). Figure 3.2 shows a crack in an FGM under two-dimensional fields in local Cartesian and polar coordinates originating at the crack tip. The auxiliary displacement, strain, and stress fields are chosen as [147, 131]:

$$u^{aux} = K_I^{aux} f^I(r^{1/2}, \theta, a^{tip}) + K_{II}^{aux} f^{II}(r^{1/2}, \theta, a^{tip}), \tag{3.1}$$

$$\varepsilon^{aux} = (\text{sym}\nabla)u^{aux}, \tag{3.2}$$

$$\sigma^{aux} = K_I^{aux} g^I(r^{-1/2}, \theta, a^{tip}) + K_{II}^{aux} g^{II}(r^{-1/2}, \theta, a^{tip}), \tag{3.3}$$

where K_I^{aux} and K_{II}^{aux} are the auxiliary mode I and mode II SIFs, respectively, and a^{tip} denotes contracted notation of the compliance tensor S evaluated at the crack tip, which is explained in Appendix A.2. The representative functions $f(r^{1/2}, \theta, a^{tip})$ and $g(r^{-1/2}, \theta, a^{tip})$ are given in Appendix A.3 and can also be found in other references, e.g. [131, 33].

3.2.2 Fields for T-stress

For evaluating T-stress, the auxiliary displacement, strain, and stress fields are chosen from those due to a point force in the x_1 direction, applied to the tip of a semi-infinite crack in an infinite homogeneous body as shown in Figure 3.3. The auxiliary displacements, strains, and stresses are
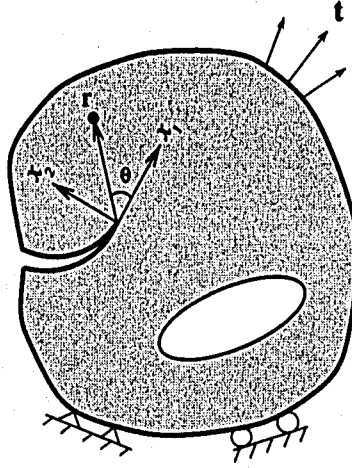
Figure 3.2: Cartesian (x_1, x_2) and polar (r, θ) coordinates originating from the crack tip in a nonhomogeneous material subjected to traction (**t**) and displacement boundary conditions.

chosen as [137, 95, 136]:

$$u^{aux} \;=\; t^u(\ln r, \theta, F, a^{tip}), \tag{3.4}$$

$$\varepsilon^{aux} \;=\; (\mathrm{sym}\nabla)u^{aux}, \tag{3.5}$$

$$\sigma^{aux} \;=\; t^s(r^{-1}, \theta, F, a^{tip}), \tag{3.6}$$

where F is the point force applied to the crack tip, and a^{tip} denote contracted notation of the compliance tensor a evaluated at the crack tip, which is defined in Appendix A.2. The representative functions $t^u(\ln r, \theta, F, a^{tip})$ and $t^s(r^{-1}, \theta, F, a^{tip})$ are given in Appendix A.4 and can be found in other references, e.g. [137, 136]. For orthotropic materials, the auxiliary fields may be determined by either the Lekhnitskii or Stroh formalism [85]. There is no difficulty in determining the auxiliary fields in the case of isotropic materials [82].

3.3   M-integral formulations

The standard J-integral [120] is given by

$$J = \lim_{\Gamma_s \to 0} \int_{\Gamma_s} \left(\mathcal{W}\delta_{1j} - \sigma_{ij}\, u_{i,1} \right) n_j \; d\Gamma, \tag{3.7}$$

56
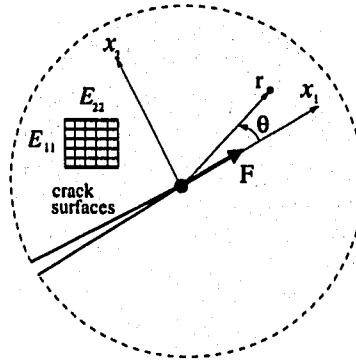
Figure 3.3: A point force applied at the crack tip in the direction parallel to the crack surface in a *homogeneous* body.

where $\mathcal{W}$ is the strain energy density expressed by

$$\mathcal{W} = \frac{1}{2}\sigma_{ij}\varepsilon_{ij} = \frac{1}{2}\,C_{ijkl}\varepsilon_{kl}\varepsilon_{ij}, \tag{3.8}$$

and n_j is the outward normal vector to the contour Γ_s, as shown in Figure 3.4.
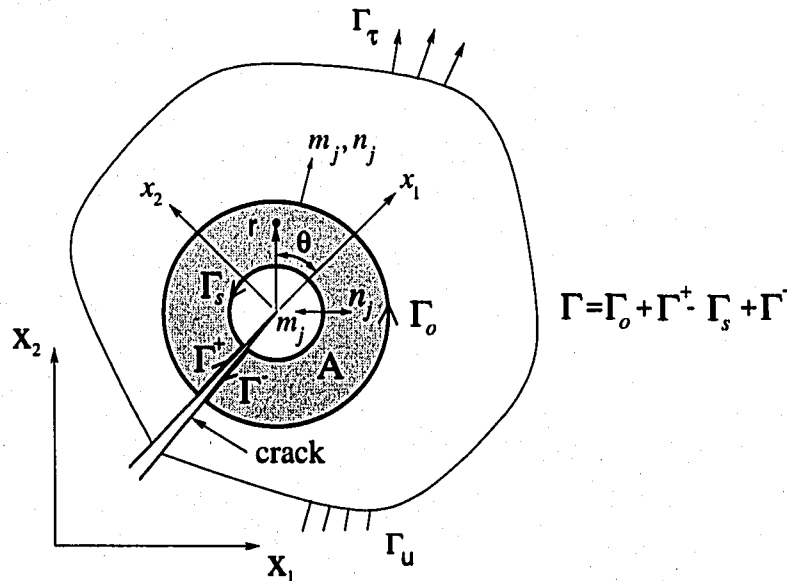
Figure 3.4: Conversion of the contour integral into an equivalent domain integral (EDI) where $\Gamma = \Gamma_o + \Gamma^+ - \Gamma_s + \Gamma^-$, $m_j = n_j$ on Γ_o and $m_j = -n_j$ on Γ_s. The notation of Γ with applied displacements is denoted Γ_u, and the notation of Γ with applied traction is denoted Γ_τ. Moreover $\Gamma = \Gamma_u + \Gamma_\tau$.

To convert the contour integral into an EDI, the following contour integral is defined:

$$\mathcal{H} = \oint_{\Gamma} (W\delta_{1j} - \sigma_{ij}\, u_{i,1})\, m_j q\, d\Gamma \tag{3.9}$$

where $\Gamma = \Gamma_o + \Gamma^+ - \Gamma_s + \Gamma^-$, m_j is a unit vector outward normal to the corresponding contour (i.e. $m_j = n_j$ on Γ_o and $m_j = -n_j$ on Γ_s), and q is a weight function defined as a smoothly varying function from $q = 1$ on Γ_s to $q = 0$ on Γ_o (see Figure 3.5). Taking the limit $\Gamma_s \to 0$ leads to

$$
\begin{aligned}
\lim_{\Gamma_s \to 0} \mathcal{H} &= \lim_{\Gamma_s \to 0} \oint_{\Gamma} (\mathcal{W}\delta_{1j} - \sigma_{ij}\, u_{i,1})\, m_j q\, d\Gamma \\
&= \lim_{\Gamma_s \to 0} \int_{\Gamma_o + \Gamma^+ + \Gamma^- - \Gamma_s} (\mathcal{W}\delta_{1j} - \sigma_{ij}\, u_{i,1})\, m_j q\, d\Gamma \\
&= \lim_{\Gamma_s \to 0} \left[\int_{\Gamma_o + \Gamma^+ + \Gamma^-} (\mathcal{W}\delta_{1j} - \sigma_{ij}\, u_{i,1})\, m_j q\, d\Gamma + \int_{-\Gamma_s} (\mathcal{W}\delta_{1j} - \sigma_{ij}\, u_{i,1})\, m_j q\, d\Gamma \right] \\
&= \lim_{\Gamma_s \to 0} \left[\int_{\Gamma_o + \Gamma^+ + \Gamma^-} (\mathcal{W}\delta_{1j} - \sigma_{ij}\, u_{i,1})\, m_j q\, d\Gamma - \int_{\Gamma_s} (\mathcal{W}\delta_{1j} - \sigma_{ij}\, u_{i,1})\, n_j q\, d\Gamma \right].
\end{aligned}
\tag{3.10}
$$
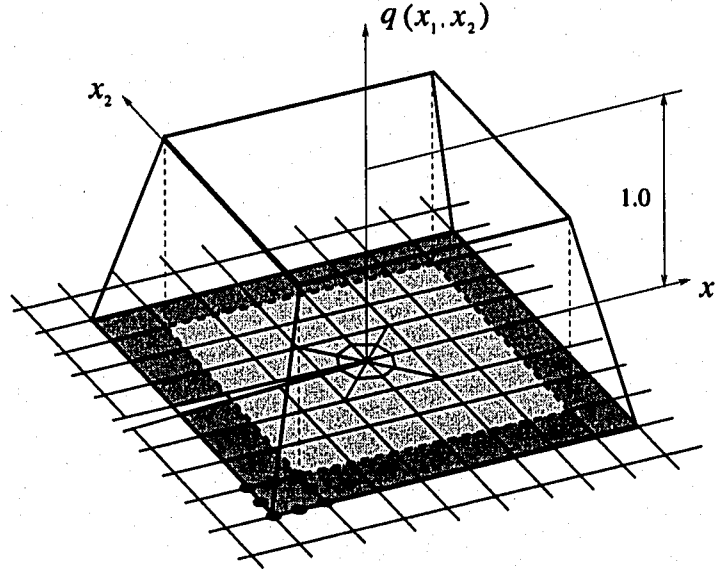
Figure 3.5: Plateau weight function (q function).

Because $q = 0$ on Γ_o and the crack faces are assumed to be traction-free, Eq.(3.10) becomes

$$J = -\lim_{\Gamma_s \to 0} \mathcal{H} = -\lim_{\Gamma_s \to 0} \oint_{\Gamma} (\mathcal{W}\delta_{1j} - \sigma_{ij}\, u_{i,1})\, m_j q\, d\Gamma. \tag{3.11}$$

Applying the divergence theorem to Eq.(3.11) and using the weight function q, the equivalent domain integral (EDI) is obtained as:

$$J = \int_A (\sigma_{ij} u_{i,1} - \mathcal{W}\delta_{1j}) q_{,j} \, dA + \int_A (\sigma_{ij} u_{i,1} - \mathcal{W}\delta_{1j})_{,j} \, q \, dA. \qquad (3.12)$$

The J-integral of the superimposed fields (actual and auxiliary fields) is obtained as:

$$\begin{aligned}
J^s &= \int_A \left\{ (\sigma_{ij} + \sigma_{ij}^{aux}) (u_{i,1} + u_{i,1}^{aux}) - \frac{1}{2}(\sigma_{ik} + \sigma_{ik}^{aux})(\varepsilon_{ik} + \varepsilon_{ik}^{aux})\delta_{1j} \right\} q_{,j} \, dA \\
&+ \int_A \left\{ (\sigma_{ij} + \sigma_{ij}^{aux}) (u_{i,1} + u_{i,1}^{aux}) - \frac{1}{2}(\sigma_{ik} + \sigma_{ik}^{aux})(\varepsilon_{ik} + \varepsilon_{ik}^{aux})\delta_{1j}) \right\}_{,j} q \, dA, \quad (3.13)
\end{aligned}$$

which is conveniently decomposed into

$$J^s = J + J^{aux} + M, \qquad (3.14)$$

where J^{aux} is given by

$$J^{aux} = \int_A (\sigma_{ij}^{aux} u_{i,1}^{aux} - \mathcal{W}^{aux}\delta_{1j}) q_{,j} \, dA + \int_A \left\{ \sigma_{ij}^{aux} u_{i,1}^{aux} - \frac{1}{2}\sigma_{ik}^{aux}\varepsilon_{ik}^{aux}\delta_{1j} \right\}_{,j} q \, dA,$$

and the resulting interaction integral (M) is given by

$$\begin{aligned}
M &= \int_A \left\{ \sigma_{ij} u_{i,1}^{aux} + \sigma_{ij}^{aux} u_{i,1} - \frac{1}{2}(\sigma_{ik}\varepsilon_{ik}^{aux} + \sigma_{ik}^{aux}\varepsilon_{ik})\delta_{1j} \right\} q_{,j} dA \\
&+ \int_A \left\{ \sigma_{ij} u_{i,1}^{aux} + \sigma_{ij}^{aux} u_{i,1} - \frac{1}{2}(\sigma_{ik}\varepsilon_{ik}^{aux} + \sigma_{ik}^{aux}\varepsilon_{ik})\delta_{1j} \right\}_{,j} q \, dA. \qquad (3.15)
\end{aligned}$$

3.3.1 Non-equilibrium formulation

Kim and Paulino [84] developed the non-equilibrium formulation for the interaction integral method. A summary for the derivation is given below. The name of the formulation is based on the fact that the auxiliary stress field

$$\sigma_{ij}^{aux} = C_{ijkl}(x) \, \varepsilon_{kl}^{aux} \qquad (3.16)$$

59

does not satisfy equilibrium because it differs from

$$\sigma_{ij}^{aux} = (C_{ijkl})_{\text{tip}}\, \varepsilon_{kl}^{aux}, \tag{3.17}$$

where $C_{ijkl}(x)$ is the constitutive tensor of the actual FGM and $(C_{ijkl})_{\text{tip}}$ is the constitutive tensor at the crack tip (see Figure 3.1).

The derivatives of the auxiliary stress field are

$$
\begin{aligned}
\sigma_{ij,j}^{aux} &= C_{ijkl,j}(x)\, \varepsilon_{kl}^{aux} + C_{ijkl}(x)\, \varepsilon_{kl,j}^{aux} \\
&= \underline{(C_{ijkl})_{\text{tip}}\, \varepsilon_{kl,j}^{aux}} + C_{ijkl,j}(x)\, \varepsilon_{kl}^{aux} + \left(C_{ijkl}(x) - (C_{ijkl})_{\text{tip}}\right) \varepsilon_{kl,j}^{aux},
\end{aligned}
\tag{3.18}
$$

where the underlined term in Eq.(3.18) vanishes. Thus this argument confirms that the auxiliary stress field selected in this formulation (Eq.(3.16)) does not satisfy equilibrium, i.e. $\sigma_{ij,j}^{aux} \neq 0$ (no body forces or inertia). This choice of the auxiliary fields has been discussed by Dolbow and Gosz [31], but a non-equilibrium formulation was not provided in their paper. The non-equilibrium in the stress field has to be taken into account in the interaction integral formulation, which is discussed in detail below.

Using the following equality

$$\sigma_{ij}\varepsilon_{ij}^{aux} = C_{ijkl}(x)\varepsilon_{kl}\varepsilon_{ij}^{aux} = \sigma_{kl}^{aux}\varepsilon_{kl} = \sigma_{ij}^{aux}\varepsilon_{ij}, \tag{3.19}$$

one rewrites Eq.(3.15) as

$$
\begin{aligned}
M &= \int_A \left\{\sigma_{ij}u_{i,1}^{aux} + \sigma_{ij}^{aux}u_{i,1} - \sigma_{ik}\varepsilon_{ik}^{aux}\delta_{1j}\right\} q_{,j}dA \\
&\quad + \int_A \left\{\sigma_{ij}u_{i,1}^{aux} + \sigma_{ij}^{aux}u_{i,1} - \sigma_{ik}\varepsilon_{ik}^{aux}\delta_{1j}\right\}_{,j} q\, dA \\
&= M_1 + M_2.
\end{aligned}
\tag{3.20}
$$

60

The last term of the second integral (M_2) in Eq.(3.20) is expressed as

$$
\begin{aligned}
(\sigma_{ik}\varepsilon_{ik}^{aux}\delta_{1j})_{,j} &= (\sigma_{ik}\varepsilon_{ik}^{aux})_{,1} = (\sigma_{ij}\varepsilon_{ij}^{aux})_{,1} = (C_{ijkl}\varepsilon_{kl}\varepsilon_{ij}^{aux})_{,1} \\
&= C_{ijkl,1}\varepsilon_{kl}\varepsilon_{ij}^{aux} + C_{ijkl}\varepsilon_{kl,1}\varepsilon_{ij}^{aux} + C_{ijkl}\varepsilon_{kl}\varepsilon_{ij,1}^{aux} \\
&= C_{ijkl,1}\varepsilon_{kl}\varepsilon_{ij}^{aux} + \sigma_{ij}^{aux}\varepsilon_{ij,1} + \sigma_{ij}\varepsilon_{ij,1}^{aux}.
\end{aligned} \tag{3.21}
$$

Substitution of Eq.(3.21) into Eq.(3.20) leads to

$$
\begin{aligned}
M_2 &= \int_A \left(\sigma_{ij,j}u_{i,1}^{aux} + \sigma_{ij}u_{i,1j}^{aux} + \sigma_{ij,j}^{aux}u_{i,1} + \sigma_{ij}^{aux}u_{i,1j} \right) q \, dA \\
&\quad - \int_A \left(C_{ijkl,1}\varepsilon_{kl}\varepsilon_{ij}^{aux} + \sigma_{ij}^{aux}\varepsilon_{ij,1} + \sigma_{ij}\varepsilon_{ij,1}^{aux} \right) q \, dA.
\end{aligned} \tag{3.22}
$$

Using compatibility (actual and auxiliary) and equilibrium (actual) (i.e. $\sigma_{ij,j} = 0$ with no body force), one simplifies Eq.(3.22) as

$$
M_2 = \int_A \left\{ \sigma_{ij,j}^{aux}u_{i,1} - C_{ijkl,1}\varepsilon_{kl}\varepsilon_{ij}^{aux} \right\} q \, dA, \tag{3.23}
$$

Therefore the resulting interaction integral (M) becomes

$$
\begin{aligned}
M &= \int_A \left\{ \sigma_{ij}u_{i,1}^{aux} + \sigma_{ij}^{aux}u_{i,1} - \sigma_{ik}\varepsilon_{ik}^{aux}\delta_{1j} \right\} q_{,j}dA \\
&\quad + \int_A \left\{ \underline{\sigma_{ij,j}^{aux}u_{i,1}} - C_{ijkl,1}\varepsilon_{kl}\varepsilon_{ij}^{aux} \right\} q \, dA,
\end{aligned} \tag{3.24}
$$

where the underlined term is a non-equilibrium term, which appears due to non-equilibrium of the auxiliary stress fields.

The existence of the integral involving the non-equilibrium term as r goes to zero is proved below. The stiffness tensor involving material properties $E(r,\theta)$ and $\nu(r,\theta)$ must be continuous and differentiable function, and thus it can be written as [34]

$$
C_{ijkl}(r,\theta) = (C_{ijkl})_{tip} + rC_{ijkl}^{(1)}(\theta) + \frac{r^2}{2}C_{ijkl}^{(2)}(\theta) + O(r^3) + \dots \tag{3.25}
$$

where $C_{ijkl}^{(n)}(\theta)$ ($n = 1, 2, \dots$) are angular functions. In Eq.(3.18) for $\sigma_{ij,j}^{aux}$, the first term vanishes

because of the equilibrium, and here we focus on the third term.

For the auxiliary fields for SIFs ($u_i^{aux}(\sqrt{r}, \theta)$, $\varepsilon_{ij}^{aux}(r^{-1/2}, \theta)$), the integral, as the limit r goes to zero, becomes

$$
\begin{aligned}
\lim_{A \to 0} \int_A \sigma_{ij,j}^{aux} \, u_{i,1} \, q \, dA &= \lim_{r \to 0} \int_\theta \int_r \sigma_{ij,j}^{aux} \, u_{i,1} \, q \, r \, dr \, d\theta \\
&= \lim_{r \to 0} \int_\theta \int_r (C_{ijkl}(r,\theta) - (C_{ijkl})_{tip}) \, \varepsilon_{kl,j}^{aux} \, u_{i,1} \, q \, r \, dr \, d\theta \\
&= \lim_{r \to 0} \int_\theta \int_r O(r) \, O(r^{-3/2}) \, O(r^{-1/2}) \, q \, r \, dr \, d\theta \\
&= \lim_{r \to 0} O(r) = 0.
\end{aligned}
\tag{3.26}
$$

For the auxiliary fields for T-stress ($u_i^{aux}(\ln r, \theta)$, $\varepsilon_{ij}^{aux}(r^{-1}, \theta)$), the integral, as the limit r goes to zero, becomes

$$
\begin{aligned}
\lim_{A \to 0} \int_A \sigma_{ij,j}^{aux} \, u_{i,1} \, q \, dA &= \lim_{r \to 0} \int_\theta \int_r \sigma_{ij,j}^{aux} \, u_{i,1} \, q \, r \, dr \, d\theta \\
&= \lim_{r \to 0} \int_\theta \int_r (C_{ijkl}(r,\theta) - (C_{ijkl})_{tip}) \, \varepsilon_{kl,j}^{aux} \, u_{i,1} \, q \, r \, dr \, d\theta \\
&= \lim_{r \to 0} \int_\theta \int_r O(r) \, O(r^{-2}) \, O(r^{-1/2}) \, q \, r \, dr \, d\theta \\
&= \lim_{r \to 0} O(r^{1/2}) = 0.
\end{aligned}
\tag{3.27}
$$

3.3.2 Incompatibility formulation

The incompatibility formulation satisfies equilibrium ($\sigma_{ij,j}^{aux} = 0$ with no body forces) and the constitutive relationship ($\varepsilon_{ij}^{aux} = S_{ijkl}(x)\sigma_{kl}^{aux}$), but violates compatibility conditions ($\varepsilon_{ij}^{aux} \neq (u_{i,j}^{aux} + u_{j,i}^{aux})/2$). The expressions in Eqs.(3.19), (3.21), and (3.22) are also valid for this formulation. Thus

$$
\begin{aligned}
M_2 &= \int_A \left(\sigma_{ij,j} u_{i,1}^{aux} + \sigma_{ij} u_{i,1j}^{aux} + \sigma_{ij,j}^{aux} u_{i,1} + \sigma_{ij}^{aux} u_{i,1j} \right) q \, dA \\
&\quad - \int_A \left(C_{ijkl,1} \varepsilon_{kl} \varepsilon_{ij}^{aux} + \sigma_{ij}^{aux} \varepsilon_{ij,1} + \sigma_{ij} \varepsilon_{ij,1}^{aux} \right) q \, dA.
\end{aligned}
\tag{3.28}
$$

62

Using equilibrium (actual and auxiliary) and compatibility (actual), one simplifies M_2 as

$$M_2 \;=\; \int_A \left\{ \sigma_{ij}(u_{i,1j}^{aux} - \varepsilon_{ij,1}^{aux}) - C_{ijkl,1}\varepsilon_{kl}\varepsilon_{ij}^{aux} \right\} q\, dA,$$

Therefore the resulting interaction integral (M) becomes

$$M \;=\; \int_A \left\{ \sigma_{ij}u_{i,1}^{aux} + \sigma_{ij}^{aux}u_{i,1} - \sigma_{ik}\varepsilon_{ik}^{aux}\delta_{1j} \right\} q_{,j} dA$$
$$+ \int_A \left\{ \sigma_{ij}(u_{i,1j}^{aux} - \varepsilon_{ij,1}^{aux}) - C_{ijkl,1}\varepsilon_{kl}\varepsilon_{ij}^{aux} \right\} q\, dA, \tag{3.29}$$

where the underlined term is an incompatible term, which appears due to incompatibility of the auxiliary strain fields.

The existence of the integral involving the incompatible term as r goes to zero is proved below. The term $\sigma_{ij}\varepsilon_{ij,1}^{aux}$ in Eq.(3.29) can be written as

$$\sigma_{ij}\varepsilon_{ij,1}^{aux} \;=\; \sigma_{ij}\{ S_{ijkl,1}(\boldsymbol{x})\, \sigma_{kl}^{aux} + S_{ijkl}(\boldsymbol{x})\, \sigma_{kl,1}^{aux} \}$$
$$=\; \sigma_{ij}(S_{ijkl})_{tip}\, \sigma_{kl,1}^{aux} + \sigma_{ij}S_{ijkl,1}(\boldsymbol{x})\, \sigma_{kl}^{aux} + \underline{\sigma_{ij}(S_{ijkl}(\boldsymbol{x}) - (S_{ijkl})_{tip})\, \sigma_{kl,1}^{aux}}$$
$$=\; \sigma_{ij}u_{i,1j}^{aux} + \sigma_{ij}S_{ijkl,1}(\boldsymbol{x})\, \sigma_{kl}^{aux} + \underline{\sigma_{ij}(S_{ijkl}(\boldsymbol{x}) - (S_{ijkl})_{tip})\, \sigma_{kl,1}^{aux}}. \tag{3.30}$$

Thus

$$\sigma_{ij}(u_{i,1j}^{aux} - \varepsilon_{ij,1}^{aux}) = -\sigma_{ij}S_{ijkl,1}(\boldsymbol{x})\, \sigma_{kl}^{aux} - \underline{\sigma_{ij}(S_{ijkl}(\boldsymbol{x}) - (S_{ijkl})_{tip})\, \sigma_{kl,1}^{aux}} \tag{3.31}$$

where we focus on the underlined term.

The compliance tensor involving material properties $E(r,\theta)$ and $\nu(r,\theta)$ must be continuous and differentiable function, and thus it can be written as [34]

$$S_{ijkl}(r,\theta) = (S_{ijkl})_{tip} + rS_{ijkl}^{(1)}(\theta) + \frac{r^2}{2}S_{ijkl}^{(2)}(\theta) + O(r^3) + \ldots \tag{3.32}$$

where $S_{ijkl}^{(n)}(\theta)$ $(n = 1, 2, \ldots)$ are angular functions.

For the auxiliary fields for SIFs $(u_i^{aux}(\sqrt{r},\theta),\ \sigma_{ij}^{aux}(r^{-1/2},\theta))$, the integral, as the limit r goes

to zero, becomes

$$
\begin{aligned}
\lim_{A \to 0} \int_A \sigma_{ij}(u_{i,1j}^{aux} - \varepsilon_{ij,1}^{aux}) \, q \, dA
&= \lim_{r \to 0} \int_\theta \int_r \sigma_{ij}(u_{i,1j}^{aux} - \varepsilon_{ij,1}^{aux}) \, q \, r \, dr \, d\theta \\
&= -\lim_{r \to 0} \int_\theta \int_r \sigma_{ij} \left(S_{ijkl}(r,\theta) - (S_{ijkl})_{tip} \right) \sigma_{kl,1}^{aux} \, q \, r \, dr \, d\theta \\
&= -\lim_{r \to 0} \int_\theta \int_r O(r^{-1/2}) \, O(r) \, O(r^{-3/2}) \, q \, r \, dr \, d\theta \\
&= -\lim_{r \to 0} \, O(r) = 0.
\end{aligned}
\tag{3.33}
$$

For the auxiliary fields for T-stress $(u_i^{aux}(\ln r, \theta), \sigma_{ij}^{aux}(r^{-1}, \theta))$, the integral, as the limit r goes to zero, becomes

$$
\begin{aligned}
\lim_{A \to 0} \int_A \sigma_{ij}(u_{i,1j}^{aux} - \varepsilon_{ij,1}^{aux}) \, q \, dA
&= \lim_{r \to 0} \int_\theta \int_r \sigma_{ij}(u_{i,1j}^{aux} - \varepsilon_{ij,1}^{aux}) \, q \, r \, dr \, d\theta \\
&= -\lim_{r \to 0} \int_\theta \int_r \sigma_{ij} \left(S_{ijkl}(r,\theta) - (S_{ijkl})_{tip} \right) \sigma_{kl,1}^{aux} \, q \, r \, dr \, d\theta \\
&= -\lim_{r \to 0} \int_\theta \int_r O(r^{-1/2}) \, O(r) \, O(r^{-2}) \, q \, r \, dr \, d\theta \\
&= -\lim_{r \to 0} \, O(r^{1/2}) = 0.
\end{aligned}
\tag{3.34}
$$

3.3.3 Constant-constitutive-tensor formulation

The constant-constitutive-tensor formulation satisfies equilibrium ($\sigma_{ij,j}^{aux} = 0$ with no body forces) and compatibility conditions ($\varepsilon_{ij}^{aux} = (u_{i,j}^{aux} + u_{j,i}^{aux})/2$), but violates the constitutive relationship ($\sigma_{ij}^{aux} = (C_{ijkl})_{tip} \varepsilon_{kl}^{aux}$ with $(C_{ijkl})_{tip} \neq C_{ijkl}(x)$). Notice that $\sigma_{ij} \varepsilon_{ij}^{aux} \neq \sigma_{ij}^{aux} \varepsilon_{ij}$ due to the violated constitutive relationship. Thus Eq.(3.15) becomes

$$
\begin{aligned}
M = {}& \int_A \left\{ \sigma_{ij} u_{i,1}^{aux} + \sigma_{ij}^{aux} u_{i,1} - \frac{1}{2}(\sigma_{ik}\varepsilon_{ik}^{aux} + \sigma_{ik}^{aux}\varepsilon_{ik})\delta_{1j} \right\} q_{,j} \, dA \\
& + \int_A \left\{ \sigma_{ij,j} u_{i,1}^{aux} + \sigma_{ij} u_{i,1j}^{aux} + \sigma_{ij,j}^{aux} u_{i,1} + \sigma_{ij}^{aux} u_{i,1j} \right. \\
& \qquad \left. - \frac{1}{2}(\sigma_{ij,1}\varepsilon_{ij}^{aux} + \sigma_{ij}\varepsilon_{ij,1}^{aux} + \sigma_{ij,1}^{aux}\varepsilon_{ij} + \sigma_{ij}^{aux}\varepsilon_{ij,1}) \right\} q \, dA.
\end{aligned}
\tag{3.35}
$$

Using equilibrium and compatibility conditions for both actual and auxiliary fields, one obtains M as

$$M = \int_A \left\{ \sigma_{ij} u_{i,1}^{aux} + \sigma_{ij}^{aux} u_{i,1} - \frac{1}{2}(\sigma_{ik}\varepsilon_{ik}^{aux} + \sigma_{ik}^{aux}\varepsilon_{ik})\delta_{1j} \right\} q_{,j} dA$$

$$+ \int_A \frac{1}{2} \left\{ \sigma_{ij}\varepsilon_{ij,1}^{aux} - \sigma_{ij,1}\varepsilon_{ij}^{aux} + \sigma_{ij}^{aux}\varepsilon_{ij,1} - \sigma_{ij,1}^{aux}\varepsilon_{ij} \right\} q \, dA. \qquad (3.36)$$

Notice that the resulting M involves derivatives of the actual strain and stress fields, which arises due to the material mismatch, and may cause loss of accuracy from a numerical point of view.

The existence of the second integral of Eq.(3.36) as r goes to zero is proved below. The each term in the second integral becomes

$$\sigma_{ij}\varepsilon_{ij,1}^{aux} = C_{ijkl}(x) \, \varepsilon_{kl} \, \varepsilon_{ij,1}^{aux},$$

$$-\sigma_{ij,1}\varepsilon_{ij}^{aux} = -[C_{ijkl,1}(x) \, \varepsilon_{kl} \, \varepsilon_{ij}^{aux} + C_{ijkl}(x) \, \varepsilon_{kl,1} \, \varepsilon_{ij}^{aux}],$$

$$\sigma_{ij}^{aux}\varepsilon_{ij,1} = (C_{ijkl})_{tip} \, \varepsilon_{kl}^{aux} \, \varepsilon_{ij,1},$$

$$-\sigma_{ij,1}^{aux}\varepsilon_{ij} = -(C_{ijkl})_{tip} \, \varepsilon_{kl,1}^{aux} \, \varepsilon_{ij}. \qquad (3.37)$$

Combination of the above terms leads to

$$\sigma_{ij}\varepsilon_{ij,1}^{aux} - \sigma_{ij,1}\varepsilon_{ij}^{aux} + \sigma_{ij}^{aux}\varepsilon_{ij,1} - \sigma_{ij,1}^{aux}\varepsilon_{ij} =$$

$$(C_{ijkl}(x) - (C_{ijkl})_{tip}) \, \varepsilon_{kl} \, \varepsilon_{ij,1}^{aux} - (C_{ijkl}(x) - (C_{ijkl})_{tip}) \, \varepsilon_{kl,1} \, \varepsilon_{ij}^{aux} - C_{ijkl,1}(x) \, \varepsilon_{kl} \, \varepsilon_{ij}^{aux}, \qquad (3.38)$$

where we focus on the first term.

For the auxiliary fields for SIFs ($u_i^{aux}(\sqrt{r},\theta)$, $\varepsilon_{ij}^{aux}(r^{-1/2},\theta)$, $\sigma_{ij}^{aux}(r^{-1/2},\theta)$), the integral, as the limit r goes to zero, becomes

$$\lim_{A\to 0} \int_A \left\{ \sigma_{ij}\varepsilon_{ij,1}^{aux} - \sigma_{ij,1}\varepsilon_{ij}^{aux} + \sigma_{ij}^{aux}\varepsilon_{ij,1} - \sigma_{ij,1}^{aux}\varepsilon_{ij} \right\} q \, dA$$

$$= \lim_{r\to 0} \int_\theta \int_r (C_{ijkl}(x) - (C_{ijkl})_{tip}) \, \varepsilon_{kl} \, \varepsilon_{ij,1}^{aux} \, q \, r \, dr \, d\theta$$

$$= \lim_{r\to 0} \int_\theta \int_r O(r) \, O(r^{-1/2}) \, O(r^{-3/2}) \, q \, r \, dr \, d\theta$$

$$= \lim_{r\to 0} O(r) = 0. \qquad (3.39)$$

For the auxiliary fields for T-stress $(u_i^{aux}(\ln r, \theta),\ \varepsilon_{ij}^{aux}(r^{-1}, \theta),\ \sigma_{ij}^{aux}(r^{-1}, \theta))$. The integral, as the limit r goes to zero, becomes

$$
\begin{aligned}
\lim_{A \to 0} \int_A &\left\{ \sigma_{ij}\varepsilon_{ij,1}^{aux} - \sigma_{ij,1}\varepsilon_{ij}^{aux} + \sigma_{ij}^{aux}\varepsilon_{ij,1} - \sigma_{ij,1}^{aux}\varepsilon_{ij} \right\}\ q\ dA \\
&= \lim_{r \to 0} \int_\theta \int_r (C_{ijkl}(x) - (C_{ijkl})_{tip})\ \varepsilon_{kl}\ \varepsilon_{ij,1}^{aux}\ q\ r\ dr\ d\theta \\
&= \lim_{r \to 0} \int_\theta \int_r O(r)\ O(r^{-1/2})\ O(r^{-2})\ q\ r\ dr\ d\theta \\
&= \lim_{r \to 0}\ O(r^{1/2}) = 0.
\end{aligned}
\tag{3.40}
$$

3.4 Extraction of stress intensity factors

For mixed-mode crack problems on orthotropic materials, the energy release rates $\mathcal{G}_I$ and $\mathcal{G}_{II}$ are related to mixed-mode SIFs as follows [131]:

$$
\mathcal{G}_I = -\frac{K_I}{2}a_{22}^{\text{tip}}\ \text{Im}\left[\frac{K_I(\mu_1^{\text{tip}} + \mu_2^{\text{tip}}) + K_{II}}{\mu_1^{\text{tip}}\mu_2^{\text{tip}}} \right]
\tag{3.41}
$$

$$
\mathcal{G}_{II} = \frac{K_{II}}{2}a_{11}^{\text{tip}}\ \text{Im}[K_{II}(\mu_1^{\text{tip}} + \mu_2^{\text{tip}}) + K_I(\mu_1^{\text{tip}}\mu_2^{\text{tip}})],
\tag{3.42}
$$

where Im denotes the imaginary part of the complex function. Thus

$$
J_{\text{local}} = \mathcal{G} = \mathcal{G}_I + \mathcal{G}_{II} = c_{11}K_I^2 + c_{12}K_IK_{II} + c_{22}K_{II}^2,
\tag{3.43}
$$

where

$$
\begin{aligned}
c_{11} &= -\frac{a_{22}^{\text{tip}}}{2}\ \text{Im}\left(\frac{\mu_1^{\text{tip}} + \mu_2^{\text{tip}}}{\mu_1^{\text{tip}}\mu_2^{\text{tip}}} \right), \\
c_{12} &= -\frac{a_{22}^{\text{tip}}}{2}\ \text{Im}\left(\frac{1}{\mu_1^{\text{tip}}\mu_2^{\text{tip}}} \right) + \frac{a_{11}^{\text{tip}}}{2}\ \text{Im}\left(\mu_1^{\text{tip}}\mu_2^{\text{tip}} \right), \\
c_{22} &= \frac{a_{11}^{\text{tip}}}{2}\text{Im}(\mu_1^{\text{tip}} + \mu_2^{\text{tip}}),
\end{aligned}
\tag{3.44}
$$

For two admissible fields, which are the actual (u, ε, σ) and auxiliary $(u^{aux}, \varepsilon^{aux}, \sigma^{aux})$ fields,

one obtains [140]

$$
\begin{aligned}
J^s_{\text{local}} &= c_{11}(K_I + K_I^{aux})^2 + c_{12}(K_I + K_I^{aux})(K_{II} + K_{II}^{aux}) + c_{22}(K_{II} + K_{II}^{aux})^2 \\
&= J_{\text{local}} + J^{aux}_{\text{local}} + M_{\text{local}}
\end{aligned}
\tag{3.45}
$$

where J_{local} is given by Eq.(3.43), J^{aux}_{local} is given by

$$
J^{aux}_{\text{local}} = c_{11}(K_I^{aux})^2 + c_{12}K_I^{aux}K_{II}^{aux} + c_{22}(K_{II}^{aux})^2
\tag{3.46}
$$

and M_{local} is given by

$$
M_{\text{local}} = 2c_{11}K_I K_I^{aux} + c_{12}(K_I K_{II}^{aux} + K_I^{aux}K_{II}) + 2c_{22}K_{II}K_{II}^{aux}.
\tag{3.47}
$$

The mode I and mode II SIFs are evaluated by solving the following linear algebraic equations:

$$
M^{(1)}_{\text{local}} = 2c_{11}K_I + c_{12}K_{II}, \quad (K_I^{aux} = 1.0, K_{II}^{aux} = 0.0),
\tag{3.48}
$$

$$
M^{(2)}_{\text{local}} = c_{12}K_I + 2c_{22}K_{II}, \quad (K_I^{aux} = 0.0, K_{II}^{aux} = 1.0),
\tag{3.49}
$$

where the superscript in $M^{(i)}_{local}$ $(i = 1, 2)$ is used just to indicate that the values are distinct in each case. For isotropic materials, the off-diagonal terms of c_{ij} drop, and Eqs.(3.48) and (3.49) become

$$
M^{(1)}_{\text{local}} = \frac{2}{E^*_{\text{tip}}}K_I, \quad (K_I^{aux} = 1.0, K_{II}^{aux} = 0.0),
\tag{3.50}
$$

$$
M^{(2)}_{\text{local}} = \frac{2}{E^*_{\text{tip}}}K_{II}, \quad (K_I^{aux} = 0.0, K_{II}^{aux} = 1.0),
\tag{3.51}
$$

respectively, where $E^*_{\text{tip}} = E_{\text{tip}}$ for plane stress and $E^*_{\text{tip}} = E_{\text{tip}}/(1 - \nu^2_{\text{tip}})$ for plane strain. The relationships of Eqs.(3.48) and (3.49), and Eqs.(3.50) and (3.51) are the same as those for homogeneous orthotropic [140] and isotropic [151] materials, respectively, except that, for FGMs, the material properties are evaluated at the crack-tip location. Notice that, for the orthotropic case, there is no need for Newton's iteration, which is needed with other approaches such as the path-independent J_k-integral [81] and the modified crack closure (MCC) integral [78]. Here the SIFs for mode I and

mode II are decoupled (cf. Eqs.(3.48) and (3.49)).

3.5 Extraction of T-stress

The T-stress can be extracted from the interaction integral by nullifying the contributions of both higher-order (i.e. $O(r^{1/2})$ and higher) and singular (i.e. $O(r^{-1/2})$) terms. The contribution of the higher-order terms is canceled by taking the limit $r \to 0$ with respect to the domain A shown in Figure 3.4. By doing so, the non-equilibrium term of Eq.(3.24) vanishes as explained earlier. Moreover, the explicit derivative of the strain energy density in Eq.(3.24) vanishes for the following reason. Derivatives of the elastic moduli are assumed to be bounded at the crack tip, i.e. $\lambda_1(x)$ and $\mu_1(x)$ are $O(r^\alpha)$ with $\alpha \geq 0$. Therefore $C_{ijkl,1}$, ε_{kl}, and ε_{ij}^{aux} are $O(r^\alpha)$, $O(r^{-1/2})$, and $O(r^{-1})$, respectively, and the domain integral involving material derivatives in Eq.(3.23) vanishes as $r \to 0$:

$$
\begin{aligned}
\int_A C_{ijkl,1}\varepsilon_{kl}\varepsilon_{ij}^{aux} \, q \, dA &= \int_{-\pi}^{\pi}\int_0^r C_{ijkl,1}\varepsilon_{kl}\varepsilon_{ij}^{aux} \, q \, r \, dr \, d\theta \\
&\propto \int_{-\pi}^{\pi}\int_0^r O(r^\alpha)O(r^{-1/2})O(r^{-1}) \, q \, r \, dr \, d\theta \\
&\propto O(r^{\alpha+1/2}). \tag{3.52}
\end{aligned}
$$

Therefore,

$$
M = \int_A \left\{ (\sigma_{ij}u_{i,1}^{aux} + \sigma_{ij}^{aux}u_{i,1}) - \frac{1}{2}(\sigma_{ik}\varepsilon_{ik}^{aux} + \sigma_{ik}^{aux}\varepsilon_{ik})\delta_{1j} \right\} \, q_{,j} \, dA. \tag{3.53}
$$

which has the same expression for homogeneous materials. Equation (3.53) can be rewritten as

$$
M_{\text{local}} = \int_A \left[\left\{ (\sigma_{ij}u_{i,1}^{aux} + \sigma_{ij}^{aux}u_{i,1}) - \frac{1}{2}(\sigma_{ik}\varepsilon_{ik}^{aux} + \sigma_{ik}^{aux}\varepsilon_{ik})\delta_{1j} \right\} q \right]_{,j} \, dA, \tag{3.54}
$$

because its expansion leads to

$$
\begin{aligned}
M_{\text{local}} &= \int_A \left\{ (\sigma_{ij}u_{i,1}^{aux} + \sigma_{ij}^{aux}u_{i,1}) - \frac{1}{2}(\sigma_{ik}\varepsilon_{ik}^{aux} + \sigma_{ik}^{aux}\varepsilon_{ik})\delta_{1j} \right\} q_{,j} \, dA \\
&+ \int_A \left\{ (\sigma_{ij}u_{i,1}^{aux} + \sigma_{ij}^{aux}u_{i,1}) - \frac{1}{2}(\sigma_{ik}\varepsilon_{ik}^{aux} + \sigma_{ik}^{aux}\varepsilon_{ik})\delta_{1j} \right\}_{,j} q \, dA, \tag{3.55}
\end{aligned}
$$

and the second domain integral of Eq.(3.55) vanishes. Now in order to convert the EDI of Eq.(3.54) into a line integral, applying divergence theorem yields

$$M_{\text{local}} = \lim_{\Gamma_s \to 0} \oint_{\Gamma} \left\{ (\sigma_{ij} u_{i,1}^{aux} + \sigma_{ij}^{aux} u_{i,1}) - \frac{1}{2}(\sigma_{ik} \varepsilon_{ik}^{aux} + \sigma_{ik}^{aux} \varepsilon_{ik}) \delta_{1j} \right\} m_j q \, d\Gamma. \quad (3.56)$$

Because $m_j = -n_j$ and $q = 1$ on Γ_s, $m_j = n_j$ and $q = 0$ on Γ_o, and the crack faces are assumed to be traction-free, Eq.(3.56) becomes

$$M_{\text{local}} = \lim_{\Gamma_s \to 0} \int_{\Gamma_s} \left[\frac{1}{2}(\sigma_{ik} \varepsilon_{ik}^{aux} + \sigma_{ik}^{aux} \varepsilon_{ik}) \delta_{1j} - (\sigma_{ij} u_{i,1}^{aux} + \sigma_{ij}^{aux} u_{i,1}) \right] n_j \, d\Gamma. \quad (3.57)$$

Using the equality in Eq.(3.19), one reduces Eq.(3.57) to

$$M_{\text{local}} = \lim_{\Gamma_s \to 0} \int_{\Gamma_s} \left[\sigma_{ik} \varepsilon_{ik}^{aux} \delta_{1j} - (\sigma_{ij} u_{i,1}^{aux} + \sigma_{ij}^{aux} u_{i,1}) \right] n_j \, d\Gamma. \quad (3.58)$$

The actual stress fields are given by

$$\sigma_{ij} = K_I (2\pi r)^{-1/2} f_{ij}^I(\theta) + K_{II} (2\pi r)^{-1/2} f_{ij}^{II}(\theta) + T \delta_{1i} \delta_{1j} + O(r^{1/2}), \quad (3.59)$$

where the angular functions $f_{ij}^I(\theta)$ and $f_{ij}^{II}(\theta)$ $(i,j = 1,2)$ are given, for example, in reference [33]. As the contour Γ_s (see Figure 3.4) shrinks to the crack tip region, the higher-order terms cancel out as mentioned above, and the only term that contributes to M is the term involving T. In other words, there is no contribution from the singular terms because the integration from $\theta = -\pi$ to $+\pi$ of sinusoidal functions, which are the coefficients of the singular term $O(r^{-1/2})$, becomes zero regardless of the resulting singularity of order $O(r^{-1/2})$. Thus from Eq.(3.59)

$$\sigma_{ij} = T \delta_{1i} \delta_{1j}, \quad (3.60)$$

which refers to the stress parallel to the crack direction. Substituting Eq.(3.60) into Eq.(3.58), one obtains

$$M_{\text{local}} = -\lim_{\Gamma_s \to 0} \int_{\Gamma_s} \sigma_{ij}^{aux} n_j u_{i,1} \, d\Gamma = T a_{11}^{\text{tip}} \lim_{\Gamma_s \to 0} \int_{\Gamma_s} \sigma_{ij}^{aux} n_j \, d\Gamma. \quad (3.61)$$

Because the force F is in equilibrium (see Figure 3.3)

$$F = -\lim_{\Gamma_s \to 0} \int_{\Gamma_s} \sigma_{ij}^{aux} n_j \, d\Gamma,$$ (3.62)

and thus the following relationship is obtained

$$T = \frac{M_{\text{local}}}{F a_{11}^{\text{tip}}},$$ (3.63)

where a_{11}^{tip} is a material parameter at the crack tip location for plane stress, and is replaced by b_{11}^{tip} for plane strain (cf. Eq.(A.93)). For isotropic materials, Eq.(3.63) becomes

$$T = \frac{E_{\text{tip}}^*}{F} M_{\text{local}},$$ (3.64)

where $E_{\text{tip}}^* = E_{\text{tip}}$ for plane stress and $E_{\text{tip}}^* = E_{\text{tip}}/(1 - \nu_{\text{tip}}^2)$ for plane strain.

3.6 Comparison and critical assessment

The three formulations presented above are *consistent* in the sense that extra terms are added to account for the difference in response between homogeneous and nonhomogeneous materials. However, each formulation has an independent final form (see Eqs.(3.24), (3.29), and (3.36)) due to the different characteristics of the auxiliary fields. The final form of the M-integral for each of these formulations is compared and assessed from a theoretical point of view below.

The non-equilibrium formulation results in the simplest final M-integral thus requiring the least computation and implementation effort among the three formulations. This is observed by comparing Eqs.(3.24), (3.29), and (3.36). Moreover, the non-equilibrium formulation is equivalent to the incompatibility formulation, because both formulations involve the same constitutive relations and corresponding material derivatives. This equivalence is observed in the numerical examples that follow. However, the constant-constitutive-tensor formulation [117] requires the derivatives of the actual stress field, which may introduce accuracy problems with standard C^0 elements commonly used in the displacement-based FEM.

In order to further compare the three consistent formulations, let's consider an exponentially

graded material in which Poisson's ratio is constant and Young's modulus varies in any direction (see Figure 3.6)

$$E(x_1) \quad = \quad E_0 \exp{(\delta x_1)} \quad = \quad E_0 \exp{(\beta_1 X_1 + \beta_2 X_2)}, \tag{3.65}$$

$$\nu \quad = \quad \text{constant},$$

where $\mathbf{X} = (X_1, X_2)$ refers to a global coordinate system, x_1 is the direction of material gradation (inclined by θ_m with respect to the X_1 coordinate), and the nonhomogeneity parameters δ, β_1, and β_2 are related by

$$\beta_1 = \delta \cos \theta_m, \quad \beta_2 = \delta \sin \theta_m. \tag{3.66}$$
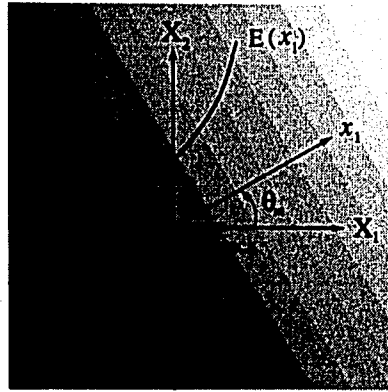
Figure 3.6: Crack geometry in a nonhomogeneous material.

This selection of material property leads to simplification of the resulting M-integrals and allows one to better assess and compare the characteristics of the formulations. Moreover, exponentially graded materials have been extensively investigated in the technical literature, e.g. [31, 7, 76, 81, 35, 28, 39, 19, 29, 49, 126, 127, 61, 108, 109, 77, 125, 89, 112]. The resulting M-integrals corresponding to the three formulations are derived below in the global coordinate system, which is used in the numerical implementation.

3.6.1 Non-equilibrium formulation

For exponentially graded materials defined by Eq.(3.65), the auxiliary stress fields chosen in this formulation are identical to the asymptotic stresses derived by Erdogan [35], which are given by

$$\sigma_{ij}(r, \theta) = \exp[r(\beta_1 \cos \theta + \beta_2 \sin \theta)] \left[\frac{K_I}{\sqrt{2\pi r}} g_{ij}^I(\theta) + \frac{K_{II}}{\sqrt{2\pi r}} g_{ij}^{II}(\theta) \right]. \qquad (3.67)$$

The derivatives of interest, with respect to the global coordinate system, are ($m = 1, 2$)

$$
\begin{aligned}
\sigma_{ij,j}^{aux} &= C_{ijkl,j}(\boldsymbol{X}) \, \varepsilon_{kl}^{aux} + C_{ijkl}(\boldsymbol{X}) \, \varepsilon_{kl,j}^{aux} = \beta_j C_{ijkl}(\boldsymbol{X}) \, \varepsilon_{kl}^{aux} + C_{ijkl}(\boldsymbol{X}) \, \varepsilon_{kl,j}^{aux} \\
&= \beta_j C_{ijkl}(\boldsymbol{X}) \, \varepsilon_{kl}^{aux} + \alpha_p (C_{ijkl})_{\text{tip}} \, \varepsilon_{kl,j}^{aux} = \beta_j \sigma_{ij}^{aux}, \qquad (3.68)
\end{aligned}
$$

$$C_{ijkl,m} = \beta_m C_{ijkl}(\boldsymbol{X}), \qquad (3.69)$$

where $\alpha_p = \exp(\beta_1 X_1 + \beta_2 X_2)$ is a factor that arises due to the proportionality of C_{ijkl} for the material gradation considered. The global interaction integral $(M_m)_{\text{global}}$ ($m = 1, 2$) is given by

$$
\begin{aligned}
(M_m)_{\text{global}} &= \int_A \left\{ \sigma_{ij} u_{i,m}^{aux} + \sigma_{ij}^{aux} u_{i,m} - \sigma_{ik} \varepsilon_{ik}^{aux} \delta_{1j} \right\} q_{,j} dA \\
&+ \int_A \left\{ \sigma_{ij,j}^{aux} u_{i,m} - C_{ijkl,m} \varepsilon_{kl} \varepsilon_{ij}^{aux} \right\} q \, dA, \qquad (3.70)
\end{aligned}
$$

Substitution of Eqs. (3.68) and (3.69) into Eq.(3.70) yields ($m = 1, 2$)

$$
\begin{aligned}
(M_m)_{\text{global}} &= \int_A \left\{ \sigma_{ij} u_{i,m}^{aux} + \sigma_{ij}^{aux} u_{i,m} - \sigma_{ik} \varepsilon_{ik}^{aux} \delta_{mj} \right\} \frac{\partial q}{\partial X_j} \, dA \\
&+ \int_A \left\{ \beta_j \sigma_{ij}^{aux} u_{i,m} - \beta_m \sigma_{ij} \varepsilon_{ij}^{aux} \right\} q \, dA. \qquad (3.71)
\end{aligned}
$$

Notice that, for this particular case, a simpler expression than that for the general case is obtained (cf. Eq.(3.24)). The derivatives of material properties are represented by material nonhomogeneity β in Eq.(3.71). Moreover, the contribution of the non-equilibrium term to the M-integral is related to the value of β.

3.6.2 Incompatibility formulation

The derivatives of interest, with respect to the global coordinate system, are $(m = 1, 2)$

$$
\begin{aligned}
\varepsilon_{ij,m}^{aux} &= S_{ijkl,m}(\boldsymbol{X})\,\sigma_{kl}^{aux} + S_{ijkl}(\boldsymbol{X})\,\sigma_{kl,m}^{aux} \\
&= -\beta_m S_{ijkl}(\boldsymbol{X})\,\sigma_{kl}^{aux} + S_{ijkl}(\boldsymbol{X})\,\sigma_{kl,m}^{aux} \\
&= -\beta_m \varepsilon_{ij}^{aux} + S_{ijkl}(\boldsymbol{X})\,\sigma_{kl,m}^{aux}
\end{aligned}
\tag{3.72}
$$

together with Eq.(3.69). The global interaction integral $(M_m)_{\text{global}}$ $(m = 1, 2)$ is given by

$$
\begin{aligned}
(M_m)_{\text{global}} &= \int_A \left\{ \sigma_{ij} u_{i,m}^{aux} + \sigma_{ij}^{aux} u_{i,m} - \sigma_{ik} \varepsilon_{ik}^{aux} \delta_{mj} \right\} q_{,j}\, dA \\
&\quad + \int_A \left\{ \sigma_{ij}(u_{i,mj}^{aux} - \varepsilon_{ij,m}^{aux}) - C_{ijkl,m} \varepsilon_{kl} \varepsilon_{ij}^{aux} \right\} q\, dA.
\end{aligned}
\tag{3.73}
$$

Substitution of Eqs.(3.72) and (3.69) into Eq.(3.73) yields $(m = 1, 2)$

$$
\begin{aligned}
(M_m)_{\text{global}} &= \int_A \left\{ \sigma_{ij} u_{i,m}^{aux} + \sigma_{ij}^{aux} u_{i,m} - \sigma_{ik} \varepsilon_{ik}^{aux} \delta_{mj} \right\} \frac{\partial q}{\partial X_j}\, dA \\
&\quad + \int_A \left\{ \sigma_{ij} u_{i,mj}^{aux} - \sigma_{ij,m}^{aux} \varepsilon_{ij} \right\} q\, dA.
\end{aligned}
\tag{3.74}
$$

Notice that, for this particular case, the final M-integral does not involve any derivatives of material properties (cf. Eq.(3.29)). In this formulation, the first integral of Eq.(3.74) is the same as that for the non-equilibrium formulation, because both formulation use the same constitutive tensor $C(\boldsymbol{X})$.

3.6.3 Constant-constitutive-tensor formulation

The derivatives of interest, with respect to the global coordinate system (X_j), are $(m = 1, 2)$

$$
\begin{aligned}
\sigma_{ij,m} &= C_{ijkl,m}(\boldsymbol{X})\,\varepsilon_{kl} + C_{ijkl}(\boldsymbol{X})\,\varepsilon_{kl,m} \\
&= \beta_m C_{ijkl}(\boldsymbol{X})\,\varepsilon_{kl} + C_{ijkl}(\boldsymbol{X})\,\varepsilon_{kl,m} \\
&= \beta_m \sigma_{ij} + C_{ijkl}(\boldsymbol{X})\,\varepsilon_{kl,m} \\
\sigma_{ij,m}^{aux} &= (C_{ijkl})_{\text{tip}} \varepsilon_{kl,m}^{aux}.
\end{aligned}
\tag{3.75}
$$

The global interaction integral $(M_m)_{\text{global}}$ $(m = 1, 2)$ is given by

$$
\begin{aligned}
M &= \int_A \left\{ \sigma_{ij} u_{i,m}^{aux} + \sigma_{ij}^{aux} u_{i,m} - \frac{1}{2} (\sigma_{ik} \varepsilon_{ik}^{aux} + \sigma_{ik}^{aux} \varepsilon_{ik}) \delta_{mj} \right\} q_{,j} dA \\
&\quad + \int_A \frac{1}{2} \left\{ \sigma_{ij} \varepsilon_{ij,m}^{aux} - \sigma_{ij,m} \varepsilon_{ij}^{aux} + \sigma_{ij}^{aux} \varepsilon_{ij,m} - \sigma_{ij,m}^{aux} \varepsilon_{ij} \right\} q \, dA.
\end{aligned}
\tag{3.76}
$$

Substitution of Eq.(3.75) into Eq.(3.76) yields $(m = 1, 2)$

$$
\begin{aligned}
M &= \int_A \left\{ \sigma_{ij} u_{i,m}^{aux} + \sigma_{ij}^{aux} u_{i,m} - \frac{1}{2} (\sigma_{ik} \varepsilon_{ik}^{aux} + \sigma_{ik}^{aux} \varepsilon_{ik}) \delta_{mj} \right\} q_{,j} dA \tag{3.77} \\
&\quad + \int_A \frac{1}{2} \left\{ \sigma_{ij} \varepsilon_{ij,m}^{aux} - \beta_m \sigma_{ij} \varepsilon_{ij}^{aux} - C_{ijkl} \varepsilon_{kl,m} \varepsilon_{ij}^{aux} + \sigma_{ij}^{aux} \varepsilon_{ij,m} - (C_{ijkl})_{tip} \varepsilon_{kl,m}^{aux} \varepsilon_{ij} \right\} q \, dA,
\end{aligned}
$$

where $C_{ijkl} \equiv C_{ijkl}(\boldsymbol{X})$. Notice that, for this case, the final M-integral requires the derivatives of the actual strain field, which may have numerical accuracy problems. The derivatives of material properties are represented by material nonhomogeneity β. Moreover, the first integral of Eq.(3.77) is different from those for the other two formulations.

3.7 Some numerical aspects

For numerical computation by means of the FEM, the M-integral is evaluated first in global coordinates $((M_m)_{\text{global}})$ and then transformed to local coordinates (M_{local}). Thus one obtains M_{local} as

$$
M_{\text{local}} = (M_1)_{\text{local}} = (M_1)_{\text{global}} \cos\theta + (M_2)_{\text{global}} \sin\theta. \tag{3.78}
$$

The M-integrals $(M_m)_{\text{global}}$ for the three consistent formulations have derivatives of material properties in common. In this thesis, closed-form expressions for derivatives of material properties are not used because these expressions would be specific to each specific function or micromechanics model. Thus, for the sake of generality, such derivatives are determined by using shape function derivatives of finite elements [76, 77].

The derivatives involving material derivatives for each formulation are

- Non-equilibrium: $\sigma_{ij,j}^{aux} = C_{ijkl,j}\ \varepsilon_{kl}^{aux} + C_{ijkl}\ \varepsilon_{kl,j}^{aux}$ (3.79)

- Incompatibility: $\varepsilon_{ij,m}^{aux} = S_{ijkl,m}\ \sigma_{kl}^{aux} + S_{ijkl}\ \sigma_{kl,m}^{aux}$ (3.80)

- Constant-constitutive-tensor: $\sigma_{ij,m} = C_{ijkl,m}\ \varepsilon_{kl} + C_{ijkl}\ \varepsilon_{kl,m}$ (3.81)

A simple and general approach to evaluate such derivatives consists of using shape function derivatives [82]. Thus the derivatives of a generic quantity P (e.g. C_{ijkl}, S_{ijkl}, or ε_{ij}) are obtained as

$$\frac{\partial P}{\partial X_m} = \sum_{i=1}^{n} \frac{\partial N_i}{\partial X_m} P_i, \quad (m = 1, 2),$$ (3.82)

where n is the number of element nodes and $N_i = N_i(\xi, \eta)$ are the element shape functions which can be found in many references, e.g. [26]. The derivatives $\partial N_i/\partial X_m$ are obtained as

$$\left\{ \begin{array}{c} \partial N_i/\partial X_1 \\ \\ \partial N_i/\partial X_2 \end{array} \right\} = J^{-1} \left\{ \begin{array}{c} \partial N_i/\partial \xi \\ \\ \partial N_i/\partial \eta \end{array} \right\}$$ (3.83)

where J^{-1} is the inverse of the standard Jacobian matrix relating (X_1, X_2) with (ξ, η) [26].

3.8 Numerical examples

All the examples consist of SIFs and/or T-stress results for both isotropic and orthotropic FGMs, and those results are obtained by means of the non-equilibrium and incompatibility formulations of the interaction integral in conjunction with the FEM. In order to validate SIFs and T-stress solutions, the FEM results for the first example (an inclined center crack in an exponentially graded plate subjected to fixed-grip loading) are compared with available semi-analytical and numerical solutions. The second example involves four-point bending specimen with delaminated cracks. The third example investigates a curved crack subjected to far-field tractions. The fourth example involves an edge crack in an FGM strip under fixed-grip loading. The fifth example provides

benchmark solutions for biaxiality ratios for laboratory specimens, and the sixth examples inves-
tigates scaling of FGM specimens. The seventh example investigates the effects of Poisson's ratio
and boundary conditions considering two kinds of crack orientation with respect to material grada-
tions. The last example investigates a crack in a multi-layered region including two homogeneous
materials and an FGM region between those regions.

3.8.1 Plate with an inclined center crack

Figure 3.7(a) shows an inclined center crack of length $2a$ located with a geometric angle θ (counter-
clockwise) in a plate subjected to fixed-grip loading; Figure 3.7(b) shows the complete mesh con-
figuration; Figure 3.7(c) shows five contours used for EDI computation of the M-integral; and
Figure 3.7(d) shows the mesh detail using 12 sectors (S12) and 4 rings (R4) of elements around the
crack tips.

The displacement boundary condition is prescribed such that $u_2 = 0$ along the lower edge, and
$u_1 = 0$ for the node at the lower left-hand-side. The mesh discretization consists of 1641 Q8, 94
T6, and 24 T6qp elements, with a total of 1759 elements and 5336 nodes.

The fixed-grip loading results in a uniform strain $\varepsilon_{22}(X_1, X_2) = \bar{\varepsilon}$ in a corresponding uncracked
structure, which corresponds to $\sigma_{22}(X_1, 10) = \bar{\varepsilon} E^0 e^{\beta X_1}$ for isotropic FGMs and $\sigma_{22}(X_1, 10) =
\bar{\varepsilon} E_{22}^0 e^{\beta X_1}$ for orthotropic FGMs (see Figure 3.7(a)). Young's moduli and shear modulus are expo-
nential functions of X_1, while Poisson's ratio is constant. The following data were used in the FEM
analyses:

plane stress, 2×2 Gauss quadrature,

$a/W = 0.1, \; L/W = 1.0, \; \theta = 0°$ to $90°, \beta a = 0.5, \bar{\varepsilon} = 1,$

Isotropic case :

$E(X_1) = E^0 e^{\beta X_1}, \; \nu(X_1) = \nu, \; E^0 = 1.0, \; \nu = 0.3$

Orthotropic case :

$E_{11}(X_1) = E_{11}^0 e^{\beta X_1}, \; E_{22}(X_1) = E_{22}^0 e^{\beta X_1}, \; G_{12}(X_1) = G_{12}^0 e^{\beta X_1}, \; \nu_{12}(X_1) = \nu_{12}^0$

$E_{11}^0 = 10^4, \; E_{22}^0 = 10^3, \; G_{12}^0 = 1216, \; \nu_{12}^0 = 0.3.$

76
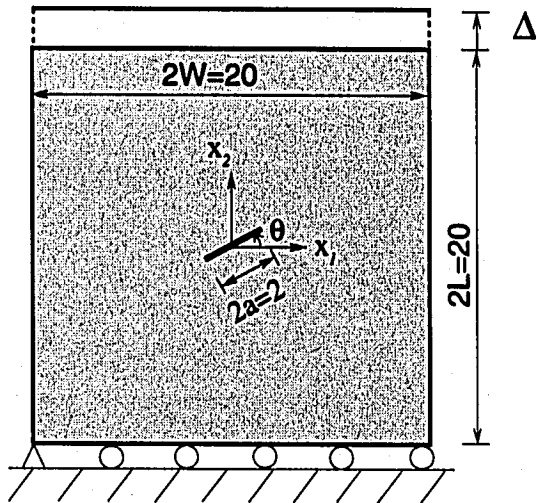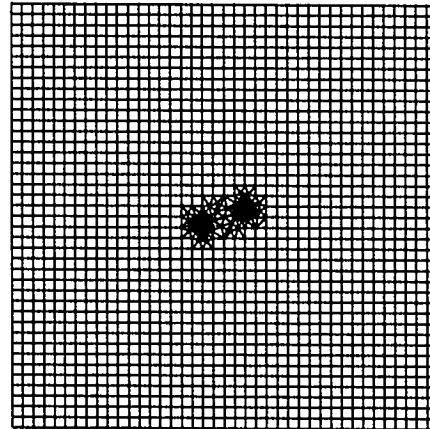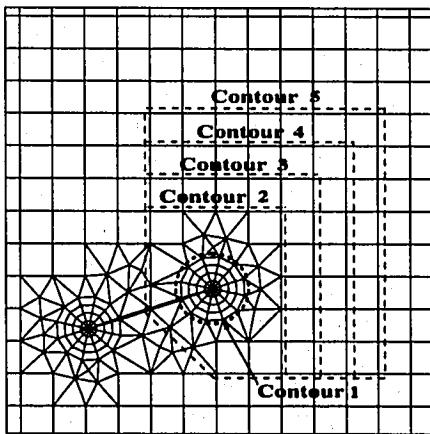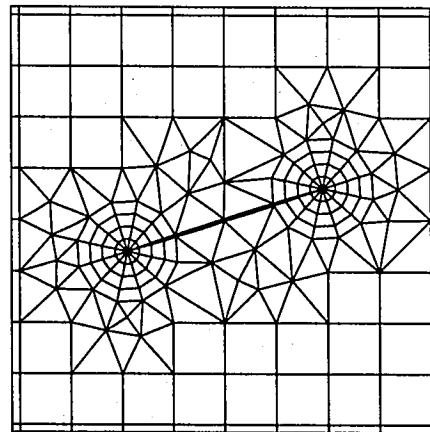
Figure 3.7: Example 1: FGM plate with an inclined crack with geometric angle θ: (a) geometry and BCs under fixed-grip loading; (b) typical finite element mesh; (c) contours for EDI computation of M-integral; (d) mesh detail using 12 sectors (S12) and 4 rings (R4) around the crack tips ($\theta = 18°$ counter-clockwise).

77

Table 3.2 compares the present FEM results for normalized SIFs obtained by the non-equilibrium formulation of the M-integral with semi-analytical solutions provided by Konda and Erdogan [89] for various geometric angles of a crack in isotropic FGMs. Notice that the present results for normalized SIFs are in remarkable agreement with those by Konda and Erdogan [89] (maximum difference 1.3%, average difference 0.6%).

Table 3.2: Example 1: comparison of normalized mixed-mode SIFs in *isotropic* FGMs for βa=0.5 ($K_0 = \bar{\varepsilon} E^0 \sqrt{\pi a}$) (see Figure 3.7).

Method	θ	K_I^+/K_0	K_{II}^+/K_0	K_I^-/K_0	K_{II}^-/K_0
Konda & Erdogan [89]	0°	1.424	0.000	0.674	0.000
	18°	1.285	0.344	0.617	0.213
	36°	0.925	0.548	0.460	0.365
	54°	0.490	0.532	0.247	0.397
	72°	0.146	0.314	0.059	0.269
	90°	0.000	0.000	0.000	0.000
Non-equilibrium	0°	1.4234	0.0000	0.6657	0.0000
	18°	1.2835	0.3454	0.6104	0.2112
	36°	0.9224	0.5502	0.4559	0.3625
	54°	0.4880	0.5338	0.2451	0.3943
	72°	0.1451	0.3147	0.0587	0.2670
	90°	0.0000	0.0000	0.0000	0.0000

Figure 3.8 shows $J = (K_I^2 + K_{II}^2)/E_{tip}$ value calculated by the interaction integral for the right crack tip of an inclined crack with $\theta = 18°$ using five contours for EDI computations as shown in Figure 3.7(c). The non-equilibrium formulation is used both considering and neglecting the non-equilibrium term (see Eq.(3.24)), and the incompatibility formulation is used both considering and neglecting the incompatible term (see Eq.(3.29)). The solutions obtained by considering the non-equilibrium term for the non-equilibrium formulation, and the incompatible term for the incompatibility formulation are not distinguishable in a graphical form. Notice that the converged solution is obtained when including either the non-equilibrium or the incompatibility term, however, such behavior is not observed when neglecting either term.

Table 3.3 compares the present FEM results for normalized SIFs obtained by the non-equilibrium formulation of the M-integral with those obtained by the incompatibility formulation for various geometric angles of a crack in orthotropic FGMs. Notice that the two formulations provide similar FEM results for SIFs for each geometric angle. Comparison of Tables 3.2 and 3.3 indicates that the material orthotropy shows significant effect on SIFs, and the SIFs K_I^+ (right crack tip) and K_{II}^- (left crack tip) for the orthotropic case are greater than or equal to those for the isotropic case,

78
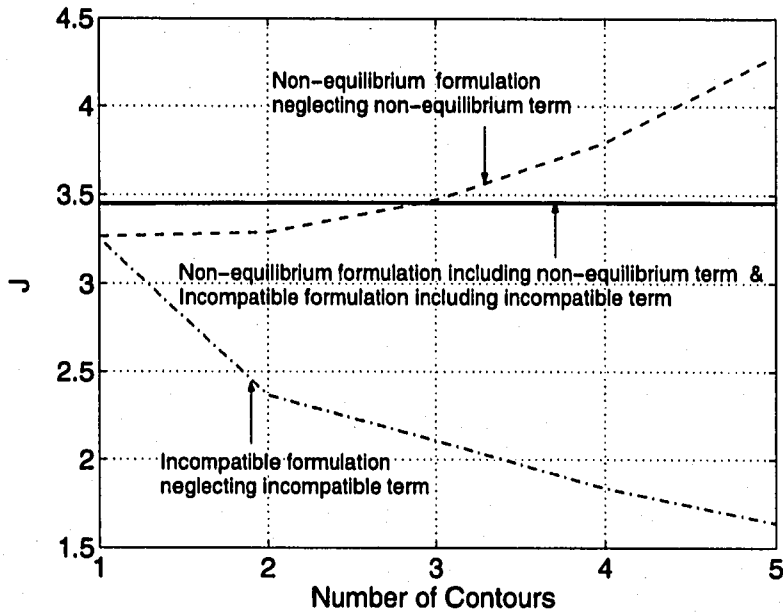
Figure 3.8: Example 1: comparison of $J = (K_I^2 + K_{II}^2)/E_{tip}$ for the right crack tip of an inclined crack with $\theta = 18°$ using the M-integral. The non-equilibrium formulation is used both considering and neglecting the non-equilibrium term (see Eq.(3.24)). The incompatibility formulation is used both considering and neglecting the incompatible term (see Eq.(3.29)).

however, the SIFs K_{II}^+ and K_I^- for the orthotropic case are smaller than or equal to those that for the isotropic case.

Table 3.3: Example 1: comparison of normalized mixed-mode SIFs in *orthotropic* FGMs for βa=0.5 ($K_0 = \bar{\varepsilon} E_{22}^0 \sqrt{\pi a}$) (see Figure 3.7).

Formulation	θ	K_I^+/K_0	K_{II}^+/K_0	K_I^-/K_0	K_{II}^-/K_0
	0°	1.4279	0.0000	0.6663	0.0000
	18°	1.3224	0.2176	0.5997	0.2436
Non-equilibrium	36°	1.0177	0.4097	0.4150	0.4160
	54°	0.6008	0.4477	0.1814	0.4379
	72°	0.2154	0.2906	0.0056	0.2822
	90°	0.0000	0.0000	0.0000	0.0000
	0°	1.4285	0.0000	0.6663	0.0000
	18°	1.3224	0.2194	0.5997	0.2427
Incompatibility	36°	1.0177	0.4111	0.4149	0.4156
	54°	0.6008	0.4480	0.1809	0.4373
	72°	0.2158	0.2906	0.0052	0.2823
	90°	0.0000	0.0000	0.0000	0.0000

Table 3.4 compares the present FEM results for normalized T-stress in isotropic FGMs obtained by the non-equilibrium formulation of the M-integral with those reported by Paulino and Dong [112]

who used the singular integral equation method. Table 3.5 compares the present FEM results for normalized T-stress obtained by the non-equilibrium formulation of the M-integral with those obtained by the incompatibility formulation for orthotropic FGMs. Notice that the two formulations provide similar FEM results for T-stress for each geometric angle. For the isotropic case, T-stress at both right and left crack tips changes sign in the range of angle $\theta = 30°$ to $45°$ (see Table 3.4), while, for the orthotropic case, it changes sign in the range of angle $\theta = 15°$ to $30°$ (see Table 3.5). Comparison of Tables 3.4 with 3.5 indicates that the material orthotropy shows significant effect on T-stress in terms of its sign and magnitude.

Table 3.4: Example 1: comparison of normalized T-stress in *isotropic* FGMs for βa=0.5 ($\sigma_0 = \bar{\varepsilon}E^0$)(see Figure 3.7).

θ	Non-equilibrium		Paulino and Dong [112]	
	$T(+a)/\sigma_0$	$T(-a)/\sigma_0$	$T(+a)/\sigma_0$	$T(-a)/\sigma_0$
0°	-0.896	-0.858	-0.867	-0.876
15°	-0.773	-0.747	-0.748	-0.763
30°	-0.434	-0.436	-0.420	-0.444
45°	0.036	0.011	0.039	0.010
60°	0.513	0.484	0.513	0.490
75°	0.868	0.850	0.870	0.858
90°	0.994	0.994	1.000	1.000

Table 3.5: Example 1: comparison of normalized T-stress in *orthotropic* FGMs for βa=0.5 ($\sigma_0 = \bar{\varepsilon}E_{22}^0$)(see Figure 3.7).

θ	Non-equilibrium		Incompatibility	
	$T(+a)/\sigma_0$	$T(-a)/\sigma_0$	$T(+a)/\sigma_0$	$T(-a)/\sigma_0$
0°	-2.822	-2.725	-2.832	-2.712
15°	-1.407	-1.402	-1.384	-1.407
30°	0.156	0.079	0.168	0.074
45°	0.785	0.700	0.785	0.702
60°	0.971	0.909	0.970	0.910
75°	1.003	0.973	1.002	0.973
90°	0.996	0.996	0.997	0.997

3.8.2 Four-point bending specimen

Gu and Asaro [49] investigated the effect of material orthotropy on mixed-mode SIFs in FGMs considering a four-point bending specimen with exponentially varying Young's moduli, shear modulus, and Poisson's ratio. This example investigates SIFs and T-stress by means of the interaction integral method.
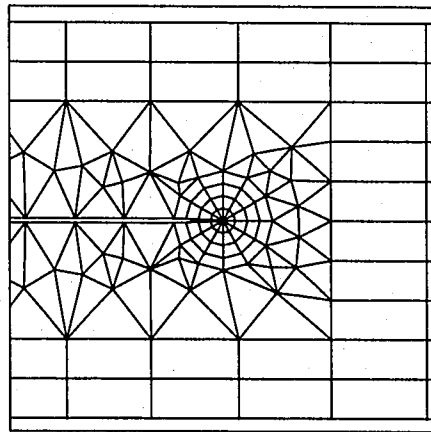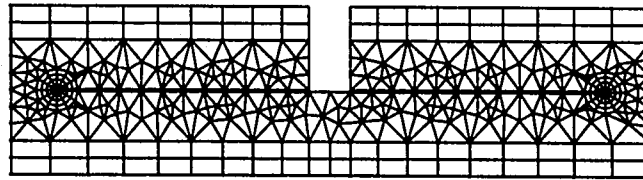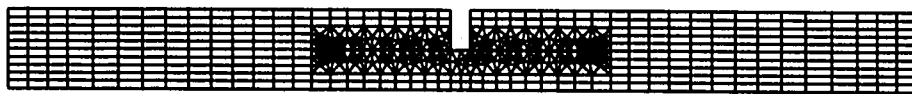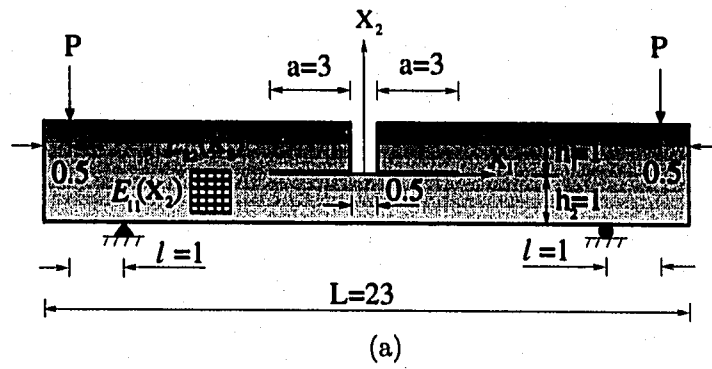
Figure 3.9: Example 2: Four-point bending specimen: (a) geometry and BCs; (b) complete finite element mesh; (c) mesh detail using 12 sectors (S12) and 4 rings (R4) around crack tips; (d) enlarged view of the right crack tip.

81

Figure 3.9(a) shows the four-point bending specimen geometry and BCs, Figure 3.9(b) shows the complete FEM mesh configuration, Figure 3.9(c) shows a mesh detail around the crack, and Figure 3.9(d) shows a zoom of the right crack tip. The point loads of magnitude P are applied at the nodes $(X_1, X_2) = (\pm 11, 1.0)$. The displacement boundary conditions are prescribed such that $(u_1, u_2) = (0, 0)$ for the node at $(X_1, X_2) = (-10, -1.0)$ and $u_2 = 0$ for the node at $(X_1, X_2) = (10, -1.0)$.

For the evaluation of SIFs, Young's moduli, shear modulus, and Poisson's ratios are assumed as exponential functions of X_2 given by

$$E_{11}(X_2) = E_{11}^0 e^{\beta X_2}, \quad E_{22}(X_2) = E_{22}^0 e^{\beta X_2};$$

$$\nu_{12}(X_2) = \nu_{12}^0 (1 + \epsilon X_2) e^{\beta X_2}, \quad \nu_{21}(X_2) = \nu_{21}^0 (1 + \epsilon X_2) e^{\beta X_2};$$

$$G_{12}(X_2) = E_{22}(X_2)/[2(\sqrt{\lambda} + \nu_{21}(X_2))]; \quad \lambda = E_{22}(X_2)/E_{11}(X_2), \tag{3.84}$$

respectively.

For the evaluation of T-stress, Young's moduli and shear modulus are assumed as exponential functions of X_2, while Poisson's ratio is constant. The material properties are given by

$$E_{11}(X_2) = E_{11}^0 e^{\beta X_2}, \quad E_{22}(X_2) = E_{22}^0 e^{\beta X_2}, G_{12}(X_2) = G_{12}^0 e^{\beta X_2}$$

$$\nu_{12}(X_2) = \nu_{12}^0, \quad \lambda = E_{22}(X_2)/E_{11}(X_2). \tag{3.85}$$

Moreover, the numerical values of properties adopted are given in Table 3.6.

Table 3.6: Example 2: numerical values of material properties.

λ	E_{11}^0	E_{22}^0	G_{12}^0	ν_{12}^0
0.1	1	0.1	0.5	0.3
1	1	1	0.3846	0.3
10	1	10	0.5	0.03

The mesh discretization consists of 625 Q8, 203 T6, and 24 T6qp elements, with a total of 852

elements and 2319 nodes. The following data were used for the FEM analysis:

$$\text{plane stress, } 2 \times 2 \text{ Gauss quadrature,}$$

$$a = 3.0, \quad h_1/h_2 = 1.0, \quad \epsilon = -0.9, \quad P = 1.0. \tag{3.86}$$

Figures 3.10 and 3.11 show comparison of the SIF $|K|h_1^{3/2}/Pl$ with $|K| = \sqrt{K_I^2 + K_{II}^2}$, and the phase angle $\psi = \tan^{-1}(K_{II}/K_I)$, respectively, obtained by the interaction integral method with those reported by Gu and Asaro [49]. There is quite good agreement between the two solutions, although Gu and Asaro [49] did not provide geometry information. Notice that as βh_1 increases, both the SIF and the phase angle ψ increase, and the material orthotropy (measured by $\lambda = E_{22}/E_{11}$) shows significant influence on the results. Moreover, for a fixed βh_1, as λ increases the SIF increases, however, the phase angle decreases.
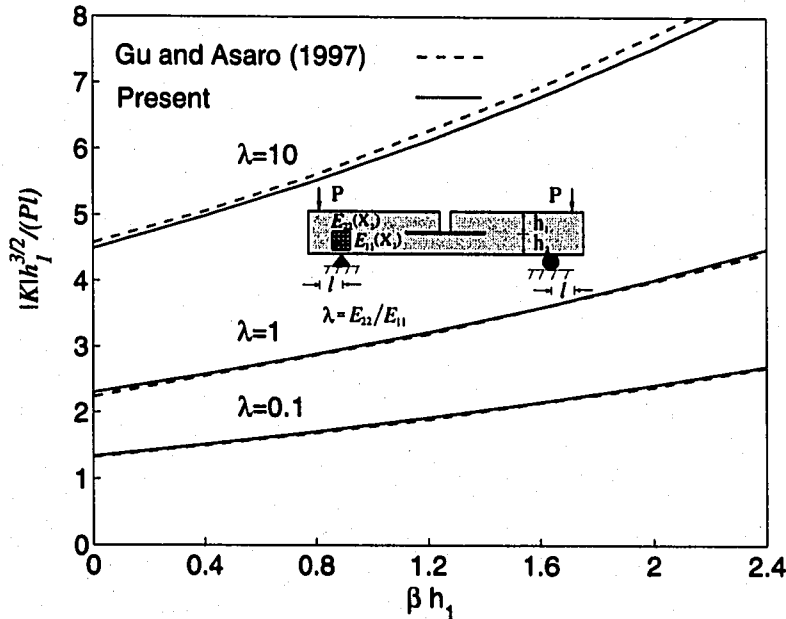
Figure 3.10: Example 2: The normalized norm of mixed-mode SIFs $|K|h_1^{3/2}/Pl$ for a four-point bending specimen. The parameter $\lambda = E_{22}/E_{11}$.

Figure 3.12 shows the FEM results for the T-stress obtained by the interaction integral method in conjunction with the Lekhnitskii formalism. Notice that T-stresses are all positive for the range of the material orthotropy $\lambda = E_{22}/E_{11}$ and material nonhomogeneity parameter βh_1. The T-stress for the right crack tip is the same that for the left crack tip due to the symmetry, and this feature
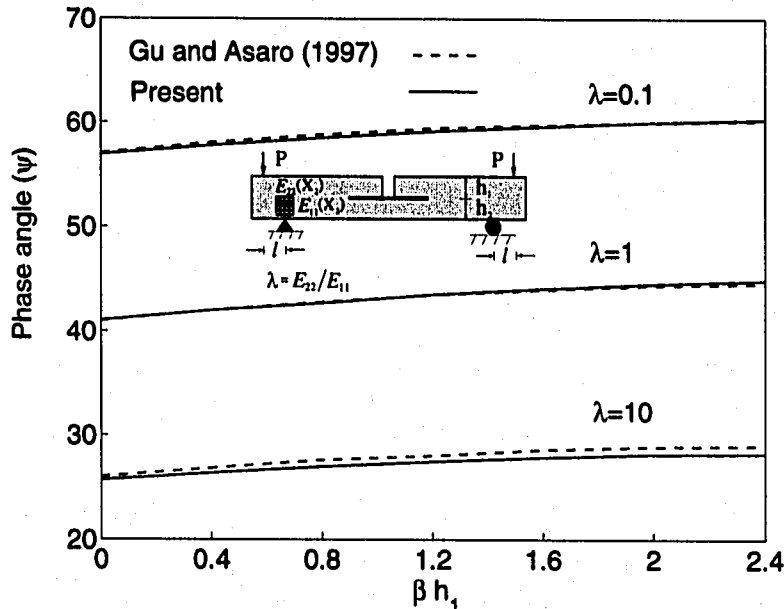
Figure 3.11: Example 2: The phase angle $\psi = \tan^{-1}(K_I/K_{II})$ for a four-point bending specimen. The parameter $\lambda = E_{22}/E_{11}$.

is captured by the present FEM implementation. There is a significant influence of the material orthotropy λ and material nonhomogeneity βh_1 on the T-stress. As either βh_1 or λ increases, the T-stress increases. With increasing material nonhomogeneity βh_1, the effect of material orthotropy λ on T-stress becomes pronounced.

3.8.3 Plate with a curved crack

Muskhelishvili [103] used conformal mapping and provided the exact solutions for SIFs of a curved crack in a homogeneous medium under far-field traction, according to the scheme shown in Figure 3.13.

The exact solutions for SIFs are given by

$$K_I = \frac{\sigma\sqrt{\pi R \sin\theta}}{2}\left[F(\theta)\cos\frac{\theta}{2} + \sin 2\omega \sin^3\frac{\theta}{2} + \cos\left(2\omega - \frac{3\theta}{2}\right)\right],$$
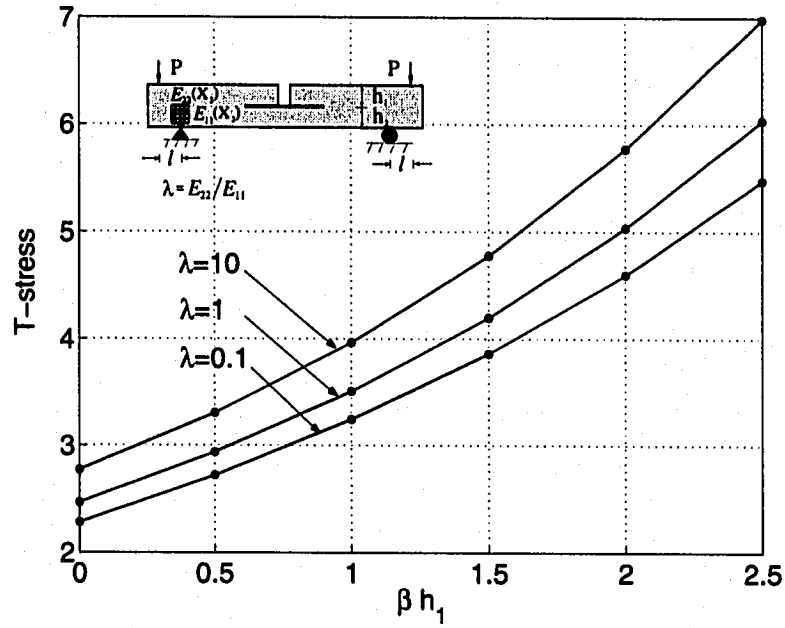
Figure 3.12: Example 2: T-stress for four-point bending specimen. The parameter $\lambda = E_{22}/E_{11}$ is the orthotropy ratio. Notice that the parameters λ and βh_1 influence T-stress.
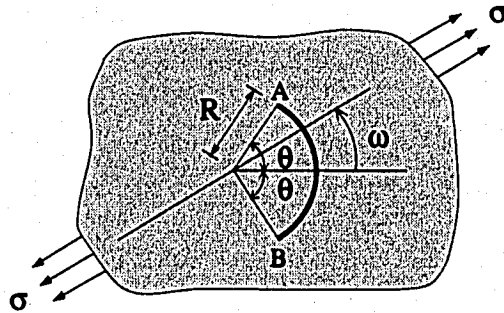
Figure 3.13: Example 3: A curved crack (circular) under far-field traction.

$$K_{II} = \frac{\sigma\sqrt{\pi R \sin\theta}}{2}\left[F(\theta)\sin\frac{\theta}{2} - \sin 2\omega \sin^2\frac{\theta}{2}\cos\frac{\theta}{2} - \sin\left(2\omega - \frac{3\theta}{2}\right)\right], \qquad (3.87)$$

where

$$F(\theta) = \frac{1 - \cos 2\omega \, \sin^2(\theta/2)\cos^2(\theta/2)}{1 + \sin^2(\theta/2)}$$

in which ω indicates the angle of the direction of applied traction σ with respect to the horizontal line, and K_I and K_{II} are the SIFs at the top crack tip (Tip A). The mode I SIF at the bottom crack tip (Tip B) is the same as K_I in Eq.(3.87), however, the mode II SIF changes sign. Our numerical solution (M-integral) will be tested against these theoretical (reference) solutions.

Figures 3.14(a) and 3.14(b) show a circular-shaped crack located in a finite two-dimensional plate under remote uniform tension loading for two different boundary conditions. These boundary conditions are prescribed such that, for the first set of BCs (Figure 3.14(a)), $u_1 = u_2 = 0$ for the node in the middle of the left edge, and $u_2 = 0$ for the node in the middle of the right edge; while for the second set of BCs (Figure 3.14(b)), $u_1 = 0$ for all the nodes along the left edge and $u_2 = 0$ for the bottom-corner node. Figure 3.14(c) shows the complete finite element mesh configuration, and Figure 3.14(d) shows a mesh detail using 12 sectors (S12) and 5 rings (R5) around the crack tips. The applied load corresponds to $\sigma_{22}(X_1, \pm L) = \pm\sigma = \pm 1.0$ for the BC in Figure 3.14(a) and $\sigma_{11}(\pm W, X_2) = \pm\sigma = \pm 1.0$ for the BC in Figure 3.14(b).

The mesh discretization consists of 1691 Q8, 184 T6, and 24 T6qp elements, with a total of 1875 elements and 5608 nodes. The following data are used in the FEM analyses:

plane stress, 2×2 Gauss quadrature, $R = 1.0$, $L/W = 1.0$,

Isotropic case (Homogeneous) : $E = 1.0$, $\nu = 0.3$

Orthotropic case :

$$E_{11}(X_1) = E_{11}^0 e^{\beta X_1}, \ E_{22}(X_1) = E_{22}^0 e^{\beta X_1}, \ G_{12}(X_1) = G_{12}^0 e^{\beta X_1},$$

$$E_{11}(X_2) = E_{11}^0 e^{\beta X_2}, \ E_{22}(X_2) = E_{22}^0 e^{\beta X_2}, \ G_{12}(X_2) = G_{12}^0 e^{\beta X_2},$$

$$E_{11}^0 = 1.0, \ E_{22}^0 = 0.5, \ G_{12}^0 = 0.25, \ \nu_{12} = 0.3, \ \beta R = (0.0 \text{ to } 0.5)$$
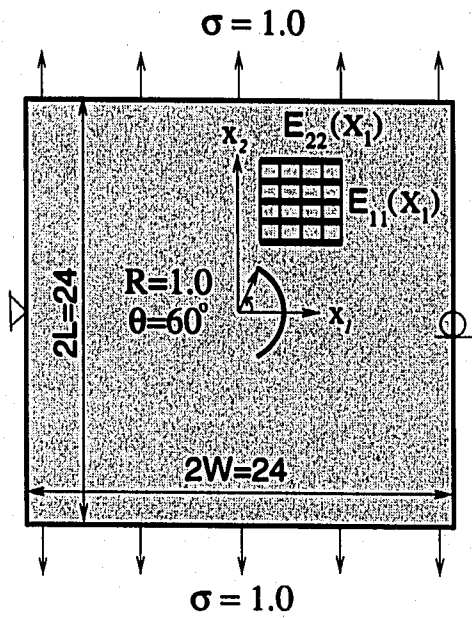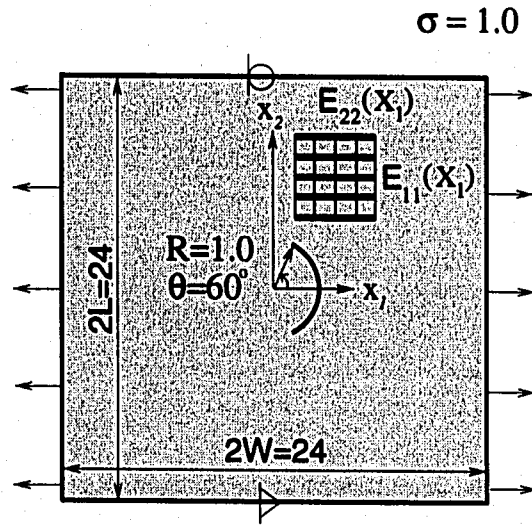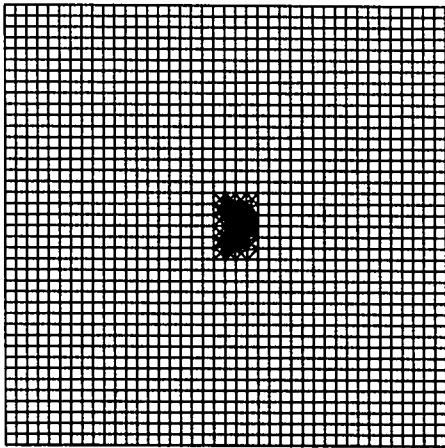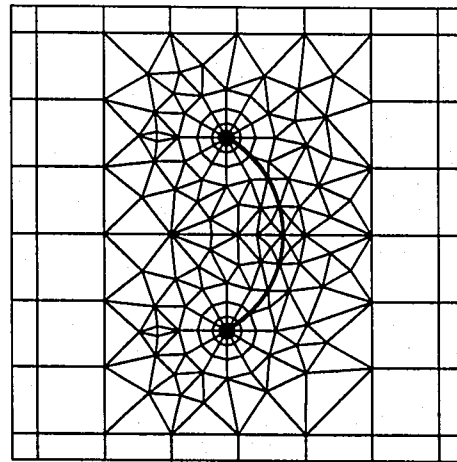
Figure 3.14: Example 3: plate with a single curved crack: (a) geometry and BCs (first set of BCs); (b) geometry and BCs (second set of BCs); (c) complete finite element mesh; (d) mesh detail with 12 sectors (S12) and 5 rings (R5) around the crack tip (S12,R5) - the thick line indicates the crack faces.

Table 3.7 shows FEM results for SIFs for both the top and bottom crack tips obtained by means of the incompatibility formulation of the interaction integral method for a semi-circular crack con-

sidering the two sets of boundary conditions and the two choices of gradation directions, i.e. X_1 and X_2. It also compares the present results with the available reference solutions of Muskhelishvili [103] for the homogeneous isotropic case. In this latter case, the numerical solutions are obtained as a particular case of the general formulation for nonhomogeneous orthotropic materials. The calculated SIFs agree well with the reference solutions. For material gradation along the direction X_1, the mode II SIF at the bottom crack tip changes sign because of symmetry, however, for material gradation along the X_2 direction, both mode I and mode II SIFs change in magnitude and sign.

Table 3.7: Example 3: FEM results for SIFs for a semi-circular crack. **Case 1:** first set of BCs - Figure 3.14(a); **Case 2:** second set of BCs - Figure 3.14(b). The exact solution for homogeneous isotropic materials was reported by Muskhelishvili (1953).

Crack Tip	Case	Material	βR	Gradation Direction	M-integral		MCC		Exact	
					K_I	K_{II}	K_I	K_{II}	K_I	K_{II}
Top	1	Iso	0.0	-	0.6872	-0.4314	0.6765	-0.4303	0.6785	-0.4330
		Ortho	0.0	-	0.6868	-0.4362	0.6853	-0.4321	-	-
			0.1	X_1	0.8240	-0.3718	0.8218	-0.3678	-	-
				X_2	0.6602	-0.4498	0.6596	-0.4451	-	-
	2	Iso	0.0	-	0.4690	1.0890	0.4692	1.0890	0.4643	1.0928
		Ortho	0.0	-	0.5059	1.0470	0.5053	1.0412	-	-
			0.1	X_1	0.5131	1.0489	0.5125	1.0425	-	-
				X_2	0.6160	1.0771	0.6159	1.0734	-	-
Bottom	1	Ortho	0.1	X_2	0.6739	0.4351	0.6700	0.4306	-	-
	2	Ortho	0.1	X_2	0.5341	-1.0692	0.5338	-1.0628	-	-

Figures 3.15(a) and 3.15(b) show curved crack surface displacement profile considering the isotropic homogeneous case and the orthotropic FGM case with gradation along the X_1 direction, respectively, for the first set of BCs (see Figure 3.14(a)). Notice that the curved crack geometry naturally creates mode-mixity which is observed around crack-tip elements. Moreover, the symmetry of crack opening profiles exists with respect to the Cartesian direction X_1 for this case, i.e. the homogeneous case and FGM case with gradation of X_1. The crack faces interpenetrate for the isotropic homogeneous case, while this behavior does not occur for the orthotropic FGM case. Figures 3.16(a) and 3.16(b) show curved crack surface displacement profile considering the orthotropic FGM case with gradation of X_2 for the first and second set of BCs, respectively. We observe that the interpenetration of the crack faces is also observed for the orthotropic FGM case with gradation of X_2 using the first set of BCs. As expected, the symmetry of crack opening profiles is naturally

lost for the FGM with gradation along X_2 direction.
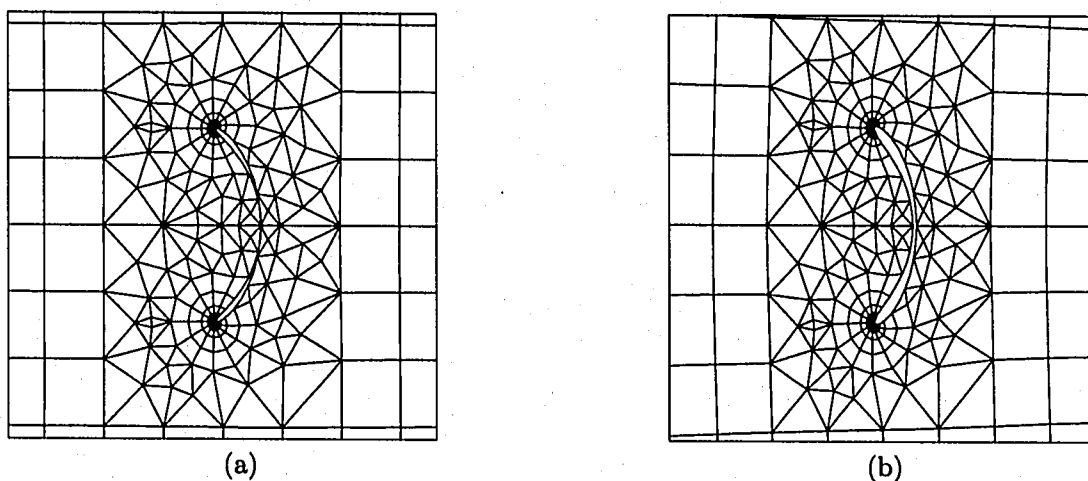
Figure 3.15: Example 3: Curved crack surface displacement profile (deformed shape) considering the first set of BCs: (a) isotropic homogeneous case; (b) orthotropic FGM with gradation along the X_1 direction.
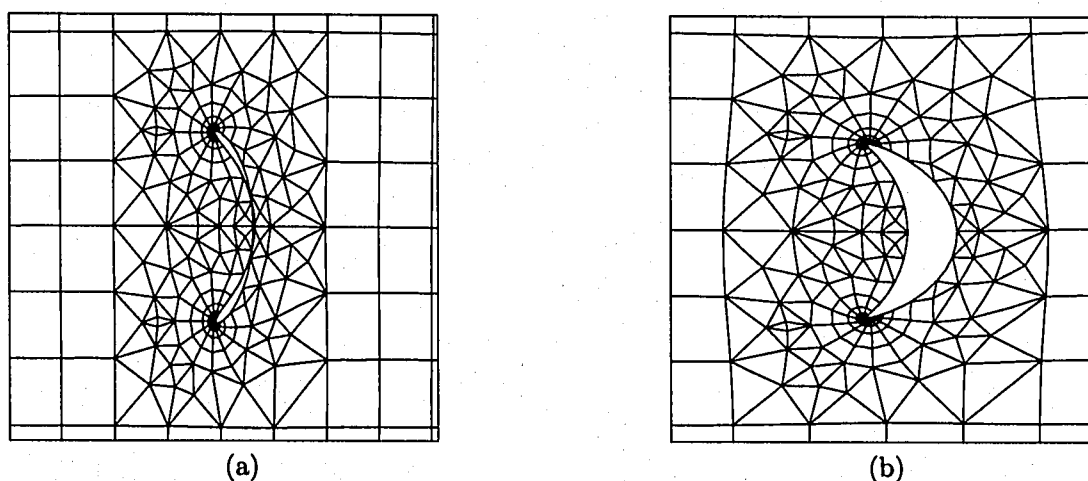
Figure 3.16: Example 3: Curved crack surface displacement profile (deformed shape) considering gradation along the X_2 direction in orthotropic FGMs: (a) first set of BCs; (b) second set of BCs.

Tables 3.8 and 3.9 show FEM results for T-stress obtained by means of the interaction integral in conjunction with the Lekhnitskii formalism for a single curved crack considering the two sets of boundary conditions illustrated by Figures 3.14(a) and 3.14(b) and gradation along the X_1 direction. There is a significant influence of material orthotropy and material nonhomogeneity (parameter βR) on the T-stress. Because of the symmetry, the T-stress on the top and bottom

89

crack tips are identical. The T-stress for orthotropic homogeneous material differs significantly from that for isotropic homogeneous material. For orthotropic materials, the nonhomogeneity parameter βR increases the T-stress for the first set of BCs (Case 1: Figure 3.14(a), Table 3.8) and decreases the T-stress for the second set of BCs (Case 2: Figure 3.14(b), Table 3.9). Moreover, for Case 1, the T-stress remains negative for the range of βR investigated ($0 \leq \beta R \leq 0.5$), however, for Case 2, it changes sign at $\beta R \approx 0.47$. The change in the sign of T-stress indicates that the nonhomogeneity parameter βR influences crack path stability.

Table 3.8: Example 3: T-stress for a single curved crack. **Case 1**: first set of BCs – see Figure 3.14(a).

Case	Material	βR	T-stress
1	Iso	0.0	-0.3684
	Ortho	0.0	-0.2748
		0.1	-0.2724
		0.2	-0.2520
		0.3	-0.2099
		0.4	-0.1513
		0.5	-0.0981

Table 3.9: Example 3: T-stress for a single curved crack. **Case 2**: second set of BCs – see Figure 3.14(b).

Case	Material	βR	T-stress
2	Iso	0.0	0.6076
	Ortho	0.0	0.4057
		0.1	0.3230
		0.2	0.2389
		0.3	0.1516
		0.4	0.0655
		0.5	-0.0185

3.8.4   Strip with an edge crack

Figure 3.17(a) shows an edge crack of length "a" in a plate, and Figure 3.17(b) shows the complete mesh discretization using 12 sectors (S12) and 4 rings (R4) of elements around the crack tip. Figures 3.17(c), 3.17(d), and 3.17(e) illustrate the three considered types of hyperbolic-tangent material gradation with respect to the crack tip: reference configuration, translation to the left, and translation to the right, respectively. The fixed-grip displacement loading results in a uniform strain $\varepsilon_{22}(X_1, X_2) = \bar{\varepsilon}$ in a corresponding uncracked structure.

90

The displacement boundary condition is prescribed such that $u_2 = 0$ along the lower edge and $u_1 = 0$ for the node at the left-hand-side.

(a)

(b)

(c)

(d)

(e)
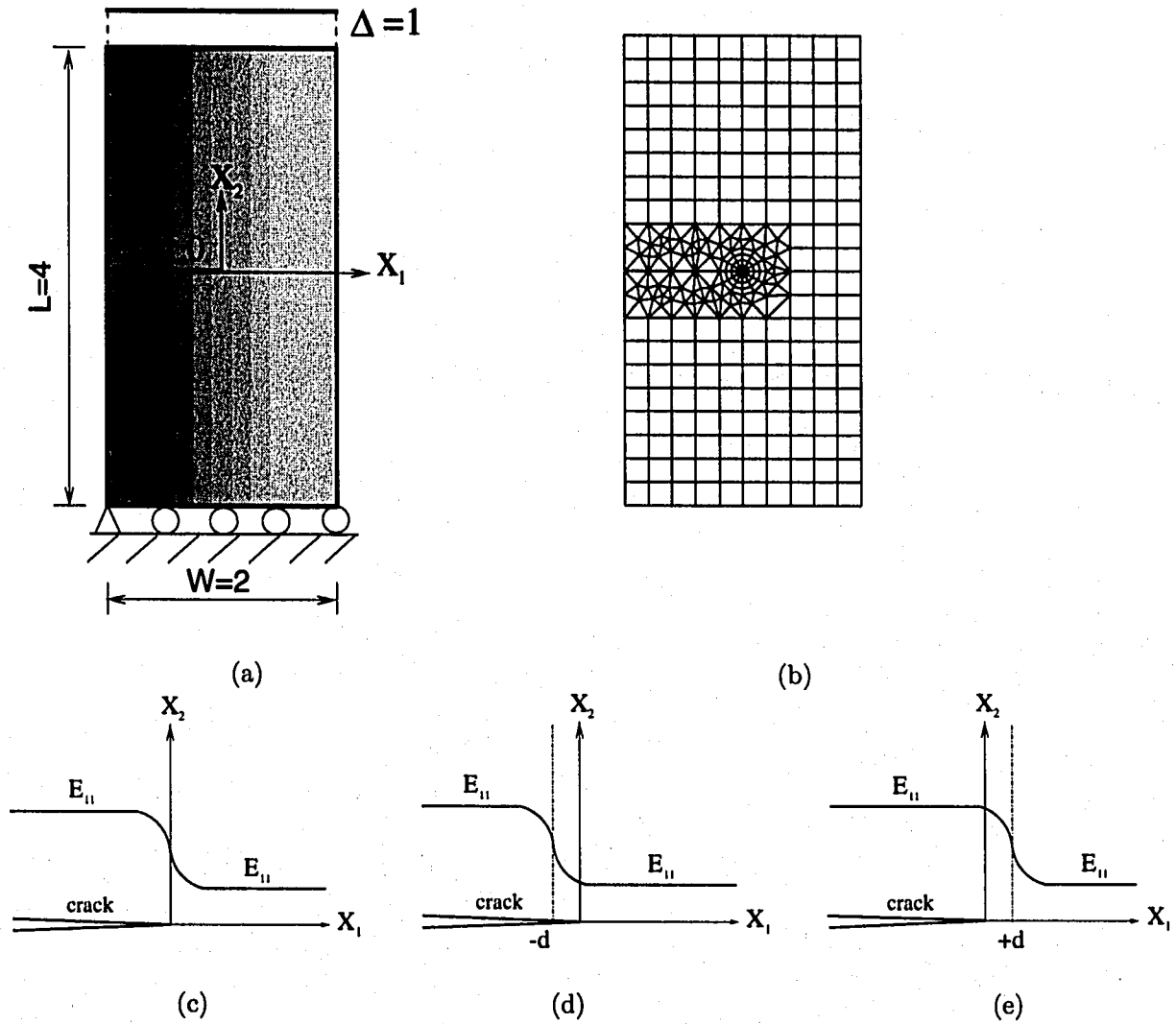
Figure 3.17: Example 4: Strip with an edge crack in hyperbolic-tangent materials: (a) geometry and BCs; (b) complete finite element mesh with 12 sectors (S12) and 4 rings (R4) around the crack tip; (c) reference configuration ($d = 0.0$); (d) translation of material gradation to the left ($d = +0.5$); (e) translation of material gradation to the right ($d = -0.5$).

The mesh discretization consists of 208 Q8, 37 T6, and 12 T6qp elements, with a total of 257 elements and 1001 nodes.

Young's moduli and shear modulus are hyperbolic-tangent functions with respect to the global (X_1, X_2) Cartesian coordinates, while Poisson's ratio is constant. The following data were used for
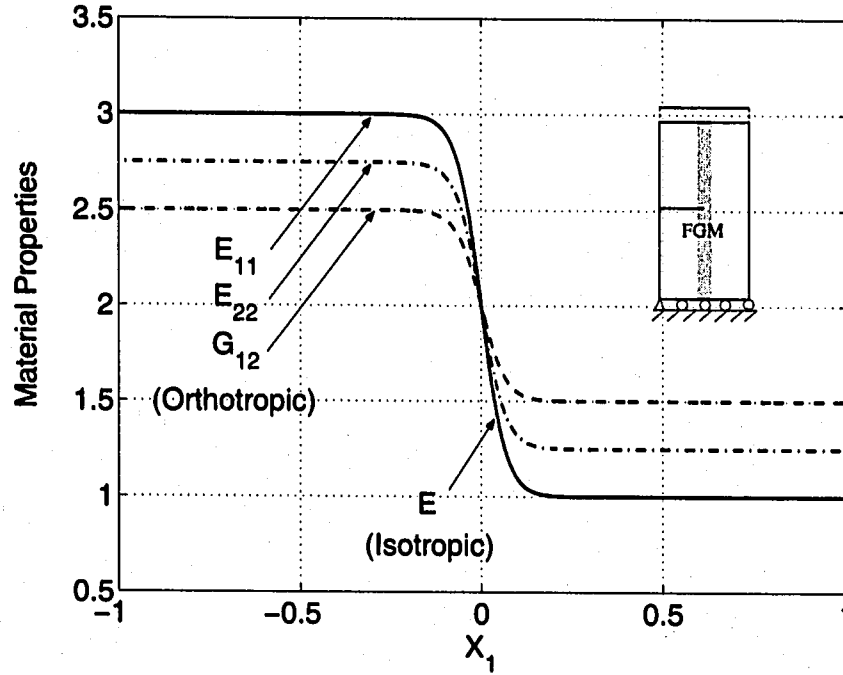
Figure 3.18: Example 4: Variation of material properties: E_{11}, E_{22}, and G_{12} for the orthotropic case, and E for the isotropic case.

the FEM analysis (see Figure 3.18):

$$\text{plane strain}, 2 \times 2 \text{ Gauss quadrature},$$

$$a/W = 0.5, L/W = 2.0, \bar{\varepsilon} = 0.25, \quad d = (-0.5 \text{ to } 0.5)$$

Isotropic case :

$$E(X_1) = (E^- + E^+)/2 + \tanh\left[\beta(X_1 + d)\right](E^- - E^+)/2,$$

$$\beta a = 15.0, \quad \nu = 0.3, \quad (E^-, E^+) = (1.00, 3.00)$$

Orthotropic case :

$$E_{11}(X_1) = (E_{11}^- + E_{11}^+)/2 + \tanh\left[\alpha(X_1 + d)\right](E_{11}^- - E_{11}^+)/2,$$

$$E_{22}(X_1) = (E_{22}^- + E_{22}^+)/2 + \tanh\left[\beta(X_1 + d)\right](E_{22}^- - E_{22}^+)/2,$$

$$G_{12}(X_1) = (G_{12}^- + G_{12}^+)/2 + \tanh\left[\gamma(X_1 + d)\right](G_{12}^- - G_{12}^+)/2,$$

$$\alpha a = \beta a = \gamma a = 15.0, \quad \nu_{12} = 0.3,$$

$$(E_{11}^-, E_{11}^+) = (1.00, 3.00), \quad (E_{22}^-, E_{22}^+) = (1.25, 2.75), \quad (G_{12}^-, G_{12}^+) = (1.50, 2.50).$$

Table 3.10 compares the present FEM results for mode I SIF (K_I) obtained by the non-equilibrium formulation with those obtained by the incompatibility formulation for various translation factors "d" of hyperbolic-tangent material variation considering both isotropic and orthotropic FGMs.

Table 3.10: Example 4: comparison of mode I SIF (K_I) for an edge crack considering translation (d) of hyperbolic-tangent material variation (see Figure 3.17).

d	Non-equilibrium		Incompatibility	
	Iso	Ortho	Iso	Ortho [85]
-0.5	1.212	1.164	1.186	1.158
-0.4	1.211	1.167	1.201	1.163
-0.3	1.211	1.175	1.190	1.173
-0.2	1.218	1.189	1.209	1.189
-0.1	1.231	1.212	1.212	1.217
0	1.030	1.047	1.026	1.049
0.1	0.595	0.701	0.588	0.697
0.2	0.486	0.615	0.487	0.614
0.3	0.451	0.585	0.451	0.585
0.4	0.430	0.567	0.430	0.567
0.5	0.419	0.554	0.419	0.554

For the orthotropic case, the FEM results obtained by the non-equilibrium formulation are compared with those obtained by the incompatibility formulation reported by Kim and Paulino [85]. Notice that the two equivalent formulations provide similar FEM results for mode I SIF for each translation factor "d". For the isotropic FGMs, the mode I SIF decreases with the translation factor "d" for the range between -0.1 and 0.5. For the orthotropic FGMs, the mode I SIF increases with the translation factor "d" for the range between -0.5 and -0.1, however, it decreases as "d" increases further. Table 3.10 also indicates that mode I SIFs for the orthotropic case are smaller than those for the isotropic case for each translation factor "d" from -0.5 to -0.1, however, the SIFs for the orthotropic case are greater than those for the isotropic case for $d = 0$ to 0.5.

Table 3.11 compares the present FEM results for T-stress obtained by the non-equilibrium formulation with those obtained by the incompatibility formulation for various translation factors "d" of hyperbolic-tangent material variation considering both isotropic and orthotropic FGMs. Notice that the two formulations provide similar FEM results, and the T-stresses are negative for all the translation factors "d" considered. For both isotropic and orthotropic FGMs, the T-stress decreases with the translation factor "d" for the range between -0.5 and 0.0, however, it increases as "d" increases further. Table 3.11 also indicates that T-stress for the orthotropic case is greater than or

equal to that for the isotropic case for each translation factor.

Table 3.11: Example 4: comparison of T-stress for an edge crack considering translation (d) of hyperbolic-tangent material variation (see Figure 3.17).

d	Non-equilibrium		Incompatibility	
	Iso	Ortho	Iso	Ortho
-0.5	-0.463	-0.393	-0.452	-0.394
-0.4	-0.478	-0.407	-0.470	-0.406
-0.3	-0.507	-0.434	-0.493	-0.439
-0.2	-0.580	-0.499	-0.571	-0.501
-0.1	-0.797	-0.686	-0.797	-0.702
0	-1.123	-0.923	-1.181	-0.962
0.1	-0.444	-0.364	-0.431	-0.362
0.2	-0.218	-0.205	-0.217	-0.205
0.3	-0.175	-0.171	-0.175	-0.171
0.4	-0.157	-0.157	-0.157	-0.157
0.5	-0.152	-0.151	-0.152	-0.152

3.8.5 Benchmark examples: laboratory specimens

This example investigates the following benchmark laboratory specimens:

- Single edge notched tension (SENT)

- Single edge notched bending (SENB)

- Center cracked tension (CCT)

- Double edge notched tension (DENT)

- Compact tension (CT)

A similar study for homogeneous materials was conducted by Sherry *et al.* [129]. They investigated T-stress for two and three dimensional cracked geometries, and provided T-stress and the biaxiality ratio for the above specimen types, but the dimensions are different from those considered in this paper. Figures 3.19(a) to 3.19(e) show SENT, SENB, CCT, DENT, and CT specimens, respectively. Figures 3.20(a) to 3.20(d) show the complete finite element meshes for SENT or SENB, CCT, DENT, and CT specimens, respectively, and Figure 3.20(e) shows the mesh detail of the CCT specimen using 12 sectors (S12) and 4 rings (R4) around the crack tips.

The applied loads are as follows:

$$\sigma_{22}(X_1, \pm L) = \pm 1 \quad \text{for SENT,}$$

$$P(W, 0) = -1 \quad \text{for SENB,}$$

$$\sigma_{22}(X_1, \pm L) = \pm 1 \quad \text{for CCT and DENT,}$$

$$P(0, \pm 0.275) = \pm 1 \quad \text{for CT,}$$

where σ_{22} is equidistributed traction on the boundary of FGM specimens.

The displacement boundary condition is prescribed as follows:

$$(u_1, u_2)(W, 0) = (0, 0), \ u_2(a, 0) = 0 \quad \text{for SENT and CT,}$$

$$(u_1, u_2)(0, L) = (0, 0), \ u_1(0, -L) = 0 \quad \text{for SENB,}$$

$$(u_1, u_2)(0, 0) = (0, 0), \ u_2(2W, 0) = 0 \quad \text{for CCT,}$$

$$(u_1, u_2)(a, 0) = (0, 0), \ u_2(2W - a, 0) = 0 \quad \text{for DENT.}$$

Young's modulus is an exponential function given by

$$E(X_1) = E_1 e^{\gamma X_1}, \tag{3.88}$$

where $E_1 = E(0)$ and $E_2 = E(W)$ for SENT, SENB, and CT specimens and $E_1 = E(0)$ and $E_2 = E(2W)$ for CCT and DENT specimens. The Poisson's ratio is taken as constant for all the specimens. The following data are used for the FEM analyses:

$$\text{plane strain, } 2 \times 2 \text{ Gauss quadrature,}$$

$$a/W = (0.1 \text{ to } 0.8), \ L = 6.0, \ W = 1.0,$$

$$E_2/E_1 = (0.1, 0.2, 1.0, 5, 10), \ E_1 = 1.0, \ \nu = 0.3. \tag{3.89}$$

Figure 3.21 shows biaxiality ratio ($\beta = T\sqrt{\pi a}/K_I$) versus the ratio of crack length to width a/W for various specimens considering homogeneous materials ($E_2 = E_1$). The mode I SIF K_I is calculated by the non-equilibrium formulation of the interaction integral method involving auxiliary
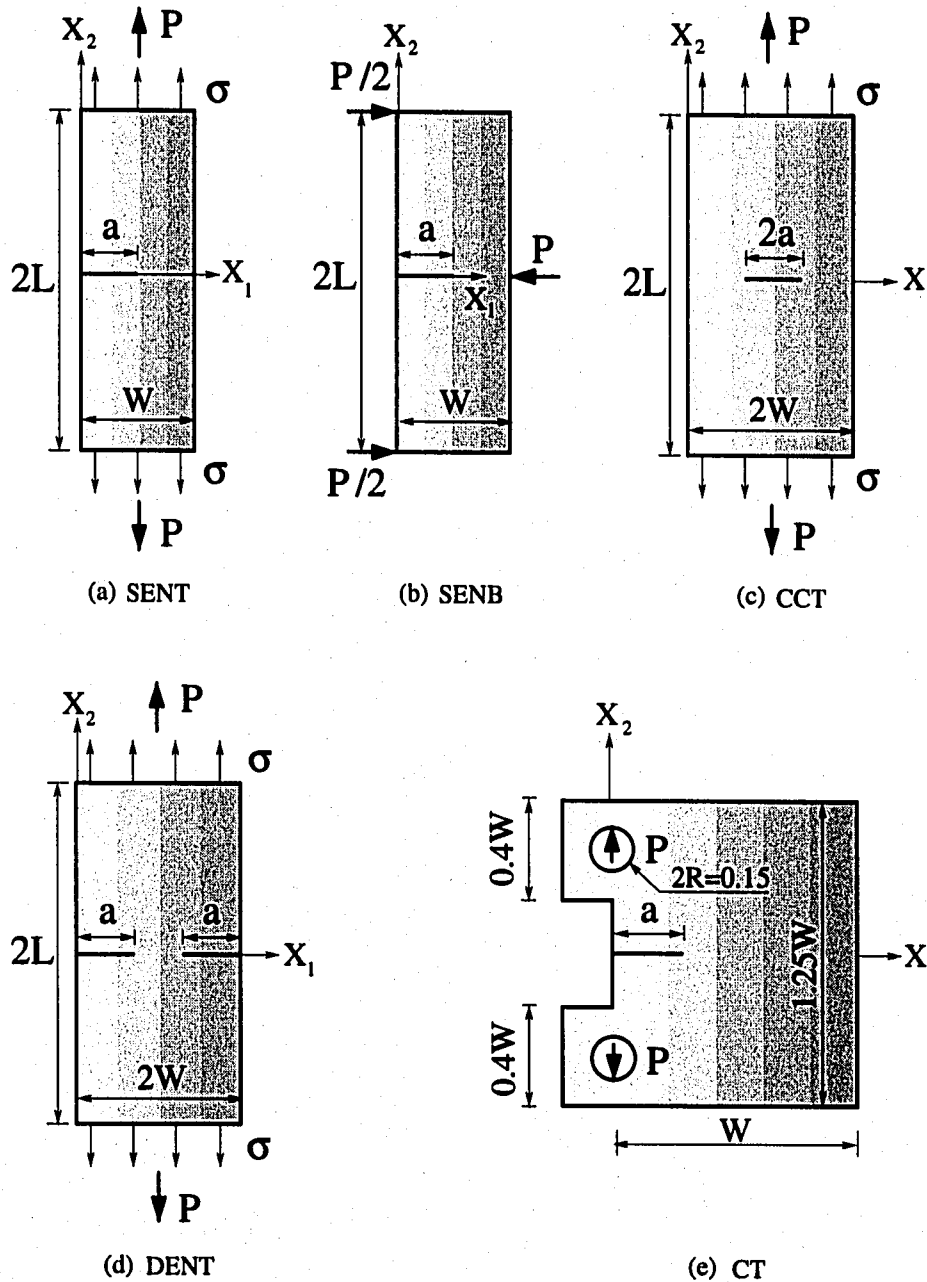
Figure 3.19: Example 5: laboratory specimens of thickness t: (a) single edge notched tension (SENT); (b) single edge notched bending (SENB); (c) center cracked tension (CCT); (d) double edge notched tension (DENT); (e) compact tension (CT). The load P is the point force for the SENB and CT specimens or the resultant for the equidistributed tractions (σ) on the boundary of the SENT, CCT, and DENT specimens.

fields given in the paper by Kim and Paulino [84]. Notice that the sign of biaxiality ratio changes from negative to positive as the ratio of crack length to width (a/W) is about 0.22 for CT, 0.35 for

SENB, and 0.60 for SENT specimen, however, it remains negative for DENT and CCT specimens.

Figure 3.22 shows biaxiality ratio ($\beta = T\sqrt{\pi a}/K_I$) versus a/W for various specimens considering exponentially graded materials with $E_2/E_1 = 10$. For the CCT and DENT specimens, which have two crack tips, the biaxiality ratio is calculated for the right crack tip. By comparing Figures 3.21 and 3.22, it is observed that the transition point of the sign of biaxiality ratio shifts to the left due to the material gradation in the CT, SENB, and SENT specimens. Moreover, the behavior of the biaxiality ratio for CCT and DENT is significantly different from that for a homogeneous material.

The T-stress and biaxiality ratio are evaluated for all the specimens considering various ratios of E_2/E_1. Figure 3.23 shows the biaxiality ratio ($\beta = T\sqrt{\pi a}/K_I$) versus a/W for the SENT specimen. The transition point of the sign of biaxiality ratio shifts to the left as E_2/E_1 increases. For a fixed value of a/W considered here, the biaxiality ratio ($\beta = T\sqrt{\pi a}/K_I$) increases with increasing E_2/E_1.

Figure 3.24 shows the biaxiality ratio versus a/W for the SENB specimen. The transition point of the sign of biaxiality ratio shifts to the left as E_2/E_1 increases. For a fixed value of a/W considered here, the biaxiality ratio increases with increasing E_2/E_1.

Figure 3.25 shows biaxiality ratio ($\beta = T\sqrt{\pi a}/K_I$) versus a/W for the CCT specimen. For the range of a/W considered, the T-stress and biaxiality ratio are negative. For a fixed value of a/W, the biaxiality ratio ($\beta = T\sqrt{\pi a}/K_I$) increases with increasing E_2/E_1.

Figure 3.26 shows the biaxiality ratio ($\beta = T\sqrt{\pi a}/K_I$) versus a/W for the DENT specimen. For the range of a/W between 0.1 and 0.7, the T-stress and biaxiality ratio are negative. For $E_2/E_1 = 0.1$, as the ratio a/W increases from 0.75 to 0.8, the biaxiality ratio becomes positive.

Figure 3.27 shows biaxiality ratio ($\beta = T\sqrt{\pi a}/K_I$) versus a/W for the CT specimen. The transition point of the sign of biaxiality ratio shifts to the left as E_2/E_1 increases. For a fixed value of a/W, the biaxiality ratio increases with increasing E_2/E_1. Based on the above investigations, it is observed that the material gradation (represented by the ratio E_2/E_1) significantly influences the T-stress and biaxiality ratio for all the specimens considered.

For graded laboratory specimens, the mode I SIF (K_I) is associated with material nonhomogeneity, and it can be given by

$$K_I = \frac{P}{t\sqrt{W}} f(\frac{a}{W}, \gamma), \tag{3.90}$$

where t is the thickness of the specimen, and P is either the point force for the SENB and CT specimens or the resultant for the equidistributed tractions (σ) on the boundary of the SENT, CCT, DENT specimens (see Figure 3.19). For homogeneous specimens, there is no effect of γ [5]. Using $\beta = T\sqrt{\pi a}/K_I$, one obtains

$$T = \frac{\beta P}{t\sqrt{\pi a W}} f(\frac{a}{W}, \gamma),$$ (3.91)

Notice that T-stress is also a function of the material nonhomogeneity parameter γ.

To investigate the effect of material orthotropy on the biaxiality ratio, the compact tension specimen is considered. Let's assume that Young's moduli and shear modulus are exponential functions of X_1, while the Poisson's ratio is constant. The material properties are given by

$$E_{11} = E_{11}^0 e^{\gamma X_1}, \;\; E_{22} = E_{22}^0 e^{\gamma X_1}, G_{12} = G_{12}^0 e^{\gamma X_1}, \;\; \nu_{12} = \nu_{12}^0$$ (3.92)

with

$$E_{11}^0 = 1, \;\; E_{22}^0 = 2, G_{12}^0 = 0.5, \;\; \nu_{12}^0 = 0.15.$$ (3.93)

Figure 3.28 shows biaxiality ratios $\beta = T\sqrt{\pi a}/K_I$ versus a/W ratio obtained for isotropic and orthotropic FGMs. The mode I SIF K_I is also evaluated by means of the interaction integral method. For both isotropic and orthotropic cases, as the ratio $E_R = \exp(\gamma W)$ increases, the biaxiality ratio increases and the transition points for sign-change of the biaxiality ratio shift to the left. Both material orthotropy and nonhomogeneity show a significant influence on the T-stress and biaxiality ratio.
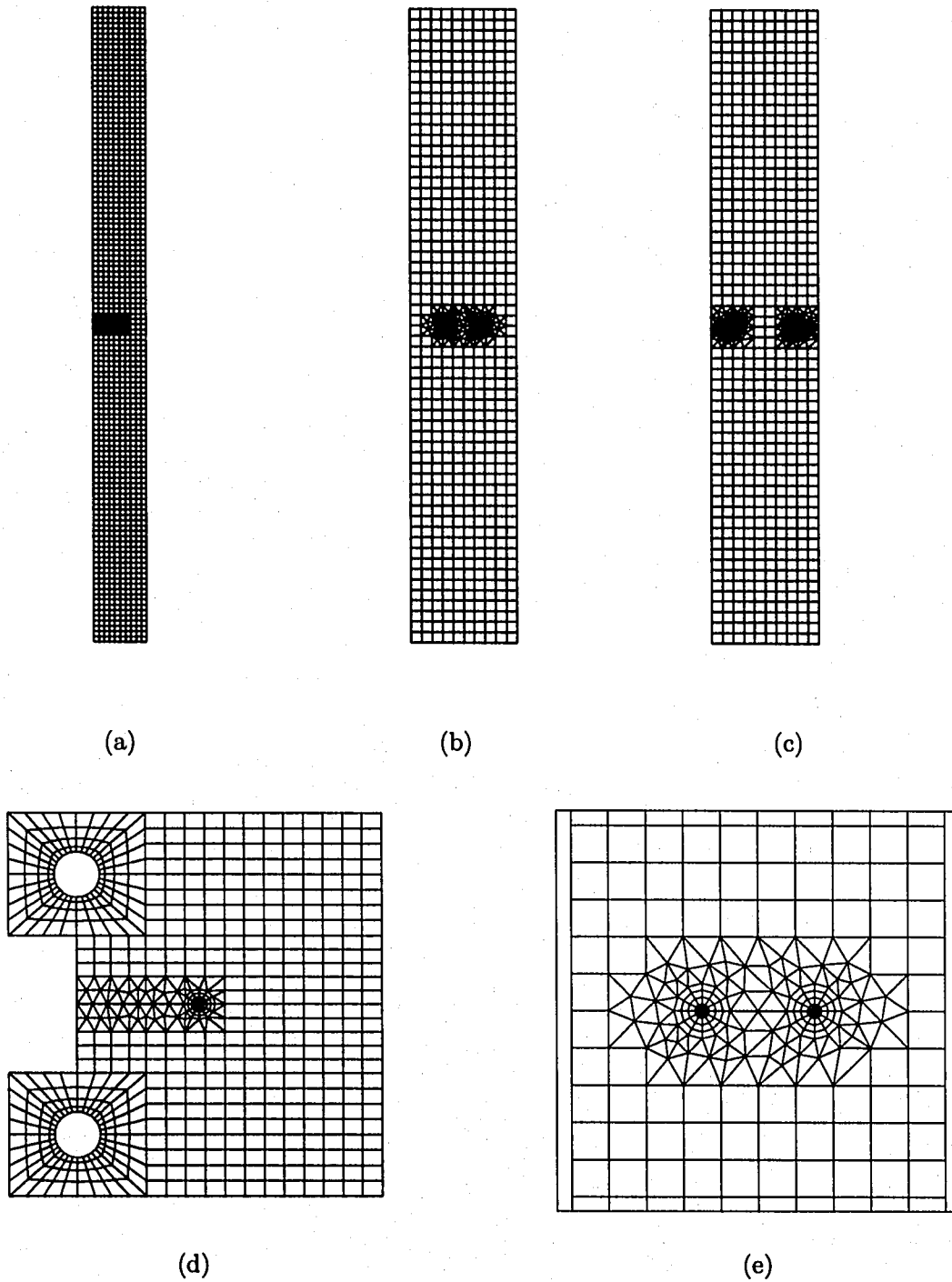
Figure 3.20: Example 5: Finite element meshes: (a) single edge notched tension (SENT) and single edge notched bending (SENB); (b) center cracked tension (CCT); (c) double edge notched tension (DENT); (d) compact tension (CT); (e) mesh detail of the CCT specimen using 12 sectors (S12) and 4 rings (R4) around the crack tips.
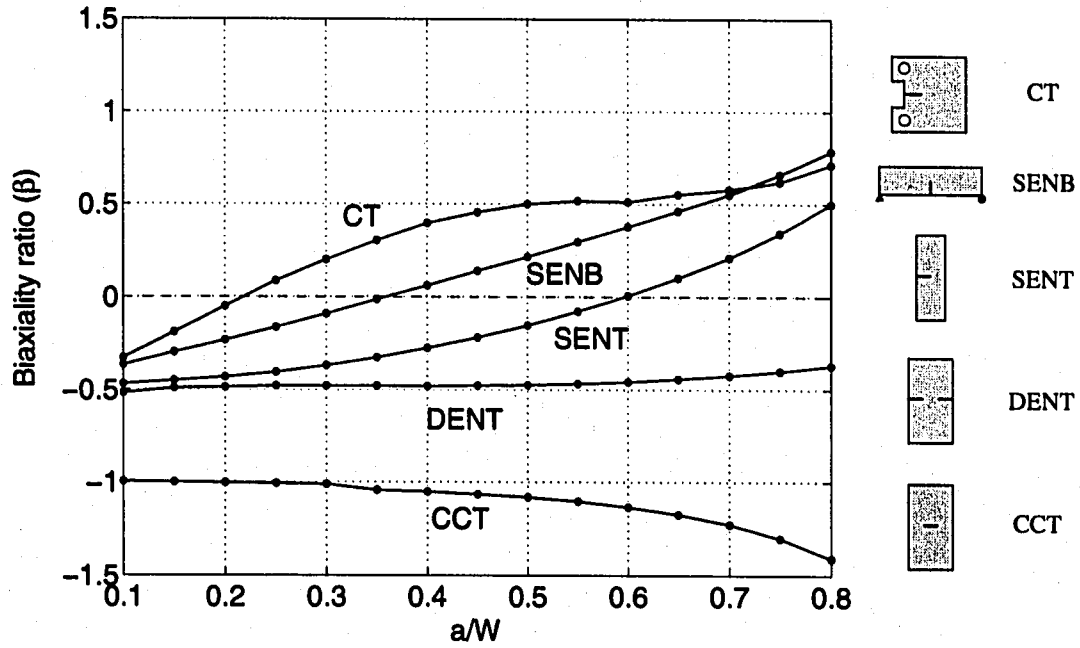
Figure 3.21: Example 5: Biaxiality ratio ($\beta = T\sqrt{\pi a}/K_I$) for a homogeneous material ($E_1 = E_2$).
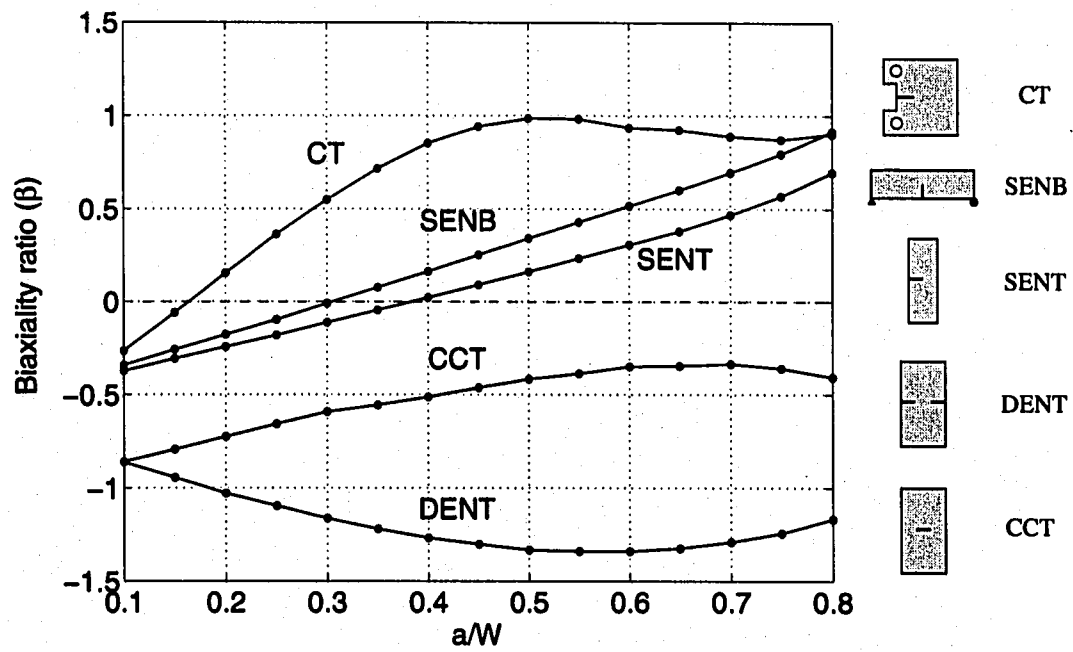
Figure 3.22: Example 5: Biaxiality ratio ($\beta = T\sqrt{\pi a}/K_I$) for an FGM considering $E_2/E_1 = 10$. For center cracked tension (CCT) and double edge notched tension (DENT) specimens, the biaxiality ratio is evaluated at the right crack tip.
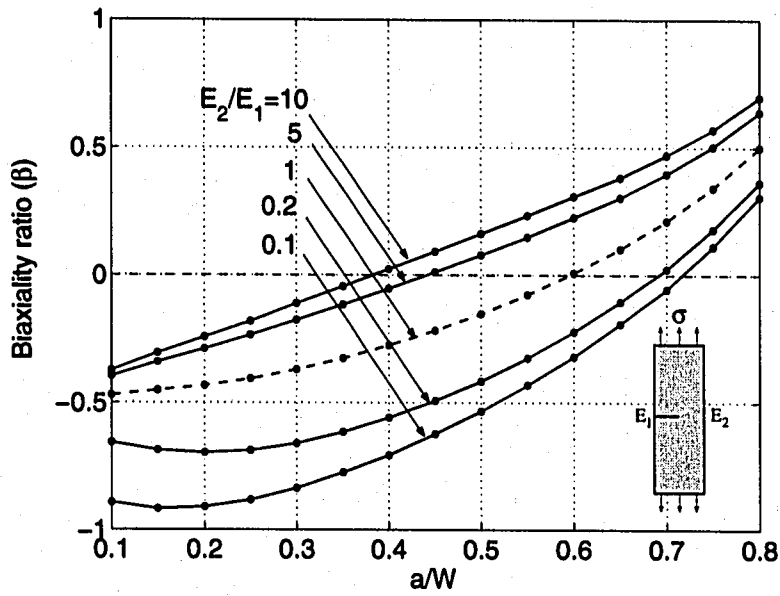
Figure 3.23: Example 5: Biaxiality ratio ($\beta = T\sqrt{\pi a}/K_I$) for the single edge notched tension (SENT) specimen (see Figure 3.19(a)).
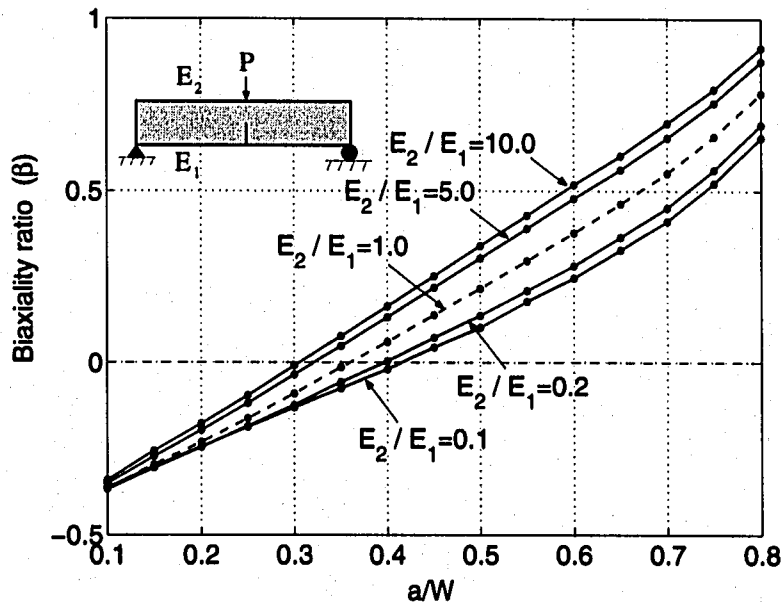
Figure 3.24: Example 5: Biaxiality ratio ($\beta = T\sqrt{\pi a}/K_I$) for the single edge notched bending (SENB) specimen (see Figure 3.19(b)).
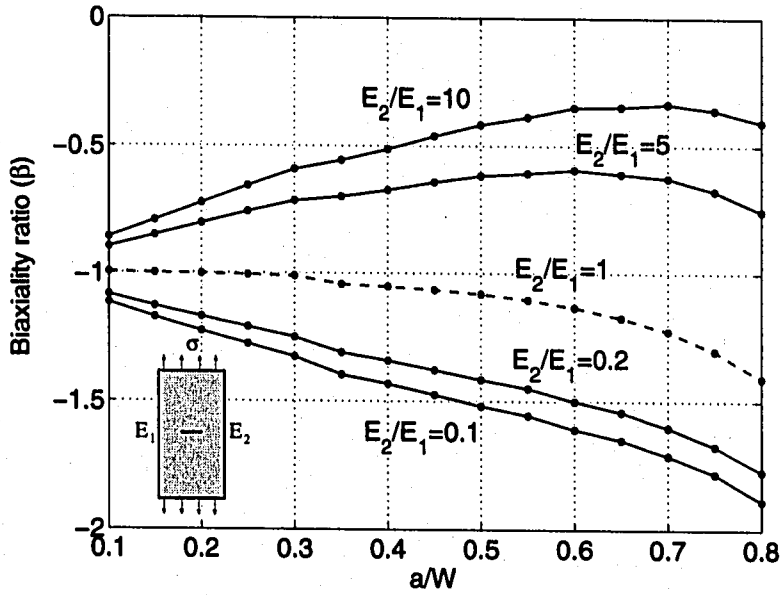
Figure 3.25: Example 5: Biaxiality ratio ($\beta = T\sqrt{\pi a}/K_I$) evaluated at the right crack tip for the center cracked tension (CCT) specimen.
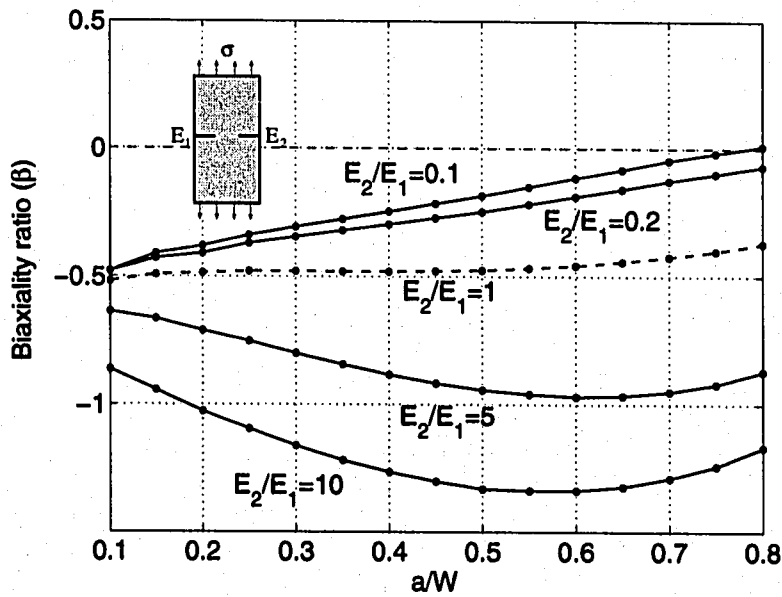
Figure 3.26: Example 5: Biaxiality ratio ($\beta = T\sqrt{\pi a}/K_I$) evaluated at the right crack tip for the double edge notched tension (DENT) specimen.

102
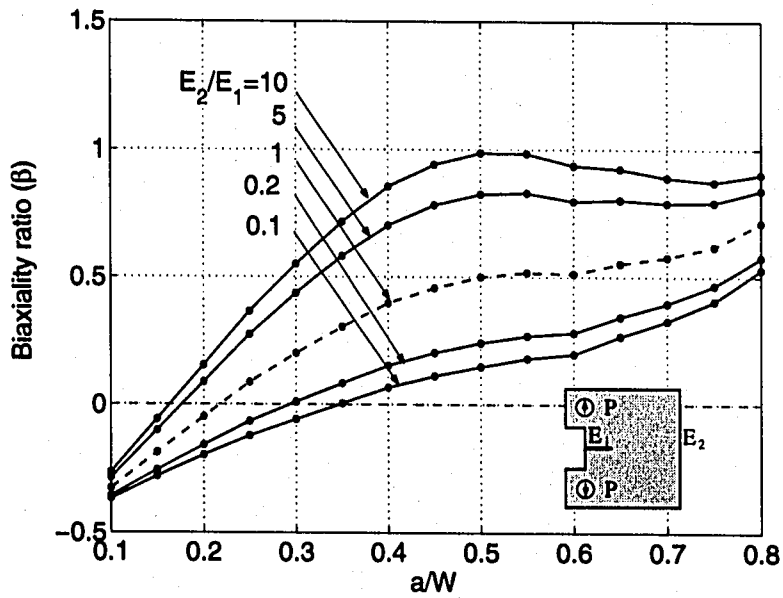
Figure 3.27: Example 5: Biaxiality ratio ($\beta = T\sqrt{\pi a}/K_I$) for the compact tension (CT) specimen.
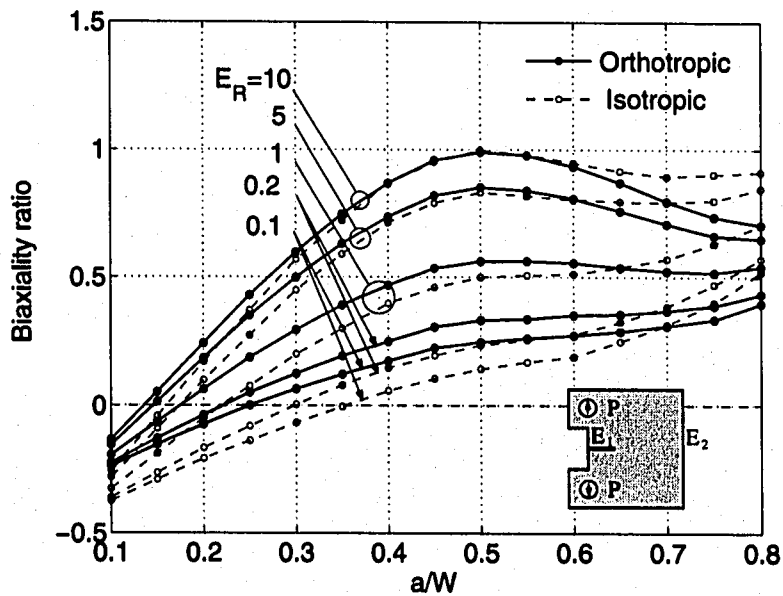
Figure 3.28: Example 5: Comparison of biaxiality ratio ($\beta = T\sqrt{\pi a}/K_I$) for a compact tension (CT) specimen considering isotropic and orthotropic FGMs. Here $E_R = E_{11}(W)/E_{11}(0) = E_{22}(W)/E_{22}(0) = G_{12}(W)/G_{12}(0) = \exp(\beta W)$.

3.8.6 On scaling of FGM specimens

This example investigates the effect of scaling of FGM specimens on the T-stress and biaxiality ratio. Here the compact tension (CT) specimen is considered for a fixed a/W ratio and two geometries, where one is twice as large as the other. The loads are applied considering a given value of J (or K_I). Figures 3.29(a) and 3.29(b) show the geometry and BCs for the two specimens A and B, respectively. Figure 3.20(d) shows the complete finite element mesh adopted for these two CT specimens. For the large specimen (B) to have the same K_I as that for the small specimen (A), the applied load to specimen B should be $\sqrt{2}P$ (see Eq.(3.90)).
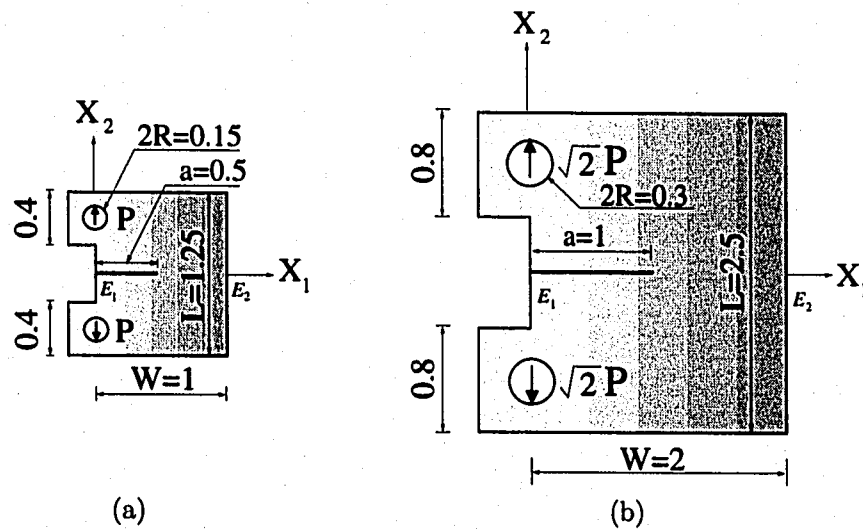
Figure 3.29: Example 6: Two graded compact tension (CT) specimens with $a/W = 0.5$: (a) Specimen A; (b) Specimen B, which is two times as large as specimen A. For both specimens, J is the same, and the Young's modulus varies along the X_1 direction from E_1 on the left to E_2 on the right-hand-side.

The Young's modulus is taken as an exponential function given by

$$E(X_1) = E_1 e^{\gamma X_1}, \tag{3.94}$$

where $E_1 = E(0)$, however, the present argument is independent of the specific material variation considered. Notice that as $\gamma = \log[E(W)/E(0)]/W$, the nonhomogeneity parameter γ_B for specimen B is half of γ_A for specimen A. Thus, for both specimens $E_2 = E(W) = E_1 e^{\gamma W}$. The Poisson's ratio is taken as constant for the two specimens.

104

For these specific relations of nonhomogeneity parameters, i.e. $\gamma_A = 2\gamma_B$, the biaxiality ratio remains unchanged. Using

$$T = \beta \, \frac{K_I}{\sqrt{\pi a}}, \tag{3.95}$$

one observes that T-stress is proportional to $1/\sqrt{a}$. Thus

$$T_A = \sqrt{2} T_B, \tag{3.96}$$

where T_A and T_B denote the T-stress for specimens A (small) and B (large), respectively.

This theoretical argument is also observed in the numerical calculation. The following data are used for the FEM analyses:

$$\text{plane strain, } 2 \times 2 \text{ Gauss quadrature,}$$
$$a/W = 0.5, \ W = 1.0, 2.0 \ , E_2/E_1 = 10, \ E_1 = 1.0, \ \nu = 0.3, \ P = 1. \tag{3.97}$$

For specimen A, the mode I SIF (K_I), T-stress, biaxiality ratio are obtained as (cf. Figure 3.27)

$$(K_I)_A = 7.130, \ T_A = 5.607, \beta_A = 0.985. \tag{3.98}$$

For specimen B, the mode I SIF (K_I), T-stress, biaxiality ratio are obtained as (cf. Figure 3.27)

$$(K_I)_B = 7.130, \ T_B = 3.964, \beta_B = 0.985. \tag{3.99}$$

Notice that, numerically, $T_A/T_B = 1.4144$, which is very close to $\sqrt{2}$. Therefore the biaxiality ratio plays an important role as a non-dimensional parameter not only for homogeneous materials and but also for FGMs.

3.8.7 Crack orientation versus material gradation

The following two examples employ the following averaged material parameters: the effective Young's modulus E, the effective Poisson's ratio ν, the stiffness ratio δ^4 and the shear parameter κ_0. They replace the independent engineering constants E_{ii}, G_{ij} and ν_{ij} $((\nu_{ij}/E_{ii}) = (\nu_{ji}/E_{jj}))$ $(i,j = 1,2)$, i.e. [90]

$$E = \sqrt{E_{11}E_{22}}, \quad \nu = \sqrt{\nu_{12}\nu_{21}}, \quad \delta^4 = \frac{E_{11}}{E_{22}} = \frac{\nu_{12}}{\nu_{21}}, \quad \kappa_0 = \frac{E}{2G_{12}} - \nu, \tag{3.100}$$

for plane stress. The bounds on Poisson's ratios ν_{12} and ν_{21} for plane orthotropy are given by [24]:

$$|\nu_{12}| < (E_{11}/E_{22})^{1/2}, \quad |\nu_{21}| < (E_{22}/E_{11})^{1/2}, \tag{3.101}$$

respectively. Therefore the bound on the effective Poisson's ratio[2] is $\nu < 1.0$. The first two examples also consider proportional material nonhomogeneity, i.e.

$$\beta = \frac{1}{2H}log\left[\frac{E_{11}(H)}{E_{11}(-H)}\right] = \frac{1}{2H}log\left[\frac{E_{22}(H)}{E_{22}(-H)}\right] = \frac{1}{2H}log\left[\frac{G_{12}(H)}{G_{12}(-H)}\right], \tag{3.102}$$

where H is the length of material gradation considered, e.g. $H = W$ for the first example and $H = L$ for the second example. The nonhomogeneity parameter β has units $[length]^{-1}$.

Plate with a crack parallel to material gradation

This example investigates a plate with a crack parallel to material gradation. Figures 3.30(a) and 3.30(b) show a center crack of length $2a$ located in a finite two-dimensional plate under fixed grip loading or constant traction, respectively. Figures 3.30(c) and 3.30(d) show the complete finite element mesh, a mesh detail with 16 sectors (S16) and 4 rings (R4) around crack tips, and a zoom of the right crack tip region, respectively.

For fixed-grip loading, the applied load results in uniform strain $\varepsilon_{22}(X_1, X_2) = \varepsilon_0$ for a corresponding uncracked plate; and for constant traction, the applied load $\sigma_{22}(X_1, \pm L) = \pm 1.0$ along the top and bottom edges. The displacement boundary conditions are prescribed such that $u_1 = u_2 = 0$

---

[2]Notice that the effective Poisson's ratio ν (see Eq.(A.36)) can be bigger than 0.5 for orthotropic materials.
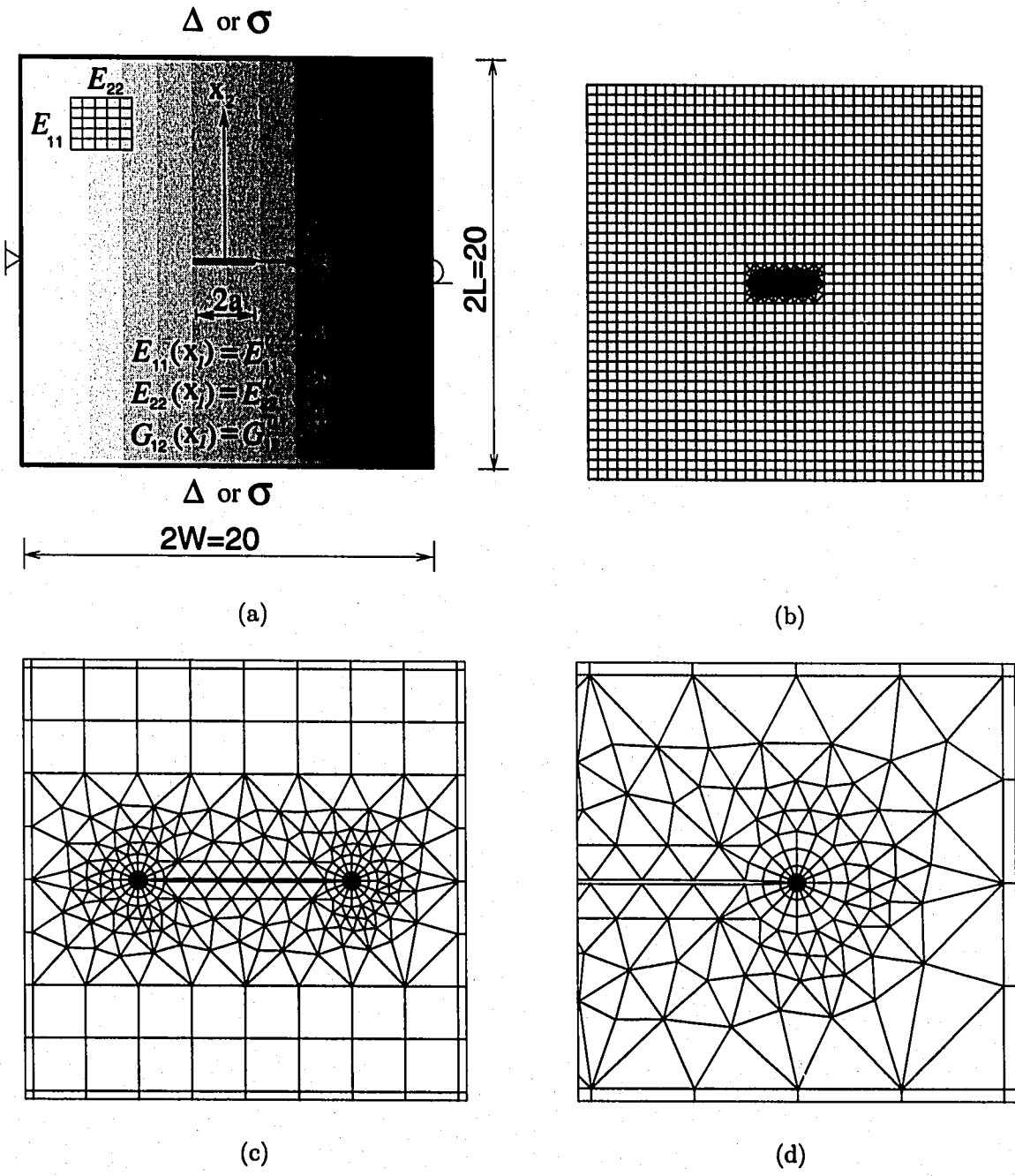
Figure 3.30: Example 7: plate with a center crack parallel to the material gradation: (a) geometry and BCs considering either fixed-grip loading (Δ) or far-field traction (σ) on the (far-field) horizontal edges; (b) complete finite element mesh; (c) mesh detail using 16 sectors (S16) and 4 rings (R4) around crack tips; (d) zoom of the right crack tip.

for the center node on the left edge, and $u_2 = 0$ for the center node on the right edge.

The variations of E_{11}, E_{22}, and G_{12} are assumed to be an exponential function of X_1 and *proportional* to one another, while the Poisson's ratio ν_{12} is constant. The mesh has 1666 Q8, 303 T6, and 32 T6qp crack-tip singular elements with a total of 2001 elements and 5851 nodes (see Figure 3.30(b)). The following data are used for the FEM analysis:

$$a/W = 0.1, \quad L/W = 1.0, \quad \varepsilon_0 = 1.0, \quad \beta a = 0.5,$$

$$E_{11}(X_1) = E_{11}^0 e^{\beta X_1}, E_{22}(X_1) = E_{22}^0 e^{\beta X_1}, G_{12}(X_1) = G_{12}^0 e^{\beta X_1}, \qquad (3.103)$$

$$\kappa_0 = 0.5, \quad \nu = (0.1, 0.2, 0.3, 0.4, 0.5, 0.7, 0.9),$$

$$\text{plane stress, } 2 \times 2 \text{ Gauss quadrature.}$$

Table 3.12 shows the effect of material nonhomogeneity on normalized mode I SIF for the nonhomogeneous orthotropic plate of Figure 3.30 under fixed grip loading considering $\nu = 0.3$ and $\kappa_0 = 0.5$. The FEM results obtained by means of the incompatibility formulation of the interaction integral method agree very well with those obtained by the MCC [78]. As the dimensionless nonhomogeneity parameter βa increases, the mode I SIF at the right crack tip increases, but the mode I SIF at the left crack tip decreases. This is expected due to the nature of the exponential material gradation with the origin of the Cartesian coordinate system at the center of the plate.

Table 3.12: Example 7: The effect of material nonhomogeneity on normalized mode I SIF in a nonhomogeneous orthotropic plate under fixed grip loading ($\nu = 0.3$, $\kappa_0 = 0.5$, $K_0 = \varepsilon_0 \overline{E}^0 \sqrt{\pi a}$; $\overline{E}^0 = E^0/\delta^2$; $E^0 = \sqrt{E_{11}^0 E_{22}^0}$) – see Figure 3.30.

βa	M-integral [80]		MCC	
	$K_I(+a)/K_0$	$K_I(-a)/K_0$	$K_I(+a)/K_0$	$K_I(-a)/K_0$
0.00	0.9969	0.9969	0.9986	0.9986
0.10	1.0750	0.9247	1.0791	0.9251
0.25	1.2043	0.8245	1.2101	0.8233
0.50	1.4371	0.6706	1.4484	0.6680
0.75	1.7055	0.5404	1.7255	0.5358
1.00	2.0318	0.4335	2.0639	0.4285

Table 3.13 shows the effect of the Poisson's ratio ν on mode I SIF for the nonhomogeneous orthotropic plate of Figure 3.30 under fixed grip loading considering $\beta a = 0.5$ and $\kappa_0 = 0.5$. The FEM results obtained by means of the M-integral agree with the SIFs obtained by Ozturk and

Erdogan [108] to within 1%.

Table 3.13: Example 7: Normalized mode I SIF in a nonhomogeneous orthotropic plate under fixed grip loading for various effective Poisson's ratios $\nu = \sqrt{\nu_{12}\nu_{21}}$ ($\beta a = 0.5$, $\kappa_0 = 0.5$, $K_0 = \varepsilon_0 \overline{E}^0 \sqrt{\pi a}$; $\overline{E}^0 = E^0/\delta^2$; $E^0 = \sqrt{E_{11}^0 E_{22}^0}$) – see Figure 3.30.

ν	M-integral [80]		Ozturk & Erdogan [108]	
	$K_I(+a)/K_0$	$K_I(-a)/K_0$	$K_I(+a)/K_0$	$K_I(-a)/K_0$
0.1	1.4300	0.6668	1.4183	0.6647
0.2	1.4334	0.6685	1.4233	0.6676
0.3	**1.4371**	**0.6706**	1.4280	0.6704
0.4	1.4405	0.6731	1.4325	0.6730
0.5	1.4438	0.6751	1.4368	0.6755
0.7	1.4505	0.6785	1.4449	0.6802
0.9	1.4563	0.6827	1.4524	0.6846

The effective Poisson's ratio $\nu = \sqrt{\nu_{12}\nu_{21}}$ has a negligible effect on the SIFs for a mode I crack problem. With respect to the M-integral, notice that the results of Table 3.12 considering βa=0.5 coincide with those of Table 3.13 for $\nu = 0.3$. These results are presented in bold at these Tables. In order to assess the accuracy of the present interaction integral method (M-integral), Table 3.14 shows normalized SIFs computed by other methods, such as J_k^*-integral, the MCC, and the DCT. By comparing Tables 3.13 and 3.14, and adopting Ozturk and Erdogan's [108] semi-analytical solution as reference, the interaction integral provides the best accuracy with respect to the aforementioned schemes.

Table 3.14: Example 7: Comparison of normalized mode I SIF in a nonhomogeneous orthotropic plate under fixed grip loading for various effective Poisson's ratios ($\beta a = 0.5$, $\kappa_0 = 0.5$, $K_0 = \varepsilon_0 \overline{E}^0 \sqrt{\pi a}$; $\overline{E}^0 = E^0/\delta^2$; $E^0 = \sqrt{E_{11}^0 E_{22}^0}$) – see Figure 3.30 [80]. The J_k^*-integral results were reported by Kim and Paulino [81]. Cf. Tables 3.13 and 3.14.

ν	J_k^*-integral		MCC		DCT	
	$K_I(+a)/K_0$	$K_I(-a)/K_0$	$K_I(+a)/K_0$	$K_I(-a)/K_0$	$K_I(+a)/K_0$	$K_I(-a)/K_0$
0.1	1.4451	0.6776	1.4405	0.6630	1.4363	0.6764
0.2	1.4488	0.6802	1.4442	0.6655	1.4405	0.6789
0.3	1.4522	0.6822	1.4480	0.6676	1.4446	0.6814
0.4	1.4559	0.6843	1.4517	0.6697	1.4484	0.6839
0.5	1.4593	0.6864	1.4551	0.6718	1.4517	0.6864
0.7	1.4655	0.6902	1.4618	0.6760	1.4576	0.6902
0.9	1.4718	0.6939	1.4684	0.6802	1.4588	0.6923

The crack opening displacements are evaluated for both homogeneous and nonhomogeneous medium considering either fixed-grip loading or far-field constant traction, as shown in Figure 3.30(a). Figure 3.31 shows the crack opening displacement (COD) in a nonhomogeneous medium ($\beta a = 0.5$)

under far-field constant traction with $E = E(X_1) = E^0 e^{X_1/2a}$ ($E^0 = \sqrt{E_{11}^0 E_{22}^0}$) and also in homogeneous materials with $E(-a) = E^0 e^{-0.5}$, $E(0) = E^0$, and $E(a) = E^0 e^{0.5}$. The COD for the right crack tip ($X_1 = a$) in the nonhomogeneous medium is greater than that in the corresponding homogeneous medium with $E(a) = E^0 e^{0.5}$. Thus the mode I SIF K_I in the nonhomogeneous medium is greater than that in the homogeneous medium. Similarly, the mode I SIF (K_I) at the left crack tip ($X_1 = -a$) in the nonhomogeneous medium is lower than that in the corresponding homogeneous medium with $E(-a) = E^0 e^{-0.5}$. The COD for $E = E^0$ serves as a reference curve between those curves for $E = E^0 e^{0.5}$ and $E = E^0 e^{-0.5}$.

Figure 3.32 shows the COD in a nonhomogeneous medium under fixed-grip loading with $E = E(X_1) = E^0 e^{X_1/2a}$ and also in homogeneous materials with $E(-a) = E^0 e^{-0.5}$, $E(0) = E^0$, and $E(a) = E^0 e^{0.5}$.
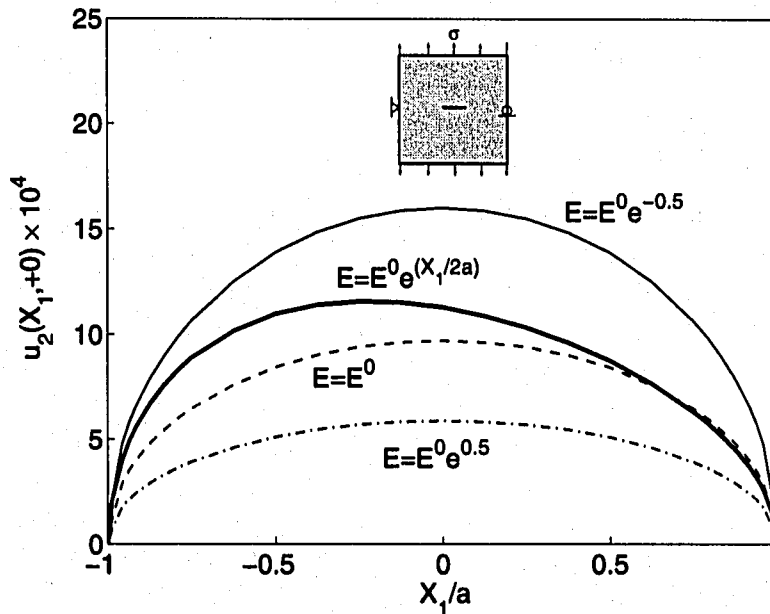
Figure 3.31: Example 7: COD $u_2 \times 10^4$ in orthotropic FGMs under far-field constant traction considering $\kappa_0 = 0.5$, $\nu = 0.3$, and $\beta a = 0.5$. The COD for the crack in the FGM is indicated by a thicker line.

Notice that, for the fixed-grip loading, the crack opening displacement doesn't depend on material properties in the homogeneous medium. The mode SIF K_I for a homogeneous medium under
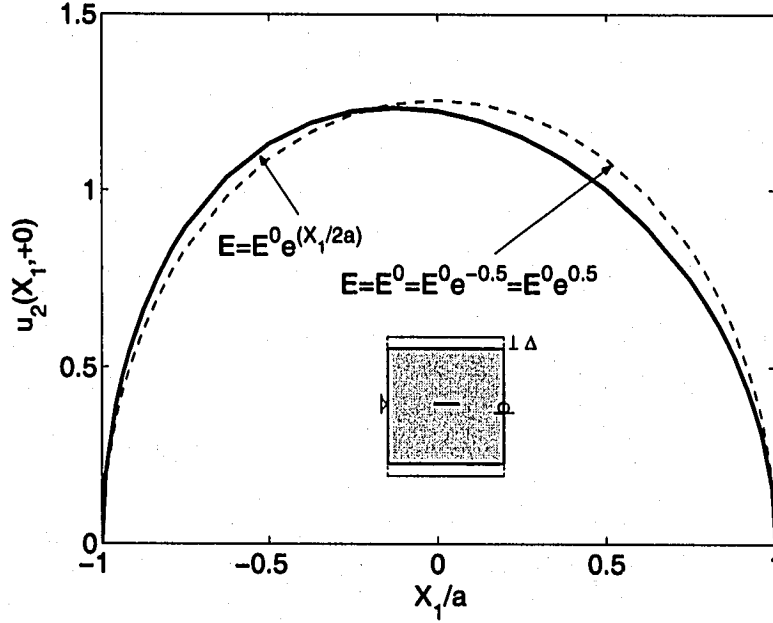
Figure 3.32: Example 7: COD u_2 in orthotropic FGMs under fixed-grip loading considering $\kappa_0 = 0.5$, $\nu = 0.3$, and $\beta a = 0.5$. The COD for the crack in the FGM is indicated by a thicker line.

pure mode I loading is given by ($\theta = 180°$):

$$K_I = u_2 \sqrt{\frac{\pi}{2r}} \Big/ \left[\mathrm{Re} \left\{ \frac{i}{\mu_1 - \mu_2} (\mu_1 q_2 - \mu_2 q_1) \right\} \right] \tag{3.104}$$

where $q_k = a_{12}\mu_k + a_{22}/\mu_k - a_{26}$ ($k = 1, 2$). The material properties for the three homogeneous materials considered are proportional to one another. In this case, the roots μ_k ($k = 1, 2$) of the characteristic equation (A.95) are identical. Moreover, for the case where the Cartesian coordinate system coincide with the principal directions of material orthotropy,

$$a_{11} = \frac{1}{E_{11}}, \quad a_{12} = \frac{-\nu_{12}}{E_{11}}, \quad a_{16} = 0.$$

Thus, with the same crack surface displacement u_2 and Poisson's ratio ν_{12}, the mode I SIF K_I is proportional to E_{11}, as illustrated by Table 3.15.

By comparison of the solution of a nonhomogeneous medium with that of a homogeneous medium having the material properties at the right crack tip ($X_1 = a$), the crack opening displacement in the nonhomogeneous medium is smaller than that in the corresponding homogeneous

Table 3.15: Example 7: Homogeneous orthotropic material with properties sampled at the crack tips ($X_1 = \pm 1.0$) and at the mid-point of the crack ($X_1 = 0$) in the corresponding FGM – see Eq.(4.9). For all the cases, $\kappa_0 = 0.5$, $K_0 = \varepsilon_0 \overline{E}^0 \sqrt{\pi a}$; $\overline{E}^0 = E^0 / \delta^2$; $E^0 = \sqrt{E_{11}^0 E_{22}^0}$. Also, notice that $E = E^0 e^{\beta X_1}$. The superscript in K_I^1 indicates case 1.

Parameter	Case		
	1	2	3
E_{11}	$E_{11}^0 e^{-\beta}$	E_{11}^0	$E_{11}^0 e^{\beta}$
K_I / K_0	K_I^1 / K_0	$K_I^1 e^{\beta} / K_0$	$K_I^1 e^{2\beta} / K_0$
K_I / K_0 (numerical)	0.6046	0.9969	1.6436

medium with $E(a) = E^0 e^{0.5}$, and thus the SIF (K_I) in the nonhomogeneous medium is lower than that for the corresponding homogeneous medium. Similarly, the mode I SIF (K_I) at the left crack tip ($X_1 = -a$) in the nonhomogeneous medium is greater than that in the corresponding homogeneous medium with $E(-a) = E^0 e^{-0.5}$.

Plate with a crack perpendicular to material gradation

This example investigates a plate with a crack parallel to material gradation. Figures 3.33(a) and 3.33(b) show a crack of length $2a$ located in a finite two-dimensional plate under remote uniform tension loading for two different boundary conditions. These boundary conditions are prescribed such that, for Figure 3.33(a), $u_1 = 0$ along the left and right edges, and $u_2 = 0$ for the node in the middle of left edge; while for Figure 3.33(b), $u_1 = 0$ for the left corner node of the bottom edge and $u_2 = 0$ along the bottom edge. The finite element mesh configurations are the same as in the previous example (see Figures 3.30(b) and 3.30(c)). The applied load corresponds to $\sigma_{22}(X_1, \pm L) = \pm \sigma = \pm 1.0$ for the BC in Figure 3.33(a) and $\sigma_{22}(X_1, L) = \sigma = 1.0$ for the BC in Figure 3.33(b).

The variations of E_{11}, E_{22}, and G_{12} are exponential functions of X_2 and are *proportional* to one another, while the Poisson's ratio ν_{12} is constant. The following data were used for the FEM

analysis:

$$a/W = 0.1, \quad L/W = 1.0, \quad \beta a = (0.0 \text{ to } 0.5)$$

$$E_{11}(X_2) = E_{11}^0 e^{\beta X_2}, \quad E_{22}(X_2) = E_{22}^0 e^{\beta X_2}, \quad G_{12}(X_2) = G_{12}^0 e^{\beta X_2},$$

$$\delta^4 = E_{11}/E_{22} = (0.25, 0.5, 1.0, 3.0, 10.0),$$

$$\kappa_0 = (-0.25, 0.0, 0.5, 1.0, 2.0, 5.0), \quad \nu = 0.30,$$

plane stress, 2×2 Gauss quadrature.

Figures 3.34(a) and 3.34(b) show seven contours used for evaluating the J-integral considering $\delta^4 = 10$, $\kappa_0 = 5.0$, $\nu = 0.3$, and $\beta a = 0.5$. Figures 3.35 and 3.36 show the effect of the incompatible term (see Eq.(3.23)) on the convergence of the J-integral obtained from Eq.(3.43) considering the two sets of BCs, respectively. Notice that J is obtained after evaluation of SIFs (see Eq.(3.43)). As the contours become larger, the solution converges when the incompatible term is considered, however, it diverges if such term is neglected. Figure 3.37 shows strain energy release rates $\mathcal{G}/\mathcal{G}_0$ in a nonhomogeneous orthotropic plate under uniform tension for two different boundary conditions for a fixed stiffness ratio $\delta^4 = 10$ and constant Poisson's ratio $\nu=0.3$ with varying material nonhomogeneity βa and κ_0. This figure clearly indicates that the boundary conditions have a significant influence in strain energy release rates (and SIFs). For the first set of BCs (see Figure 3.33(a)), the FEM results agree with the strain energy release rates $(\mathcal{G}/\mathcal{G}_0)$ obtained by Ozturk and Erdogan [109]. The strain energy release rates $\mathcal{G}/\mathcal{G}_0$ monotonically increase with κ_0 and βa. However, for the second set of BCs (see Figure 3.33(b)), the present results agree with the strain energy release rates $(\mathcal{G}/\mathcal{G}_0)$ obtained by the MCC, and the FEM results are significantly different from those for the previous BCs. Notice that the two bullets along the line $\beta a = 0.5$ indicate energy release rates which are the converged solutions for J as shown in Figures 3.35 and 3.36. The FEM results for various δ^4 and κ_0 obtained by the interaction integral compare well to those obtained by the path-independent J_k^*-integral [81], which are not presented in this thesis. Further numerical results investigating the effect of boundary conditions, Poisson's ratio, and plate size on the strain energy release rates considering the two BCs of Figure 3.33 can be found in the papers by Kim and Paulino [78, 83].

113
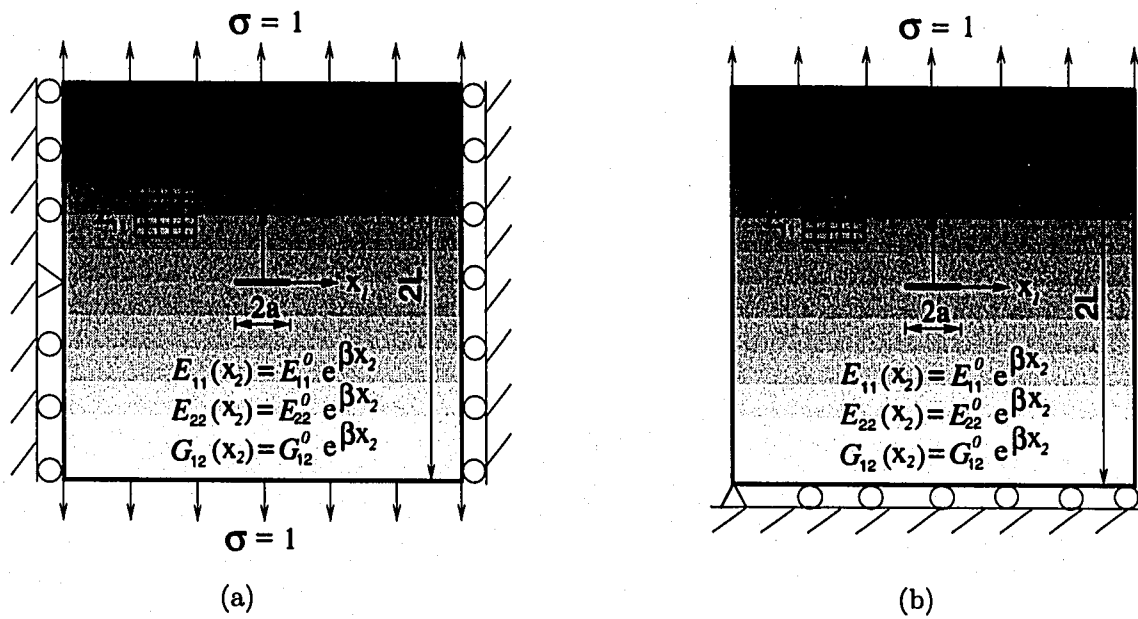
Figure 3.33: Example 7: plate with a center crack perpendicular to the material gradation: (a) first set of BCs; (b) second set of BCs.
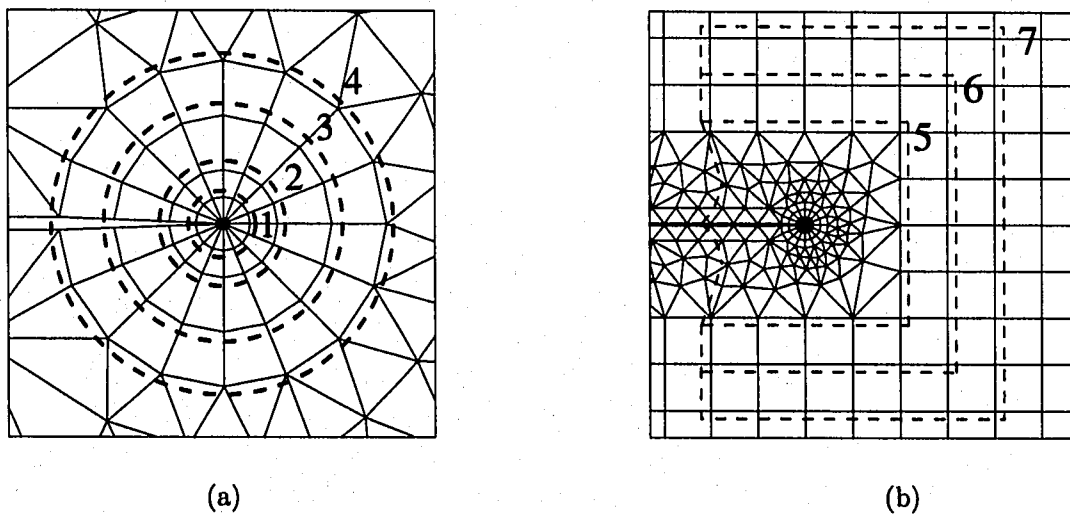
Figure 3.34: Example 7: Contours used to evaluate the J-integral: (a) Contours 1, 2, 3, and 4; (b) Contours 5, 6, and 7.
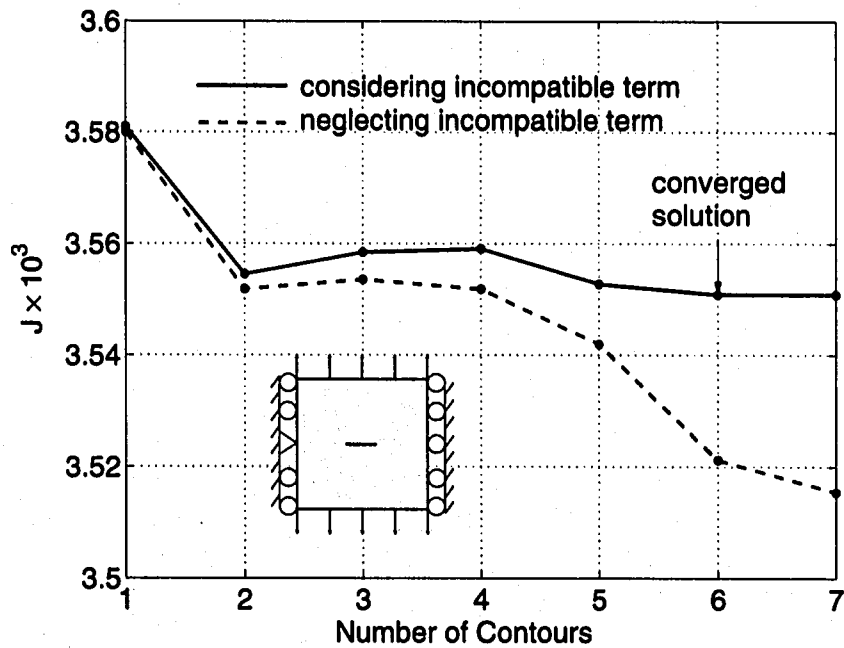
Figure 3.35: Example 7: Effect of the "incompatible term" on the path-independence of the J-integral considering the first set of BCs. The region associated with each contour is illustrated by Figure 3.34.
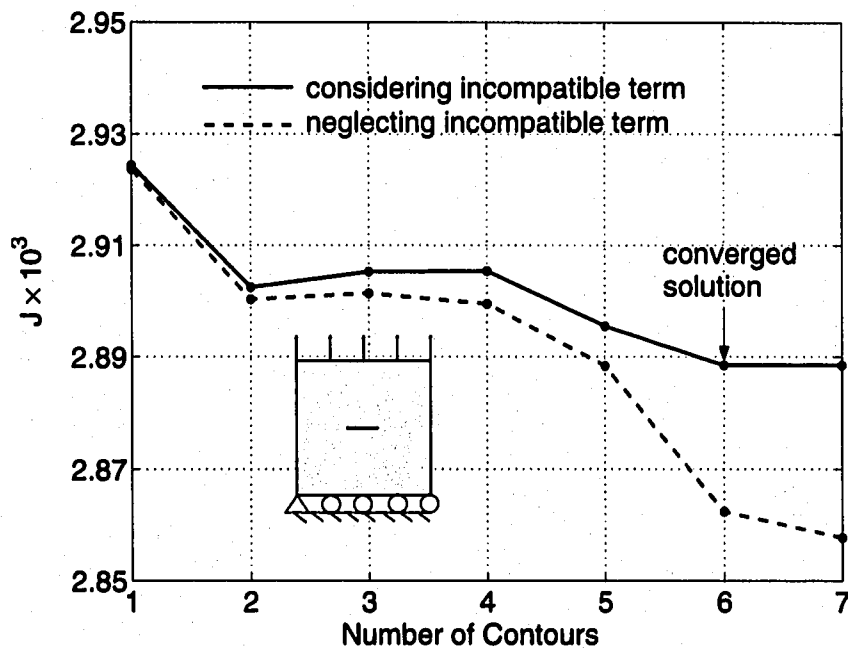
Figure 3.36: Example 7: Effect of the "incompatible term" on the path-independence of the J-integral considering the second set of BCs. The region associated with each contour is illustrated by Figure 3.34.
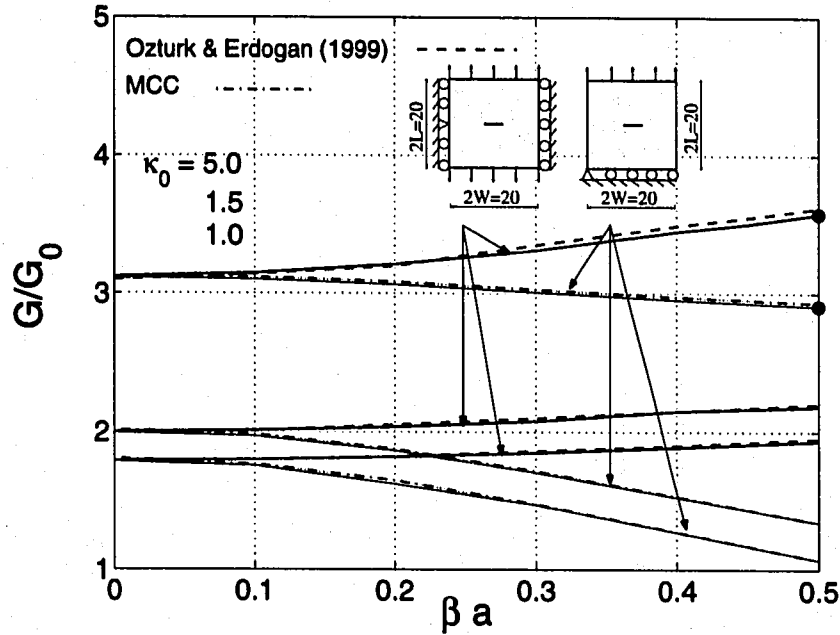
Figure 3.37: Example 7: Normalized strain energy release rate versus the nonhomogeneity parameter βa and the shear parameter κ_0 considering uniformly applied tension $(\sigma_{22}(X_1, \pm L) = \pm\sigma$ for the first set of BCs, and $\sigma_{22}(X_1, L) = \sigma$ for the second set of BCs) and $\delta^4 = 10.0, \nu = 0.3, \mathcal{G}_0 = \pi\sigma^2 a/E^0$. The dashed lines indicate the results reported by Ozturk and Erdogan [109], and the dash-dotted lines indicate the results obtained by means of the MCC method. The solid lines indicate the results by means of the present M-integral considering the two BCs, and the two bullets at $\beta a = 0.5$ indicate the converged solutions for J considering $\kappa_0 = 5.0$ as shown in Figures 3.35 and 3.36, respectively.

3.8.8 Crack in a multi-layered region

This example investigates a crack in a multi-layered region which includes two homogeneous materials and an FGM region in between those two regions. This example is similar to those investigated by Ambrico et al. [4], who investigated thin multi-layers comprised of repeating patterns of different material sections, such as interconnect-dielectric structures in microelectronics. The material gradation for the FGM region has various ratios of Young's modulus. Figures 3.38(a) and 3.38(b) show edge and interior cracks in a multi-layered region, respectively. Figures 3.38(c), 3.38(d), and 3.38(e) show the complete mesh configuration, the mesh detail around the top edge, and the mesh detail around the crack tip using 12 sectors (S12) and 4 rings (R4), respectively.
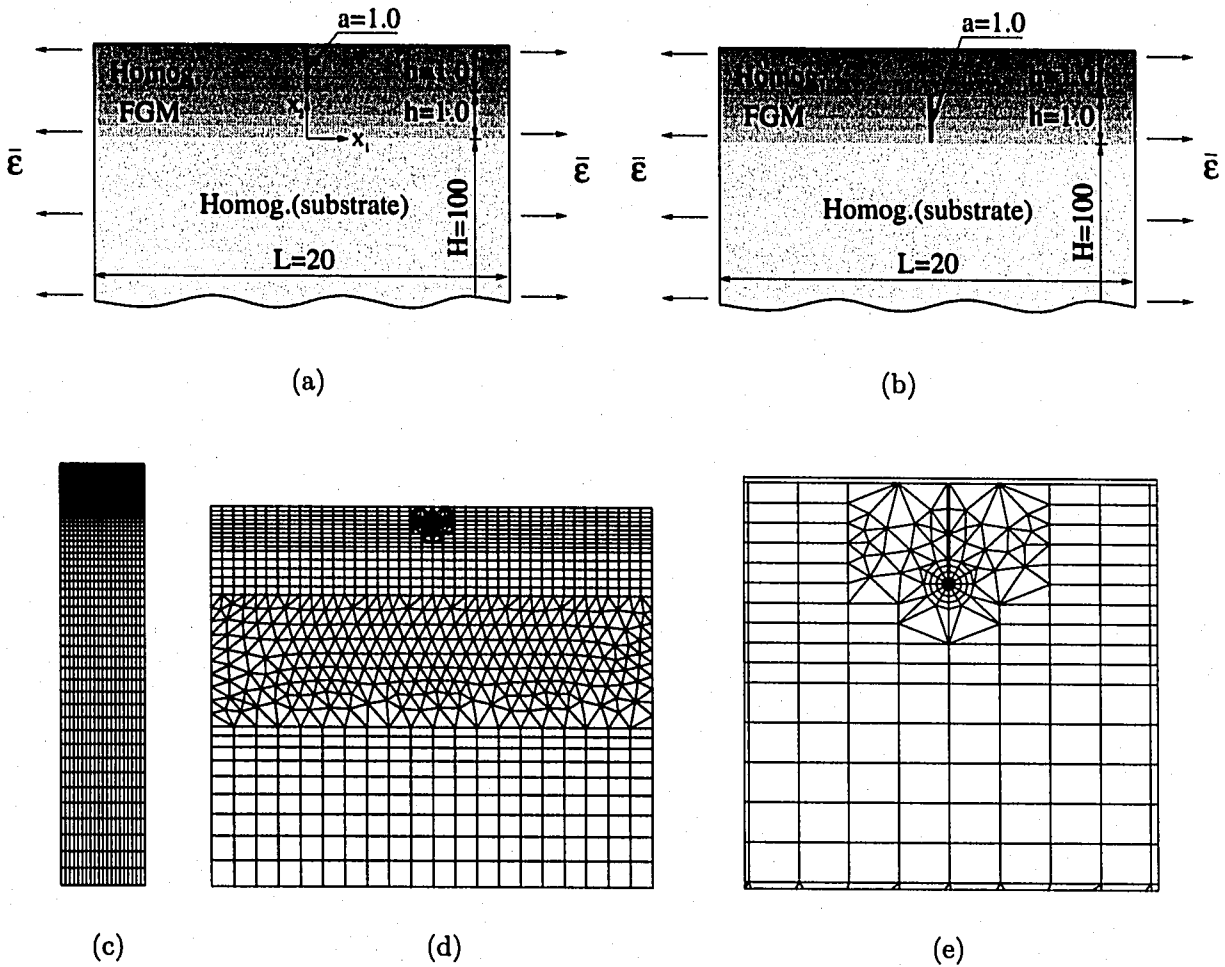
Figure 3.38: Example 8: crack in a multi-layered region: (a) geometry and BCs with an edge crack; (b) geometry and BCs with an interior crack; (c) complete finite element mesh; (d) mesh detail around the top edge; (e) mesh detail around the crack tips with 12 sectors (S12) and 4 rings.

The fixed-grip displacement loading is applied on the right edge, i.e. $\Delta(10, X_2) = 10$. The displacement boundary condition is prescribed such that $(u_1, u_2) = (0, 0)$ for the left-bottom corner node and $u_1 = 0$ for the nodes on the left edge. The mesh discretization consists of 1938 Q8, 96 T6, and 12 T6qp elements, with a total of 2046 elements and 5705 nodes. Young's modulus is constant for the top and bottom (substrate) homogeneous materials, and it is a linear function of X_2 in the

FGM region, while Poisson's ratio is constant. The following data were used for the FEM analysis:

$$a = 1.0, \ L = 20, H = 100, \ \bar{\varepsilon} = \Delta/L = 0.5, \ \nu = 0.30$$

$$E_1/E_2 = (0.1, 0.5, 0.75, 1.0, 2.0, 10.0),$$

$$\text{plane strain, } 2 \times 2 \text{ Gauss quadrature.}$$

Table 3.16 shows the FEM results for SIFs and T-stresses for edge and interior cracks in a multi-region plate. For an edge crack, the ratio E_2/E_1 has a significant effect on the T-stress as well as the mode I SIF. Notice that the T-stress changes sign from positive to negative as the ratio E_2/E_1 increases, and the sign changes between $E_2/E_1 = 0.1$ and $E_2/E_1 = 0.5$. For an interior crack, the T-stress remains negative for all the ratios of E_2/E_1 considered. For both cases, the mode I SIF increases and the T-stress decreases with an increasing ratio of E_2/E_1.

Table 3.16: Example 8: the FEM results for SIFs and T-stresses for edge and interior cracks in a multi-layered region. The (+) and (−) denotes the upper crack tip of an interior crack, respectively. (see Figure 3.38).

E_2/E_1	Edge crack		Interior crack			
	K_I	T	K_I^+	K_I^-	T^+	T^-
0.1	0.069	0.027	0.116	0.684	-0.156	-0.351
0.5	0.465	-0.115	0.383	0.674	-0.346	-0.461
0.75	0.748	-0.242	0.544	0.685	-0.458	-0.506
1	1.047	-0.382	0.706	0.700	-0.568	-0.546
2	2.333	-0.998	1.372	0.767	-0.988	-0.692
10	14.26	-6.538	7.346	1.274	-3.999	-1.768

3.9 Concluding remarks

This chapter makes a critical assessment and comparison of three consistent formulations: non-equilibrium, incompatibility, and constant-constitutive-tensor formulations. Each formulation leads to a consistent form of the interaction integral in the sense that extra terms are added to compensate for the difference in response between homogeneous and nonhomogeneous materials. These extra terms play a key role in ensuring path-independence of the interaction integral for FGMs. In terms of numerical computations, the non-equilibrium formulation leads to the simplest final form of the M-integral among the three formulations.

In terms of numerical accuracy, the non-equilibrium formulation is equivalent to the incompatibility formulation, which is verified in numerical examples involving various types of material gradation. The constant-constitutive-tensor formulation requires the derivatives of the actual stress and strain field, and may have numerical accuracy problems with standard C^0 elements commonly used in the displacement-based FEM.

From numerical investigations, it is observed that both material gradation and orthotropy have a significant influence on SIFs and T-stress (i.e. both sign and magnitude), and the crack tip location also shows a significant influence on the fracture parameters in hyperbolic-tangent materials. It is also observed that the extra terms (e.g. non-equilibrium or incompatible terms) ensure convergence to target solutions (SIFs or T-stress).

Chapter 4

T-stress effect on crack initiation angles in functionally graded materials

4.1 Introduction

The fracture parameters describing the crack tip fields in functionally graded materials (FGMs) include not only stress intensity factors (SIFs) but also T-stress (non-singular stress). These two fracture parameters are important for determining the crack initiation angle under mixed-mode loading conditions in brittle FGMs (e.g. ceramic/ceramic such as TiC/SiC).

Among several fracture criteria [36, 66, 130] developed to predict crack initiation angle, Erdogan and Sih [36] proposed the maximum hoop stress criterion, which has been successfully used for homogeneous brittle materials. Williams and Ewing [146], and Ueda et al. [138] performed experiments using polymethyl-methacrylate (PMMA) with a slanted internal crack, and found that there was a difference in crack initiation angles obtained by the maximum hoop stress criterion and by their experiments. They observed that the elastic T-stress, which is the non-singular term in Williams [147] series expansion of stresses, has a significant influence on crack initiation angle. Thus to account for the difference, they modified the maximum hoop stress criterion into a generalized maximum hoop stress criterion, which incorporates the T-stress effect. For linearly elastic brittle materials, this criterion involves the mixed-mode SIFs, the T-stress, and the fracture process zone size r_c, which is assumed to be very small relative to the crack size and specimen dimensions. For instance, Chao and Zhang [21] adopted a set of experimental data obtained

by Richardson and Goree [121], who experimented half-dogbone tension (HDT), compact tension (CT), single edge-notched tension (SENT), and delta tension (DT) specimens fabricated by using PMMA (Young's modulus E=2.76 GPa, Yield stress $\sigma_Y = 55.2$ MPa, Toughness K_c=1.02 MPa$\sqrt{m}$, Poisson's ratio $\nu = 0.33$). Based on curve fitting of PMMA tests, Chao and Zhang [21] found that $r_c \approx 0.5$mm for stress-controlled fracture and $r_c \approx 0.03$mm for strain-controlled fracture (the choice of the model depends on the fracture mechanisms of the material). Notice that both values are bigger than the plastic zone size estimated for brittle materials under plane strain, i.e. $r_p = (K_c/\sigma_Y)^2/8\pi \approx 0.0187$mm, which somehow justifies the application of linear elastic crack tip fields. Moreover, based on experiments using thin plates of PMMA with an internal crack of length $2a$, Williams and Ewing [146] have suggested the critical parameter $c = \sqrt{2r_c/a} \approx 0.1$. This parameter was also advocated by Ueda et al. [138], although the actual physical reason for this parameter has not been clarified yet.

In this chapter, the generalized maximum hoop stress criterion is extended to the FGM case. A methodology is presented to evaluate mixed-mode SIFs and T-stress for FGMs, and these basic parameters are used to predict crack initiation angle. Thus the Williams's [147] asymptotic expansion of the stress field around the crack tip shown in Figure 3.2 takes the form

$$\sigma_{ij} = \frac{K_I}{\sqrt{2\pi r}}f_{ij}^I(\theta) + \frac{K_{II}}{\sqrt{2\pi r}}f_{ij}^{II}(\theta) + T\delta_{1i}\delta_{1j} + O(r^{1/2}), \qquad (4.1)$$

where σ_{ij} denotes the stress tensor, K_I and K_{II} are the mode I and mode II SIFs, respectively, T is the nonsingular elastic T-stress, and the angular functions $f_{ij}(\theta)$ can be found in several references, e.g. [33].

Although SIFs are well-known fracture parameters, T-stress is less understood, and thus its implications in fracture of FGMs need to be investigated further. For homogeneous materials, T-stress has a significant influence on crack growth under mixed-mode loading [146, 138, 133] and crack path stability in mode I loading considering a small imperfection [27]. T-stress has been also shown to have a significant influence on crack-tip constraint and toughness [32, 105]. Because of the importance of T-stress in fracture, investigations of T-stress have been extensively performed for homogeneous materials. Larsson and Carlsson [92] investigated T-stress in mode I loading and found that it affects the size and shape of the plastic zone. Leevers and Radon [94] used a

121

variational formulation to evaluate T-stress. Afterwards, Cardew *et al.* [16] and Kfouri [75] used the path-independent J-integral in conjunction with the interaction integral to calculate T-stress in mode I crack problems. Sladek *et al.* [132] used another type of path-independent integral, based on Betti-Rayleigh reciprocal theorem, for evaluating T-stress in mixed-mode loading. Recently Chen *et al.* [22] investigated T-stress under mode I loading by means of both the Betti-Rayleigh reciprocal theorem and Eshelby's energy momentum tensor (i.e. path-independent J-integral) using the p-version finite element method, and addressed the accuracy of numerical computations.

For brittle FGMs (e.g. MoSi$_2$/SiC [18], TiC/SiC [70]), T-stress is also considered to have a significant influence in crack initiation angle [82] and crack stability. However, it is worth mentioning that the present analysis is **not** analogous to the influence of T-stress in changing "constraint", as discussed in many references [32, 105, 92, 5]. Considerations of "constraint" are **not** applicable to the analysis of ideal linearly elastic brittle materials (cf. [133]). Recent work in the field of FGMs include that by Becker *et al.* [72] who have investigated T-stress and finite crack kinking by using a hyperbolic-tangent material gradation with steep gradient of Young's modulus. They found that T-stress in FGMs is affected by both the far-field loading and the far-field phase angle, and that the magnitude of T-stress in FGMs is, on average, greater than that for homogeneous materials with identical geometry. They calculated T-stress using the stress difference along $\theta = 0$, i.e. $\sigma_{xx} - \sigma_{yy}$. On the other hand, Kim and Paulino [82], and Paulino and Kim [114] evaluated T-stress in FGMs using the interaction integral in conjunction with the FEM, and obtained quite accurate results.

4.2 A fracture criterion incorporating T-stress

Fracture criteria can be revisited to incorporate T-stress. For instance, the generalized maximum hoop stress criterion [146, 138, 133] was introduced to incorporate T-stress effect into the conventional maximum hoop stress criterion for homogeneous materials. Due to the local nature of the criterion, the basic formulation for FGMs is the same as that for homogeneous materials. The

asymptotic stresses for linear elastic isotropic FGMs are given in polar coordinates as:

$$\sigma_{rr} = \frac{1}{\sqrt{2\pi r}} \cos\frac{\theta}{2} \left[K_I \left(1 + \sin^2\frac{\theta}{2} \right) + \frac{3}{2}K_{II} \left(\sin\theta - 2\tan\frac{\theta}{2} \right) \right] + T\cos^2\theta,$$

$$\sigma_{\theta\theta} = \frac{1}{\sqrt{2\pi r}} \cos\frac{\theta}{2} \left[K_I \cos^2\frac{\theta}{2} - \frac{3}{2}K_{II}\sin\theta \right] + T\sin^2\theta,$$

$$\sigma_{r\theta} = \frac{1}{2\sqrt{2\pi r}} \cos\frac{\theta}{2} \left[K_I\sin\theta + K_{II}(3\cos\theta - 1) \right] - T\sin\theta\cos\theta, \qquad (4.2)$$

where K_I, K_{II} and T denote the mixed-mode SIFs and T-stress, respectively. The conventional maximum hoop stress criterion was proposed for brittle materials by Erdogan and Sih [36]. They postulated that the crack will grow in the direction along which the maximum hoop stress $\sigma_{\theta\theta}$ occurs and the shear stress $\sigma_{r\theta}$ is zero. Therefore the crack initiation angle θ_0 is obtained from

$$\partial\sigma_{\theta\theta}/\partial\theta = 0 \quad \Rightarrow \quad \theta = \theta_0. \qquad (4.3)$$

Substitution of $\sigma_{\theta\theta}$ from Eq.(4.2) into Eq.(4.3) leads to [133]

$$\cos\frac{\theta_0}{2} \left[K_I\sin\theta_0 + K_{II}(3\cos\theta_0 - 1) - \frac{16}{3}T\sqrt{2\pi r_c}\sin\frac{\theta_0}{2}\cos\theta_0 \right] = 0, \qquad (4.4)$$

where r_c is an additional length scale representing the fracture process zone size. The crack initiation angle is evaluated by means of Eq.(4.4). For instance, for an inclined center crack in a homogeneous plate subjected to far-field constant traction as shown in Figure 4.1, the closed-form solutions for SIFs and T-stress are given by [133]

$$K_I = \sigma\sqrt{\pi a}(\lambda\cos^2\alpha + \sin^2\alpha), \qquad K_{II} = \sigma\sqrt{\pi a}(1 - \lambda)\sin\alpha\cos\alpha,$$

$$T = \sigma(1 - \lambda)\cos 2\alpha. \qquad (4.5)$$

Figure 4.2 plots the crack initiation angles versus crack angles for various critical distances r_c by using Eq.(4.4). Notice that the positive T-stress increases the crack initiation angle for $0° \leq \theta \leq 45°$, while the negative T-stress decreases the crack initiation angle for $45° \leq \theta \leq 90°$.

Once the crack initiation angle is determined, the crack initiation condition is obtained by
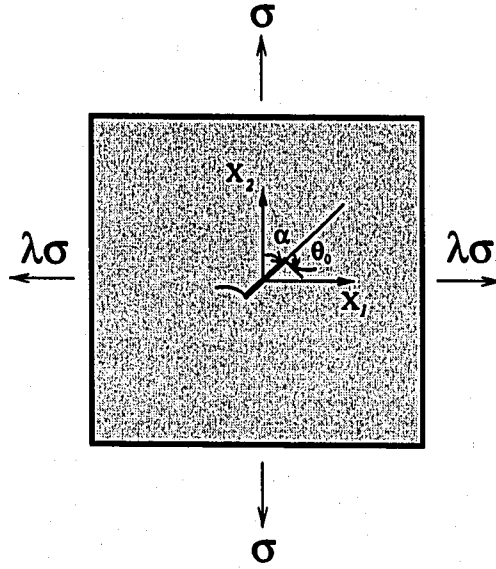
Figure 4.1: An inclined center crack in a biaxially loaded homogeneous plate with crack angle α and crack initiation angle θ_0.

considering the critical hoop stress $(\sigma_{\theta\theta})_c$ at the distance r_c. Then [133]

$$\sqrt{2\pi r_c}(\sigma_{\theta\theta})_c = \cos\frac{\theta_0}{2}\left[K_I\cos^2\frac{\theta_0}{2} - \frac{3}{2}K_{II}\sin\theta_0\right] + \sqrt{2\pi r_c}\,T\sin^2\theta_0. \tag{4.6}$$

For pure mode I when K_{II}, θ_0, and T are all equal to zero, K_I can be replaced by the mode I fracture toughness K_{Ic}. Therefore

$$\sqrt{2\pi r_c}(\sigma_{\theta\theta})_c = K_{Ic}. \tag{4.7}$$

Substitution $\sigma_{\theta\theta}$ of Eq.(4.7) into Eq.(4.6) yields the crack initiation condition [133]:

$$\cos\frac{\theta_0}{2}\left[K_I\cos^2\frac{\theta_0}{2} - \frac{3}{2}K_{II}\sin\theta_0\right] + \sqrt{2\pi r_c}T\sin^2\theta_0 = K_{Ic}. \tag{4.8}$$

The fracture locus can be obtained by using Eq.(4.4) and Eq.(4.8). For the inclined center crack in a homogeneous plate subjected to far-field constant traction, Figure 4.3 shows the fracture loci K_{II}/K_{Ic} versus K_I/K_{Ic} for various critical distances r_c.

124

Figure 4.2: Crack initiation angle predicted by generalized maximum hoop stress criterion $(M(\sigma_{\theta\theta})_{max})$ for an inclined center crack in a homogeneous plate under far-field axial loading.

Figure 4.3: Fracture loci predicted by generalized maximum hoop stress criterion $(M(\sigma_{\theta\theta})_{max})$ for an inclined center crack in a homogeneous plate under far-field axial loading.

4.3 Numerical examples

The first example is presented as a means to validate the implementation, and it consists of two parts. The first part has analytical closed-form solutions for SIFs, T-stress, and crack initiation angle, and it is investigated for an inclined center crack in a homogeneous finite plate ($a/W = 0.1$), which approximates an infinite domain. The second part of the first example is investigated both for an FGM plate with exponentially graded material properties, and for materials determined by the self-consistent model. The FEM results for T-stresses for an FGM plate with exponentially graded materials are compared with reference solutions obtained by means of the singular integral equation method by Paulino and Dong [112]. Thus the first example provides reference solutions for crack initiation angles in FGMs. The second example makes use of hyperbolic-tangent materials, which can model various material properties such as homogeneous, "bi-material", and smoothly varying FGM. The third example investigates an inclined center crack in a circular disk with exponentially radially-graded materials. Finally, the last example deals with the effect of material nonhomogeneity on the crack initiation angle for an edge-crack emanating from a semi-circular hole.

4.3.1 Plate with an inclined center crack

Figure 4.4(a) shows an inclined center-crack of length $2a$ located with angle α (clockwise) in a homogeneous plate under constant traction, and Figure 4.4(b) shows an inclined center-crack of length $2a$ located with angle α (clockwise) in an FGM plate under fixed-grip loading. Figure 4.4(c) shows the complete mesh configuration used for both cases, and Figure 4.4(d) shows the mesh detail using 12 sectors (S12) and 4 rings (R4) of elements around the crack tips. The displacement boundary condition is prescribed such that $u_2 = 0$ along the lower edge and $u_1 = 0$ for the node at the left hand side. The mesh discretization consists of 1641 Q8, 94 T6, and 24 T6qp elements, with a total of 1759 elements and 5336 nodes. The following data are used for the FEM analysis: $a/W = 0.1$; $L/W = 1.0$; $\alpha = (0°$ to $90°)$; plane stress; and 2×2 Gauss quadrature. Such data are common to both problems (i.e. Part 1 and Part 2 in Figure 4.4) which are presented next.

126
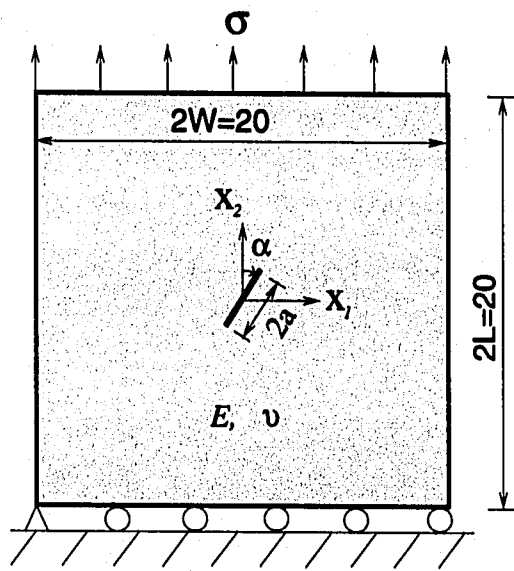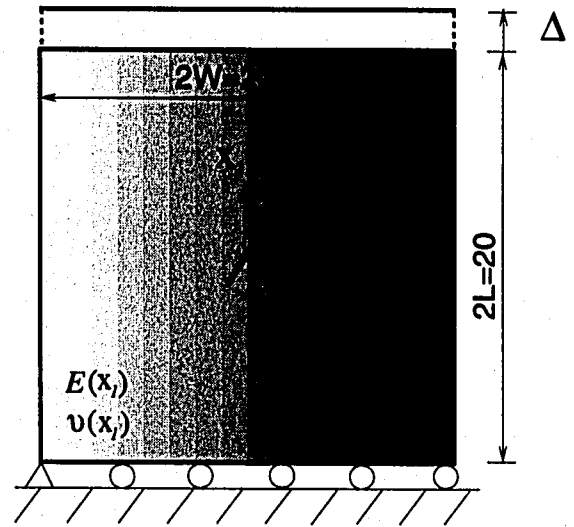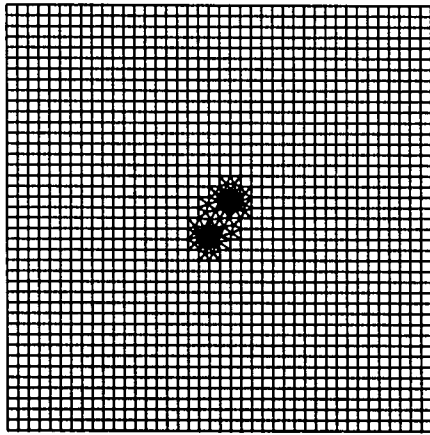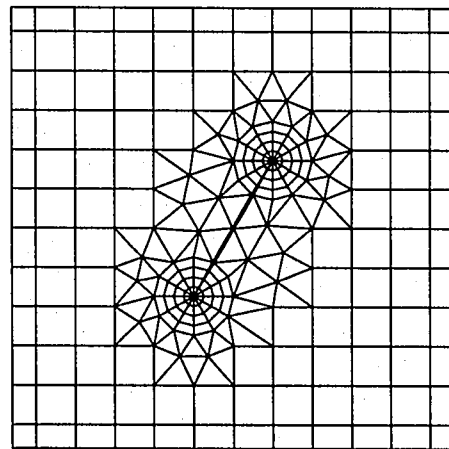
Figure 4.4: Example 1: plate with an inclined crack of angle α. (a) Part 1: geometry and BCs with constant traction; (b) Part 2: geometry and BCs with fixed-grip loading; (c) complete finite element mesh; (d) mesh detail with 12 sectors (S12) and 4 rings around the crack tips ($\alpha = 30°$ clockwise).

Homogeneous plate under constant traction

This example has analytical solutions and consists of an inclined center crack in a homogeneous plate subjected to far-field constant traction. Young's modulus and Poisson's ratio are $E = 1.0$ and $\nu = 0.3$, respectively. The applied loads correspond to $\sigma_{22}(X_1, 10) = \sigma = 1.0$ (see Figure 4.4(a)). For this case, the closed-form solutions for SIFs and T-stress are given by [133]

$$K_I = \sigma\sqrt{\pi a}\sin^2\alpha, \qquad K_{II} = \sigma\sqrt{\pi a}\sin\alpha\cos\alpha,$$

$$T = \sigma\cos 2\alpha. \tag{4.9}$$

Figure 4.5 shows comparison of the present FEM results for crack initiation angles with those obtained by closed-form solutions, i.e. Eq.(4.9), predicted by the generalized maximum hoop stress criterion $(M(\sigma_{\theta\theta})\text{max})$ for $r_c/a = 0$ and $r_c/a = 0.01$.
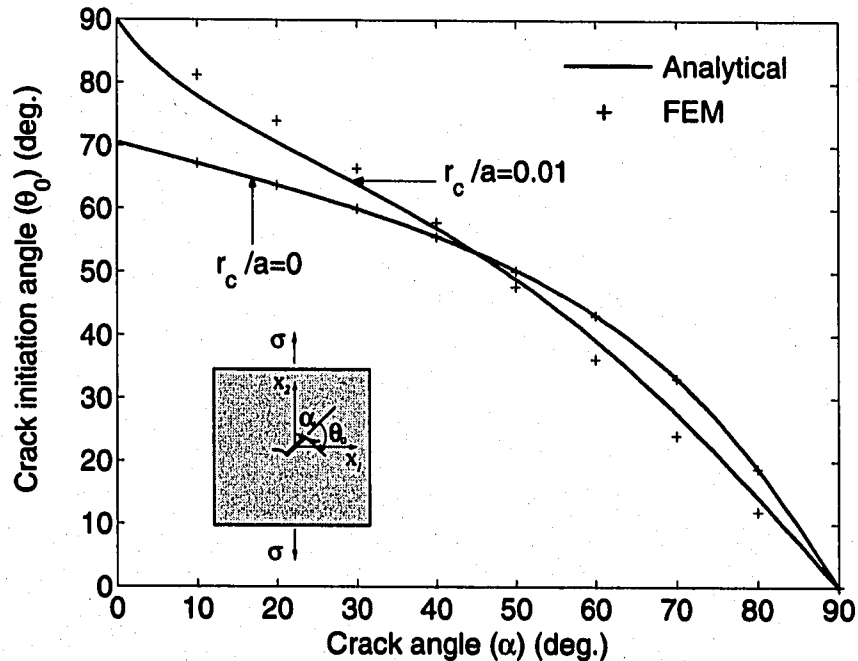
Figure 4.5: Example 1, Part 1: comparison of FEM results (denoted by +) for crack initiation angles with those obtained by closed-form solutions (solid lines), which are predicted by generalized maximum hoop stress criterion $(M(\sigma_{\theta\theta})\text{max})$ for an inclined center crack in a homogeneous plate under constant traction.

Notice that the FEM results for crack initiation angles agree well with those obtained by the closed-form solutions. Table 4.1 shows the quantitative comparison between FEM results and

closed-form solutions for SIFs and T-stresses for an inclined center crack under constant traction, and indicates good agreement between the two types of solutions.

Table 4.1: Example 1, Part 1: comparison of FEM results for SIFs and T-stresses with closed-form solutions for an inclined center crack in a homogeneous plate under far-field constant traction (see Figure 4.4(a)).

α	FEM [82]			Exact		
	K_I	K_{II}	T	K_I	K_{II}	T
0°	0.000	0.000	0.995	0.000	0.000	1.000
10°	0.054	0.305	0.934	0.053	0.303	0.939
20°	0.210	0.574	0.759	0.207	0.569	0.766
30°	0.448	0.773	0.493	0.443	0.767	0.500
40°	0.741	0.878	0.167	0.732	0.872	0.173
50°	1.052	0.878	-0.179	1.040	0.872	-0.173
60°	1.343	0.771	-0.508	1.329	0.767	-0.500
70°	1.581	0.571	-0.773	1.565	0.569	-0.766
80°	1.735	0.304	-0.947	1.719	0.303	-0.939
90°	1.788	0.000	-1.007	1.772	0.000	-1.000

FGM plate under fixed-grip loading

This example makes use of either exponential gradation or material gradation determined by means of the self-consistent model. While the first material gradation consists of a closed-form expression for the material properties, the second one provides discrete values of the material properties. The finite element analyses for SIFs, T-stresses, and crack initiation angles for both types of material gradation are performed for every 5° of crack angle from 5° to 90°. Since the solutions for 0° are not plausible, the crack angle 1° is chosen.

For exponentially graded materials, Paulino and Dong [112] evaluated T-stress by using a special integral equation method. In their analysis, Young's modulus is an exponential function of X_1, while Poisson's ratio is constant. Figure 4.6 shows the variation of Young's modulus given by

$$E(X_1) = \bar{E}e^{\beta X_1}. \tag{4.10}$$

The following data were used: $\nu = 0.3$, $\bar{E} = 1.0$, $\beta a = (0.0, 0.25, 0.5, 1.0)$. The applied load corresponds to $\sigma_{22}(X_1, 10) = \bar{\varepsilon}\bar{E}e^{\beta X_1}$ with $\bar{\varepsilon} = 1.0$ (see Figure 4.4(b)). This loading results in a uniform strain $\varepsilon_{22}(X_1, X_2) = \bar{\varepsilon}$ in a corresponding uncracked structure.

Figure 4.7 shows the FEM results for crack initiation angles versus geometric crack angles for
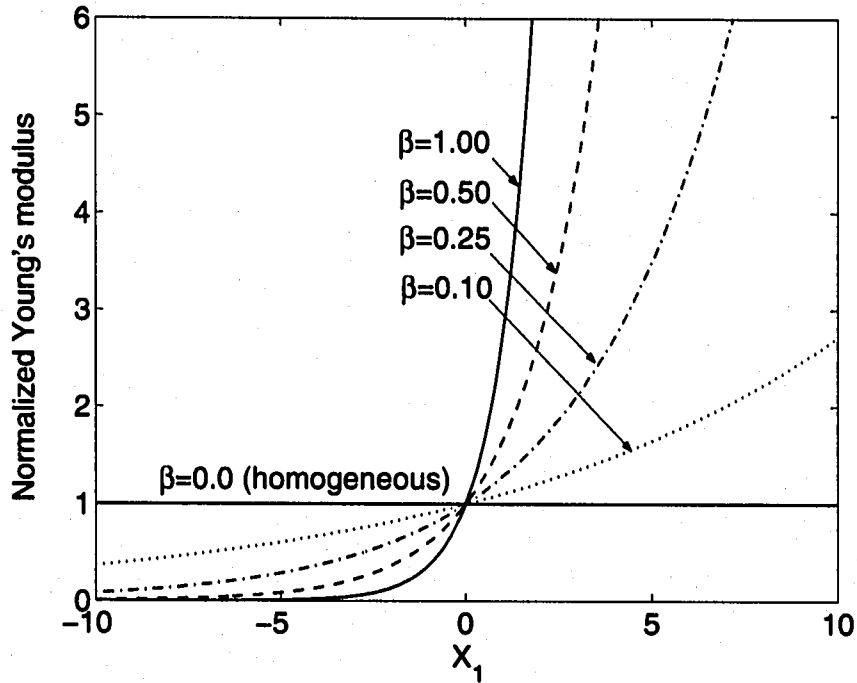
Figure 4.6: Example 1, Part 2: variation of normalized Young's modulus $(E(X_1)/\bar{E})$ with position.

the right crack tip for both homogeneous and FGM cases. Notice that positive T-stress increases crack initiation angle for the crack angle less than about 45°, and negative T-stress decreases crack initiation angle for the crack angle more than about 45° for both homogeneous and FGM cases.

Figure 4.8 shows the FEM results for crack initiation angles versus geometric crack angles for the right crack tip for the FGM case with fixed $\beta a = 0.5$. Notice that T-stress, in conjunction with the ratio r_c/a, has a significant influence on the crack initiation angle, and that, as before, positive T-stress increases the crack initiation angle, while negative T-stress decreases the crack initiation angle. Notice also that when $r_c/a = 0.0$, there is no effect of T-stress.

Figure 4.9 shows the FEM results for crack initiation angles versus crack angles for the right crack tip for various βa with a fixed $r_c/a = 0.01$. Notice that there is not much effect of material nonhomogeneity for a nearly horizontal ($\alpha \approx 90°$) or a nearly vertical ($\alpha \approx 0°$) crack, however, such effect is more pronounced in the mid-range of the plot (e.g. $10° < \alpha < 70°$).

Table 4.2 shows the FEM results for SIFs, T-stresses, and crack initiation angles for an inclined center crack under fixed-grip loading for the homogeneous material case, i.e. $\beta a = 0.0$ (see Figure 4.7). A comparison between Tables 4.1 and 4.2 reveals the influence of the loading boundary

Figure 4.7: Example 1, Part 2: the FEM results for crack initiation angles predicted by generalized maximum hoop stress criterion ($M(\sigma_{\theta\theta})_{max}$) for an inclined center crack in an FGM plate under fixed-grip loading for $\beta a = 0.0$ and $\beta a = 0.5$.

conditions (applied force versus applied displacement) on the SIFs and T-stress. Table 4.3 compares the FEM results for T-stress with the reference solutions obtained by Paulino and Dong [112] for both homogeneous ($\beta a = 0.0$) and nonhomogeneous ($\beta a \neq 0.0$) materials. Notice that the material nonhomogeneity is represented by the parameter βa, which is dimensionless. There is a reasonably good agreement between the present FEM results and the semi-analytical results of reference [112]. For both crack tips $(+a, -a)$, these results show that the T-stress changes sign for the crack angle $\alpha \approx 45°$ for $\beta a = 0.00$ and $\beta a = 0.25$, however, the angle increases as βa increases, e.g. $\beta a = 0.50$ (cf. last two columns of Table 4.3). Table 4.4 shows the FEM results for SIFs, T-stresses, and crack initiation angles for an inclined center crack under fixed-grip loading for $\beta a = 0.5$ (see Figure 4.7). For FGMs, the numerical results for SIFs, T-stresses, and crack initiation angles are different at the right and left crack tips because material gradation breaks down the symmetry achieved with homogeneous materials.

131
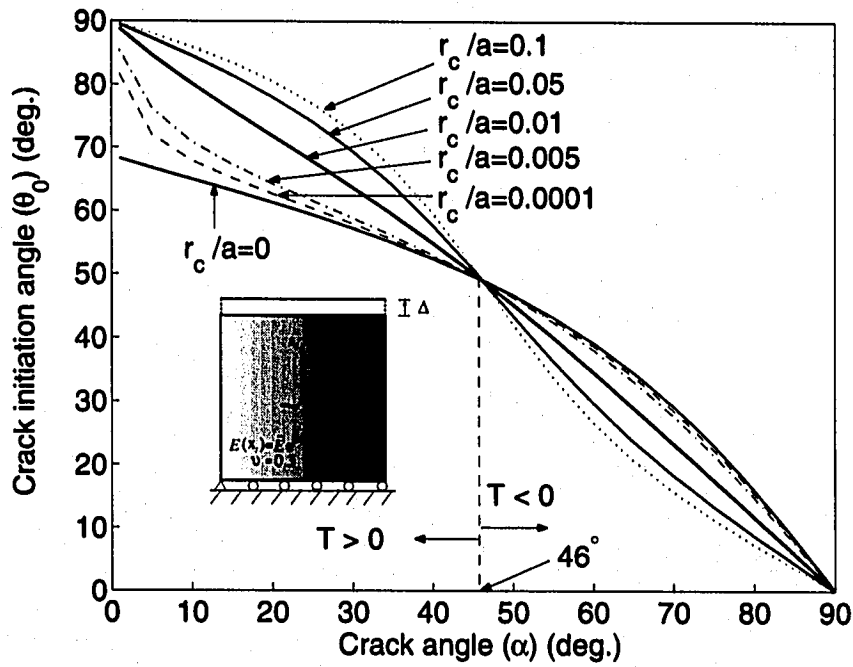
Figure 4.8: Example 1, Part 2: the FEM results for crack initiation angle predicted by generalized maximum hoop stress criterion $(M(\sigma_{\theta\theta})_{max})$ for an inclined center crack in an FGM plate under fixed-grip loading for various r_c/a values with $\beta a = 0.5$.
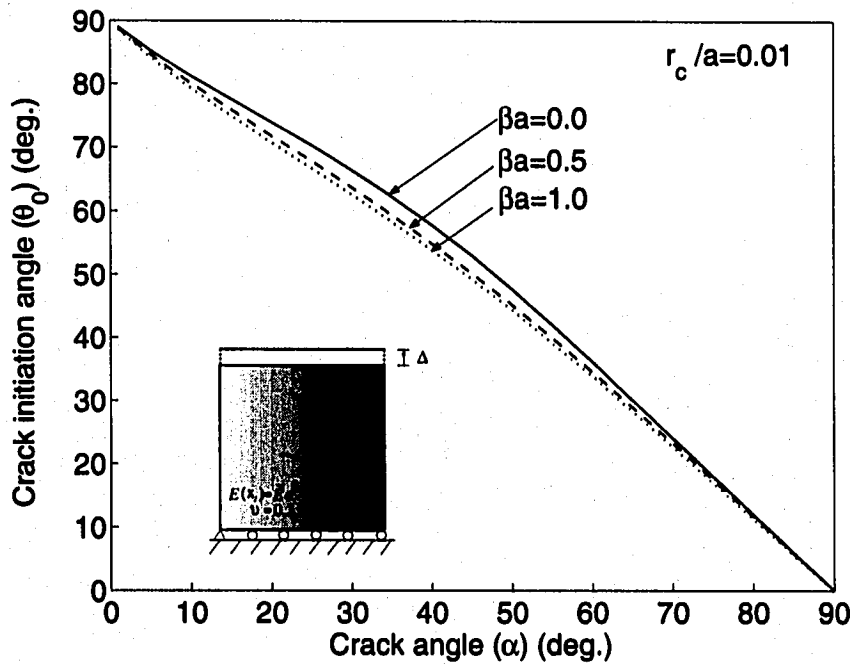
Figure 4.9: Example 1, Part 2: the FEM results for crack initiation angles predicted by generalized maximum hoop stress criterion $(M(\sigma_{\theta\theta})_{max})$ for an inclined center crack in an FGM plate under fixed-grip loading for various βa with fixed $r_c/a = 0.01$.

Table 4.2: Example 1, Part 2: SIFs, T-stresses, and crack initiation angles for an inclined center crack under fixed-grip loading for $\beta a = 0.0$, which refers to a homogeneous material. (see Figure 4.4(b)).

α	K_I	K_{II}	T	θ_0	
				$r_c/a = 0.00$	$r_c/a = 0.01$
0°	0.000	0.000	0.995	-	-
10°	0.054	0.305	0.933	68.8°	85.2°
20°	0.209	0.570	0.758	67.1°	81.2°
30°	0.446	0.768	0.491	65.4°	77.5°
40°	0.735	0.869	0.165	63.6°	73.9°
50°	1.039	0.865	-0.177	61.8°	70.2°
60°	1.323	0.758	-0.497	59.9°	66.4°
70°	1.552	0.560	-0.756	57.8°	62.2°
80°	1.700	0.298	-0.924	55.5°	57.7°
90°	1.752	0.000	-0.982	0.0°	0.0°

Table 4.3: Example 1, Part 2: comparison of FEM results for T-stresses with reference solutions [112] (see Figure 4.4(b)).

Method	α	$\beta a = 0.00$		$\beta a = 0.25$		$\beta a = 0.50$	
		$T(+a)$	$T(-a)$	$T(+a)$	$T(-a)$	$T(+a)$	$T(-a)$
Present	0°	0.9950	0.9950	0.9949	0.9948	0.9946	0.9944
	15°	0.8592	0.8592	0.8625	0.8569	0.8684	0.8505
	30°	0.4912	0.4912	0.4992	0.4905	0.5146	0.4841
	45°	-0.0055	-0.0055	-0.0077	-0.0019	0.0391	0.0109
	60°	-0.4974	-0.4974	-0.4790	-0.4763	-0.4288	-0.4371
	75°	-0.8534	-0.8534	-0.8310	-0.8191	-0.7655	-0.7494
	90°	-0.9828	-0.9828	-0.9589	-0.9430	-0.8878	-0.8606
Paulino & Dong [112]	0°	1.0000	1.0000	1.0000	1.0000	1.0000	1.0000
	15°	0.8660	0.8660	0.8665	0.8643	0.8701	0.8585
	30°	0.4999	0.5000	0.5024	0.4981	0.5132	0.4905
	45°	0.0002	0.0000	0.0106	0.0048	0.0393	0.0109
	60°	-0.5001	-0.5001	-0.4871	-0.4727	-0.4200	-0.4444
	75°	-0.8660	-0.8660	-0.8266	-0.8316	-0.7483	-0.7631
	90°	-0.9999	-0.9999	-0.9543	-0.9590	-0.8670	-0.8766

For materials determined by the self-consistent model, the shear (μ) and bulk (κ) moduli are first evaluated by solving both Eqs.(A.56) and (A.57) for a range of volume fractions, i.e. $0 \leq V_i \leq 1$ ($i = 1$ or 2), and then Young's modulus and Poisson's ratio are evaluated by

$$E = \frac{9\mu\kappa}{\mu + 3\kappa}, \quad \nu = \frac{3\kappa - 2\mu}{2(\mu + 3\kappa)}. \tag{4.11}$$

For the self-consistent model, the material properties of an engineering Ti/TiB FGM specimen are employed, which has been tested experimentally by Carpenter et al. [17], and investigated using cohesive fracture analysis by Jin et al. [71]. Material properties of Ti/TiB FGM, and the volume

Table 4.4: Example 1, Part 2: the FEM results for SIFs, T-stresses, and crack initiation angles for an inclined center crack under fixed-grip loading for $\beta a = 0.5$ (see Figure 4.4(b)).

α	K_I^+	K_{II}^+	K_I^-	K_{II}^-	T^+	T^-	θ_0^+		θ_0^-	
							$r_c/a = 0.00$	$r_c/a = 0.01$	$r_c/a = 0.00$	$r_c/a = 0.01$
0°	0.000	0.000	0.000	0.000	0.994	0.994	-	-	-	-
10°	0.094	0.316	0.019	0.286	0.939	0.926	66.7°	84.6°	69.2°	82.3°
20°	0.309	0.614	0.133	0.512	0.771	0.748	64.9°	80.1°	65.6°	75.8°
30°	0.632	0.850	0.310	0.655	0.514	0.484	63.1°	75.9°	61.8°	68.8°
40°	1.032	0.989	0.520	0.708	0.202	0.171	61.2°	71.8°	57.3°	60.1°
50°	1.465	1.006	0.729	0.676	-0.125	-0.147	59.3°	67.8°	51.9°	49.2°
60°	1.878	0.895	0.915	0.571	-0.428	-0.437	57.2°	63.6°	44.7°	36.5°
70°	2.220	0.670	1.059	0.410	-0.673	-0.665	54.9°	59.3°	34.6°	23.5°
80°	2.444	0.358	1.149	0.214	-0.832	-0.810	52.4°	54.8°	19.5°	11.2°
90°	2.522	0.000	1.179	0.000	-0.887	-0.860	0.0°	0.0°	0.0°	0.0°

fraction of Ti are used as follows:

$$E_{TiB} = 375\text{GPa}, \quad \nu_{TiB} = 0.14,$$

$$E_{Ti} = 107\text{GPa}, \quad \nu_{Ti} = 0.34,$$

$$V_{Ti}(X_1) = [(X_1 + 10)/(2W)]^{0.84} \quad (-10 \le X_1 \le 10),$$

respectively, where $2W$ is the gradation length, i.e. the width of the FGM plate (see Figure 4.4(b)). The power $p = 0.84$ was obtained by Jin et al. [71] using a least square of the actual material distribution. However, the geometrical configuration adopted here differs significantly from those used by Carpenter et al. [17] and Jin et al. [71]. Young's modulus and Poisson's ratio determined by micromechanics models are shown in Figures 4.10 and 4.11, respectively. The applied load is a uniform strain $\varepsilon_{22}(X_1, X_2) = \bar{\varepsilon} = 0.0005$ in a corresponding uncracked structure.

Figure 4.12 shows the present FEM results for crack initiation angles versus crack angles for the right crack tip. As expected, the positive T-stress increases the crack initiation angle, while the negative T-stress decreases the crack initiation angle.

Table 4.5 shows FEM results for SIFs, T-stresses, and crack initiation angles for an inclined center crack under fixed-grip loading (see Figure 4.12). Notice that SIFs, T-stresses, and crack initiation angle are very similar at both crack tips, while such similarity was not observed for exponentially graded material. This is due to the fact that, for the specific choice of material in this example, the material variation, between the crack tips, obtained by the self-consistent model
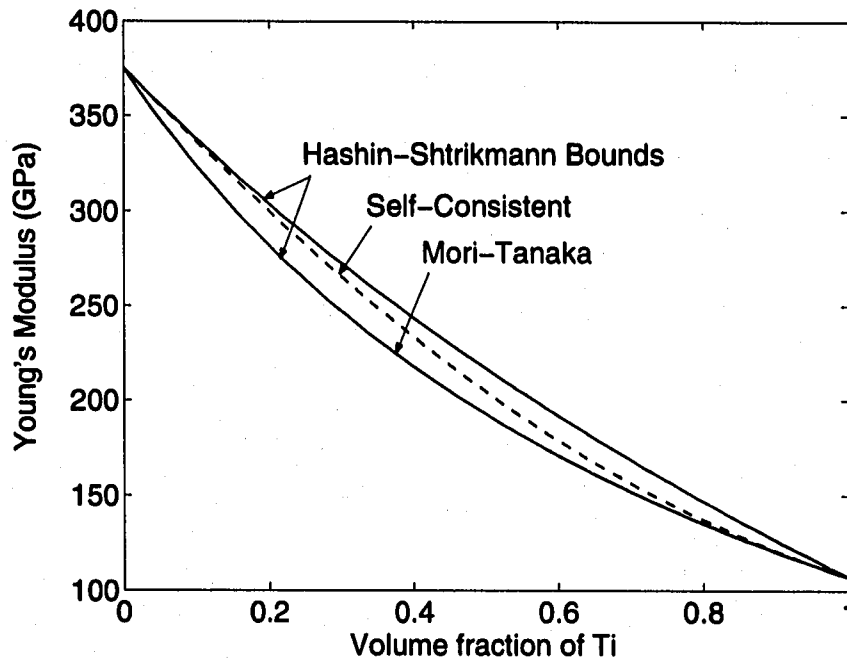
Figure 4.10: Example 1, Part 2: variation of Young's modulus versus volume fraction of Ti according to micromechanics models for composites.
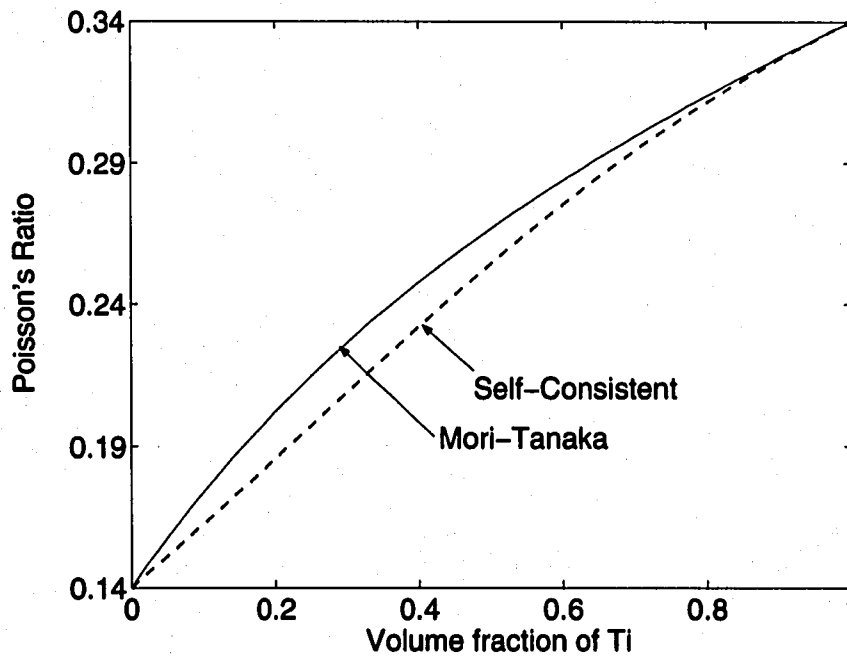
Figure 4.11: Example 1, Part 2: variation of Poisson's ratio versus volume fraction of Ti according to micromechanics models for composites.
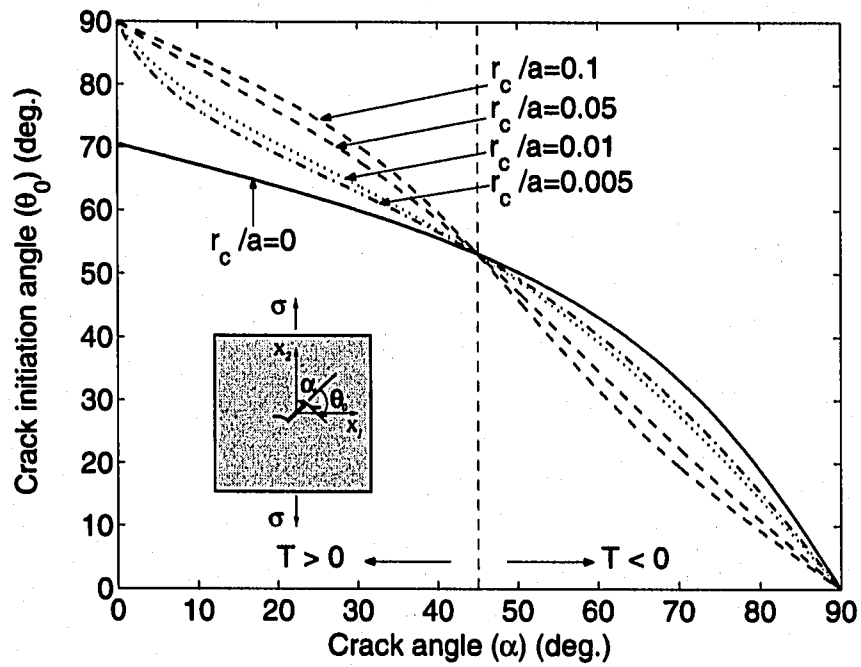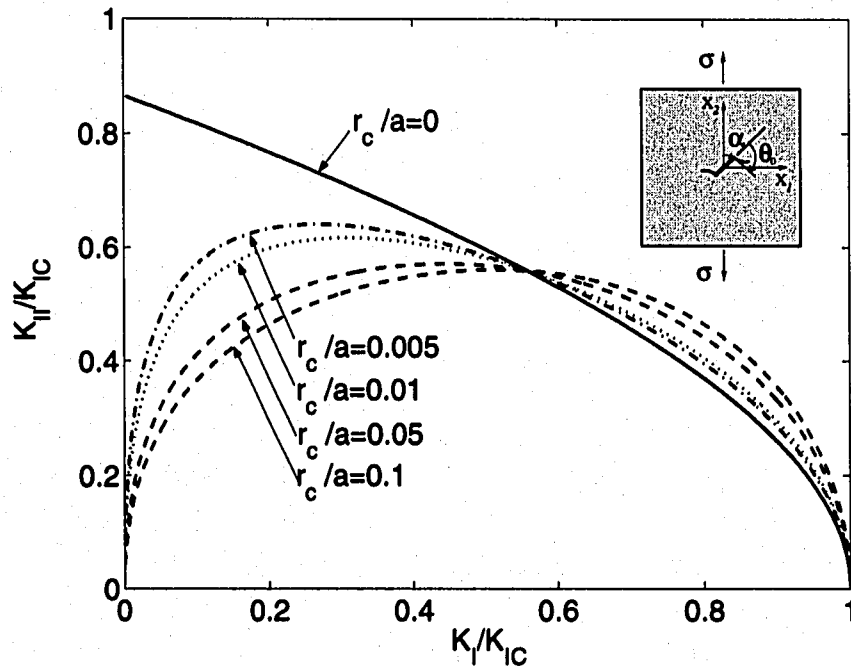
Figure 4.12: Example 1, Part 2: the FEM results for crack initiation angles predicted by generalized maximum hoop stress criterion $(M(\sigma_{\theta\theta})_{max})$ for an inclined center crack in a plate with FGMs determined by the *self-consistent model*.

is smoother than that for the exponentially graded material. Moreover, Young's modulus is a descending function of position for the micromechanics model case and it is an ascending function of position for the exponentially graded case.

Table 4.5: Example 1, Part 2: the FEM results for SIFs, T-stresses, and crack initiation angles for an inclined center crack under fixed-grip loading for FGMs determined by the self-consistent model (see Figure 4.4(b)).

α	K_I^+	K_{II}^+	K_I^-	K_{II}^-	T^+	T^-	θ_0^+		θ_0^-	
							$r_c/a = 0.00$	$r_c/a = 0.01$	$r_c/a = 0.00$	$r_c/a = 0.01$
0°	0.000	0.000	0.000	0.000	92.41	92.41	-	-	-	-
10°	4.567	28.15	5.491	28.48	86.68	86.76	67.4°	81.3°	66.8°	81.0°
20°	18.42	52.51	20.56	53.66	70.36	70.49	63.9°	74.2°	63.4°	73.6°
30°	39.58	70.14	43.41	72.39	45.59	45.74	60.2°	66.7°	59.6°	66.0°
40°	65.31	79.07	71.32	82.35	15.40	15.50	55.8°	58.1°	55.2°	57.4°
50°	92.34	78.41	100.9	82.30	-16.37	-16.36	50.4°	47.9°	49.8°	47.4°
60°	117.4	68.44	128.5	72.28	-45.97	-46.10	43.4°	36.3°	42.6°	36.0°
70°	137.7	50.50	150.9	53.58	-69.88	-70.15	33.4°	24.1°	32.7°	24.0°
80°	150.7	26.80	165.5	28.52	-85.44	-85.78	19.0°	11.9°	18.5°	11.9°
90°	155.2	0.000	170.6	0.000	-90.82	-91.20	0.0°	0.0°	0.0°	0.0°

136

4.3.2 Edge crack in a plate with hyperbolic-tangent materials

This example investigates the influence of material gradation rotation and translation on SIFs, T-stresses, and crack initiation angles. Figure 4.13(a) shows an edge crack of length a in a graded plate, and Figure 4.13(b) shows the complete mesh discretization using 12 sectors (S12) and 4 rings (R4) of elements around the crack tip. Figures 4.13(c), 4.13(d), and 4.13(e) illustrate the three considered types of hyperbolic-tangent material gradation with respect to the crack tip: rotation, translation to the left, and translation to the right, respectively. The fixed-grip displacement loading is applied corresponding to $\sigma_{22}(X_1, 2) = \bar{\varepsilon}\bar{E}(X_1) = \bar{\varepsilon}E(X_1)/(1 - \nu^2)$, which results in a uniform strain $\varepsilon_{22}(X_1, X_2) = \bar{\varepsilon}$ in a corresponding uncracked structure. The displacement boundary condition is prescribed such that $u_2 = 0$ along the lower edge and $u_1 = 0$ for the node at the left hand side.

Young's modulus is a hyperbolic-tangent function which can be expressed with respect to the local (x_1, x_2) or global (X_1, X_2) Cartesian coordinates. For the rotation of material gradation,

$$E(x_1) = \frac{E_1 + E_2}{2} + \frac{E_1 - E_2}{2} \tanh(\beta(x_1)), \tag{4.12}$$

or, using global coordinates,

$$E(X_1, X_2) = \frac{E_1 + E_2}{2} + \frac{E_1 - E_2}{2} \tanh(\beta(X_1 \cos\theta + X_2 \sin\theta)). \tag{4.13}$$

For the translation of material gradation,

$$E(X_1) = \frac{E_1 + E_2}{2} + \frac{E_1 - E_2}{2} \tanh(\beta(X_1 + d)), \tag{4.14}$$

where d is a constant for translation. In this example, Poisson's ratio is taken as constant. The following data were used for the FEM analysis:

$$a/W = 0.5, \quad L/W = 2.0, \quad \beta a = 15.0, \quad \bar{\varepsilon} = 0.25,$$

$$(E_1, E_2) = (1.0, 3.0), \quad \nu = 0.30, \quad d = (0, -0.5, 0.5),$$
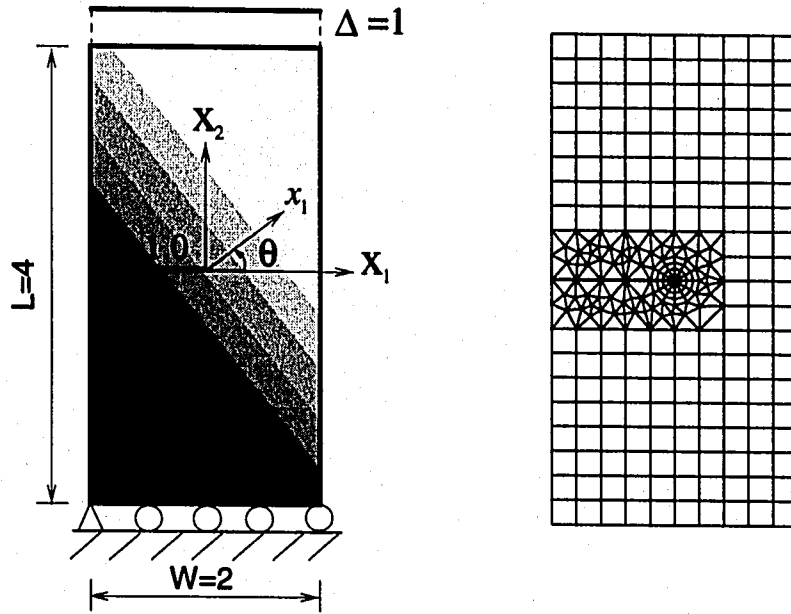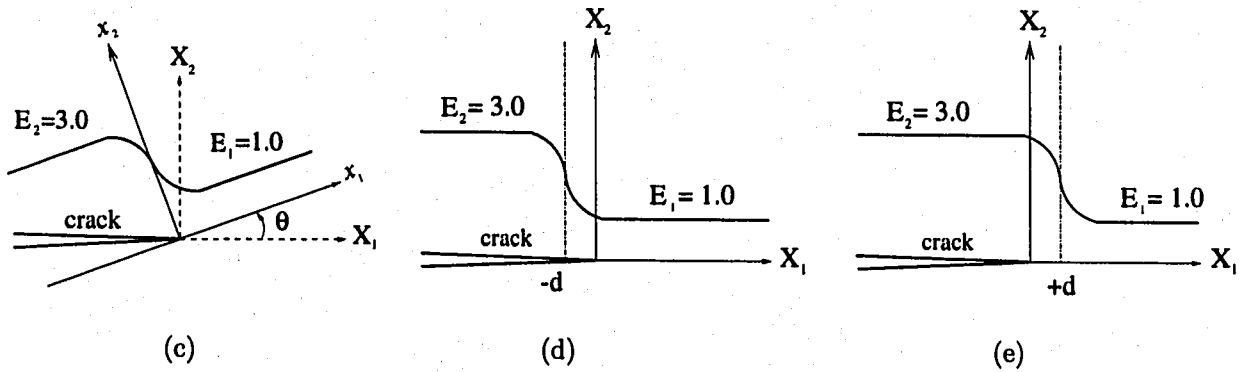
Figure 4.13: Example 2: edge crack in a plate with hyperbolic-tangent materials: (a) geometry and BCs; (b) complete finite element mesh with 12 sectors (S12) and 4 rings (R4) around the crack tip; (c) rotation of material gradation with the angle θ; (d) translation of material gradation to the left ($d = 0.5$); (e) translation of material gradation to the right ($d = -0.5$).

138

plane strain, 2 × 2 Gauss quadrature.

The mesh discretization consists of 208 Q8, 37 T6, and 12 T6qp elements, with a total of 257 elements and 1001 nodes.

Figure 4.14 shows FEM results for crack initiation angle predicted by the generalized maximum hoop stress criterion for various rotations of material gradation θ, i.e. 0° to 80°.
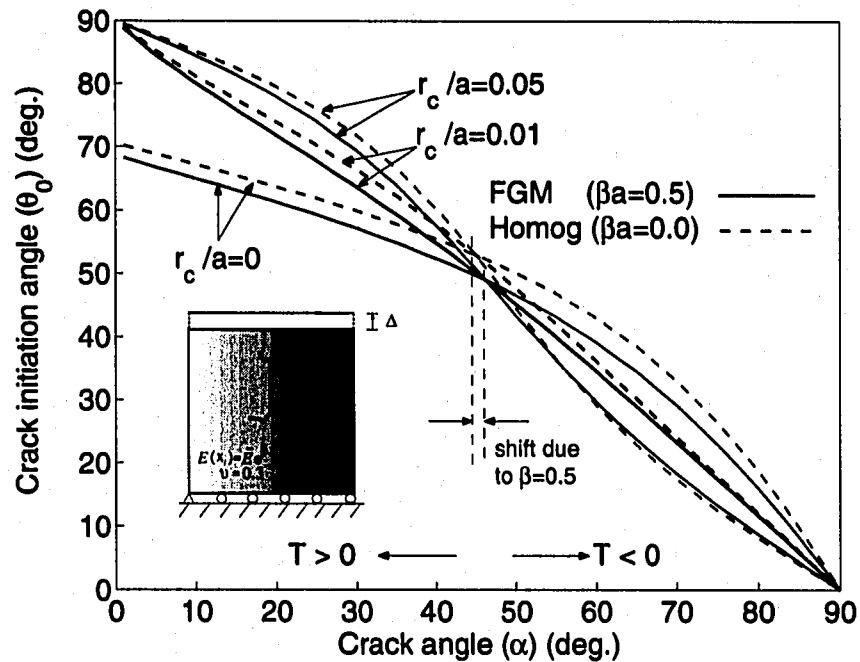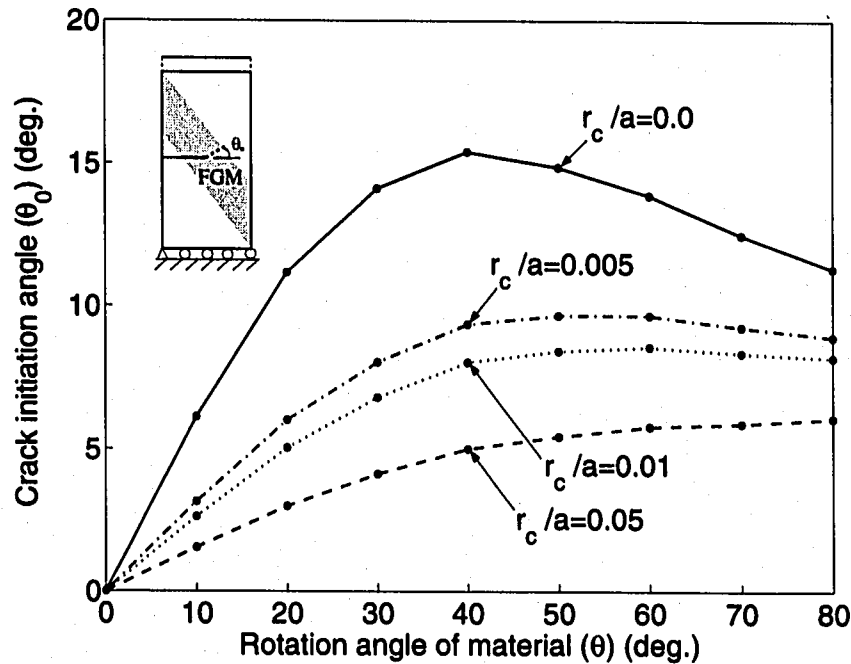

Figure 4.14: Example 2: the FEM results for crack initiation angles predicted by generalized maximum hoop stress criterion ($M(\sigma_{\theta\theta})_{max}$) for an edge crack in a plate with various rotations of hyperbolic-tangent materials under fixed-grip loading (see Figure 4.13(c)).

Notice that T-stress (negative) decreases the crack initiation angle and it also decreases with the increasing r_c/a ratio. The gap between the curve for $r_c/a = 0$ (no T-stress effect) and the various curves for $r_c/a \neq 0$ (especially $r_c/a = 0.005$) indicate the significant influence of T-stress in the FGM case. If the material were homogeneous, then the crack initiation angle $\theta_0 = 0°$. A comparison of the interaction integral with another method such as the modified crack closure [76] indicates that it loses accuracy in predicting the crack initiation angle for rotation angle of material in the range of 80° to 90°, which is not shown in Figure 4.14. Table 4.6 shows the FEM results for SIFs, T-stresses, and crack initiation angles in an edge crack for the rotation of hyperbolic-tangent

material variation ($\theta = 0°$ to $80°$) (see Figure 4.13(c)). Table 4.7 shows FEM results for SIFs and T-stresses for the translation of hyperbolic-tangent material variation by considering $d \in [-0.5, 0.5]$. Notice that T-stresses are all negative and the crack initiation angle is zero because of symmetry, i.e. $\theta = 0°$ and $K_{II} = 0$, in the particular cases illustrated by Table 4.7.

Table 4.6: Example 2: the FEM results for SIFs, T-stresses, and crack initiation angles for an edge crack with various rotations of hyperbolic-tangent material variation (see Figure 4.13(c)).

θ	K_I	K_{II}	T	$\theta_0(r_c/a = 0.00)$	$\theta_0(r_c/a = 0.01)$
0°	1.0190	0.0000	-1.176	0.00°	0.00°
10°	0.9949	-0.0535	-1.128	6.12°	2.62°
20°	0.9560	-0.0953	-1.015	11.16°	5.04°
30°	0.8932	-0.1141	-0.859	14.11°	6.80°
40°	0.8363	-0.1174	-0.696	15.40°	8.03°
50°	0.7879	-0.1064	-0.545	14.86°	8.42°
60°	0.7498	-0.0941	-0.418	13.88°	8.57°
70°	0.7209	-0.0809	-0.318	12.50°	8.36°
80°	0.6981	-0.0706	-0.236	11.31°	8.19°

Table 4.7: Example 2: the FEM results for SIFs and T-stress for an edge crack with translation (d) of hyperbolic-tangent material variation: (see Figures 4.13(d) and 4.13(e)). Notice that $K_{II} = 0$.

translation d	K_I	T
-0.5	1.163	-0.554
-0.3	1.167	-0.589
-0.1	1.190	-0.861
0.0	1.019	-1.176
0.1	0.582	-0.431
0.3	0.440	-0.211
0.5	0.410	-0.188

4.3.3 Inclined center crack in a circular disk

Figures 4.15(a), 4.15(b) and 4.15(c) show a circular disk with a center crack inclined by $\theta = 30°$ (with respect to the Cartesian X_1 axis), the complete mesh configuration, and the mesh detail around the crack tip using 12 sectors (S12) and 4 rings (R4), respectively. A point load is applied to the top and bottom nodes, i.e. $P(X_1, \pm 10) = \pm 100$. The displacement boundary condition is prescribed such that $(u_1, u_2) = (0, 0)$ for the node at $(X_1, X_2) = (-10, 0)$ and $u_2 = 0$ for the node at $(X_1, X_2) = (10, 0)$.
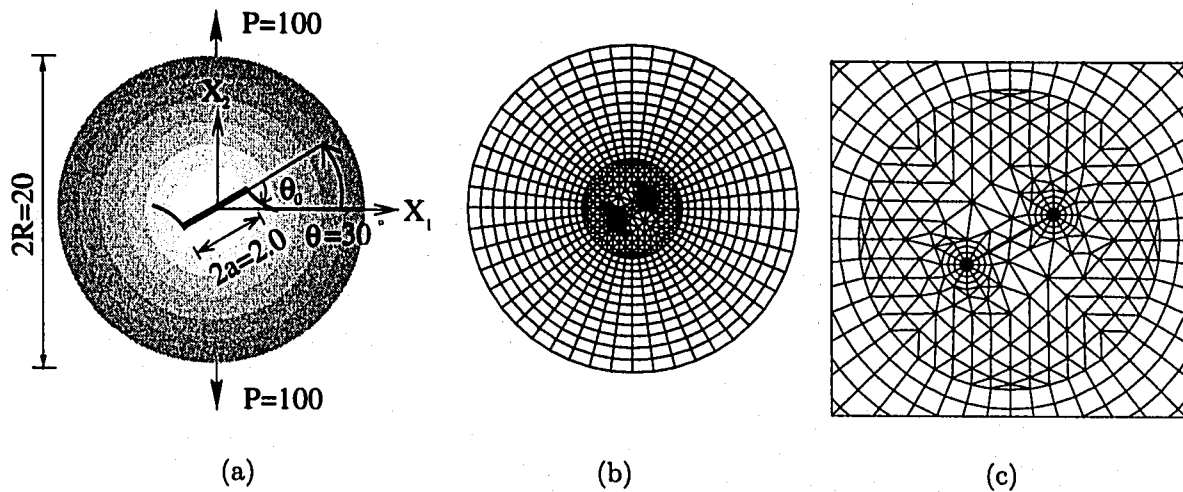
Figure 4.15: Example 3: circular disk; (a) geometry and BCs for an inclined center crack; (b) the complete mesh configuration; (c) mesh detail with 12 sectors (S12) and 4 rings (R4) around the crack tip (S12,R4).

Young's modulus is an exponential function of the radius r given by

$$E(r) = \bar{E}e^{\beta r}, \quad r = \sqrt{X_1^2 + X_2^2}. \tag{4.15}$$

The following data are used for the FEM analysis:

$$a = 1.0, \quad R = 10, \quad \beta a = (-5.0 \ to \ 5.0), \quad \bar{E} = 1.0, \quad \nu = 0.3,$$

$$\text{plane stress, } 2 \times 2 \text{ Gauss quadrature.}$$

The mesh discretization consists of 453 Q8, 228 T6, and 24 T6qp elements, with a total of 999 elements and 2712 nodes.

Figure 4.16 shows the FEM results for crack initiation angles predicted by the generalized maximum hoop stress criterion for various values of the dimensionless material nonhomogeneity parameter βa. Due to symmetry of the radial material gradation, the values of SIFs and T-stress are the same at both crack tips (see Figure 4.15(a)). Notice that the negative T-stress decreases the crack initiation angle (compare the curve for $r_c/a = 0$ with the other curves) and also the crack initiation angle decreases with the increasing r_c/a ratio. Table 4.8 shows the FEM results for SIFs, T-stresses, and crack initiation angles for various material nonhomogeneity βa. Notice that as βa

141

increases, the mixed-mode SIFs decrease and the T-stress increases substantially. The sign of the T-stress is always negative for the range of material variation investigated.
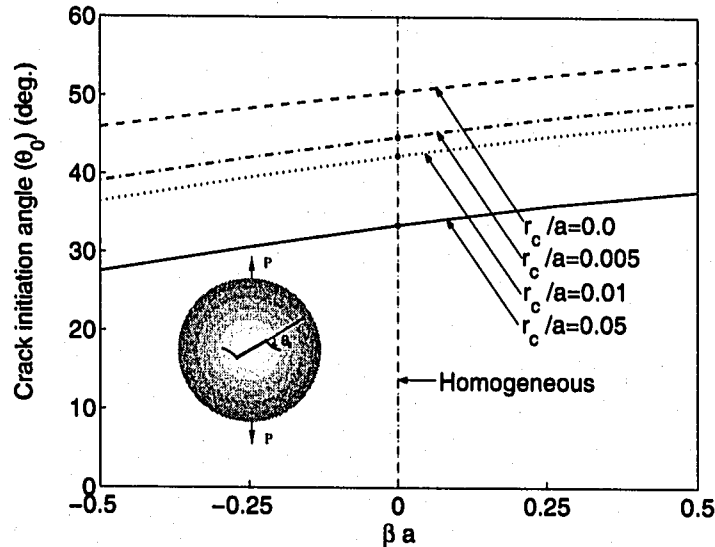
Figure 4.16: Example 3: the FEM results for crack initiation angles predicted by generalized maximum hoop stress criterion $(M(\sigma_{\theta\theta})_{max})$ for an inclined center crack in a disk subjected to a point load.

Table 4.8: Example 3: the FEM results for SIFs, T-stresses, and crack initiation angles for an inclined center crack in a circular disk (see Figure 4.15).

β	K_I	K_{II}	T	$\theta_0(r_c/a = 0.00)$	$\theta_0(r_c/a = 0.01)$
-0.50	22.91	15.19	-13.08	45.9°	36.4°
-0.25	17.53	13.21	-9.93	48.3°	39.5°
0.00	11.47	9.74	-6.53	50.4°	42.3°
0.25	5.86	5.65	-3.49	52.5°	44.8°
0.50	2.20	2.42	-1.44	54.5°	46.8°

4.3.4 Edge-crack emanating from a semi-circular hole

This example investigates the effect of material nonhomogeneity on SIFs, T-stress, and crack initiation angle for an edge-crack emanating from a semi-circle hole. Figures 4.17(a), 4.17(b) and 4.17(c) show an edge crack emanating from a semi-circle hole, the complete mesh configuration, and the mesh detail around the crack tip using 12 sectors (S12) and 4 rings (R4), respectively. The fixed-grip displacement loading is applied on the top edge, i.e. $\Delta(X_1, 5) = 10$.
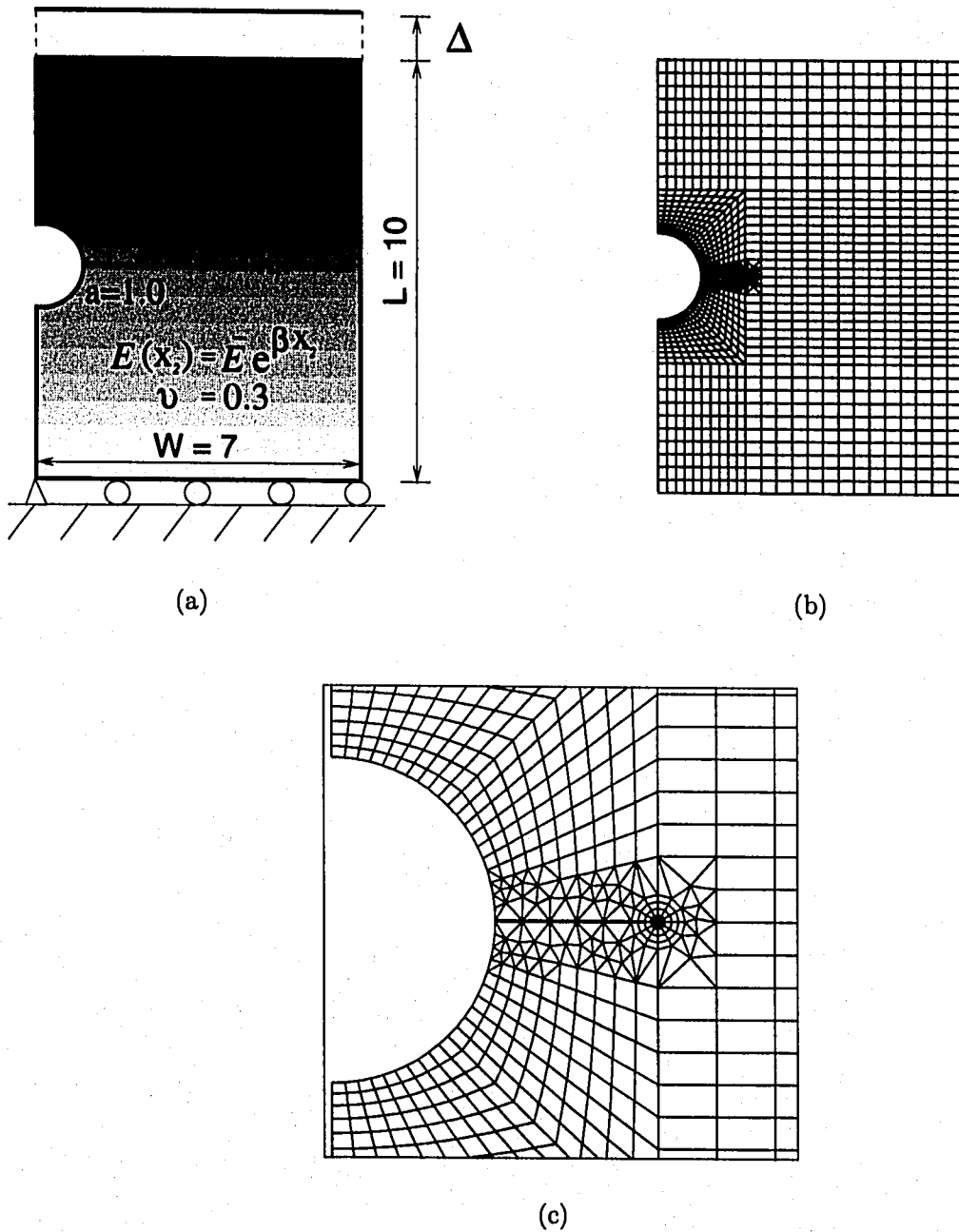
Figure 4.17: Example 4: edge crack emanating from a semi-circle hole; (a) geometry and BCs; (b) the complete mesh configuration; (c) mesh detail with 12 sectors (S12) and 4 rings (R4) around the crack tip (S12,R4).

The displacement boundary condition is prescribed such that $(u_1, u_2) = (0, 0)$ for the left-bottom corner node and $u_2 = 0$ for the nodes on the bottom edge. The mesh discretization consists

of 1142 Q8, 134 T6, and 12 T6qp elements, with a total of 1288 elements and 3903 nodes. Young's modulus is an exponential function of X_2, while Poisson's ratio is constant. The following data are used for the FEM

$$a = 1.0, \quad L = 10, \quad W = 7, \quad \beta a = (0.0 \text{ to } 1.0), \quad \bar{E} = 1.0, \quad \nu = 0.3,$$

$$\text{plane stress, } 2 \times 2 \text{ Gauss quadrature.}$$

Figure 4.18 shows the present FEM results for crack initiation angles predicted by the generalized maximum hoop stress criterion for various values of the material nonhomogeneity parameter βa. Notice that T-stress reduces the crack initiation angle and the crack initiation angle decreases with the increasing r/a ratio. It is expected that the crack initiation angle increases with the increasing material nonhomogeneity βa, while for homogeneous materials, the crack initiation angle is zero due to symmetry. Table 4.9 shows the FEM results for SIFs, T-stresses, and crack initiation angles for an edge crack emanating from a semi-circle hole. As βa deviates from zero and increases, mode I condition breaks down with the loss of symmetry and thus mode II behavior becomes more significant. Notice that the sign change for the T-stress occurs at $\beta a \approx 0.7$.

Table 4.9: Example 4: the FEM results for SIFs, mode mixity (K_I/K_{II}), T-stresses, and crack initiation angles for an edge crack emanating from a semi-circular hole (see Figure 4.17).

βa	K_I	K_{II}	K_{II}/K_I	T	$\theta_0(r_c/a = 0.00)$	$\theta_0(r_c/a = 0.01)$
0.00	2.208	0.000	0.000	-0.427	0.0°	0.0°
0.25	1.917	0.169	0.088	-0.311	9.9°	8.4°
0.50	1.310	0.232	0.177	-0.112	18.9°	17.4°
0.70	0.849	0.206	0.242	-0.0007	24.8°	24.7°
0.75	0.750	0.194	0.258	0.008	26.0°	26.2°
1.00	0.3776	0.1241	0.328	0.042	31.0°	33.7°

4.4 Concluding remarks

This chapter investigates T-stress effect on crack initiation angles in two-dimensional FGMs. Given SIFs and T-stress, a fracture criterion incorporating the T-stress effect can predict the crack initiation angle. From the numerical examples investigated, it is observed that positive T-stress increases the crack initiation angle, and negative T-stress decreases the crack initiation angle.
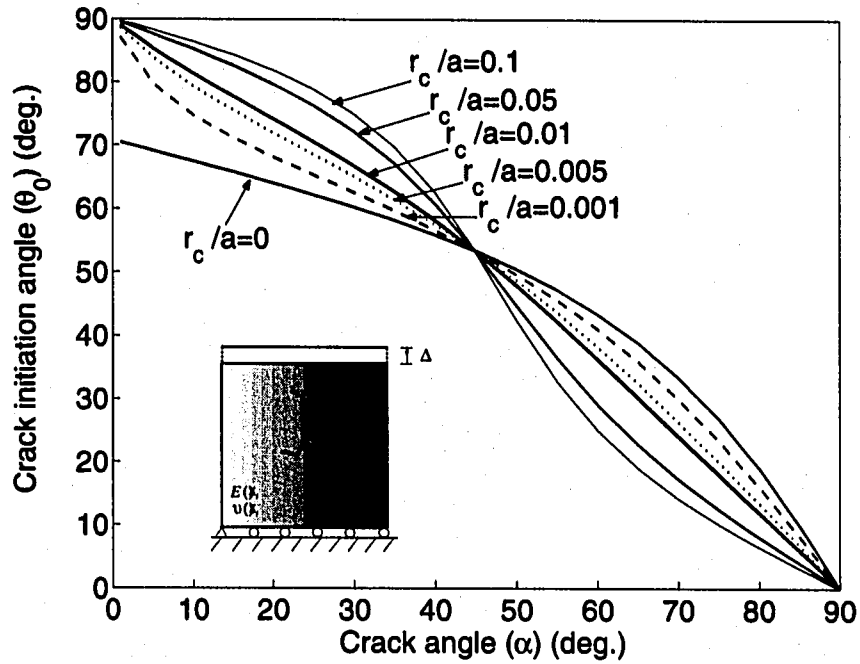
144
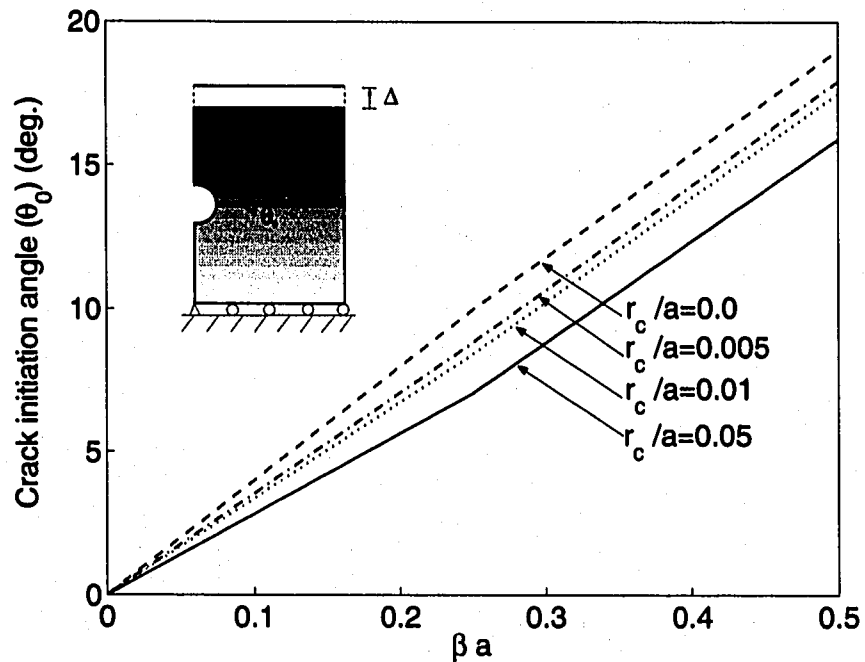
Figure 4.18: Example 4: the FEM results for crack initiation angles predicted by generalized maximum hoop stress criterion ($M(\sigma_{\theta\theta})_{max}$) for an edge crack emanating from a semi-circular hole.

Moreover, the material gradation, which may be represented by the material nonhomogeneity parameter βa, has a significant influence on the magnitude and the sign of the T-stress. The direction of material gradation also shows a significant influence on SIFs, T-stress, and the crack initiation angles. The fracture criterion adopted here involves a physical length scale r_c, which is representative of the fracture process zone size. The length scale parameter may have a significant effect on the crack initiation angle, even with the same values of T-stress and SIFs. Therefore the parameter r_c must be carefully assessed by comparing numerical solutions with experimental results.

Chapter 5

Simulation of crack propagation in functionally graded materials

5.1 Introduction

The behavior of cracks in solids and structures is important for assessing and enhancing structural integrity. In this chapter, crack growth in homogeneous and functionally graded materials (FGMs) is investigated and simulated by means of a remeshing algorithm of the finite element method considering mixed-mode and non-proportional loading. Crack initiation angle and crack increment are key factors to characterize crack growth.

The fracture parameters describing the crack tip fields in linear elastic FGMs include stress intensity factors (SIFs), which are important for determining the crack growth direction under mixed-mode loading conditions in brittle FGMs (e.g. ceramic/ceramic such as TiC/SiC). The singular terms of the stress field around the crack tip in FGMs take the form [34] (see Figure 5.1)

$$\sigma_{ij}(r,\theta) = \frac{K_I}{\sqrt{2\pi r}} f_{ij}^I(\theta) + \frac{K_{II}}{\sqrt{2\pi r}} f_{ij}^{II}(\theta), \tag{5.1}$$

where σ_{ij} denotes the stress tensor, K_I and K_{II} are the mode I and mode II SIFs, respectively, and the angular functions $f_{ij}(\theta)$ can be found in several references, e.g. [33].

The mixed-mode SIFs in FGMs are functions of material gradients, external loading and geometry. The material gradients do not affect the order of singularity and the angular functions of the singular crack tip fields, but do affect the SIFs. Thus the singular crack-tip fields of FGMs take the same forms as those for homogeneous materials. As explained in the introduction, based on local

146
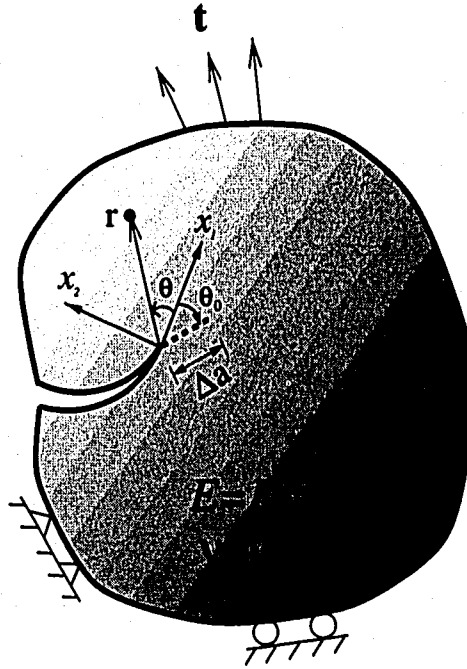
Figure 5.1: Cartesian (x_1, x_2) and polar (r, θ) coordinates originating from the crack tip in an arbitrary FGM under traction (**t**) and displacement boundary conditions. The crack initiation angle is θ_0, and Δa denotes the crack extension.

homogenization, crack initiation angles can be predicted by using the same fracture criteria as for homogeneous materials. In this chapter, the maximum energy release rate [66] and maximum hoop stress [36] criteria are used to determine crack initiation angles and to check crack growth stability.

In addition to crack initiation angle, crack increment is also important to determine crack trajectory. The present approach uses a user-defined crack increment, which needs to be provided at the beginning of each step. For homogeneous materials, Hori and Vaikuntan [62] proposed a formulation to determine the curvature and length of a small crack extension. Thorough investigation on crack increment in FGMs is needed, but it is out of the scope of the present work.

5.2 Strategy for automatic crack propagation

Automatic crack propagation in FGMs is performed by means of the I-FRANC2D (Illinois-FRANC2D) code, an interactive graphics program for simulating 2D fracture analysis. The code is

based on the FRANC2D (FRacture ANalysis Code 2D) [144, 145], which was originally developed at Cornell University. The extended capabilities of I-FRANC2D consist of special graded elements to discretize nonhomogeneous materials (see Figure 5.2), and fracture parameters such as SIFs for predicting crack initiation angle and determining stability of crack growth. The code uses quarter-
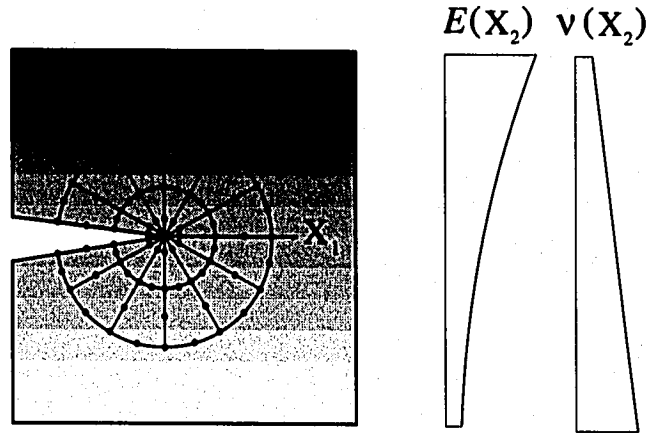
Figure 5.2: Crack-tip discretization for a crack in a nonhomogeneous material.

point six-node triangular (T6qp) elements to capture the stress singularity of $O(r^{-1/2})$, and it can perform mesh refinement around the crack tip in both radial (rings) and hoop (sectors) directions for each step of crack propagation (see Figure 5.2).

Finite element simulation of automatic crack propagation in the I-FRANC2D code involves a series of steps. Each step involves an automatic crack propagation cycle as illustrated in Figure 5.3. The I-FRANC2D code utilizes a direct stiffness FEM approach within the framework of linear elasticity. After the linear analysis involving a crack, the code computes mixed-mode SIFs using the interaction integral method. The computed SIFs are used to predict crack growth direction based on fracture criteria (e.g. maximum hoop stress, maximum energy release rate, or minimum strain energy density criteria). The SIFs are also used to determine the stability of crack growth by comparing with fracture toughness. When the new crack tip location is determined according to the user-defined crack increment, the code deletes elements along the incremental crack path, updates crack geometry, and performs automatic local remeshing.

5.3 Finite element mesh generation

The discrete crack analysis requires modification of the mesh at each step of crack propagation. The geometry update of crack propagation is modeled based on winged-edge data structure [12], which uses the FEM mesh topology such as vertices, edges and faces. Figure 5.4 illustrates the procedure for local remeshing [12]. The remeshing sequence is as follows [12]:

- Crack geometry is identified in the initial geometry by the user (see Figure 5.4(a)).

- A remeshing region is created by deleting elements near the crack in the polygon pattern, and the crack geometry is updated (see Figure 5.4(b)).

- Quarter-point six-node triangular (T6qp) elements are created around the crack tip (see Figure 5.4(c)).

- Triangular elements are generated by a triangulation algorithm (see Figure 5.4(d)).

- The local mesh refinement is done around the crack tip by increasing the number of elements in the radial and hoop directions (see Figure 5.4(e)).
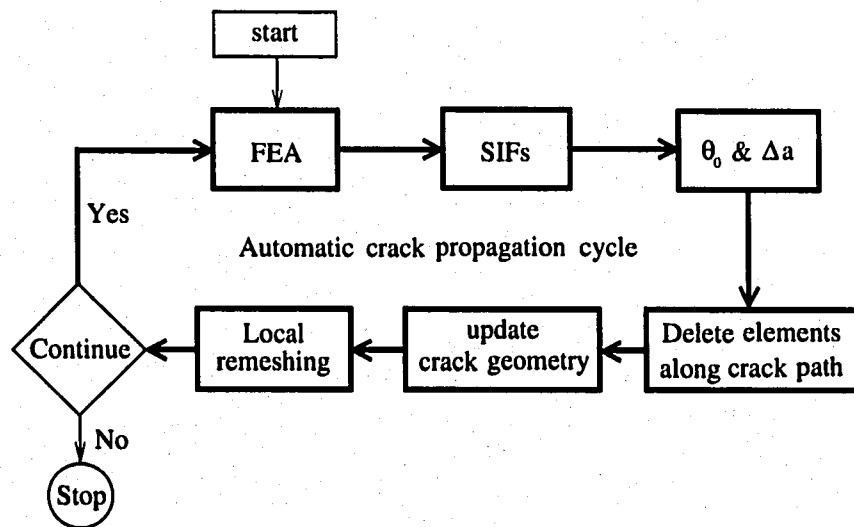
Figure 5.3: Automatic crack propagation procedure used in the I-FRANC2D code.
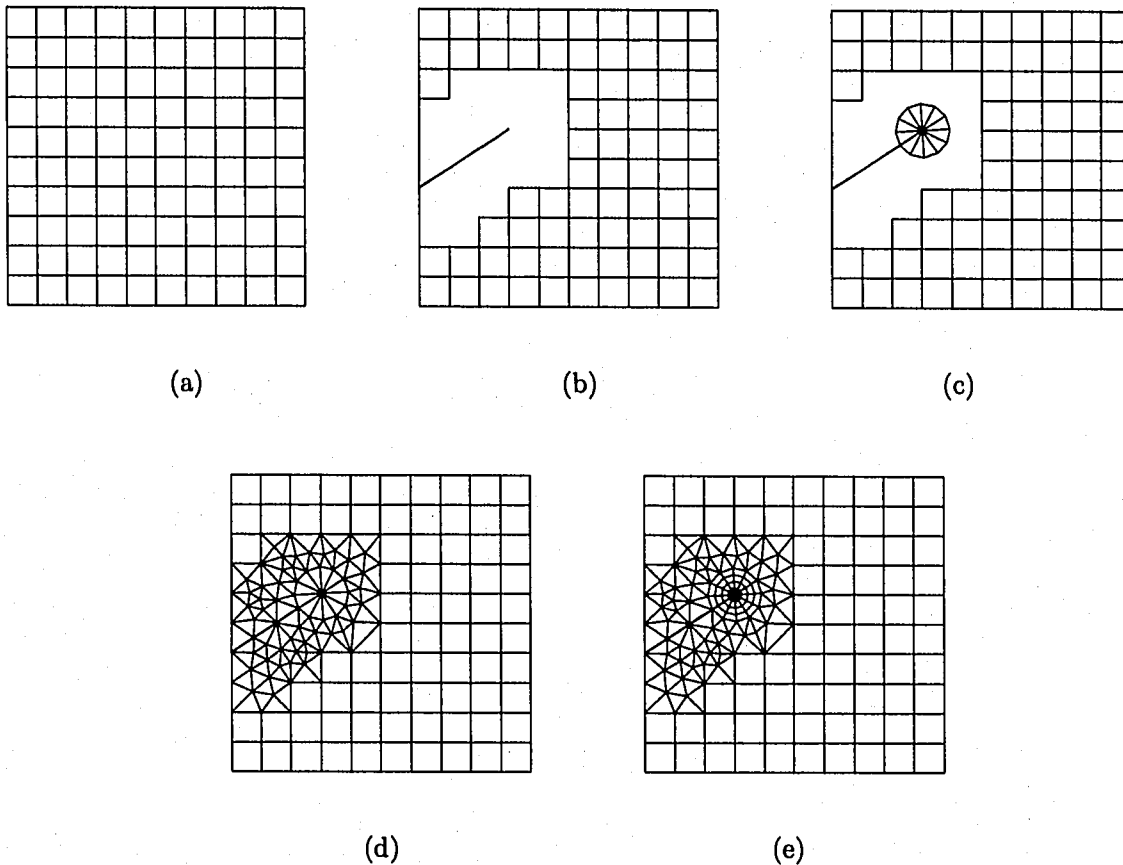
Figure 5.4: Sequential procedure for local remeshing [12]: (a) initial geometry; (b) deletion of nearby elements and construction of crack geometry; (c) meshing of singular crack-tip elements; (d) meshing of transition elements; (e) local refinement of crack-tip elements.

5.4 Remeshing algorithm

An algorithm for performing automatic crack propagation should satisfy two conditions [12]. First, the algorithm should keep compatibility between the new mesh and the existing mesh. Second, the algorithm should generate well-shaped elements with good aspect ratios especially transition zone between the crack-tip and the far-field regions.

The present remeshing algorithm used in I-FRANC2D is the recursive spatial decomposition (RSD) algorithm, which was originated in the code FRANC2D [144, 145]. The algorithm takes a region and subdivide it into smaller regions. The quadtree has been widely used for rectangular regions. The current algorithm uses the quadtree procedure and boundary-contraction scheme.

150
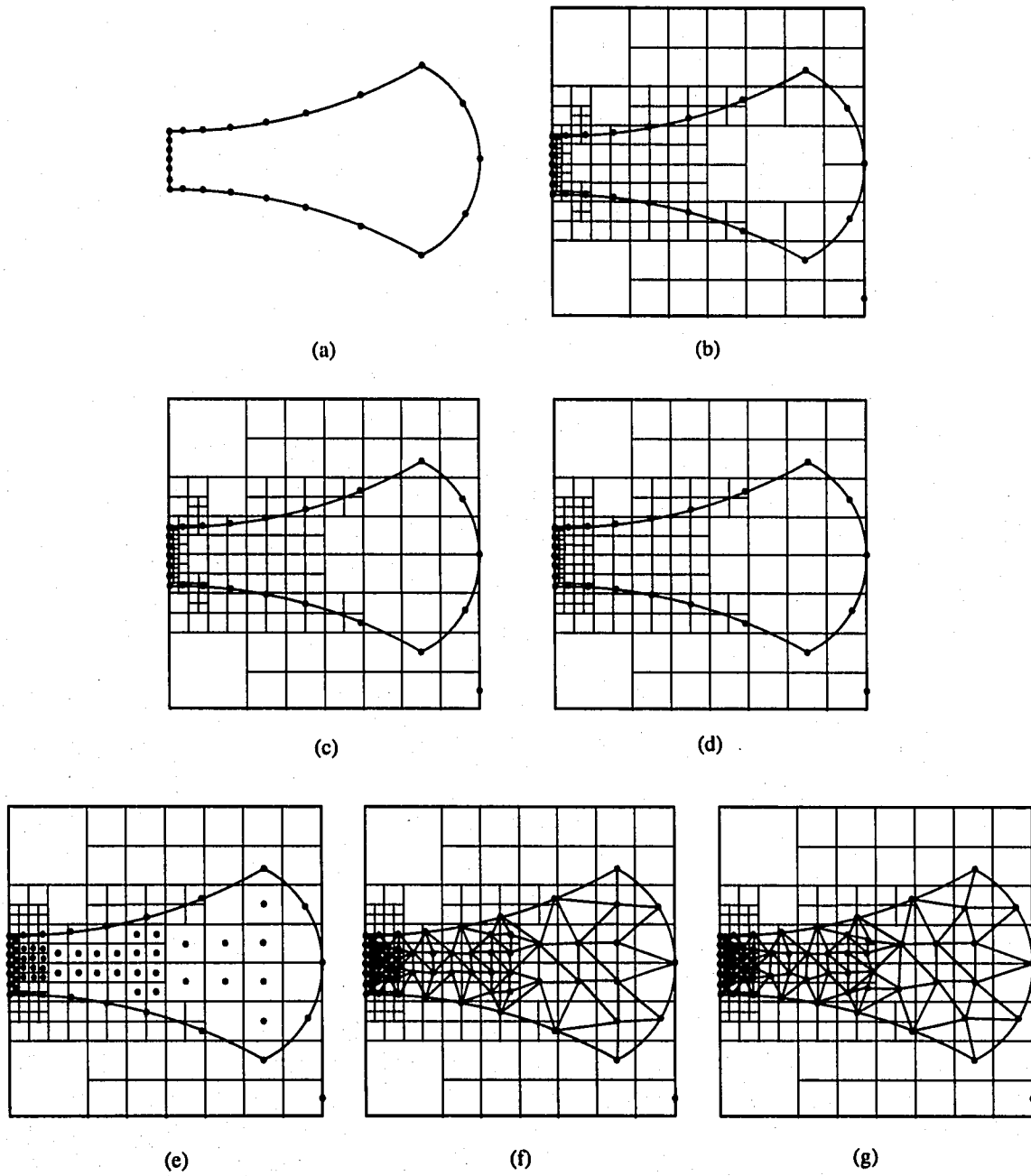
Figure 5.5: Procedure for RSD remeshing [12]: (a) input of boundary nodes and edges; (b) initial quadtree subdivision; (c) minimum subdivision of interior cells: (d) graded subdivision; (e) internal nodes generated at the center of the cells; (f) elements generated before smoothing; (g) elements generated after smoothing.

The procedure for the overall remeshing algorithm is as follows (see Figure 5.5) [12]:

- The geometry data on the boundary, i.e. nodes and edges, are given (see Figure 5.5(a)).

- Quadtree structure is generated. The given boundary data is used to determine a local subdivision level (see Figure 5.5(b)).

- The quadtree is refined to make interior cells smaller than the largest cell around the boundary (see Figure 5.5(c)).

- The quadtree is additionally refined to minimize the size difference between adjacent cells (see Figure 5.5(d)).

- Internal nodes are generated at the center of the quadtree cells (see Figure 5.5(e)).

- A boundary-contraction procedure is used to produce a trial mesh. (see Figure 5.5(f)).

- The size and shape of neighboring elements is regularized by moving internal nodes to the centroid of the adjacent nodes (see Figure 5.5(g)).

The above techniques have been also used by Paulino *et al.* [115] and extended to self-adaptive finite element analysis using the *h*-version of the FEM.

5.5 Fracture criteria

Local homogenization allows the use of fracture criteria, which have been widely used for homogeneous materials. Figure 5.6 shows a fracture locus involving mode I and II SIFs and fracture toughness K_{Ic}. If crack driving force is enough for the crack-tip fields to reach the fracture curve, then the crack does grow. The fracture locus can be obtained by experiments or theoretical fracture criteria. This chapter uses the maximum hoop stress [36] and maximum energy release rates [66] criteria. The maximum hoop stress criterion [36] is explained in the previous chapter, and maximum energy release rates criterion [66] is briefly reviewed.

152
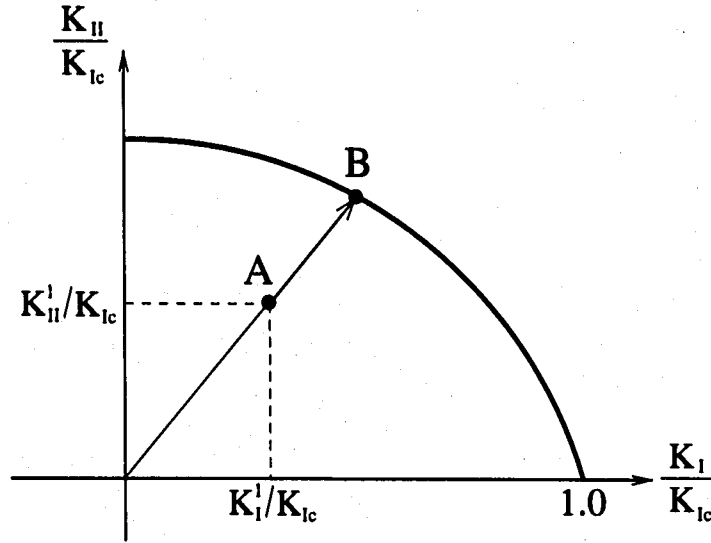
Figure 5.6: Fracture locus involving mode I and II SIFs and fracture toughness K_{Ic}.

Maximum energy release rate

Hussain *et al.* [66] proposed the maximum strain energy release rate criterion for homogeneous materials. They postulated that the crack subjected to combined loads will grow in the direction along which strain energy release is maximum and the crack will start to grow when the maximum strain energy release rate reaches a critical value. As mentioned in the introduction, here we consider a local (homogenized) version of the criterion by Hussain *et al.* [66], which is appropriate for FGMs. The concept of local homogenization was discussed by Gu and Asaro [48]. The energy release rate for combined mode I and mode II loading in FGMs is given by

$$\mathcal{G} = \frac{K_I^2 + K_{II}^2}{E_{tip}^*},$$

(5.2)

where $E_{tip}^* = E_{tip}$ for plane stress and $E_{tip}/(1 - \nu_{tip}^2)$ for plane strain. Equation (5.2) is obtained by assuming that a crack under mixed-mode loading moves along its own plane. However, in general, the crack grows in a direction which is not parallel to its initial plane. Hussain *et al.* [66] obtained an elasticity solution for a straight main crack and a branch crack extended at an arbitrary angle, and computed the energy release rate in the limit as the propagation branch vanishes. The energy

153

release rate is given by [66]

$$\mathcal{G}(\theta) = \frac{4}{E^*_{\text{tip}}} \left(\frac{1}{3 + \cos^2 \theta} \right)^2 \left(\frac{1 - \pi/\theta}{1 + \pi/\theta} \right)^{\theta/\pi}$$
$$\times \left[(1 + 3\cos^2 \theta) K_I^2 + 8\sin\theta\cos\theta K_I K_{II} + (9 - 5\cos^2 \theta) K_{II}^2 \right]. \qquad (5.3)$$

Then the crack initiation angle θ_0 is obtained from

$$\partial \mathcal{G}(\theta)/\partial \theta = 0 \quad \Rightarrow \quad \theta = \theta_0. \qquad (5.4)$$

Once the crack initiation angle is determined, the crack initiation condition is given by

$$\mathcal{G}(\theta_0) = \mathcal{G}_{\text{cr}}, \qquad (5.5)$$

where $\mathcal{G}_{\text{cr}}$ is critical energy release rate given by

$$\mathcal{G}_{\text{cr}} = \frac{K_{Ic}^2}{E^*_{\text{tip}}}. \qquad (5.6)$$

5.6   Numerical examples

Fracture analysis and crack propagation are conducted using the FEM code I-FRANC2D. The geometry is discretized with isoparametric graded elements [76]. The specific elements used consist of singular quarter-point six-node triangles (T6qp) for crack-tip discretization, eight-node serendipity elements (Q8) for a circular region around crack-tip elements, and regular six-node triangles (T6) (see Appendix A.5) in a transition zone to Q8 elements. For the calculation of SIFs by means of the interaction integral, the domain involving 12 sectors (S12) and 4 rings (R4) is used at each step of crack propagation. Quasi-static automatic crack propagation in FGMs are performed in the following examples:

(1) A crack in a beam subjected to four-point bending

(2) A crack in a beam subjected to three-point bending

(3) A crack in a beam with holes subjected to three-point bending

(4) A crack in a double cantilever beam under non-proportional loading

154

(5) Two cracks emanating from holes in a plate under tension

(6) Forked cracks in a plate under tension

In order to validate the numerical results against available experimental results, the experimental data reported by Rousseau and Tippur [123] are adopted. The first example involves mixed-mode crack propagation in a graded glass/epoxy beam under four-point loading. The second example is based on the experimental and numerical investigation on a homogeneous polymethyl-methacrylate (PMMA) three-point bending beam performed by Galvez *et al.* [42], and it is extended to a graded beam. The third example investigates a crack in a beam with three holes under three-point bending. The fourth example is based on polymethyl-methacrylate (PMMA) double cantilever beam subjected to non-proportional loading performed by Galvez *et al.* [42], and it is also extended to a graded specimen. The fifth examples investigates the interaction between two cracks in homogeneous and graded plates, and the last example investigates forked crack extending from the existing crack. For the last three examples, material variations for the FGM specimen are adopted from the experiments by Rousseau and Tippur [123]. The first example uses the maximum hoop stress [36] and maximum energy release rates [66] criteria, and compares results for crack trajectories obtained by the two criteria, and the rest of examples use the maximum energy release rates criterion [66].

5.6.1 A crack in a graded glass/epoxy beam subjected to four-point bending

Rousseau and Tippur [123] investigated crack growth behavior of a crack normal to the material gradient in a graded glass/epoxy subjected to four-point bending, and applied displacement controlled loading at a cross-head speed of 0.25 mm/min using Instron Universal Testing Machine. The FGM beam was made of solid A-glass spheres of mean diameter 42μm dispersed within a slow curing epoxy matrix, and was fabricated by using gravity assisted casting technique with two-part slow curing epoxy and uncoated solid glass sphere fillers.

Figure 5.7(a) shows specimen geometry and BCs considering three independent cracks A, B, and C, which are located at ξ=0.17, 0.58, and 1.00, respectively, Figure 5.7(b) shows the complete mesh configurations for the three cracks, and Figure 5.7(c) shows mesh detail using 12 sectors (S12) and 4 rings (R4) around the crack tip.

155

The typical mesh discretization consists of 1067 Q8, 155 T6, and 12 T6qp elements, with a total of 1234 elements and 3725 nodes. The following data are used for the FEM analyses:

plane stress, 2×2 Gauss quadrature,

$$a/W=0.25, \ t=6 \text{ mm}, \ P=P_{cr}(a + n\Delta a, \boldsymbol{X}), \tag{5.7}$$

where n refers to the number of crack propagation increments, and $\boldsymbol{X} = (X_1, X_2)$.

Figures 5.8 and 5.9 illustrate variations of Young's modulus E and Poisson's ratio ν, and fracture toughness K_{Ic} in the graded material region, respectively. The numerical values of material properties at interior points in the graded region are illustrated in Table 5.1.

Table 5.1: Example 1: Material properties (Young's modulus E, Poisson's ratio ν, and fracture toughness K_{Ic}) at interior points in the graded region.

ξ	E (MPa)	ν	K_{Ic} (MPa $\sqrt{m}$)
0.00	3000	0.35	1.2
0.17	3300	0.34	2.1
0.33	5300	0.33	2.7
0.58	7300	0.31	2.7
0.83	8300	0.30	2.6
1.00	8600	0.29	2.6

Due to the lack of information on the critical load P_{cr} and load history in the paper by Rousseau and Tippur [123], here the critical load is calculated at each step based on a fracture criterion, i.e. maximum hoop stress criterion, and applied the calculated critical load to the corresponding step. Notice that there is no effect of the load magnitude on the crack trajectory within the framework of linear elastic analysis. Table 5.2 shows critical load P_{cr}, SIFs, and the phase angle ($\psi = tan^{-1}(K_{II}/K_I)$) at the initial step considering the three crack locations ξ=0.17, 0.58, and 1.00. As ξ increases, the mode-mixity (K_{II}/K_I) decreases.

Table 5.2: Example 1: Numerical results for the critical load P_{cr}, SIFs, and phase angle ($\psi = tan^{-1}(K_{II}/K_I)$) at the initial step considering the three crack locations: ξ=0.17, 0.58, and 1.00 (($\sigma_{\theta\theta}$)max criterion.

ξ	P_{cr} (N)	K_I (MPa $\sqrt{m}$)	K_{II} (MPa $\sqrt{m}$)	$\psi = tan^{-1}(K_{II}/K_I)$
0.17	249.3	2.088	-0.127	-3.480
0.58	298.0	2.695	-0.094	-1.997
1.00	289.9	2.598	-0.013	-0.286

Figures 5.10(a), 5.10(b), and 5.10(c) show experimental results reported by Rousseau and Tippur [123] for crack trajectories and crack initiation angles (θ_0) of the crack located at ξ=0.17, ξ=0.58, and ξ=1.00, respectively. Figures 5.11(a), 5.11(b), and 5.11(c) show present numerical results for crack trajectories and crack initiation angles (θ_0) of the crack located at ξ=0.17, ξ=0.58, and ξ=1.00, respectively. The numerical results are obtained by considering maximum hoop stress criterion and crack increment $\Delta a = 1$mm. There is reasonable agreement in crack initiation angles and crack trajectories between numerical and experimental results.

Figure 5.12 shows finite element discretization and remeshing for intermediate steps of crack propagation considering the crack located at $\xi = 0.17$ and $\Delta a = 1$mm. One can observe that local mesh refinement is done around the crack tip at each step.

In order to investigate the effect of crack location on crack trajectory, cracks located at various locations in a graded beam are investigated. Figure 5.13 shows numerical results for crack trajectories and crack initiation angles (θ_0) considering various crack locations ($0 \leq \xi \leq 1$) and $\Delta a = 1$mm. Notice that, as the crack location changes from $\xi = 0.0$ to $\xi = 1.0$, the crack initiation angle θ_0 increases up to about 6.98° at $\xi = 0.17$, and then decreases. For homogeneous beam with the crack $\xi = 0.5$, the crack initiation angle is zero because of symmetry, but, for a graded beam investigated here, it is nonzero.

In order to compare the two fracture criteria, i.e. $(\sigma_{\theta\theta})_{\text{max}}$ and $(\mathcal{G})_{\text{max}}$ criteria, Figure 5.14 shows comparison of crack trajectories obtained by using between maximum hoop stress [36] and maximum energy release rates [66] criteria. There is not much difference in crack trajectories. Moreover, the crack initiation angles at the initial step obtained by maximum hoop stress [36] and maximum energy release rates [66] criteria are $\theta_0 = 6.98°$ and $\theta_0 = 7.64°$, respectively.
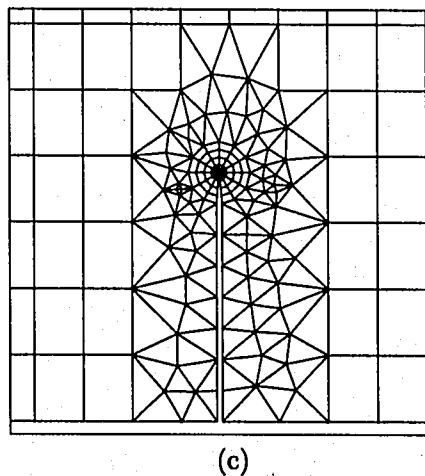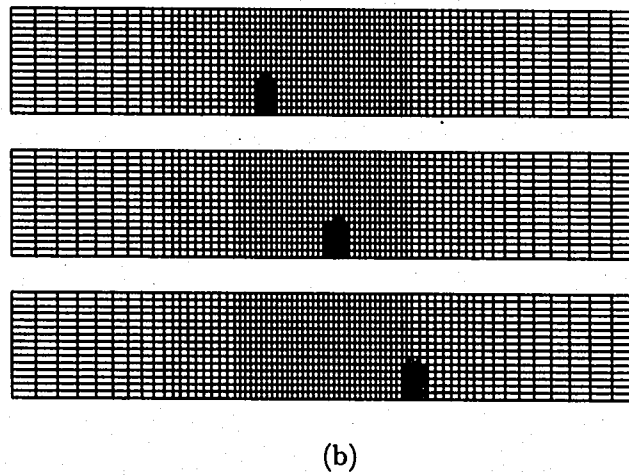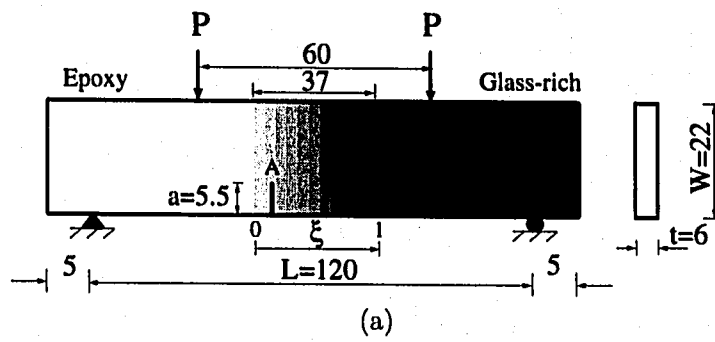
Figure 5.7: Example 1: A crack in a graded glass/epoxy beam subjected to four-point bending: (a) geometry, boundary conditions, and three independent cracks A (ξ=0.17), B (ξ=0.58) and C (ξ=1.00) (Units:N, mm); (b) the complete mesh configurations for cracks A, B, and C; (c) mesh detail using 12 sectors (S12) and 4 rings (R4) around the crack tip.
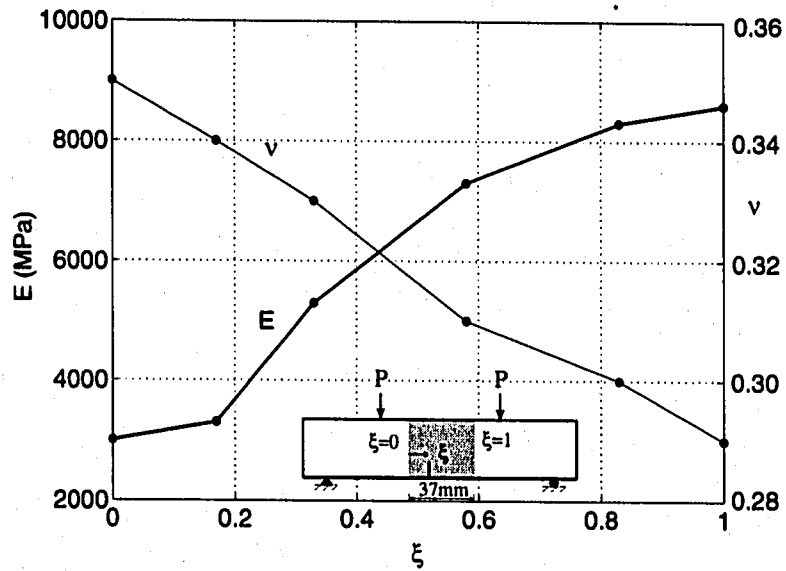
Figure 5.8: Example 1: Variations of Young's modulus E (MPa) and Poisson's ratio ν along the graded region ($0 \leq \xi \leq 1$).
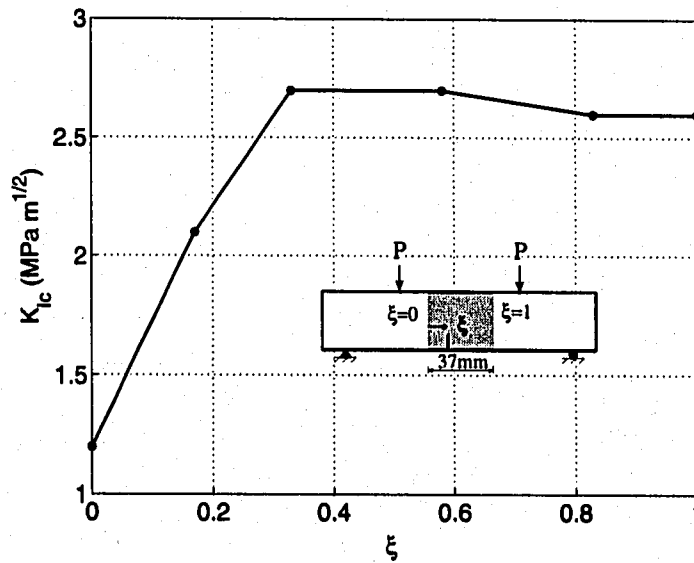
Figure 5.9: Example 1: Variation of fracture toughness K_{Ic} (MPa$\sqrt{m}$) along the graded region ($0 \leq \xi \leq 1$).

159
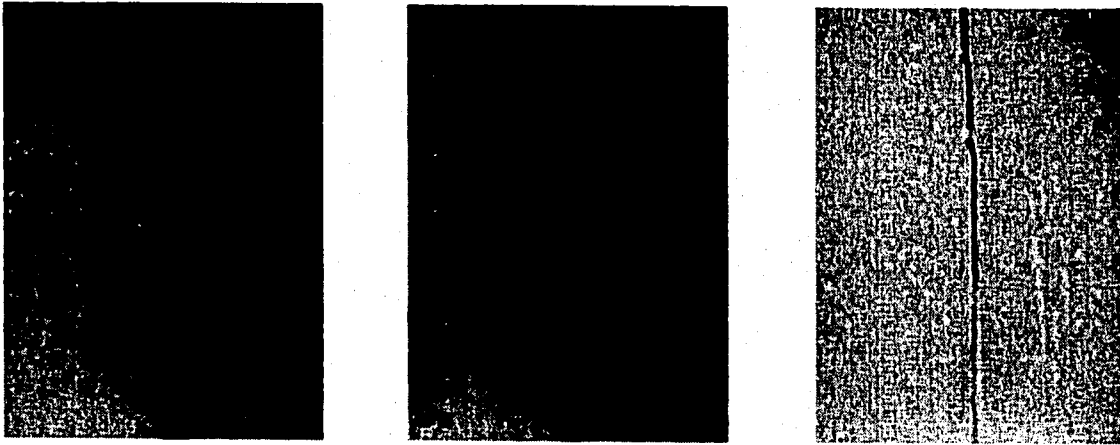
(a) ξ=0.17 ($\theta_0 = 7°$)   (b) ξ=0.58 ($\theta_0 = 4°$)   (c) ξ=1.00 ($\theta_0 = 0.5°$)

Figure 5.10: Example 1: Experimental results for crack trajectories and crack initiation angles (θ_0) of the crack in an FGM beam reported by Rousseau and Tippur [123]: (a) ξ=0.17; (b) ξ=0.58; (c) ξ=1.00.
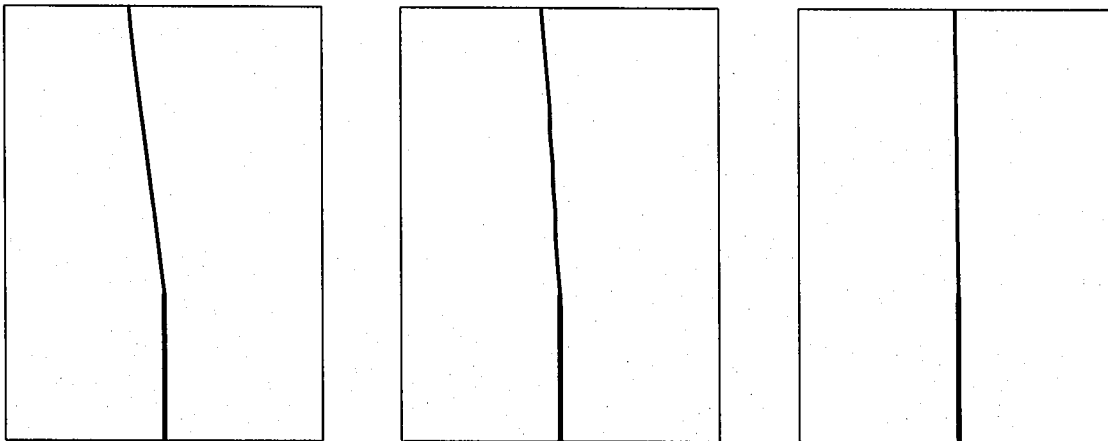
(a) ξ=0.17 ($\theta_0 = 6.98°$)   (b) ξ=0.58 ($\theta_0 = 4.01°$)   (c) ξ=1.00 ($\theta_0 = 0.59°$)

Figure 5.11: Example 1: Numerical results for crack trajectories and crack initiation angles (θ_0) of the crack in an FGM beam (($\sigma_{\theta\theta}$)max criterion): (a) ξ=0.17; (b) ξ=0.58; (c) ξ=1.00.
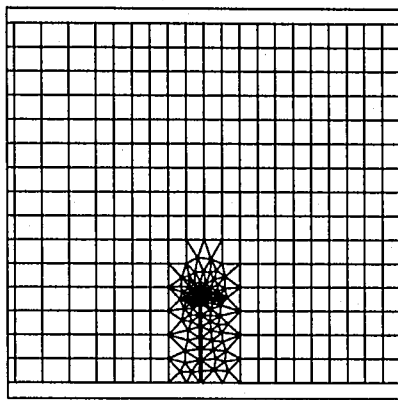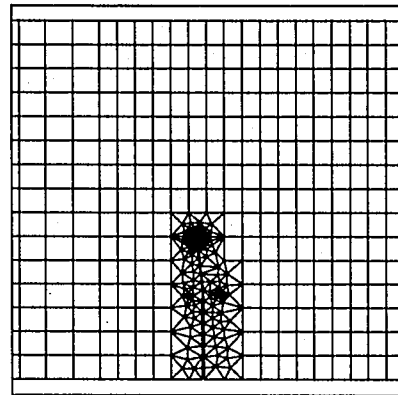
(a) Initial step

(b) Step 3
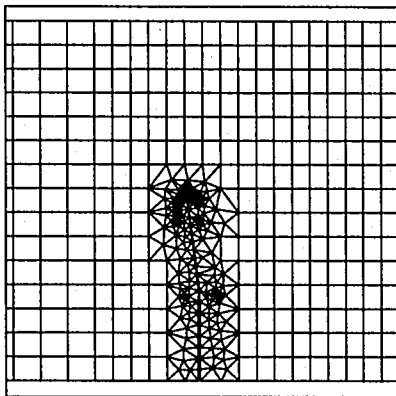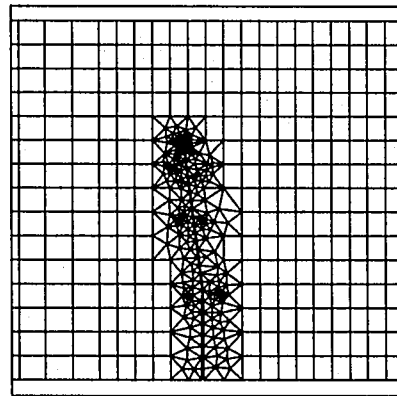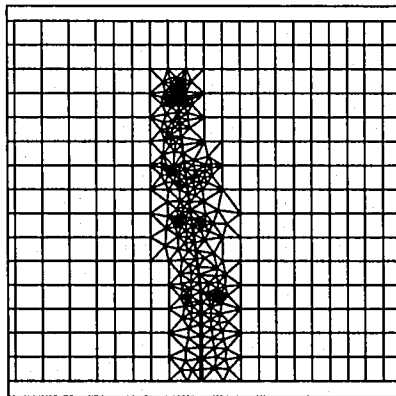
(c) Step 6
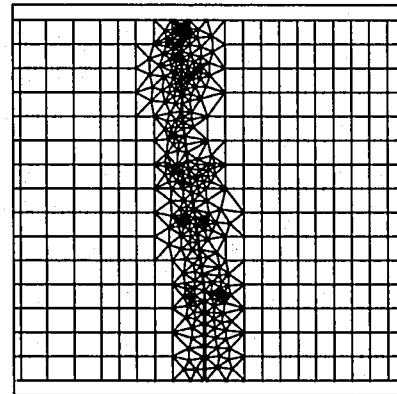
(d) Step 9

(e) Step 12

(f) Step 16

Figure 5.12: Example 1: finite element discretization and remeshing on each step of crack propagation considering $\xi = 0.17$ and $\Delta a = 1\text{mm}$ ($(\sigma_{\theta\theta})\text{max}$ criterion): (a) Initial step; (b) Step 3; (c) Step 6; (d) Step 9; (e) Step 12; (f) Step 16.

(a) ξ=0.00 ($\theta_0 = 0.22°$)   (b) ξ=0.10 ($\theta_0 = 4.45°$)   (c) ξ=0.17 ($\theta_0 = 6.98°$)

(d) ξ=0.40 ($\theta_0 = 6.76°$)   (e) ξ=0.50 ($\theta_0 = 5.33°$)   (f) ξ=0.58 ($\theta_0 = 4.01°$)

(g) ξ=0.80 ($\theta_0 = 1.68°$)   (h) ξ=1.00 ($\theta_0 = 0.59°$)
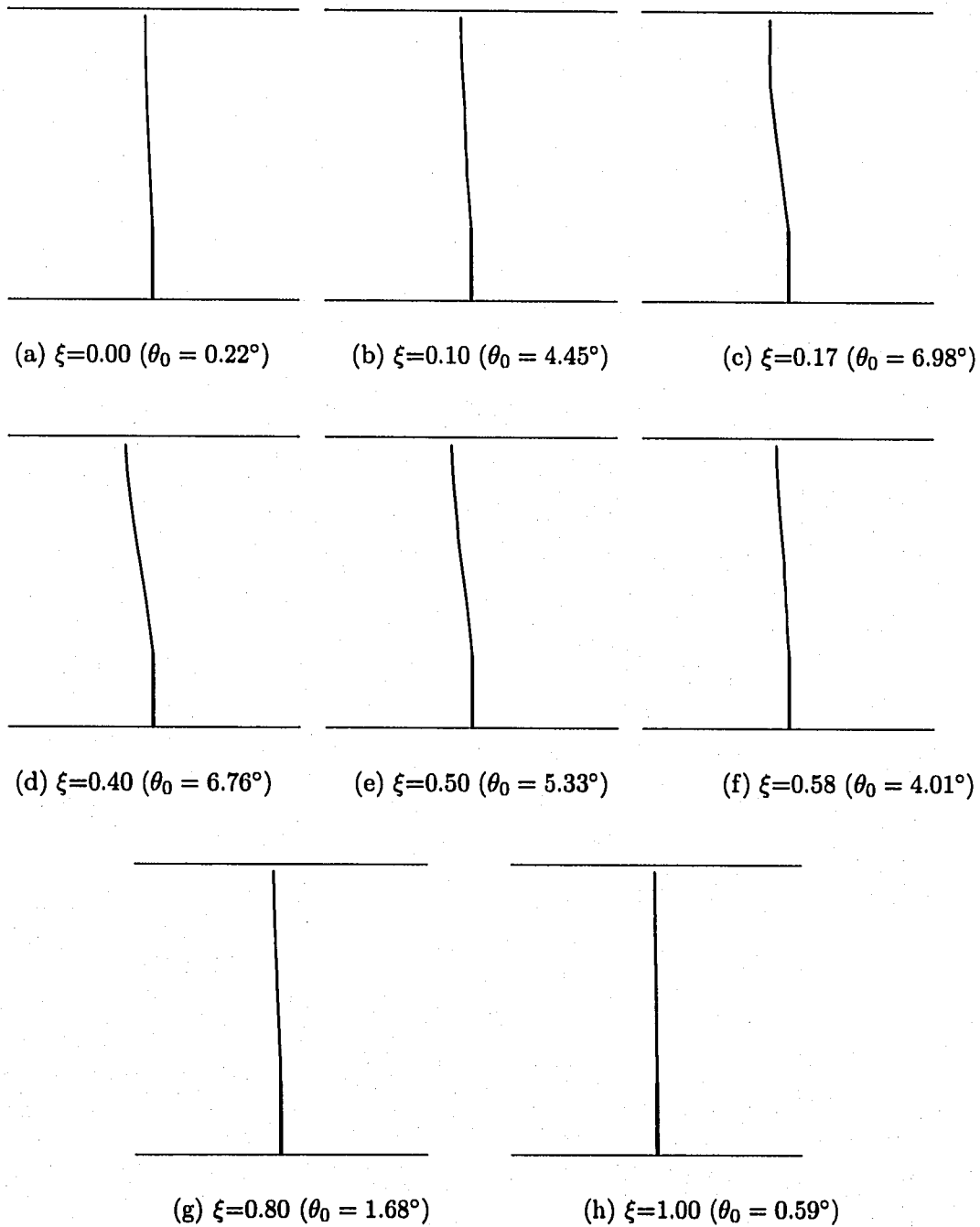
Figure 5.13: Example 1: Numerical results for crack trajectories and crack initiation angles (θ_0) of the crack in an FGM beam considering $\Delta a = 1mm$ for all the steps (($\sigma_{\theta\theta}$)max criterion): (a) ξ=0.00; (b) ξ=0.10; (c) ξ=0.17; (d) ξ=0.40; (e) ξ=0.50; (f) ξ=0.58; (g) ξ=0.80; (h) ξ=1.00.
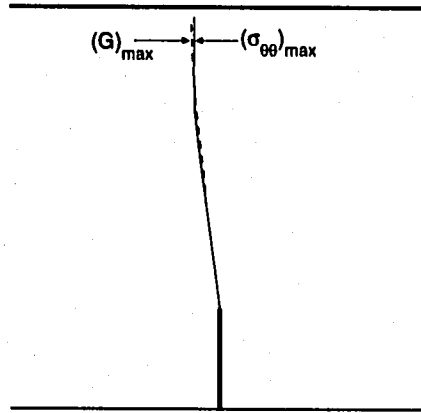
Figure 5.14: Example 1: comparison of crack trajectories obtained by using between maximum hoop stress [36] and maximum energy release rates [66] criteria. The crack initiation angles at the initial step obtained by maximum hoop stress [36] ($(\sigma_{\theta\theta})$max criterion) and maximum energy release rates [66] ($(\mathcal{G})$max criterion) criteria are $\theta_0 = 6.98°$ and $\theta_0 = 7.64°$, respectively.

5.6.2 A crack in a beam subjected to three-point bending

Galvez *et al.* [42] investigated crack growth behavior of a crack in a homogeneous PMMA beam subjected to three-point bending considering three different loading controls such as crack tip opening displacement (CMOD), displacement, and load (P). The material properties of the PMMA beam used are as follows:

$$E = 2890 \text{ MPa}, \quad \nu = 0.4, \quad K_{Ic} = 1.09 \text{ MPa}\sqrt{m}. \tag{5.8}$$

In this example, both homogeneous and graded (along the X_2 direction) beams are considered. Figures 5.15(a) and 5.15(b) show specimen the geometry and BCs for two different boundary conditions: Cases 1 and 2, respectively, Figure 5.15(c) shows the complete mesh configuration, and Figure 5.15(d) shows mesh detail using 12 sectors (S12) and 4 rings (R4) around the crack tip. Notice that the mesh of Figure 5.15(c) is valid for both cases, but the boundary conditions change.
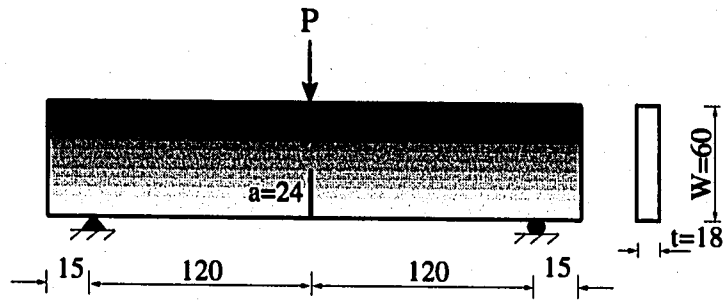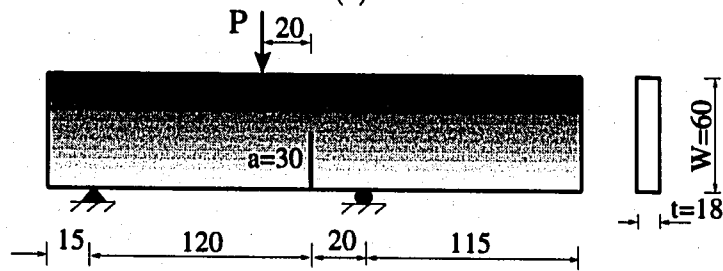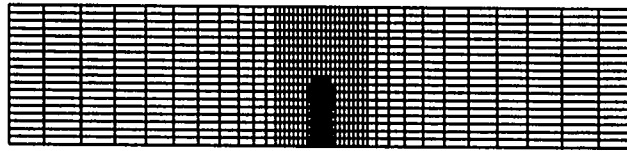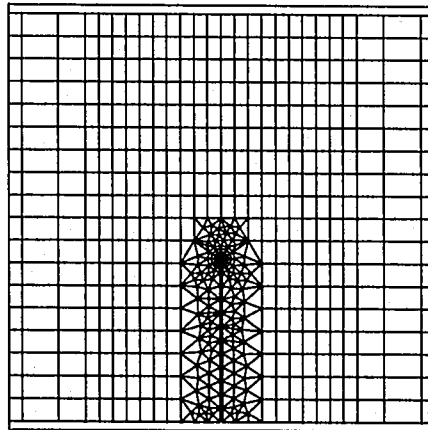
Figure 5.15: Example 2: A crack in a beam subjected to three-point bending: (a) **Case 1**: geometry and boundary conditions (Units:N, mm); (b) **Case 2**: geometry and boundary conditions (Units:N, mm); (c) the complete mesh configuration; (d) mesh detail using 12 sectors (S12) and 4 rings (R4) around the crack tip.

The mesh discretization consists of 741 Q8, 239 T6, and 12 T6qp elements, with a total of 992 elements and 2875 nodes. The following data are used for the FEM analyses:

$$\text{plane stress, } 2 \times 2 \text{ Gauss quadrature,}$$

$$\text{a/W=0.4, t=18 mm, } P=P_{cr}(a + n\Delta a, X). \tag{5.9}$$

For the homogeneous beam, the material properties of PMMA given by expressions (5.8) are used. For the graded beam, linear variations of Young's modulus, Poisson's ratio, and fracture toughness, and these properties at the end points are used and given in Table 5.3.

Table 5.3: Example 2: Material properties (Young's modulus E, Poisson's ratio ν, and fracture toughness K_{Ic}) at the end points in the graded region. The material gradation varies linearly in between the end points. The material properties at the middle point ($X_2 = 30$mm) are the same as those for the homogeneous PMMA beam.

X_2(mm)	E (MPa)	ν	K_{Ic} (MPa $\sqrt{m}$)
0	1780	0.41	0.99
60	4000	0.39	1.19

All the numerical results are obtained using the maximum energy release rates criterion [66]. Figure 5.16 shows comparison of crack trajectories for a homogeneous PMMA beam obtained by the present numerical simulation with experimental (averaging) results reported by Galvez et al. [42] for **Case 2**. The numerical results are obtained by considering $\Delta a = 1.5$mm (constant) and twenty-two steps including the initial step. There is reasonably good agreement between numerical and experimental results. Figure 5.17 shows comparison of crack trajectories for a homogeneous PMMA beam with those for a graded beam obtained by the present numerical simulation for **Case 2** considering $\Delta a = 1.5$mm and twenty-two steps including the initial step. Notice that, in this case, the material gradation has almost no effect in the crack trajectory.

Figure 5.18 shows comparison of load versus CMOD curve for a homogeneous beam with that for a graded beam obtained by the present numerical simulation for **Case 1** (mode I cracking) considering $\Delta a = 1.5$mm. As expected, the linear relationship between load and CMOD is observed up to the initial step. Notice that the critical load (P_{cr}) and corresponding CMOD at the initial step for the FGM are greater than those for the homogeneous beam. This indicates that the crack initiation is delayed due to material gradation.

165
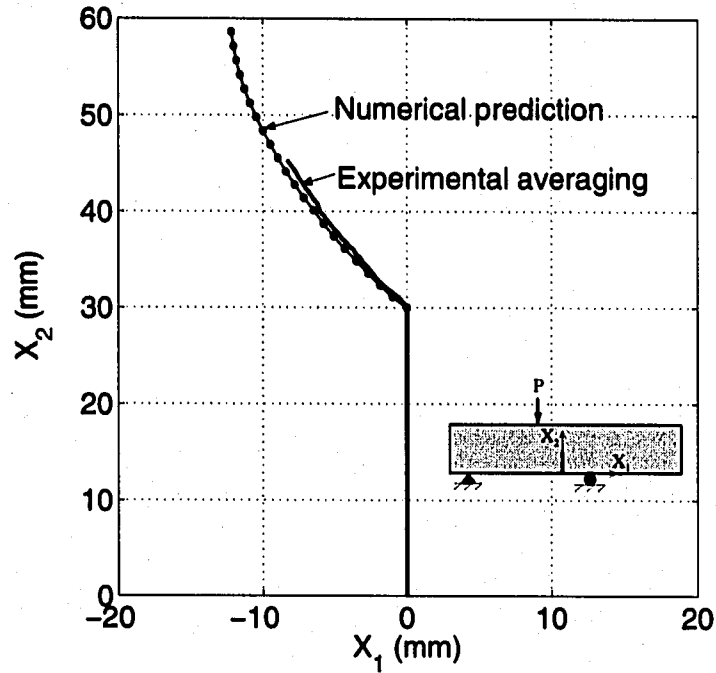
Figure 5.16: Example 2, Case 2: comparison of crack trajectories for homogeneous PMMA beam obtained by the present numerical simulation with experimental (averaging) results reported by Galvez *et al.* [42]. The numerical results are obtained considering $\Delta a = 1.5$mm (constant).

Figure 5.19 shows comparison of load versus CMOD curve for a homogeneous beam with that for a graded beam obtained by the present numerical simulation for **Case 2** (mixed-mode cracking), which also considers $\Delta a = 1.5$mm. Notice that the critical load (P_{cr}) and corresponding CMOD for the FGM at the initial step are also greater than those for the homogeneous beam. By comparing Figures 5.18 and 5.19, one can observe that, for both homogeneous and graded beams, the critical load (P_{cr}) for **Case 2** is over twice as much as that for **Case 1**.

Figure 5.20(a) shows finite element discretization and remeshing for the final step of crack propagation considering $\Delta a = 1.5$mm for both homogeneous and graded beams of Case 1. Notice that the crack grows vertically because of symmetry. Figure 5.20(b) shows finite element discretization and remeshing for the final step of crack propagation considering $\Delta a = 1.5$mm for the homogeneous beam of **Case 2**. The final mesh for the FGM beam is almost identical to the Figure 5.20(b).
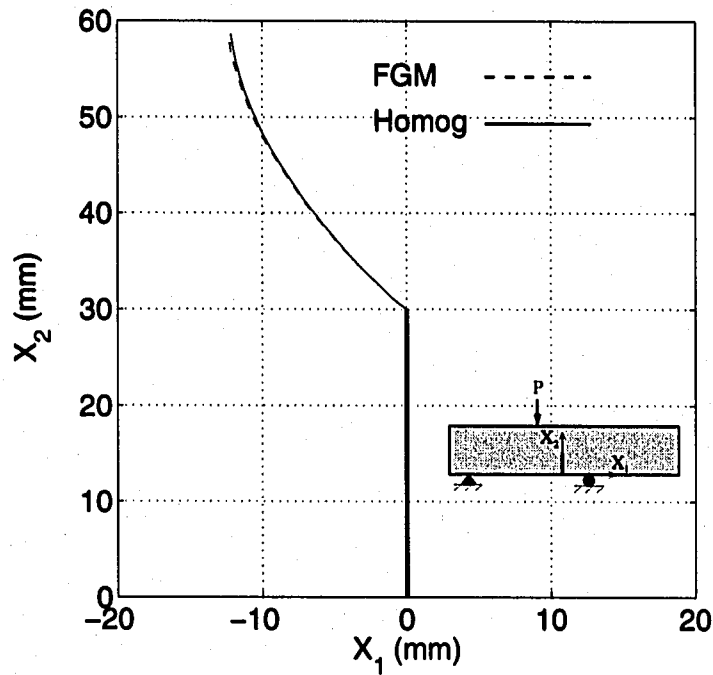
Figure 5.17: Example 2, Case 2: comparison of crack trajectories for a homogeneous beam with those for a graded beam obtained by the present numerical simulation. The numerical results are obtained considering $\Delta a = 1.5$mm (constant).
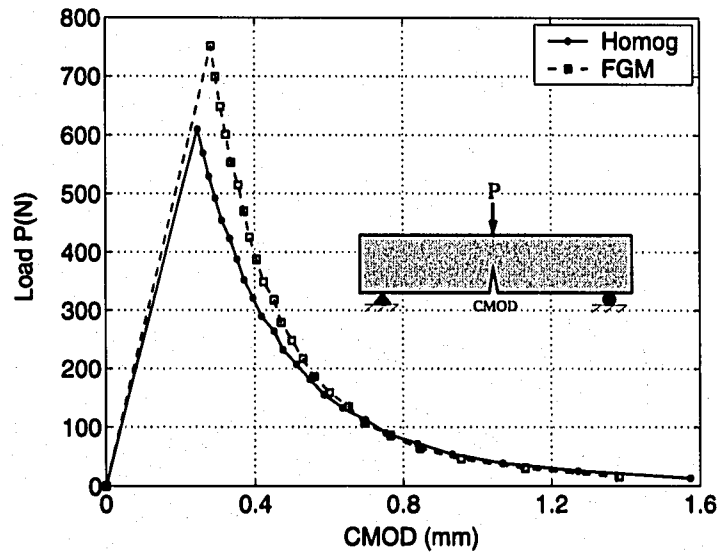
Figure 5.18: Example 2, Case 1: comparison of P-CMOD curve for a homogeneous beam with that for a graded beam obtained by the present numerical simulation. The numerical results are obtained considering $\Delta a = 1.5$mm (constant).
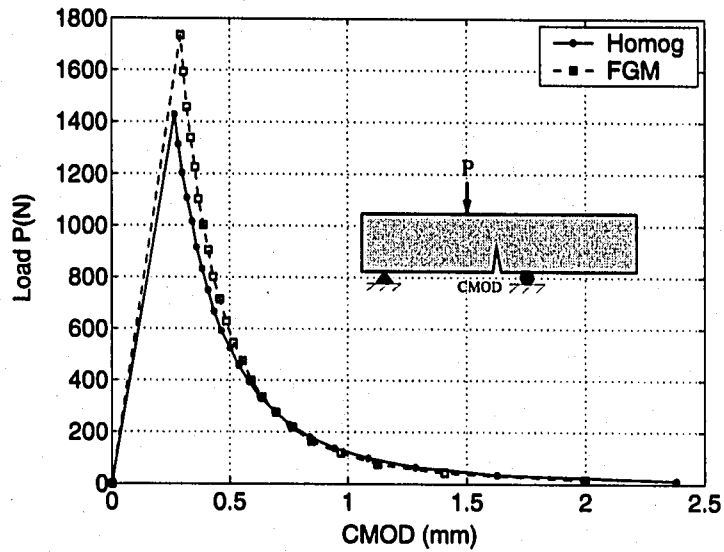
Figure 5.19: Example 2, Case 2: comparison of P-CMOD curve for a homogeneous beam with that for a graded beam obtained by the present numerical simulation. The numerical results are obtained considering $\Delta a = 1.5$mm (constant).

(a)   (b)
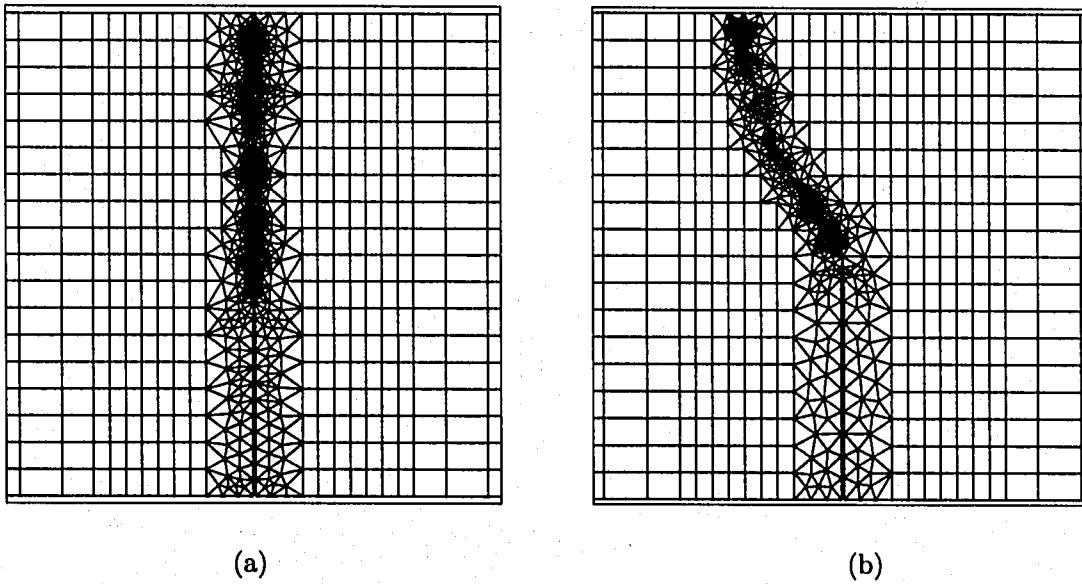
Figure 5.20: Example 2: finite element discretization and remeshing considering $\Delta a = 1.5$mm: (a) Case 1: Homogeneous and FGM beams; (b) Case 2: Homogeneous beam; the final mesh for the FGM beam is almost identical to this one (cf. Figure 5.17).

168

5.6.3 A crack in a beam with holes subjected to three-point bending

Bittencourt *et al.* [12] performed experimental and numerical investigation of a crack in a homogeneous PMMA beam with three holes subjected to three-point bending. The material properties of the homogeneous PMMA beam is as follows:

$$E = 1, \ \nu = 0.3, \ K_{Ic} = 1.0. \tag{5.10}$$

In this example, both homogeneous and graded beams are considered. Figures 5.21(a) and 5.21(b) show specimen geometry and BCs, and the complete mesh configuration, respectively, and Figure 5.21(c) shows mesh detail using 12 sectors (S12) and 4 rings (R4) around the crack tip.

The mesh discretization consists of 680 Q8, 145 T6, and 12 T6qp elements, with a total of 837 elements and 2490 nodes. The following data are used for the FEM analyses:

$$\text{plane stress, } 2 \times 2 \text{ Gauss quadrature,}$$
$$\text{a/W=0.1875, t=1, P=1.} \tag{5.11}$$

For the homogeneous beam, the material properties of PMMA given by the expressions in (5.10) are used. For the middle region of the graded beam, linear variations of Young's modulus, Poisson's ratio, and fracture toughness are used and shown in Figures 5.22 and 5.23, respectively.

All the numerical results are obtained using the maximum energy release rates criterion [66]. Figure 5.24(a) shows comparison of crack trajectories obtained by the present numerical results for the homogeneous beam with experimental results reported by Bittencourt *et al.* [12]. The numerical results are obtained by considering Δa=0.3 and 12 steps. There is excellent agreement between numerical and experimental results. Figure 5.24(b) shows comparison of crack trajectories obtained by the present numerical results for the graded beam with those for the homogeneous beam. The numerical results are obtained by considering Δa=0.3 and 11 steps. As one would expect, there is significant difference in crack trajectories. Note that, for the FGM beam, Young's modulus on the left-hand side is less than that on the right-hand side. Thus the crack growth direction is naturally inclined to the left.

Figures 5.25(a) and 5.25(b) show finite element discretization and remeshing for the final step

169
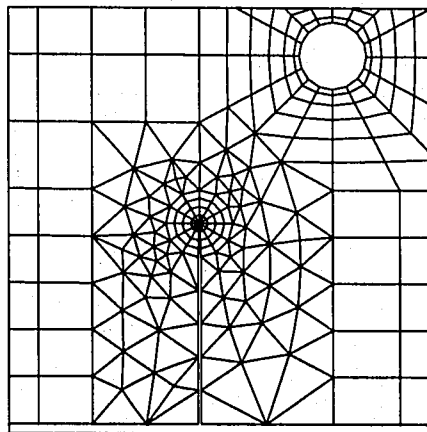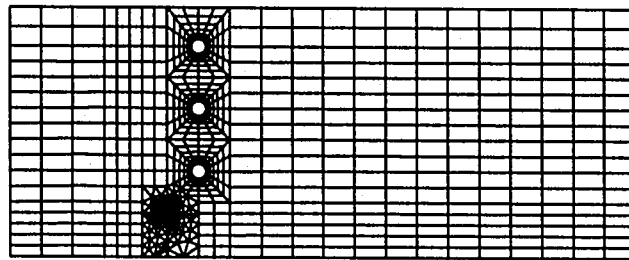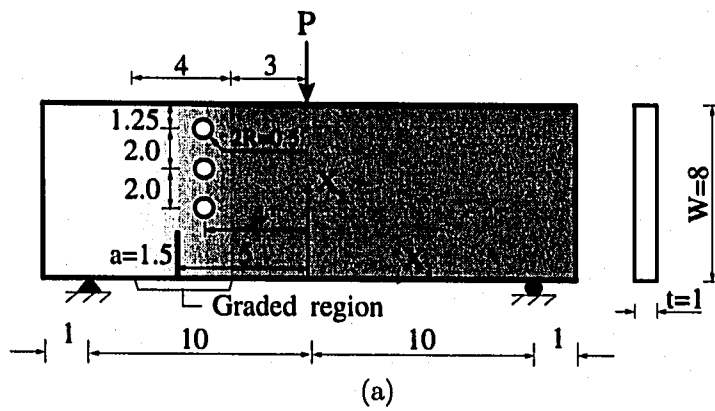
Figure 5.21: Example 3: A crack in a beam with three holes subjected to three-point bending: (a) geometry, boundary conditions; (b) the complete mesh configuration; (c) mesh detail using 12 sectors (S12) and 4 rings (R4) around the crack tip.

170
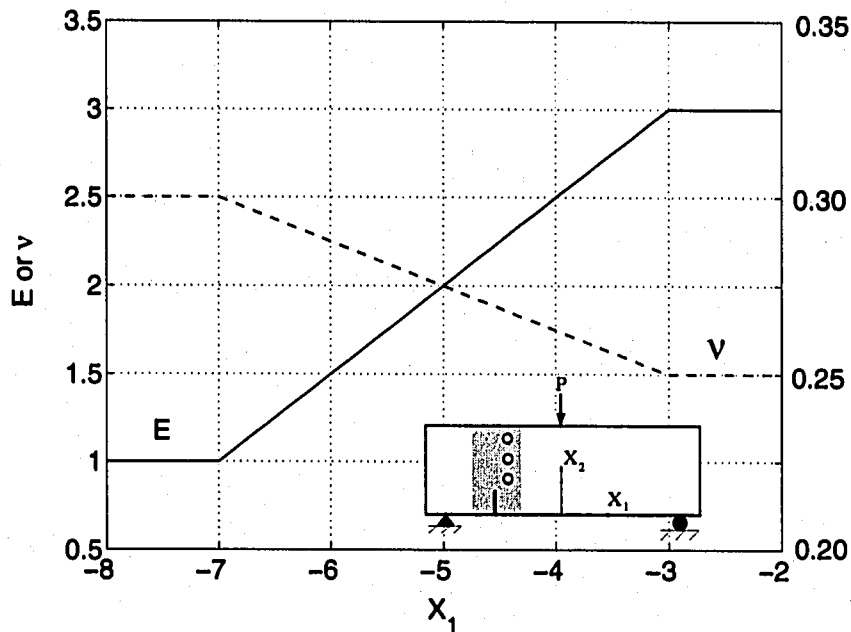
Figure 5.22: Example 3: Variations of Young's modulus E and Poisson's ratio ν in the three regions.
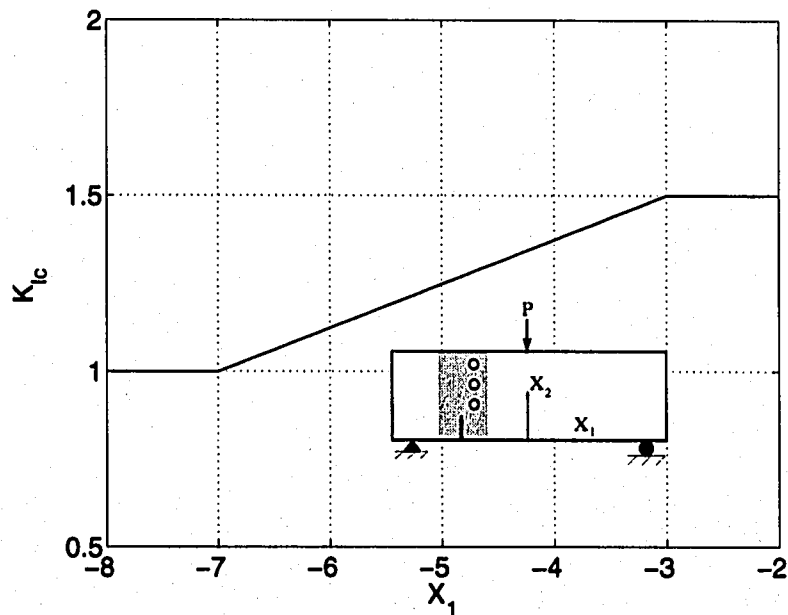
Figure 5.23: Example 3: Variations of fracture toughness K_{Ic} in the three regions.

of crack propagation considering $\Delta a = 0.3$ for both homogeneous and graded beams, respectively. Figures 5.25(c) and 5.25(d) show the contour plots for the maximum principal stress for the homogeneous and graded beams.

Figure 5.26 shows SIFs history for both homogeneous and graded beams with respect to crack
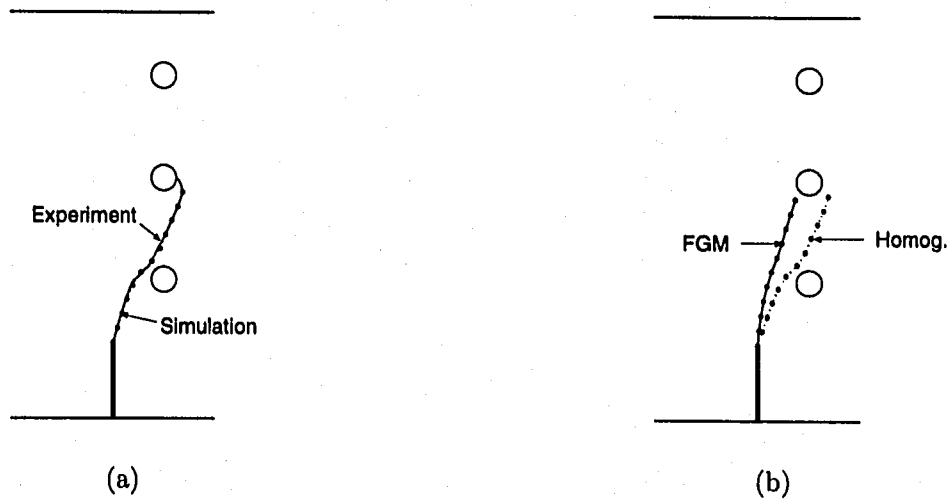
Figure 5.24: Example 3: Comparison of crack trajectories: (a) the present numerical results (dotted line) for the homogeneous beam versus experimental results (solid line) reported by Bittencourt *et al.* [12]. (b) the present numerical results for the graded beam (solid line) versus those for the homogeneous beam. The numerical results are obtained by considering Δa=0.3.

extension (Δa=0.3). There is a monotonic increasing behavior of mode I SIF (K_I) for the FGM beam, however, this behavior is not observed for the homogeneous beam, which shows decreasing SIFs from steps 5 and 6. For the homogeneous beam, this behavior is due to the hole adjacent to the crack. For both homogeneous and graded beams, the mode II SIF K_{II} oscillates around zero thus changing the sign of the crack initiation angles.
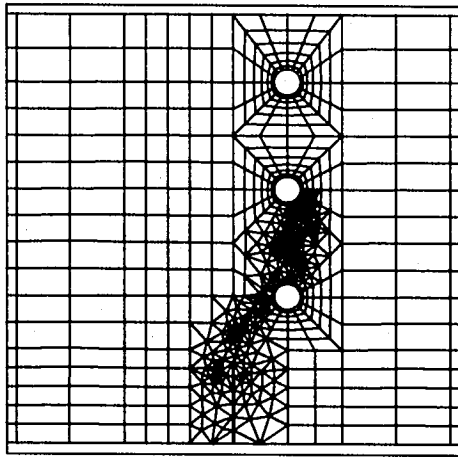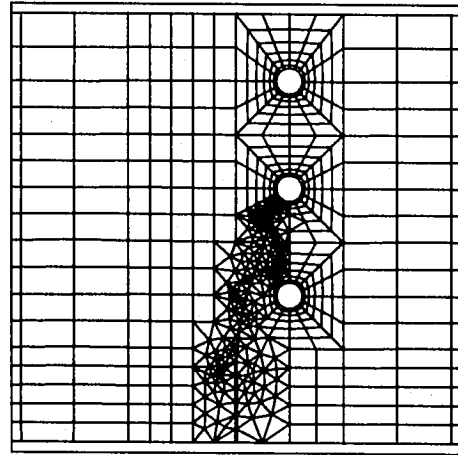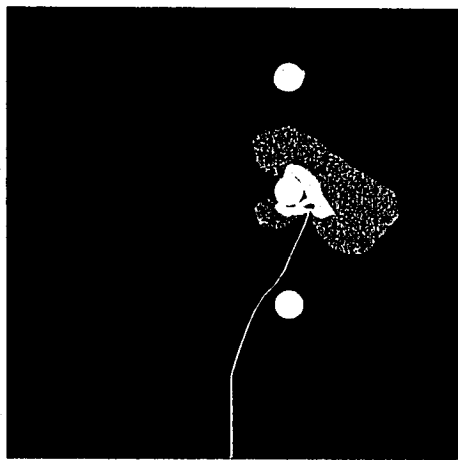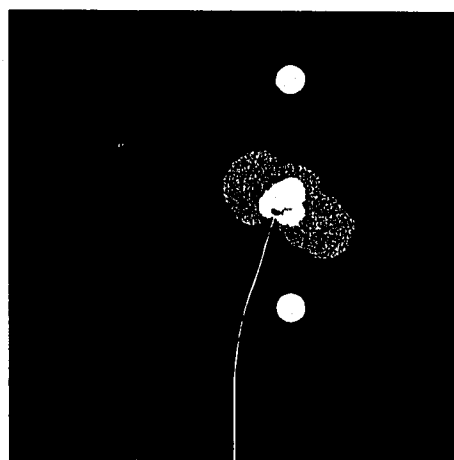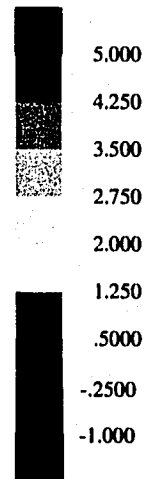
Figure 5.25: Example 3: finite element remeshing considering $\Delta a = 0.3$, and the contour plots of the maximum principal stress: (a) homogeneous beam; (b) graded beam.
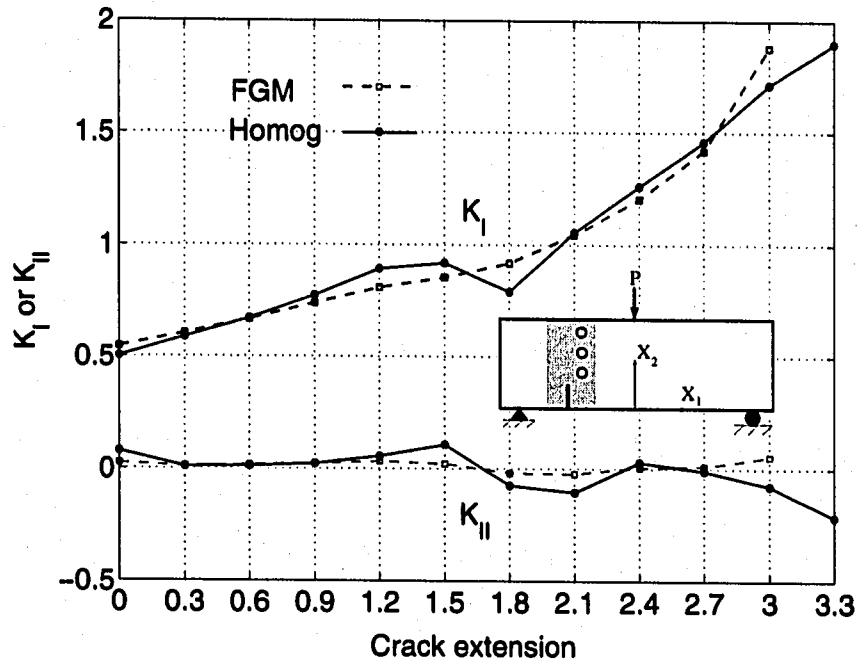
Figure 5.26: Example 3: SIFs history with respect to crack extension ($\Delta a = 0.3$). The twelve and eleven steps are performed for the homogeneous and graded beams, respectively.

5.6.4 A crack in a double cantilever beam under non-proportional loading

This example investigates crack propagation considering non-proportional loading. Let's consider a fracture envelope based on $(\mathcal{G})_{max}$ criterion for a crack subjected to two independent loadings: varying load P_1 and constant load P_2 as shown in Figure 5.27.

The mixed-mode SIFs are denoted by K_I^i and K_{II}^i for the corresponding load P_i $(i = 1, 2)$. Superposition of the two fields $P = P_1 + P_2$ leads to SIFs located at the point A inside a fracture envelope. To achieve critical SIFs at the point B for crack growth, one needs to increase P_1, for instance P_1 to $P_{cr} = P_1 + \Delta P_1$, which results in the increase of the SIFs by $(K_{II}^1/K_I^1) \times \Delta P_1$. This scheme is used to search for the critical load P_{cr} and its corresponding SIFs for non-proportional loading at each step of crack propagation.

Galvez et al. [42] performed experimental and numerical investigations on crack growth behavior of a crack in a double cantilever PMMA beam subjected to non-proportional loading. The material properties of the PMMA beam used are the same as those for the second example, and are given

Figure 5.27: Procedure for crack initiation considering non-proportional loading.

in Eq.(5.8). In this example, we consider both homogeneous and graded beams. Figure 5.28(a) shows specimen geometry and BCs, Figure 5.28(b) shows the complete mesh configuration, and Figure 5.28(c) shows mesh detail using 12 sectors (S12) and 4 rings (R4) around the crack tip.

The mesh discretization consists of 2101 Q8, 286 T6, and 12 T6qp elements, with a total of 2399 elements and 6970 nodes. The following data are used for the FEM analyses:

$$\text{plane stress, } 2 \times 2 \text{ Gauss quadrature,}$$

$$\text{a=30mm, t=18 mm, } P=P_{cr}(a + n\Delta a, X), \text{ Q=79.4 N.} \tag{5.12}$$

For the homogeneous beam, the material properties of PMMA given by Eq.(5.8) are used. For the graded beam, variation of material properties from the first example considering the graded region $-15\text{mm} \leq X_2 \leq 15\text{mm}$ corresponds to the graded region $0 \leq \xi \leq 0.81$ in the first example (cf. Figures 5.8 and 5.9). Here two cases (Cases 1 and 2) of material variation are used as shown in Figure 5.36 (cf. Figure 5.7(a)).

All the numerical results are obtained using the maximum energy release rates criterion [66]. Figure 5.30 shows comparison of crack trajectories for homogeneous PMMA double cantilever beam obtained by the present numerical simulation with those for both CMOD-controlled and displacement-controlled experiments performed by Galvez et al. [42]. For the present simulation

175

(a)

(b)

(c)

Figure 5.28: Example 4: A crack in a double cantilever beam: (a) geometry and boundary conditions; (b) the complete mesh configuration; (c) mesh detail using 12 sectors (S12) and 4 rings (R4) around the crack tip.
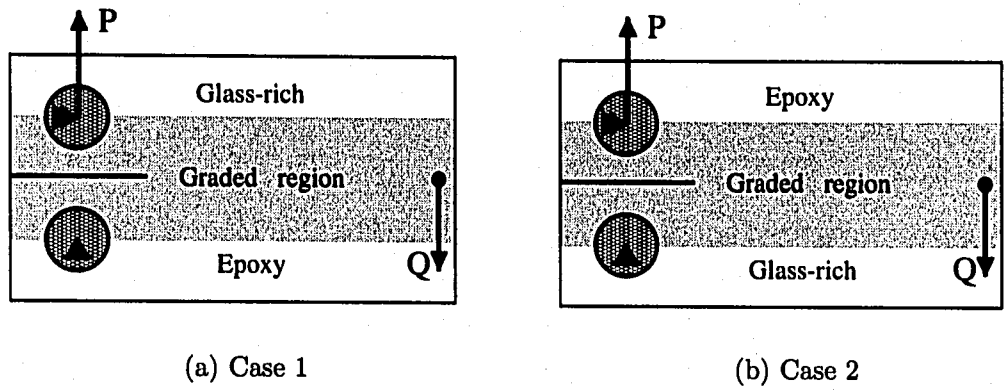
(a) Case 1   (b) Case 2

Figure 5.29: Example 4: two cases of FGM double cantilever beams: (a) Case 1; (b) Case 2. The variations of material properties are adopted from the first example considering the material gradation in the X_2 direction along the region $-15\text{mm} \le X_2 \le 15\text{mm}$ (cf. Figures 5.8 and 5.9).

and the displacement-controlled experiment [42], the load Q=79.4 N is used, however, the load Q=79.9 N is used for CMOD-controlled loading [42]. The present simulation result is similar to the CMOD-controlled experiment result.
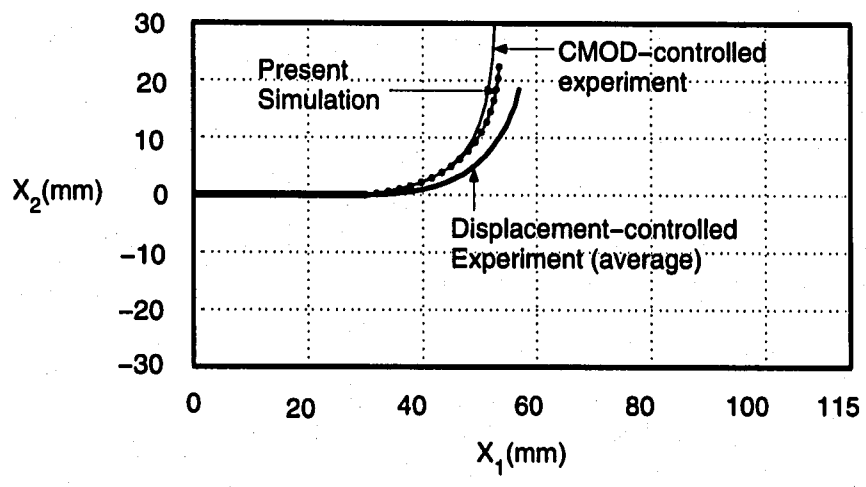
Figure 5.30: Example 4: comparison of crack trajectories for homogeneous PMMA double cantilever beam obtained by the present numerical simulation with those for CMOD-controlled and displacement-controlled experiments performed by Galvez et al. [42]. For the present simulation and the displacement-controlled experiment, the load Q=79.4 N is used, however, the load Q=79.9 N is used for CMOD-controlled loading. The numerical results are obtained by considering $\Delta a = 2.0\text{mm}$.

Figure 5.31 shows comparison of crack trajectories for homogeneous PMMA double cantilever beam obtained by the present numerical simulation with those for the FGM beams (Cases 1 and

2). The variation of Young's modulus shows much influence on crack trajectories. For Case 1, the crack grows to the compliant part of the material, and for Case 2, the crack deflects towards the left side of the crack trajectory for the homogeneous case due to the material variation.
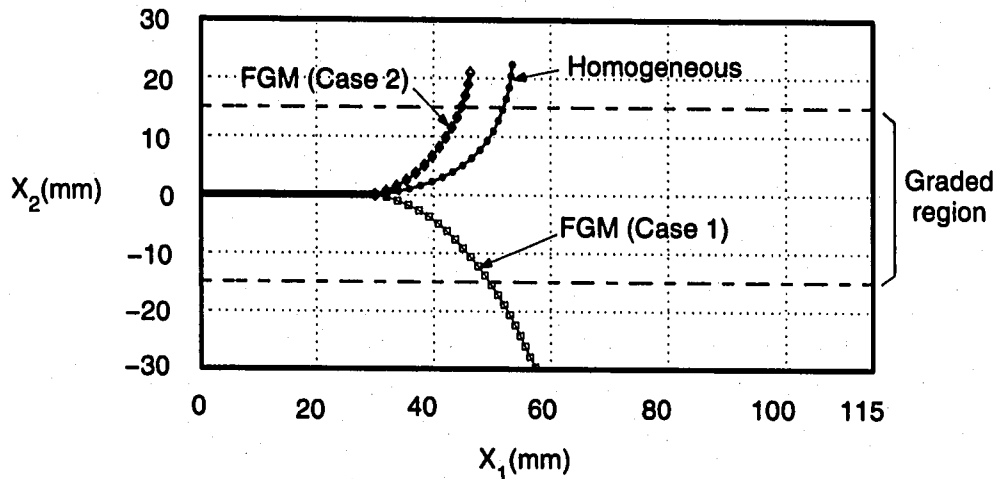
Figure 5.31: Example 4: comparison of crack trajectories for homogeneous PMMA double cantilever beam obtained by the present numerical simulation with those for the FGM beams (Cases 1 and 2). The numerical results are obtained by considering $\Delta a = 2.0$mm.

Figure 5.32 compares load versus CMOD curve for a homogeneous double cantilever beam obtained by the present numerical simulation with that for the FGM cases (Cases 1 and 2) considering $\Delta a = 2.0$mm. As expected, the linear relationship between load and CMOD is observed up to the initial step. Notice that, for the homogeneous case, as the crack grows by Δa, the load P_{cr} decreases and its corresponding CMOD generally shows an increasing behavior; however, for the FGM case, this behavior of CMOD is not observed for steps 9 to 13 in the FGM Case 1 and for steps 8 to 11 in the FGM Case 2 (see Figure 5.32). This is due to the steep gradient of fracture toughness in the graded region (see Figures 5.9 and 5.31). Due to higher fracture toughness in the FGM beams, the critical load P_{cr} at the initial step for the FGM beams is increased, and thus crack initiation is delayed. Figures 5.33, 5.34, and 5.35 show finite element discretization and remeshing for the intermediate and final steps of crack propagation considering $\Delta a = 2$mm for the homogeneous and graded (Cases 1 and 2) beams, respectively.
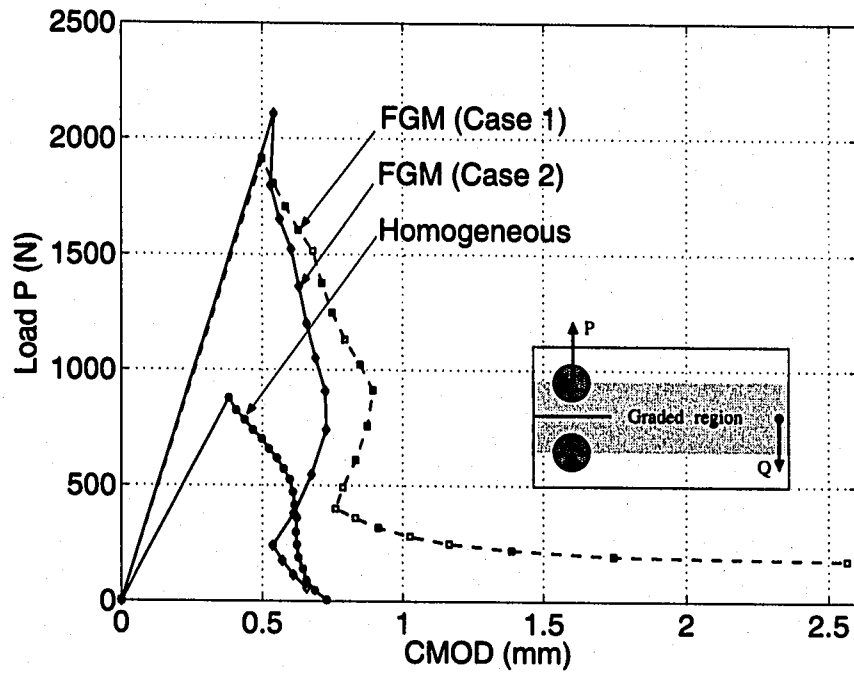
Figure 5.32: Example 4: comparison of load versus CMOD curve for a homogeneous double cantilever beam obtained by the present numerical simulation with those for the FGM beams (Cases 1 and 2). The numerical results are obtained by considering $\Delta a = 2.0$mm and Q=79.4 N.

(a)

(b)
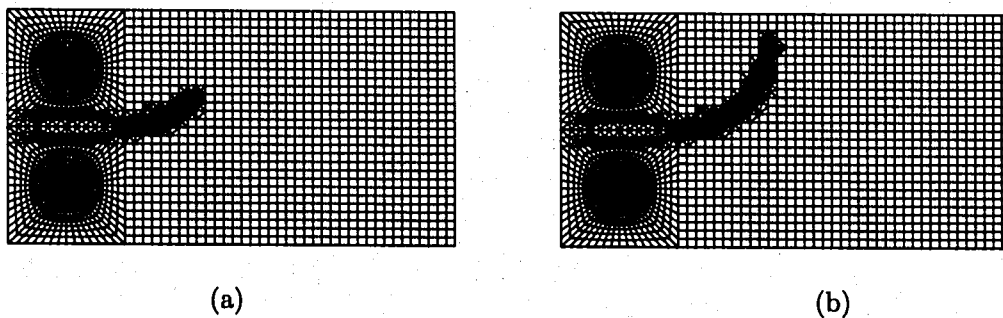
Figure 5.33: Example 4: Representative numerical results for crack trajectories considering the *homogeneous* beam: (a) step 11; (b) step 19 (final step).
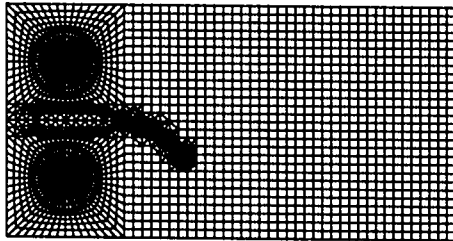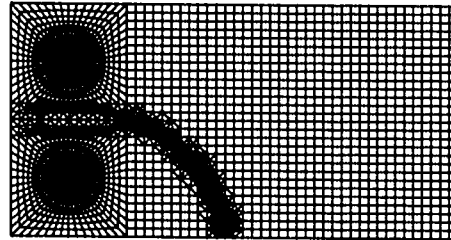
(a)   (b)

Figure 5.34: Example 4: Representative numerical results for crack trajectories considering the *FGM* beam (**Case 1**): (a) step 10; (b) step 20 (final step).
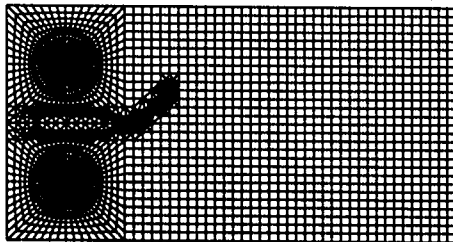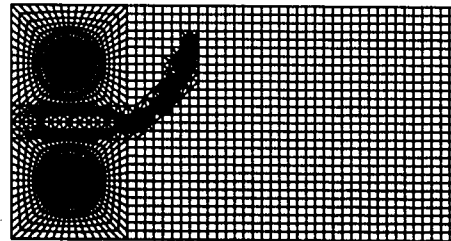
(a)   (b)

Figure 5.35: Example 4: Representative numerical results for crack trajectories considering the *FGM* beam (**Case 2**): (a) step 7; (b) step 14 (final step).

5.6.5 Two cracks emanating from holes in a plate under tension

This example investigates the interaction of two cracks emanating from holes in a plate. Figure 5.36(a) shows specimen geometry and BCs, Figure 5.36(b) shows the complete mesh configuration, Figure 5.36(c) shows mesh detail of two cracks, and Figure 5.36(c) shows zoom of the left crack tip region showing mesh of 12 sectors (S12) and 4 rings (R4) elements.

The typical mesh discretization consists of 1964 Q8, 302 T6, and 24 T6qp elements, with a total of 2290 elements and 6827 nodes. The following data are used for the FEM analyses:

$$\text{plane stress, } 2 \times 2 \text{ Gauss quadrature,}$$

$$\text{a=2 mm, t=1 mm, } \sigma = \sigma_{cr}(a + n\Delta a, X) \text{ (MPa)}. \tag{5.13}$$

Here material properties are adopted from the first example. For the homogeneous beam, the material properties of epoxy are used (see Table 5.1). For the graded beam, material gradation in the X_2 direction is considered, and the graded region $-18.5\text{mm} \leq X_2 \leq 18.5\text{mm}$ corresponds to the graded region $0 \leq \xi \leq 1$ in the first example (cf. Figures 5.8 and 5.9).

All the numerical results are obtained using the maximum energy release rates criterion [66]. Figure 5.37 shows comparison of crack trajectories obtained for the homogeneous plate with those for the graded plate. For the homogeneous plate, crack trajectories for the left and right crack tips are symmetric. For the graded plate, the upper-limit load (σ_{cr}^{upper}), which is required for both cracks to propagate, is considered for each step of crack propagation ($\Delta a = 0.5$ mm). Due to material gradation, two cracks propagate toward the compliant part of graded plate, and the symmetry breaks down.

Figure 5.38 shows crack trajectories obtained for the graded plate considering the lower-limit load (σ_{cr}^{upper}) at each step, which is required for the crack with higher crack driving force to propagate. As observed in Figure 5.38, only the left crack propagates and the right crack is shielded. This indicates that the crack driving force of the left crack is higher than that for the right crack for the entire step of crack propagation.

Figure 5.39 shows history of critical load (σ_{cr}) versus crack extension for homogeneous and graded plates ($\Delta a = 0.5$ mm). Due to higher fracture toughness in FGMs, the critical load at
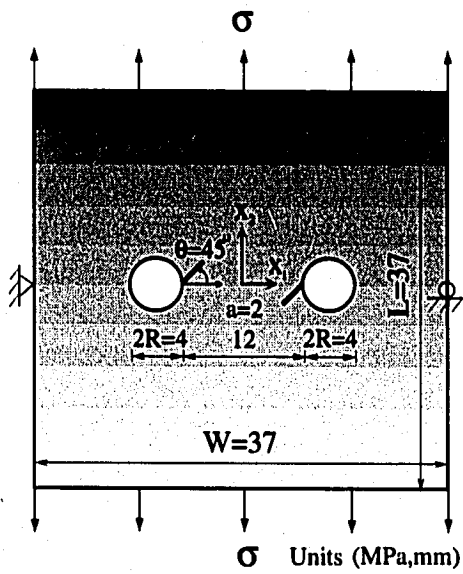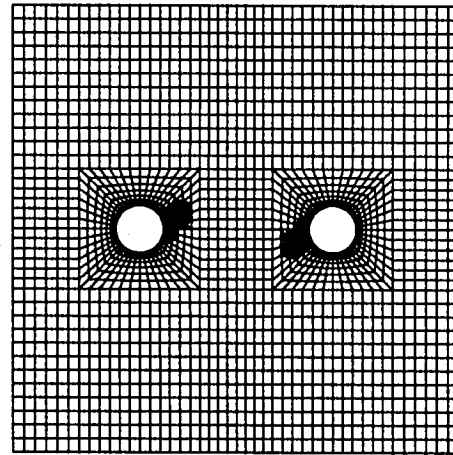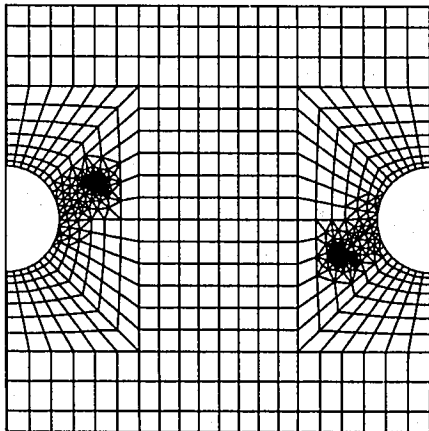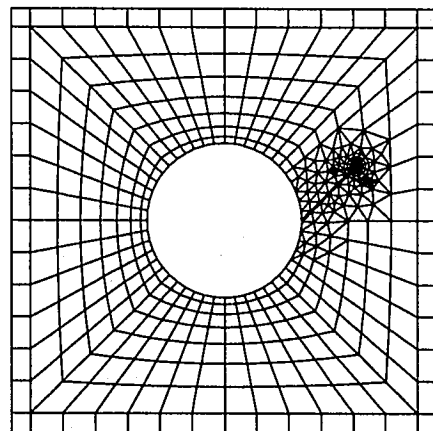
Figure 5.36: Example 5: FGM plate with two cracks emanating from holes: (a) geometry and BCs; (b) complete finite element mesh; (c) mesh details of two crack tips; (d) zoom of the left crack tip showing mesh of 12 sectors (S12) and 4 rings (R4) elements.

the initial step for the graded plate is higher than that for the homogeneous case. The critical load considering lower-limit case of the graded plate decreases with the increasing steps. However, the critical load considering upper-limit case of the graded plate decreases up to step 10 (crack
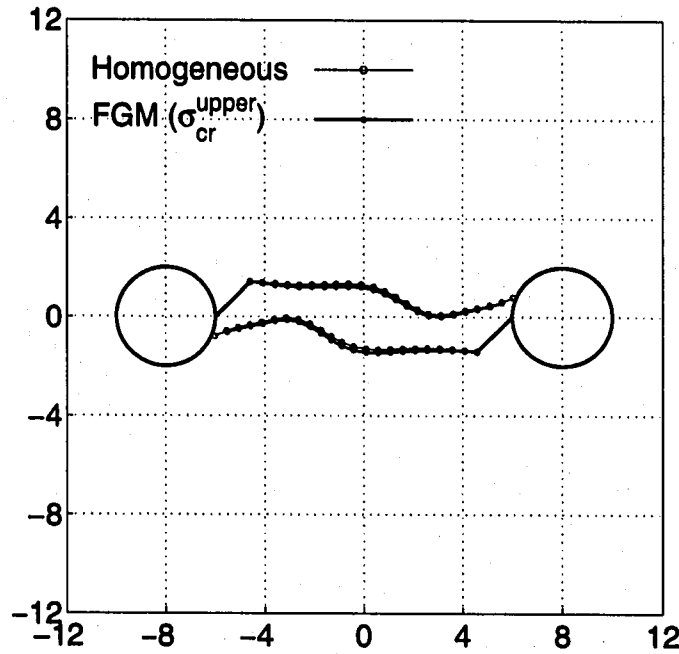
Figure 5.37: Example 5: comparison of crack trajectories for between homogeneous and graded plates. For a graded plate, the upper-limit load, which is required for both cracks to propagate, is considered for each step of crack propagation ($\Delta a = 0.5$ mm).

extension 5mm) due to the interaction between two cracks and increases thereafter, which is also observed in the homogeneous case.

Figure 5.40 shows history of SIFs (K_I and K_{II}) versus crack extension for the homogeneous plate ($\Delta a = 0.5$ mm). The SIFs for both crack tips are identical because of symmetry. Figures 5.41 and 5.42 show history of SIFs (K_I and K_{II}) versus crack extension for the graded plates considering the upper-limit and lower-limit loads, respectively. For both upper and lower limit load cases, due to higher fracture toughness and subsequent increased critical loads, one observes increased mode I SIF for both crack tips. Moreover, for the lower-limit load case, as observed in Figure 5.38, the right crack tip does not propagate, and mode II SIF for the right crack tip is positive.

Figure 5.43 shows finite element discretization in the final step of crack propagation considering $\Delta a = 0.5$mm for the homogeneous case and the lower-limit load of FGM case, respectively. The final discretization of upper-limit load case is similar to that for the homogeneous case, and thus is not shown here.

183
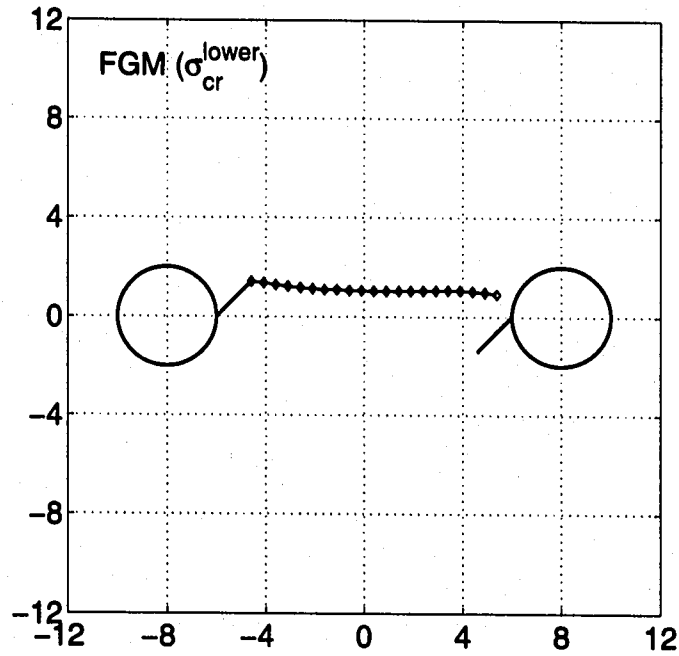
Figure 5.38: Example 5: crack trajectory for cracks in the graded plate. The lower-limit load, which is required for the crack with higher crack driving force to propagate, is considered for each step of crack propagation ($\Delta a = 0.5$ mm).
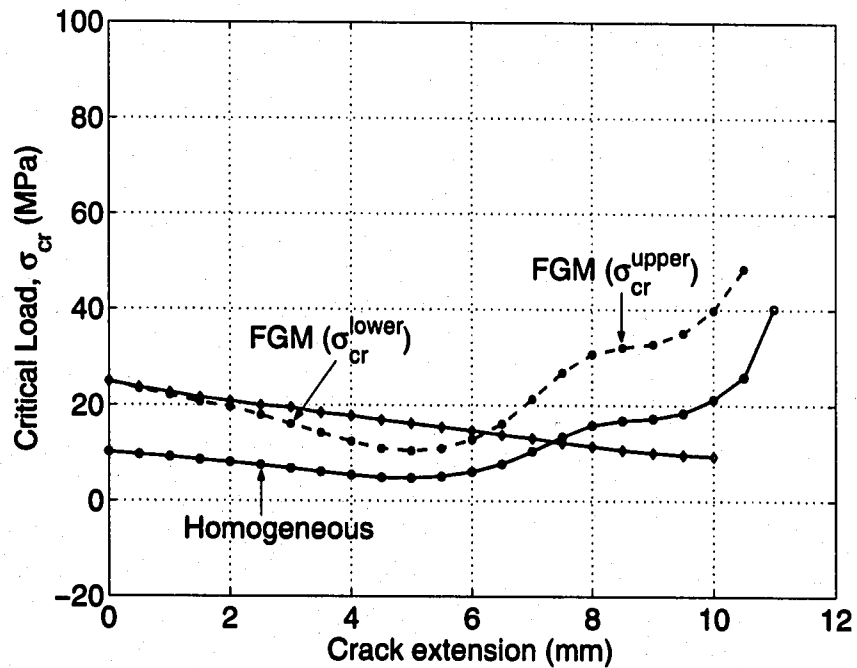
Figure 5.39: Example 5: critical load (σ_{cr}) versus crack extension history for homogeneous and graded plates ($\Delta a = 0.5$ mm).
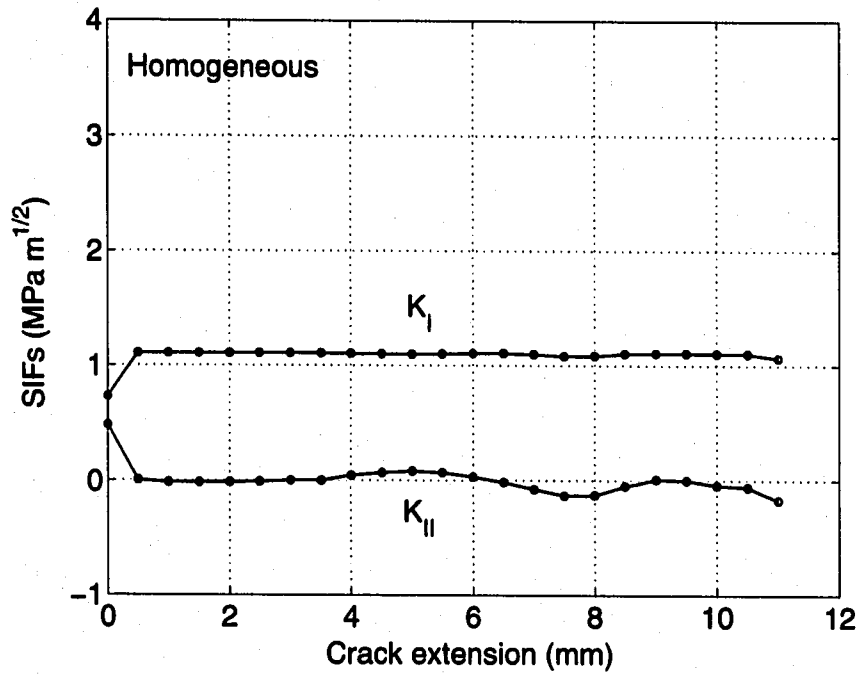
Figure 5.40: Example 5: SIFs (K_I and K_{II}) versus crack extension history for the homogeneous plate ($\Delta a = 0.5$ mm).
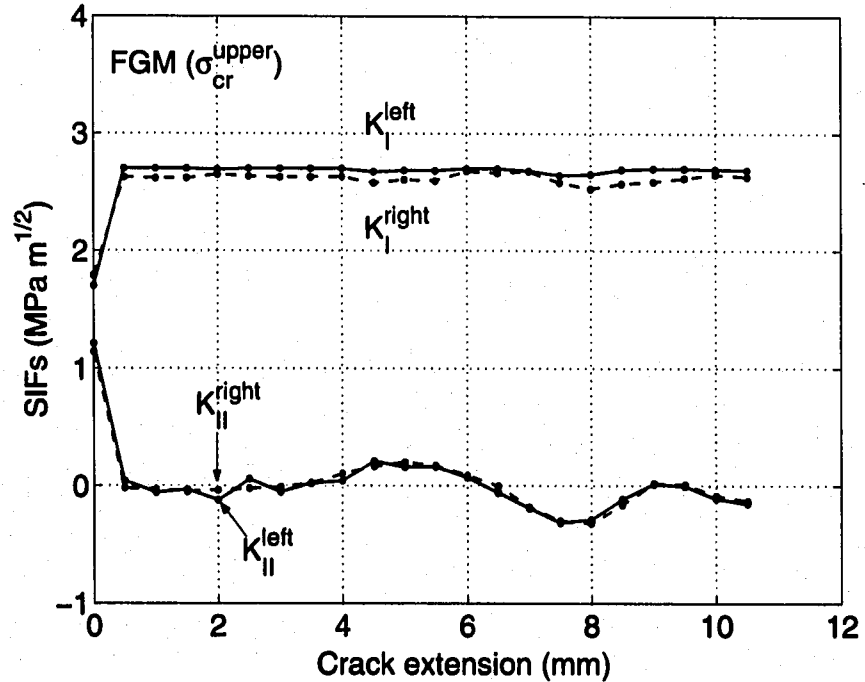
Figure 5.41: Example 5: SIFs (K_I and K_{II}) versus crack extension history for the graded plate considering the upper-limit load ($\Delta a = 0.5$ mm).

185
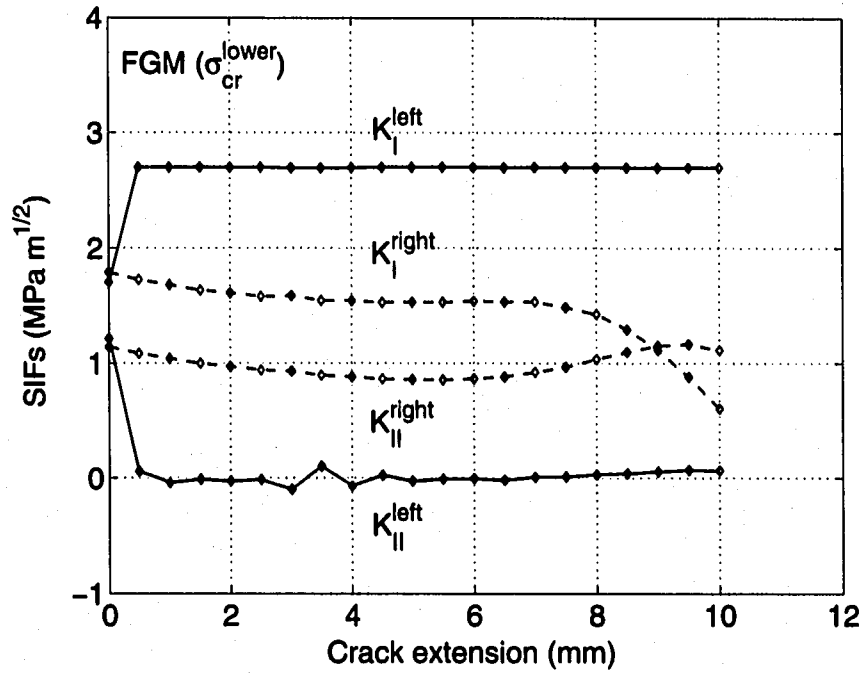
Figure 5.42: Example 5: SIFs (K_I and K_{II}) versus crack extension history for the graded plate considering the lower-limit load ($\Delta a = 0.5$ mm)

(a)   (b)
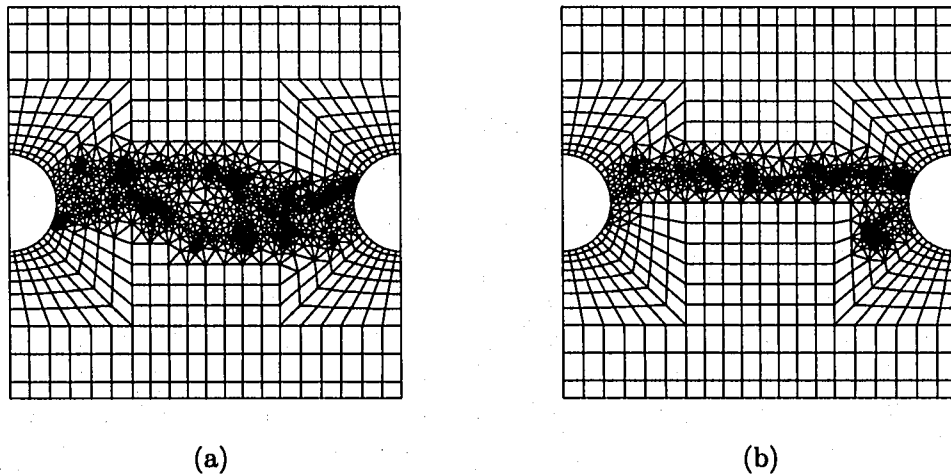
Figure 5.43: Example 5: finite element discretization in the final step of crack propagation considering $\Delta a = 0.5$mm (($\mathcal{G}$)$_{\max}$ criterion): (a) Homogeneous case; (b) the lower-limit load of FGM case. The final discretization of upper-limit load case is similar to that for the homogeneous case, and thus is not shown here.

5.6.6 Forked cracks in a plate under tension

This example investigates forked cracks extending from the existing crack tip. Figure 5.44(a) shows specimen geometry and BCs, Figure 5.44(b) shows the complete mesh configuration, Figure 5.44(c) shows mesh detail of forked cracks using 12 sectors (S12) and 4 rings (R4) elements.

The typical mesh discretization consists of 1644 Q8, 212 T6, and 24 T6qp elements, with a total of 1880 elements and 5605 nodes. The following data are used for the FEM analyses:

$$\text{plane stress, } 2 \times 2 \text{ Gauss quadrature,}$$

$$\text{a=3 mm, b=1.5 mm, t=1 mm, } \sigma = \sigma_{cr}(a + n\Delta a, \boldsymbol{X}) \text{ (MPa)}. \tag{5.14}$$

Here again material properties are adopted from the first example, and the material gradation is identical to the fifth example. For the homogeneous beam, the material properties of epoxy are used (see Table 5.1). For the graded beam, material gradation in the X_2 direction is considered, and the graded region $-18.5\text{mm} \leq X_2 \leq 18.5\text{mm}$ corresponds to the graded region $0 \leq \xi \leq 1$ in the first example (cf. Figures 5.8 and 5.9).

All the numerical results are obtained using the maximum energy release rates criterion [66]. Figure 5.45 shows comparison of crack trajectories obtained for the homogeneous plate with those for the graded plate ($\Delta a = 1.5$ mm). As observed for the upper-limit load in the previous example, due to material gradation, two cracks propagate toward the compliant part of graded plate, and the symmetry breaks down. As observed for the lower-limit load case in Figure 5.45, only the lower crack propagates and the upper crack is shielded. This indicates that the crack driving force of the lower crack is higher than that for the upper crack for the entire step of crack propagation.

Figure 5.46 shows history of critical load (σ_{cr}) versus crack extension for homogeneous and graded plates ($\Delta a = 1.5$ mm). Due to higher fracture toughness in FGMs, the critical load for the graded plate at each step is higher than that for the homogeneous case. One observes that the critical loads for all cases decrease with each step of propagation.

Figure 5.47 shows history of SIFs (K_I and K_{II}) versus crack extension for the homogeneous plate ($\Delta a = 1.5$ mm). The SIFs for both crack tips are identical because of symmetry. Figures 5.48 and 5.49 show history of SIFs (K_I and K_{II}) versus crack extension for the graded plates considering
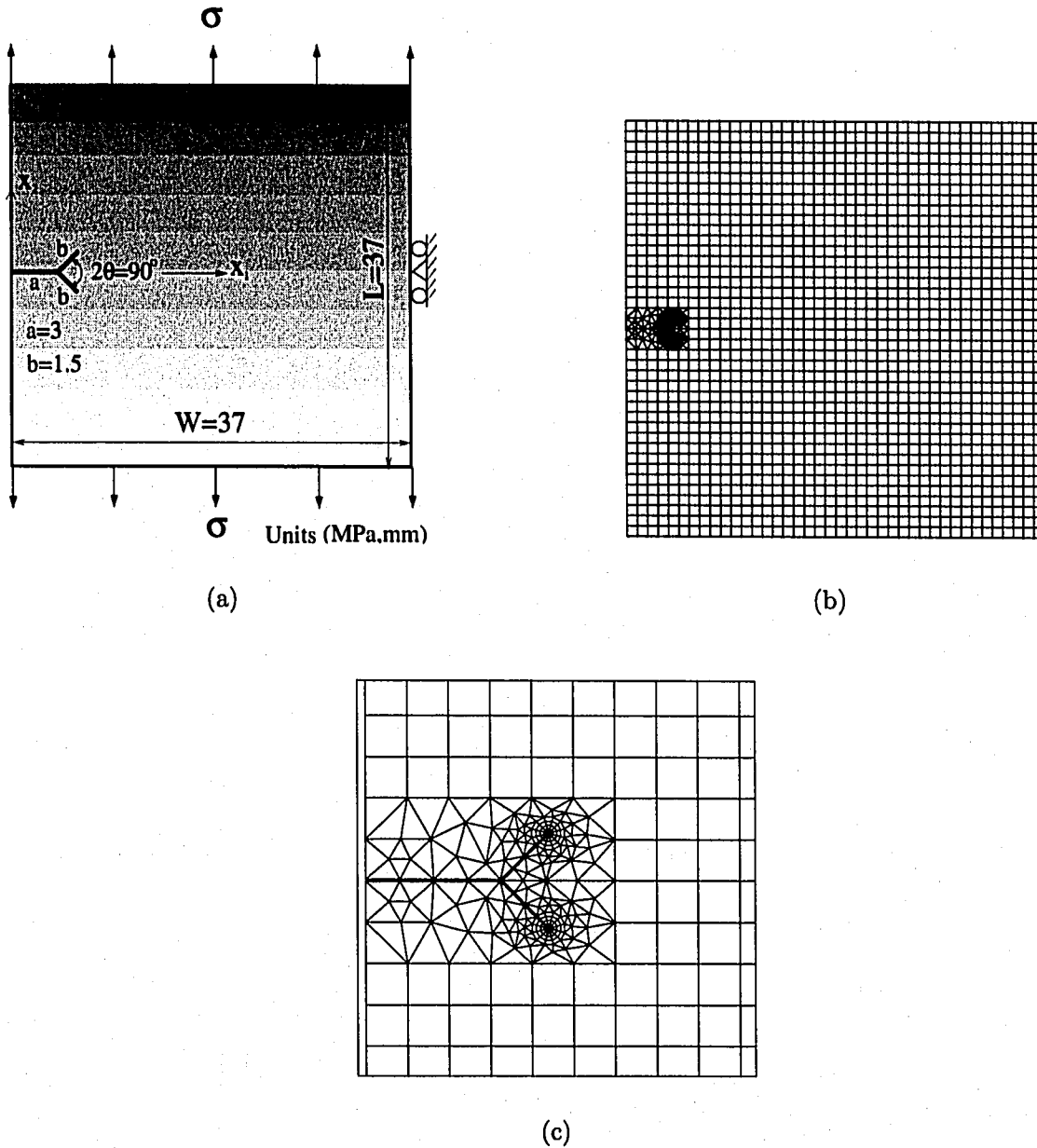
Figure 5.44: Example 6: FGM plate with forked cracks: (a) geometry and BCs; (b) complete finite element mesh; (c) mesh details using 12 sectors (S12) and 4 rings (R4) elements.

the upper-limit and lower-limit loads, respectively. For both upper and lower limit load cases, due to higher fracture toughness and subsequent increased critical loads, one observes increased mode I SIF for both crack tips. Moreover, for the upper-limit load case, as observed in Figure 5.48, mode I
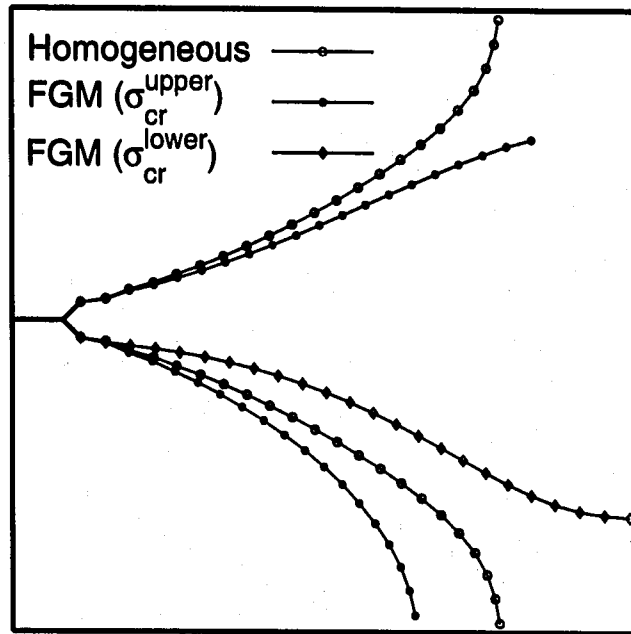
Figure 5.45: Example 6: comparison of crack trajectories between homogeneous and graded plates ($\Delta a = 1.5$ mm).
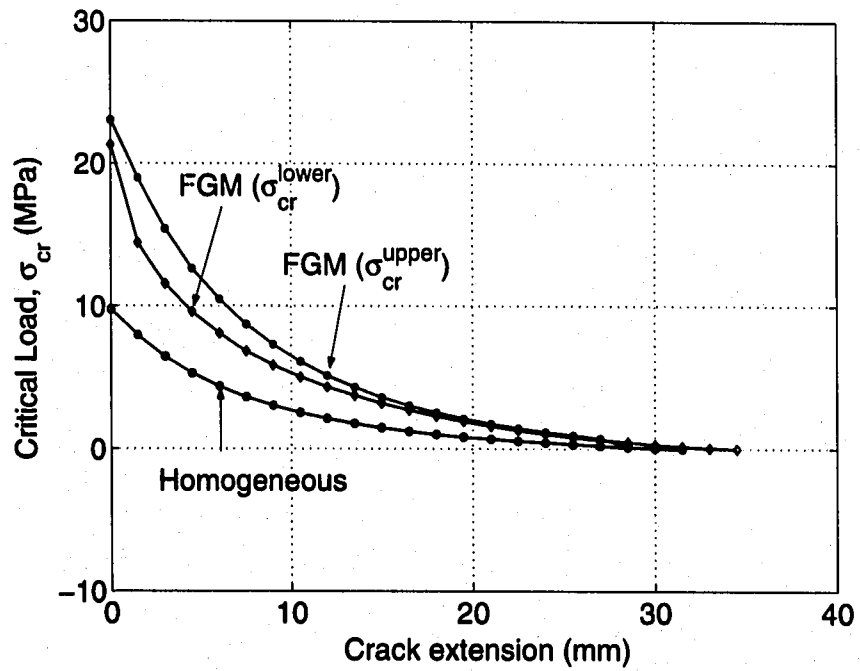
Figure 5.46: Example 6: critical load (σ_{cr}) versus crack extension history for homogeneous and graded plates ($\Delta a = 1.5$ mm).

SIF for the lower crack tip increases rapidly at the final step because it is near to the boundary. For the lower-limit load case, as observed in Figure 5.49, the upper crack tip does not propagate, and both mode I and II SIFs for the upper crack tip rapidly decreases at the early steps. Figure 5.50 shows finite element discretization in the final step of crack propagation considering $\Delta a = 1.5$mm for the homogeneous case, the upper-limit and the lower-limit loads of FGM case, respectively.
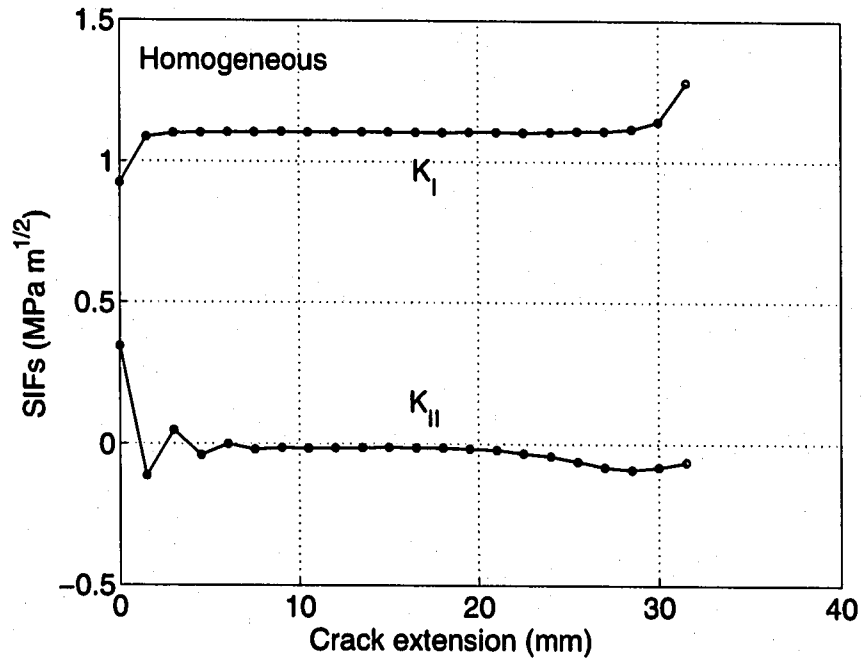
Figure 5.47: Example 6: SIFs (K_I and K_{II}) versus crack extension history for the homogeneous plate ($\Delta a = 1.5$ mm).
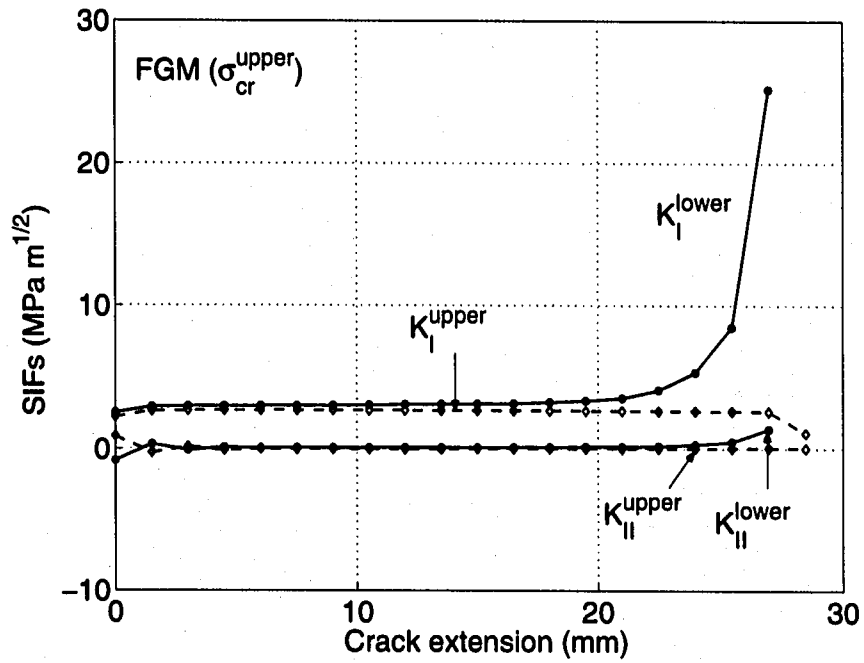
Figure 5.48: Example 6: SIFs (K_I and K_{II}) versus crack extension history for the graded plate considering the upper-limit load ($\Delta a = 1.5$ mm).
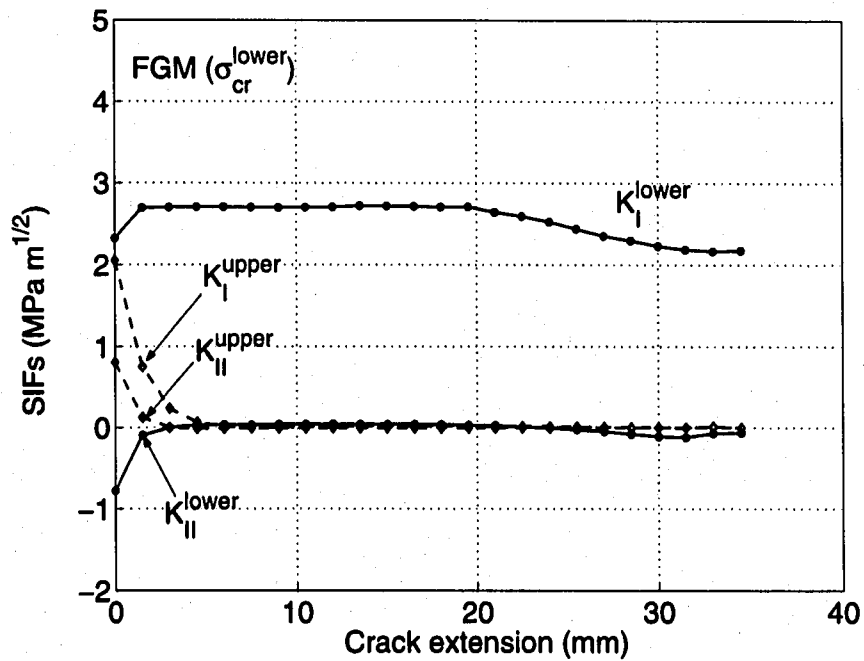
Figure 5.49: Example 6: SIFs (K_I and K_{II}) versus crack extension history for the graded plate considering the lower-limit load ($\Delta a = 1.5$ mm).
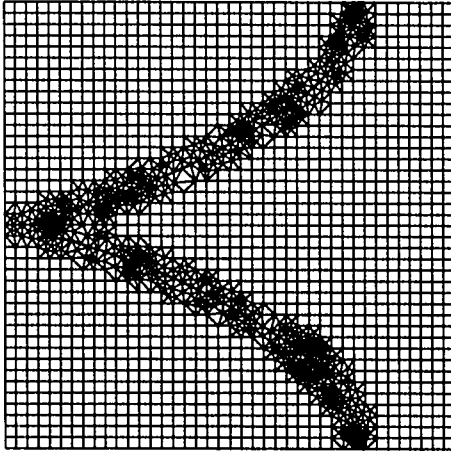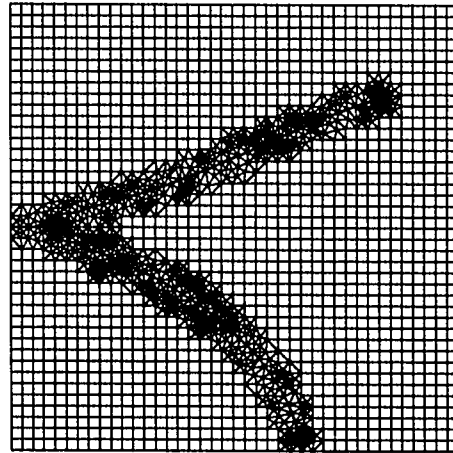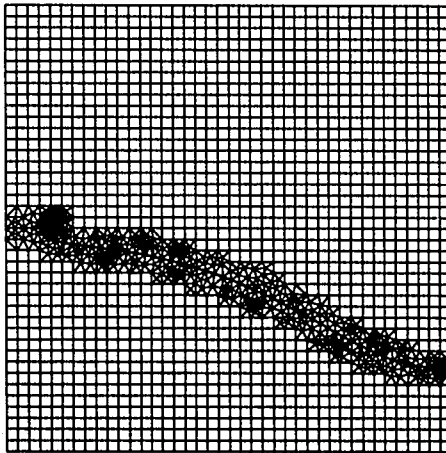
Figure 5.50: Example 6: finite element discretization in the final step of crack propagation considering $\Delta a = 0.5$mm for forked cracks ($(\mathcal{G})_{\mathrm{max}}$ criterion): (a) Homogeneous case; (b) the upper-limit load of FGM case; (c) the lower-limit load of FGM case.

5.7 Concluding remarks

This chapter investigates fracture behavior of FGMs by performing automatic simulation of crack propagation by means of a remeshing scheme of the finite element method. The crack propagation is performed under mixed-mode and non-proportional loading. Based on local homogenization, the maximum energy release rates [66] and maximum hoop stress criteria [36] are used, and both predict crack initiation angles well in comparison with experimental results. Crack trajectories obtained by both fracture criteria are similar to each other, and agree well with available experimental results for homogeneous and FGMs.

For two interacting cracks under symmetry boundary conditions, there exists symmetry in terms of fracture parameters characterizing crack-tip fields and crack growth behavior, and thus there is no competition between two cracks for homogeneous materials. However, for graded materials, the symmetry breaks down due to material gradation, and thus the crack-tip fields in one crack tip is different from those for the other. This may allow propagation of one crack and shield of the other crack under certain critical loads, which range between the critical loads for the two crack tips.

The present approach requires user-defined crack increment at the beginning of simulation. The crack increment is related to material microstructure, and need be thoroughly investigated with experiments.

Chapter 6

Conclusions and extensions

This thesis investigates fracture of FGMs through the accurate evaluation of mixed-mode SIFs and T-stress using the interaction integral method, and uses fracture criteria for crack initiation angles, and simulates mixed-mode crack propagation in homogeneous and nonhomogeneous materials under general mixed-mode and non-proportional loading. Crack growth in FGMs has been simulated by means of a remeshing algorithm of the displacement-based finite element method.

Graded finite elements, which incorporate the material property gradient at the size scale of the element, have been presented using a generalized isoparametric formulation, and have been verified against analytical solutions by means of mesh refinement. As a basic framework for fracture analysis by means of the interaction integral method, critical assessment and comparison have been made for three consistent formulations: non-equilibrium, incompatibility, and constant-constitutive-tensor formulations. Each formulation leads to a consistent form of the interaction integral in the sense that extra terms are added to compensate for the difference in response between homogeneous and nonhomogeneous materials. These extra terms play a key role in ensuring path-independence of the interaction integral for FGMs. From numerical investigations, the FEM results for such fracture parameters obtained by the method agree well with available semi-analytical or numerical solutions. It is observed that both material gradation and orthotropy have a significant influence on SIFs and T-stress (i.e. both sign and magnitude).

Based on local homogenization, this thesis uses fracture criteria such as the maximum energy release rates [66] and maximum hoop stress [36]. Crack trajectories obtained by both fracture criteria are similar to each other, and agree well with available experimental results for homogeneous and FGMs. The present approach requires user-defined crack increment at the beginning of

194

simulation. The crack increment Δa is related to material microstructure, and need be thoroughly investigated with experiments. The computational scheme developed here serves as a guideline for fracture experiments on homogeneous and FGM specimens (e.g. initiation toughness and R-curve).

An open issue consists on developing an analytical explanation regarding the excellent behavior of the interaction integral method for FGMs. Moreover, potential extension of the present work consists of developing a boundary layer model for general FGMs, assessing various fracture criteria and investigating the effect of T-stress (non-singular stress) on crack initiation angles in brittle FGMs. From the numerical investigation, positive T-stress increases the crack initiation angle, and negative T-stress decreases the crack initiation angle. A fracture criterion incorporating T-stress effect involves a physical length scale r_c, which is representative of the fracture process zone size. The length scale parameter may have a significant effect on the crack initiation angle, even with the same values of T-stress and SIFs. Therefore the parameter r_c must be carefully assessed by comparing numerical solutions with experimental results. Moreover, a natural extension involves developing nonlinear material models for FGMs, evaluating fracture parameter (J-integral), and simulating crack propagation in elastic-plastic FGMs (e.g. metal/ceramic).

Appendix A

A.1 Micromechanics models extended to FGMs

One of the basic problems in composite material theory is the prediction of the effective or average macroscopic properties in terms of the properties and relative amounts (i.e. volume fractions) of the individual phases. Many theoretical micro-mechanical models have been developed and applied to predict the effective elastic properties of composite materials. Models include the differential method, the self-consistent method, the three phase model, and the Mori-Tanaka method.

The differential method (DM) is due to Bruggeman, and it has been effectively developed and used by Roscoe [122]. The basic concept of the model is to view the overall composite as a sequence of dilute suspensions. A general bounds approach applicable to any macroscopically isotropic composite material has been derived by Hashin and Shtrikman [53], and revisited and generalized by Walpole [139]. The self-consistent method (SCM) was proposed by Hershey [54] and Kröner as a means to model the behavior of polycrystalline materials and was extended to multiphase media by Budiansky [14] and Hill [56, 57]. The three phase model (TPM) was formulated by Christensen and Lo [25]. Finally, the Mori-Tanaka method (MTM) was introduced by Mori and Tanaka [102] and revisited by Benveniste [11]. Moreover, Huang *et al.* [64] investigated several micromechanics models including the SCM, the TPM, the MTM, the DM, and Hashin and Shtrikman bounds, and Huang and Hwang [63] extended those to microcracked solids.

Now the main concern is on graded composite materials, consisting of one or more dispersed phases of spatially variable volume fractions embedded in a matrix of another phase that are subdivided by internal percolation thresholds between the different matrix phases. It is well known that the response of macroscopically homogeneous systems can be described in terms of certain

196

thermoelastic moduli that are evaluated for a selected representative volume element (RVE) subjected to uniform overall thermomechanical fields. However, such representative volumes are not easily defined for systems with variable phase volume fractions subjected to nonuniform overall fields. Regardless of such concerns, many methods developed to describe the behavior of macroscopic homogeneous composites have been applied to thermoelastic analyses of FGM composites. At the elementary level, rule-of-mixture approaches have been used by Fukui et al. [41], Lee and Erdogan [93], and Markworth and Saunders [98] in elastic systems. Giannakopoulos et al. [45] and Finot and Suresh [40] used this approach in elastic-plastic systems. Miller and Lannutti [100] estimated elastic moduli and averages of the Hashin-Shtrikman bounds for statistically homogeneous systems. There are various aspects of micromechanical modeling [47, 97, 128]. In applying micromechanical approaches to FGMs, higher order methods has been investigated using a generalized method of cells approach [116, 3, 2] and a generalized Mori-Tanaka approach [155, 156]. In addition, Zuiker [154] investigated and compared standard micromechanical methods. Reiter and Dvorak [118, 119] investigated validity of micromechanical averaging methods in applications to graded elastic composite materials with particulate and skeletal microstructures under mechanical and thermal loadings. Recently, Yin et al. [152] developed a new micromechanics models, which is applicable to FGMs, considering multiscaling modelling and particle interactions.

A.1.1   Dilute approximation

Premise

The dilute suspension problem involving a single inclusion in an infinite medium has the physical meaning that the inclusions are so small and so far apart that all interaction between inclusions can be neglected, no matter what the size of the representative volume element may be (see Figure A.1).

Bulk modulus

Let's consider a spherical inclusion of radius a embedded in an infinite medium subjected to a hydrostatic pressure ε_{kk}^0 at infinity. Due to the spherical symmetry, the equilibrium conditions are

$$\frac{\partial \sigma_{rr}}{\partial r} + \frac{2}{r}(\sigma_{rr} - \sigma_{\theta\theta}) = 0, \tag{A.1}$$
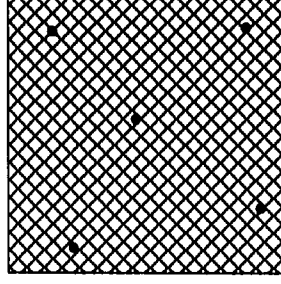
Figure A.1: No interaction between inclusions. • indicates an inclusion.

where $\sigma_{\phi\phi} = \sigma_{\theta\theta}$.

In terms of displacements, Eq.(A.1) is rewritten as

$$\frac{\partial^2}{\partial r^2}u_r + \frac{2}{r}\frac{\partial}{\partial r}u_r - \frac{2}{r^2}u_r = 0, \tag{A.2}$$

where r is the radial coordinate originating from the center of the sphere and u_r is the radial displacement. The solutions are given by [24]

$$u_r = Ar + \frac{B}{r^2}, \quad \varepsilon_{kk} = 3A. \tag{A.3}$$

The stress σ_{rr} is

$$\sigma_{rr} = \lambda\varepsilon_{kk} + 2\mu\,\frac{\partial}{\partial r}u_r, \tag{A.4}$$

where λ and μ are the *Lamé* constants. The following expressions are applicable for the matrix m and inclusion i, respectively,

$$u_r^m = Ar + \frac{B}{r^2}, \quad u_r^i = Cr, \tag{A.5}$$

where the constants A, B, and C can be determined from the continuity conditions

$$u_r^m = u_r^i, \quad \sigma_{rr}^m = \sigma_{rr}^i \quad \text{at} \quad r = a. \tag{A.6}$$

Thus

$$\frac{\varepsilon_{kk}^i}{\varepsilon_{kk}^0} = \frac{3C}{3A} = \frac{3(\lambda_m + 2\mu_m)}{3\lambda_i + 2\mu_i + 4\mu_m}. \tag{A.7}$$

Using the following equation

$$C_{ijkl}^{*}\varepsilon_{kl}^{0} = C_{ijkl}^{m}\varepsilon_{kl}^{0} + c(C_{ijkl}^{i} - C_{ijkl}^{m})\varepsilon_{kl}^{i}, \tag{A.8}$$

where c is the volume fraction of the inclusion. the effective bulk modulus can be determined as [24]

$$\kappa = \kappa_m + \frac{c(\kappa_i - \kappa_m)}{1 + (1-c)(\kappa_i - \kappa_m)/(\kappa_m + \frac{4}{3}\mu_m)} . \tag{A.9}$$

Shear modulus

Let's consider a homogeneous medium under shear deformation. The displacements in the Cartesian coordinates are [24]

$$u_x = sx, \quad u_y = -sy, \quad u_z = 0, \tag{A.10}$$

where s is the maximum shear strain. Converting to the spherical coordinates (r, θ, ϕ) yields

$$u_r = sr\sin^2\theta\cos 2\phi, \quad u_\theta = sr\sin\theta\cos\theta\cos 2\phi, \quad u_z = -sr\sin\theta\sin 2\phi. \tag{A.11}$$

In the heterogeneous system of matrix-inclusion, the general solutions can be assumed as

$$u_r = U_r(r)\sin^2\theta\cos 2\phi, \quad u_\theta = U_\theta(r)\sin\theta\cos\theta\cos 2\phi, \quad u_z = U_\phi(r)\sin\theta\sin 2\phi, \tag{A.12}$$

where U_r, U_θ and U_ϕ are unknown functions to be determined from the equilibrium equations in spherical coordinates. Then

$$U_r^m = B_1 r + \frac{3B_3}{r^4} - \frac{5 - 4\nu_m}{(1 - 2\nu_m)}\frac{B_4}{r^2}, \quad U_\theta^m = B_1 r - \frac{2B_3}{r^4} + \frac{2B_4}{r^2},$$

$$U_r^i = A_1 r - \frac{6\nu_i}{(1 - 2\nu_i)}A_2 r^3, \quad U_\theta^i = A_1 r - \frac{7 - 4\nu_i}{(1 - 2\nu_i)}A_2 r^3, \quad U_\theta + U_\phi = 0. \tag{A.13}$$

Imposing the interfacial continuity conditions for displacements and tractions at $r = a$, one obtains

$$\frac{\varepsilon_{12}^i}{\varepsilon_{12}^0} = \frac{15(1 - \nu_m)}{(7 - 5\nu_m)\mu_m + 2(4 - 5\nu_m)\mu_i}. \tag{A.14}$$

Using Eq.(A.8), one obtains the effective shear modulus as [24]

$$\frac{\mu^*}{\mu_m} = 1 - \frac{15(1 - \nu_m)(1 - \frac{\mu_i}{\mu_m})c_i}{(7 - 5\nu_m) + 2(4 - 5\nu_m)\frac{\mu_i}{\mu_m}}.$$

(A.15)

A.1.2 Hashin-Shtrikman bounds

Hashin and Shtrikman [53] derived the upper and lower bounds for the effective elastic moduli of multiphase materials of arbitrary phase geometry, consisting of isotropic phases, using the variational principles in linear elasticity and considering prescribed surface displacements. A summary of the derivation follows the derivation by Hashin and Shtrikman [53].

Let σ_{ij}^o and ε_{ij}^o be known stress and strain tensor fields in a deformed elastic body of volume V and surface S. For the case of no body forces, Hooke's law is given by [53]

$$\sigma_{ij}^o = \lambda_0 \varepsilon_{kk}^o \delta_{ij} + 2\mu_0 \varepsilon_{ij}^o = \boldsymbol{L}_0(\varepsilon_{ij}^o),$$

(A.16)

where λ_0 and μ_0 are the *Lamé* constant and the shear modulus, which for simplicity are taken to be constant throughout the body, and δ_{ij} are the Kronecker delta. The strains are given by

$$\varepsilon_{ij}^o = \frac{1}{2}(u_{i,j}^o + u_{j,i}^o).$$

(A.17)

Let part or whole of the body be changed to material of different moduli λ and μ which may vary in space, and the surface displacements $u_i^o(S)$ be held fixed. The unknown stress and strain fields in the changed body are denoted by σ_{ij} and ε_{ij}. The stress polarization tensor p_{ij} is now defined by [53]

$$\sigma_{ij} = \boldsymbol{L}_0(\varepsilon_{ij}) + p_{ij}.$$

(A.18)

Let's also define

$$u_i' = u_i - u_i^o$$

(A.19)

and

$$\varepsilon_{ij}' = \varepsilon_{ij} - \varepsilon_{ij}^o.$$

(A.20)

The ε_{ij} and σ_{ij} can be found from Eqs.(A.18) and (A.20) once ε_{ij}' and p_{ij} are known. Based on

200

variational principles involving ε'_{ij} and p_{ij}, the volume integral reads [53]

$$U_p = U_0 - \frac{1}{2} \int \left[p_{ij} \boldsymbol{H}(p_{ij}) - p_{ij}\varepsilon'_{ij} - 2p_{ij}\varepsilon^o_{ij} \right] \; dV, \qquad \text{(A.21)}$$

where

$$U_0 = \frac{1}{2} \int \sigma^o_{ij}\varepsilon^o_{ij} \; dV, \qquad \text{(A.22)}$$

which is subjected to the equilibrium condition

$$\boldsymbol{L}_0(\varepsilon'_{ij})_{,j} + p_{ij,j} = 0, \qquad \text{(A.23)}$$

and the boundary condition

$$u'_i(S) = 0. \qquad \text{(A.24)}$$

The volume integral is stationary for

$$p_{ij} = \boldsymbol{L}(\varepsilon_{ij}) - \boldsymbol{L}_0(\varepsilon_{ij}), \qquad \text{(A.25)}$$

where

$$\boldsymbol{L}(\varepsilon_{ij}) = \lambda\varepsilon_{kk}\delta_{ij} + 2\mu\varepsilon_{ij}. \qquad \text{(A.26)}$$

The operator $\boldsymbol{H}$ in Eq.(A.21) is given by

$$\boldsymbol{H} = (\boldsymbol{L} - \boldsymbol{L}_0)^{-1}. \qquad \text{(A.27)}$$

Therefore, in Eq.(A.21),

$$p_{ij}\boldsymbol{H}(p_{ij}) = -\frac{\lambda - \lambda_0}{6(\mu - \mu_0)(\kappa - \kappa_0)}p^2_{kk} + \frac{1}{2(\mu - \mu_0)}p_{ij}p_{ij} \qquad \text{(A.28)}$$

where

$$\kappa = \lambda + \frac{2}{3}\mu \qquad \text{(A.29)}$$

201

is the bulk modulus. Equation (A.23) is written as

$$(\lambda_0 + \mu_0)u'_{j,ij} + \mu_0 u'_{i,jj} + p_{ij,j} = 0. \tag{A.30}$$

The stationary value of U_p, the strain energy U stored in the changed body, is an absolute maximum for

$$\lambda > \lambda_0 \ , \ \mu > \mu_0 \tag{A.31}$$

and an absolute minimum for

$$\lambda < \lambda_0 \ , \ \mu < \mu_0. \tag{A.32}$$

Following the above procedure, Hashin and Shtrikman [53] derived the upper and lower bounds for effective properties for multiphase materials. For two-phase materials, the bounds on the effective shear and bulk moduli are given by [53] $(i, j = 1, 2)$:

$$\begin{aligned}
\mu_i^e &= \mu_i + V_j / \left\{ \frac{1}{\mu_j - \mu_i} + \frac{6(\kappa_i + 2\mu_i)V_i}{5\mu_i(3\kappa_i + 4\mu_i)} \right\} \\
\kappa_i^e &= \kappa_i + V_j / \left\{ \frac{1}{\kappa_j - \kappa_i} + \frac{3V_i}{(3\kappa_i + 4\mu_i)} \right\} , \ (i \neq j)
\end{aligned} \tag{A.33}$$

where the superscript e refers to the effective quantity, V_i is the volume fraction of phase i, μ_i is the shear modulus of phase i, and κ_i is the bulk modulus of phase i. Moreover, $\kappa_2^e > \kappa_1^e$ and $\mu_2^e > \mu_1^e$.

A.1.3 Self-consistent method

<u>Premise</u>

The method was derived as a means to model the behavior of polycrystalline materials which are just one phase media, but because of the random or partially random orientation of the crystals, discontinuities in properties exist across crystal interfaces. In the application to polycrystalline aggregates, a single anisotropic crystal is viewed as a spherical or ellipsoidal inclusion embedded in an infinite medium of the unknown isotropic properties of the aggregate. Then the system is subjected to uniform stress or strain conditions at large distances from the inclusion. Next the orientation average of the stress or strain in the inclusion is set equal to the corresponding applied value of the stress or strain. Thus the name Self-Consistent Method comes from this procedure.

A summary of the derivation follows the derivation by Hill [57]. A single inclusion, arbitrary ellipsoidal in shape, is considered to be embedded in a homogeneous mass of different materials as shown in Figure A.2.
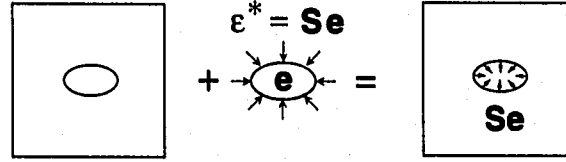
Figure A.2: Schematic of Self-Consistent Method

The tensors of elastic moduli are denoted by L and L_1, respectively, and their inverse compliances by M and M_1. The displacement at infinity is prescribed to correspond to a uniform overall strain $\bar{\varepsilon}$. Both the displacement and traction are required to be continuous across the phase interface. The principal feature is that the inclusion is strained uniformly. An overall constraint tensor L^* is introduced for the L phase, with the inverse M^*, as loading over the interface compatible with a uniform field of stress σ^*. If ε^* is the corresponding uniform strain of the ellipsoid, one obtains [57]

$$\sigma^* = -L^*\varepsilon^* \quad , \quad \varepsilon^* = -M^*\sigma^*. \tag{A.34}$$

The solution of the auxiliary problem is obtained by superimposing $\bar{\sigma}$ and $\bar{\varepsilon}$, and identifying σ^* with $\sigma_1 - \bar{\sigma}$ and ε^* with $\varepsilon_1 - \bar{\varepsilon}$ where σ_1 and ε_1 are the actual fields in the inclusion. Then [57]

$$\sigma_1 - \bar{\sigma} = L^*(\bar{\varepsilon} - \varepsilon_1) \quad , \quad \varepsilon_1 - \bar{\varepsilon} = M^*(\bar{\sigma} - \sigma_1). \tag{A.35}$$

An ellipsoid region would undergo a transformation strain e if free, but attains only the strain Se *in situ*. The components of dimensionless tensor S are functions of the moduli ratios and of the aspect ratios of the ellipsoid and its orientation in the frame of reference.

To connect L^* and M^*, one obtains, by imagining the transformation problem, as [57]

$$\varepsilon^* = Se \quad , \quad \sigma^* = L(\varepsilon^* - e). \tag{A.36}$$

Combination of Eq.(A.36) and Eq.(A.34) yields [57]

$$L^*S = L(I - S) \ , \ (I - S)M^* = SM, \tag{A.37}$$

where I is the unit tensor. Another dimensionless tensor T, the dual of S, could be admitted as follows:

$$M^*T = SM = P \ , \ TL = L^*S = Q \tag{A.38}$$

so that

$$M^*T = M(I - T) \ , \ (I - T)L^* = TL$$
$$T = L^*(L^* + L)^{-1} = (M^* + M)^{-1}M \tag{A.39}$$

Now the stress σ^* in the transformed region can be written as Ts, where s is the stress required to remove the strain e. The symbols P and Q can be introduced as [57]

$$PL + MQ = I$$
$$P = M(I - T) \quad , \quad Q = L(I - S)$$
$$P^{-1} = L^* + L \quad , \quad Q^{-1} = M^* + M. \tag{A.40}$$

Let two phase properties be denoted by subscripts 1 and 2 and let c_1 and c_2 be the volume fraction of each phase. The relations between the phase and overall averages of stress and strain are [57]

$$c_1(\overline{\sigma}_1 - \overline{\sigma}) + c_2(\overline{\sigma}_2 - \overline{\sigma}) = 0, \quad c_1(\overline{\varepsilon}_1 - \overline{\varepsilon}) + c_2(\overline{\varepsilon}_2 - \overline{\varepsilon}) = 0 \tag{A.41}$$

The self-consistency gives [57]

$$\overline{\sigma}_1 - \overline{\sigma} = L^* (\overline{\varepsilon} - \overline{\varepsilon}_1), \quad \overline{\sigma}_2 - \overline{\sigma} = L^* (\overline{\varepsilon} - \overline{\varepsilon}_2). \tag{A.42}$$

Equation (A.42) is rearranged as

$$(L^* + L_1)\bar{\varepsilon}_1 = (L^* + L_2)\bar{\varepsilon}_2 = (L^* + L)\bar{\varepsilon}. \tag{A.43}$$

or

$$(M^* + M_1)\bar{\sigma}_1 = (M^* + M_2)\bar{\sigma}_2 = (M^* + M)\bar{\sigma}. \tag{A.44}$$

Combining Eqs.(A.43) and (A.44) with Eq.(A.41) yields a pair of equivalent formulae for the overall stiffness and compliance tensors L and M

$$c_1(L^* + L_1)^{-1} + c_2(L^* + L_2)^{-1} = (L^* + L)^{-1} = P$$
$$c_1(M^* + M_1)^{-1} + c_2(M^* + M_2)^{-1} = (M^* + M)^{-1} = Q. \tag{A.45}$$

Substitution of Eq.(A.40) to Eq.(A.45) yields [57]

$$c_1(L - L_2)^{-1} + c_2(L - L_1)^{-1} = P,$$
$$c_1(M - M_2)^{-1} + c_2(M - M_1)^{-1} = Q. \tag{A.46}$$

Finally, one obtains the phase concentration factor tensors, A_1 and A_2 for strain, B_1 and B_2 for stress defined by

$$A_1^{-1}\bar{\varepsilon}_1 = A_2^{-1}\bar{\varepsilon}_2 = \bar{\varepsilon} \quad , \quad B_1^{-1}\bar{\sigma}_1 = B_2^{-1}\bar{\sigma}_2 = \bar{\sigma} \tag{A.47}$$

where

$$A_1^{-1} = P(L^* + L_1) = I + P(L_1 - L), \quad A_2^{-1} = P(L^* + L_2) = I + P(L_2 - L), \quad \text{(A.48)}$$
$$B_1^{-1} = Q(M^* + M_1) = I + Q(M_1 - M), \quad B_2^{-1} = Q(M^* + M_2) = I + Q(M_2 - M).$$

Then

$$c_1 A_1 + c_2 A_2 = I = c_1 B_1 + c_2 B_2. \tag{A.49}$$

Let's assume that the inclusions are spheres distributed in the way such that the composite is

statistically isotropic overall. The isotropic 4th-order L tensor is written as

$$L_{ijkl} = \kappa\delta_{ij}\delta_{kl} + \mu\left(\delta_{ij}\delta_{kl} + \delta_{il}\delta_{jk} - \frac{2}{3}\delta_{ij}\delta_{kl}\right),\qquad\text{(A.50)}$$

or simply in terms of the hydrostatic and deviatoric components

$$\boldsymbol{L} = (3\kappa, 2\mu)\qquad\text{(A.51)}$$

or with its inverse

$$\boldsymbol{M} = (\frac{1}{3\kappa}, \frac{1}{2\mu}).\qquad\text{(A.52)}$$

Equation (A.46) then reduces to one for the effective bulk and shear moduli, κ and μ [57]

$$\frac{c_1}{\kappa - \kappa_2} + \frac{c_2}{\kappa - \kappa_1} = \frac{\alpha}{\kappa},$$
$$\frac{c_1}{\mu - \mu_2} + \frac{c_2}{\mu - \mu_1} = \frac{\beta}{\mu},\qquad\text{(A.53)}$$

where

$$\alpha = 3 - 5\beta = \frac{\kappa}{\kappa + \frac{4}{3}\mu}\ ,\quad \beta = \frac{6(\kappa + 2\mu)}{5(3\kappa + 4\mu)}.\qquad\text{(A.54)}$$

The dimensionless quantities α and β appear in the specific form of S tensor for a sphere

$$S_{ijkl} = \frac{1}{3}(\alpha - \beta)\delta_{ij}\delta_{kl} + \frac{1}{2}\beta(\delta_{ik}\delta_{jl} + \delta_{il}\delta_{jk}).\qquad\text{(A.55)}$$

The bulk modulus κ can be solved from Eqs.(A.53) and (A.54) as [57]

$$\frac{1}{\kappa + \frac{4}{3}\mu} = \frac{c_1}{\kappa_1 + \frac{4}{3}\mu} + \frac{c_2}{\kappa_2 + \frac{4}{3}\mu}.\qquad\text{(A.56)}$$

Using Eqs.(A.53) and (A.56), one obtains the final expression for shear modulus μ [57]

$$\left(\frac{c_1\kappa_1}{\kappa_1 + \frac{4}{3}\mu} + \frac{c_2\kappa_2}{\kappa_2 + \frac{4}{3}\mu}\right) + 5\left(\frac{c_1\mu_2}{\mu - \mu_2} + \frac{c_2\mu_1}{\mu - \mu_1}\right) + 2 = 0.\qquad\text{(A.57)}$$

A.1.4 Three phase model

Premise

Three Phase Model is referred to as the Generalized Self-Consistent Method, and it is based on the original Self-Consistent Method which involves directly embedding the inclusion phase in the infinite medium of unknown effective properties.

A summary of the derivation follows the derivation by Christensen [24]. Let's consider that an infinite region is subjected to homogeneous deformation conditions at large distances from the origin. The outer layer material, being the equivalent homogeneous phase, has its unknown effective properties (see Figure A.3).
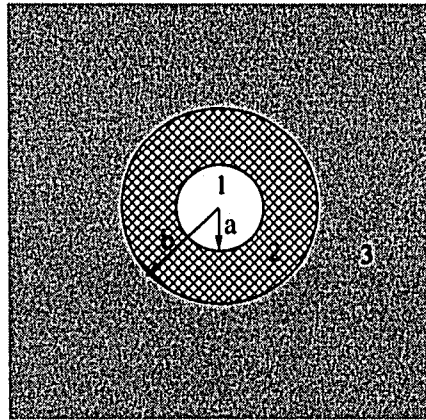
1. Spherical inclusion
2. Matrix phase
3. Equivalent homogeneous medium

Figure A.3: Three phase model

Solutions in the form of Eq.(A.12) are assumed for the condition of imposed simple shear deformation at large distance from the origin. The functions $U_r(r)$, $U_\theta(r)$ and $U_\phi(r)$ are given

by [24]

$$U_r^m = B_1 r - \frac{6\nu_m B_2 r^3}{1 - 2\nu_m} + \frac{3B_3}{r^4} + \frac{(5 - 4\nu_m)}{(1 - 2\nu_m)}\frac{B_4}{r^2} \qquad \text{(A.58)}$$

$$U_\theta^m = B_1 r - \frac{(7 - 4\nu_m)B_2 r^3}{(1 - 2\nu_m)} - \frac{2B_3}{r^4} + 2\frac{B_4}{r^2} \qquad \text{(A.59)}$$

$$U_r^i = A_1 r - \frac{6\nu_i A_2 r^3}{(1 - 2\nu_i)} \qquad \text{(A.60)}$$

$$U_\theta^i = A_1 r - \frac{(7 - 4\nu_i)}{(1 - 2\nu_i)} A_2 r^3 \qquad \text{(A.61)}$$

$$U_r^e = D_1 r + \frac{3D_3}{r^4} + \frac{(5 - 4\nu)D_4}{(1 - 2\nu)r^2} \qquad \text{(A.62)}$$

$$U_\theta^e = D_1 r - \frac{2D_3}{r^4} + 2\frac{D_4}{r^2} \qquad \text{(A.63)}$$

$$U_\theta + U_\phi = 0 \qquad \text{(A.64)}$$

where m, i, and e refer to the matrix, inclusion, and the effective medium, respectively. By imposing the interfacial conditions of perfect bonding at $r = a$ and $r = b$, the solution for shear modulus μ is given by [25, 24]

$$A\left(\frac{\mu}{\mu_m}\right)^2 + 2B\left(\frac{\mu}{\mu_m}\right) + C = 0 \qquad \text{(A.65)}$$

where

$$
\begin{aligned}
A =\ & 8\left(\frac{\mu_i}{\mu_m} - 1\right)(4 - 5\nu_m)\eta_1 V_f^{10/3} - 2\left[63(\frac{\mu_i}{\mu_m} - 1)\eta_2 + 2\eta_1\eta_3\right] V_f^{7/3} \\
& + 252(\frac{\mu_i}{\mu_m} - 1)\eta_2 V_f^{5/3} - 50(\frac{\mu_i}{\mu_m} - 1)(7 - 12\nu_m + 8\nu_m^2)\eta_2 V_f + 4(7 - 10\nu_m)\eta_2\eta_3, \\
B =\ & -2\left(\frac{\mu_i}{\mu_m} - 1\right)(1 - 5\nu_m)\eta_1 V_f^{10/3} + 2\left[63(\frac{\mu_i}{\mu_m} - 1)\eta_2 + 2\eta_1\eta_3\right] V_f^{7/3} \\
& - 252(\frac{\mu_i}{\mu_m} - 1)\eta_2 V_f^{5/3} + 75(\frac{\mu_i}{\mu_m} - 1)(3 - \nu_m)\eta_2\nu_m V_f + \frac{3}{2}(15\nu_m - 7)\eta_2\eta_3, \\
C =\ & 4\left(\frac{\mu_i}{\mu_m} - 1\right)(5\nu_m - 7)\eta_1 V_f^{10/3} - 2\left[63(\frac{\mu_i}{\mu_m} - 1)\eta_2 + 2\eta_1\eta_3\right] V_f^{7/3} \\
& + 252(\frac{\mu_i}{\mu_m} - 1)\eta_2 V_f^{5/3} + 25(\frac{\mu_i}{\mu_m} - 1)(\nu_m^2 - 7)\eta_2 V_f - (7 + 5\nu_m)\eta_2\eta_3 \qquad \text{(A.66)}
\end{aligned}
$$

with

$$\eta_1 = (49 - 50\nu_i\nu_m)\left(\frac{\mu_i}{\mu_m} - 1\right) + 35\frac{\mu_i}{\mu_m}(\nu_i - 2\nu_m) + 35(2\nu_i - \nu_m)$$

$$\eta_2 = 5\nu_i\left(\frac{\mu_i}{\mu_m} - 8\right) + 7\left(\frac{\mu_i}{\mu_m} + 4\right)$$

$$\eta_3 = \frac{\mu_i}{\mu_m}(8 - 10\nu_m) + (7 - 5\nu_m), \tag{A.67}$$

where V_f is the volume fraction of inclusions and the subscripts i and m refer to the isotropic inclusion and matrix phases, respectively. The solution for the effective bulk modulus for the 3 phase medium of Figure A.3 is given by [25, 24]

$$\kappa = \kappa_m + \frac{V_f(\kappa_i - \kappa_m)}{1 + (1 - V_f)(\kappa_i - \kappa_m)/(\kappa_m + \frac{4}{3}\mu_m)}. \tag{A.68}$$

A.1.5 Mori-Tanaka method

Premise

The key to the method is essentially mathematical rather than physical involving average strain, average stress, concentration tensors for dilute and non-dilute conditions.

The Mori-Tanaka method involves complex manipulations of the field variables and concepts of eigenstrain and backstress [102]. Benveniste [11] provided more simplified derivation of the Mori-Tanaka method. Let's consider a two-phase composite system with far field conditions providing a uniform strain $\bar{\varepsilon}$. For a two phase system, the average strain is given by [102]

$$\bar{\varepsilon} = c_1\bar{\varepsilon}_1 + c_2\bar{\varepsilon}_2. \tag{A.69}$$

Let's define the effective stiffness tensor by $\mathbf{C}$ as

$$\bar{\sigma} = \mathbf{C}\bar{\varepsilon}. \tag{A.70}$$

Then

$$\mathbf{C}\bar{\varepsilon} = \mathbf{C}_1\bar{\varepsilon} + c_2[\bar{\sigma}_2 - \mathbf{C}_1\bar{\varepsilon}_2], \tag{A.71}$$

209

where

$$\overline{\sigma}_2 = C_2 \overline{\varepsilon}_2 \qquad (A.72)$$

with C_1 and C_2 being the stiffness tensors of the two phases. Let the phase 2 be the inclusion phase. Then under dilute conditions, one writes

$$\overline{\varepsilon}_2 = T\overline{\varepsilon}, \qquad (A.73)$$

where T is the strain concentration tensor. It follows directly from the field variable solution of the dilute suspension problem. Combining Eq.(A.71) and Eq.(A.73) gives

$$C = C_1 + c_2(C_2 - C_1)T. \qquad (A.74)$$

Now the Mori-Tanaka method can be given for generalizing the dilute solution form (Eq.(A.74)) to non-dilute conditions. Let's define a tensor A through

$$\overline{\varepsilon}_2 = A\overline{\varepsilon}. \qquad (A.75)$$

Using Eq.(A.71) yields

$$C = C_1 + c_2(C_2 - C_1)A \qquad (A.76)$$

In order to determine A, let's introduce a new tensor G such that

$$\overline{\varepsilon}_2 = G\overline{\varepsilon}_1, \qquad (A.77)$$

where G is dependent upon the concentration of the inclusion phase. With some manipulation of Eqs.(A.76) and (A.77), one obtains [102]

$$A = [c_1 I + c_2 G]^{-1} G. \qquad (A.78)$$

The Mori-Tanaka method when applied to the spherical inclusion problem under non-dilute condi-

210

tion gives [102]

$$\mu = \mu_m + c_2(\mu_i - \mu_m)\frac{1}{1 + (1 - c_2)(\mu_i - \mu_m)/[\mu_m + \mu_m(9\kappa_m + 8\mu_m)/6(\kappa_m + 2\mu_m)]}, \quad (A.79)$$

$$\kappa = \kappa_m + c_2(\kappa_i - \kappa_m)\frac{1}{1 + (1 - c_2)(\kappa_i - \kappa_m)/(\kappa_m + \frac{4}{3}\mu_m)}. \quad (A.80)$$

These Mori-Tanaka results correspond to the lower bound of the Hashin-Shtrikman bounds.

A.1.6 Differential method

<u>Premise</u>

The model views the overall composite as a sequence of dilute suspensions as shown in Figure A.4.
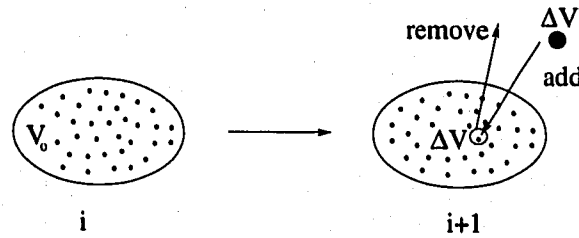
Figure A.4: Schematic of Differential Method

The original work was done by Bruggeman, but not in the mechanics context. Later Roscoe [122] developed and applied the method to model the behavior of fluid suspension. The starting point is the well known dilute suspension result for the effective shear and bulk moduli of the a macro-scopically isotropic composite containing non-interacting spherical inclusions given by

$$\kappa = \kappa_m + \frac{c(\kappa_i - \kappa_m)}{1 + (\kappa_i - \kappa_m)/(\kappa_m + \frac{4}{3}\mu_m)}, \quad (A.81)$$

$$\mu = \mu_m + \frac{c(\mu_i - \mu_m)}{1 + (\mu_i - \mu_m)/\{\mu_m + (9\kappa_m + 8\mu_m)\mu_m/(6\kappa_m + 12\mu_m)\}}, \quad (A.82)$$

where c is the volume fraction of the inclusion. One can add an infinitesimal volume ΔV in a unit volume of the homogenized material. The new mixture is a two-phase composite, with matrix moduli κ and μ, and inclusion's volume fraction $\Delta V/(1+\Delta V)$. From the classical inclusion problems

for spheres, the effective moduli increase by [122]

$$
\begin{aligned}
\kappa + d\kappa &= \kappa + \frac{\Delta V}{1 + \Delta V} \frac{\kappa_i - \kappa}{1 + (\kappa_i - \kappa)/(\kappa + \frac{4}{3}\mu)}, \\
\mu + d\mu &= \mu + \frac{\Delta V}{1 + \Delta V} \frac{\mu_i - \mu}{1 + (\mu_i - \mu)/\{\mu + (9\kappa + 8\mu)\mu/(6\kappa + 12\mu)\}}.
\end{aligned}
\tag{A.83}
$$

Since the increase in the volume fraction of the inclusion phase is given by

$$
dv = \frac{c + \Delta V}{1 + \Delta V} - c = \frac{\Delta V}{1 + \Delta V}(1 - c),
\tag{A.84}
$$

one obtains the following coupled differential equations for the effective moduli of the composite [122]

$$
\begin{aligned}
\frac{d\kappa}{dc} &= \frac{1}{1 - c} \frac{\kappa_i - \kappa}{1 + (\kappa_i - \kappa)/(\kappa + \frac{4}{3}\mu)}, \\
\frac{d\mu}{dc} &= \frac{1}{1 - c} \frac{\mu_i - \mu}{1 + (\mu_i - \mu)/\{\mu + (9\kappa + 8\mu)\mu/(6\kappa + 12\mu)\}},
\end{aligned}
\tag{A.85}
$$

where

$$
\kappa(0) = \kappa_m \ , \ \mu(0) = \mu_m \ , \ 0 \leq c \leq 1.
\tag{A.86}
$$

The solution must satisfy the condition

$$
\kappa(1) = \kappa_i \ , \ \mu(1) = \mu_i.
\tag{A.87}
$$

A.1.7 Rule of mixtures

The simplest is the classical linear rule of mixtures for two phase materials given by

$$
P = c_1 P_1 + c_2 P_2,
\tag{A.88}
$$

where P is a typical material property, and c_1 and c_2 are the volume fraction of the two constituents. Another well-known mixture rule is the harmonic mean given by

$$
P = \frac{P_1 P_2}{c_1 P_2 + c_2 P_1}.
\tag{A.89}
$$

212

A.1.8 Comparison of selected models

The comparisons of several micromechanics models are given in order. Let's consider the silicon carbide (SiC)-carbon (C) FGM system with material properties

$$E_{SiC} = 320GPa \quad , \quad \nu_{SiC} = 0.25,$$

$$E_C = 28GPa \quad , \quad \nu_C = 0.3.$$

Figures A.5 and A.6 show the effective bulk and shear moduli for a spherical inclusion in a continuous matrix as a function of SiC volume fraction using the standard micromechanical models discussed above.
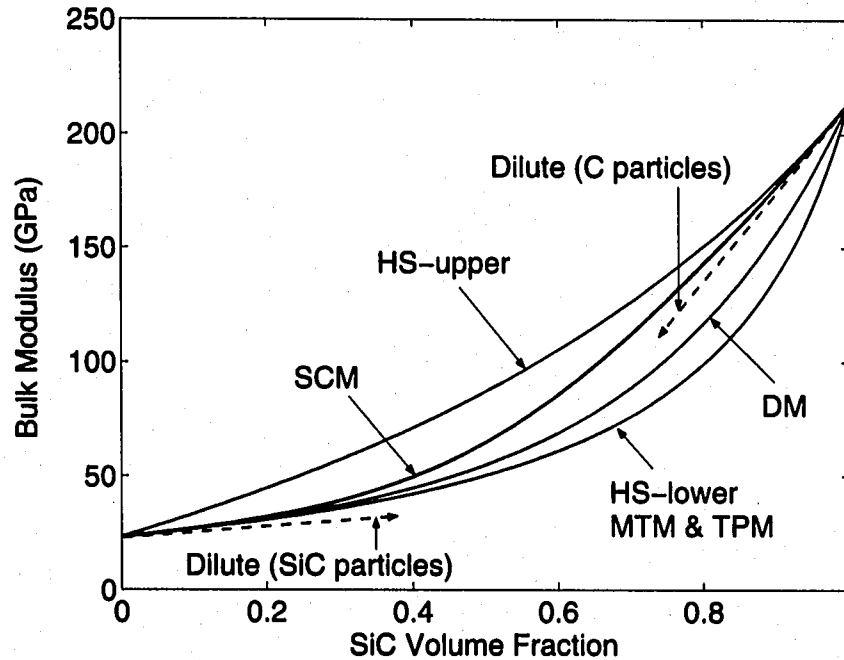
Figure A.5: Bulk modulus of the SiC/C FGM system estimated by using several micromechanics models.

Zuiker [154] investigated and compared the several standard micromechanical models on the basis of requirements of any micromechanical method applied to FGMs. The first requirement is that the effective elastic property estimates must reside within the Hashin-Shtrikman bounds. The second is that at the very low and high volume fractions the effective properties should match the
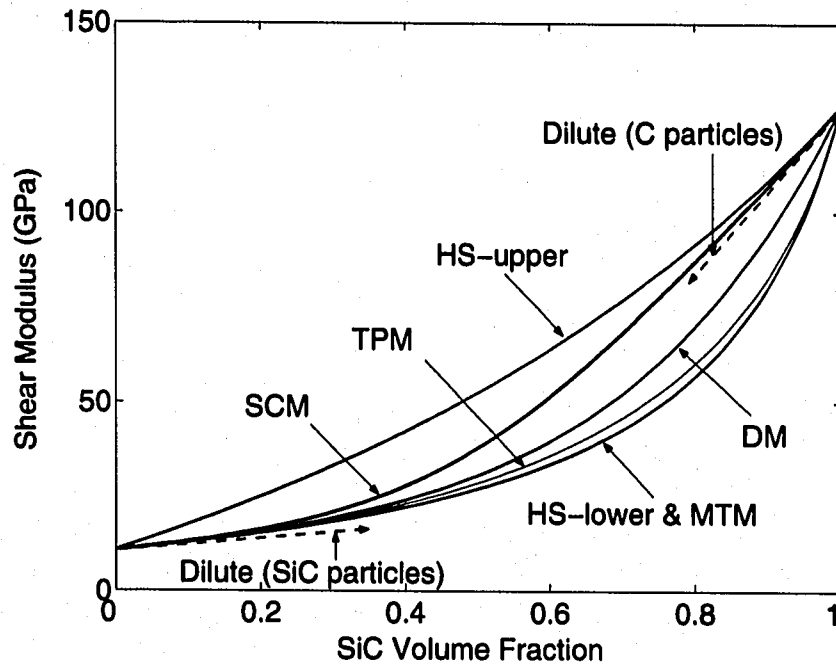
Figure A.6: Shear modulus of the SiC/C FGM system estimated by using several micromechanics models.

estimates of the dilute approximation when it is assumed that the lower volume fraction phase is the particulate phase. The Self-Consistent Method provides estimates which satisfy the Hashin-Shtrikman bounds and follow the dilute estimates in the limit at both extremes of volume fraction.

A.1.9 Matlab© Code

The several micromechanics models are written in the MATLAB code as follows.

Hashin-Shtrikman bounds

```
% material properties of each phase
e1=28;
e2=320;
v1=0.3;
v2=0.25;
mu1=e1/(2*(1+v1));
mu2=e2/(2*(1+v2));
```

```
kappa1=e1/(3*(1-2*v1));
kappa2=e2/(3*(1-2*v2));
% thickness of the graded region
h=1;
expon=1;
for j=1:expon
x=[0:0.01:1];
VF1 = 1-(x.^j/h^j);
VF2 = (x.^j/h^j);
kappa_low = kappa2+VF1./(1/(kappa1-kappa2)+(3*VF2./(3*kappa2+4*mu2)));
kappa_up = kappa1+VF2./(1/(kappa2-kappa1)+(3*VF1./(3*kappa1+4*mu1)));
mu_low = mu2+VF1./(1/(mu1-mu2)+(6*VF2.*(kappa2+2*mu2)/(5*mu2*(3*kappa2+4*mu2))));
mu_up = mu1+VF2/(1/(mu2-mu1)+(6*VF1*(kappa1+2*mu1)/(5*mu1*(3*kappa1+4*mu1))));
E_low=9*(kappa_low*mu_low)/(3*kappa_low+mu_low);
E_up=9*(kappa_up*mu_up)/(3*kappa_up+mu_up);
v_up=E_up/(2*mu_up)-1;
v_low=E_low/(2*mu_low)-1;
end
```

Self-Consistent Method

```
% material properties of each phase
e1=28;
e2=320;
v1=0.3;
v2=0.25;
mu1=e1/(2*(1+v1));
mu2=e2/(2*(1+v2));
k1=e1/(3*(1-2*v1));
```

```
k2=e2/(3*(1-2*v2));
% thickness of the graded region
h = 1;
m=0;
expon=1;
for i=0:0.01:1
c1 = 1-(i/h)^expon;
c2 = 1-c1;
nwhile=0;
aa1=32/9;
bb1= 8/3*k1+8/3*k2-32/9*mu1-32/9*mu2+4/3*c1*k1+4/3*c2*k2+80/9*c1*mu2+80/9*c2*mu1;
cc1=-8/3*k2*mu1+32/9*mu2*mu1+20/3*c1*mu2*k2-80/9*c1*mu2*mu1+20/3*c2*mu1*k1-80/9*...
c2*mu1*mu2+2*k1*k2-8/3*k1*mu2-8/3*k2*mu2-8/3*k1*mu1+c1*k1*k2-4/3*c1*k1*mu1+...
16/3*c1*k1*mu2+c2*k2*k1+16/3*c2*k2*mu1-4/3*c2*k2*mu2;
dd1=-2*k1*k2*mu1-2*k1*k2*mu2+8/3*k1*mu2*mu1-20/3*c1*mu2*k2*mu1-20/3*c2*mu1*k1*mu2...
-c1*k1*k2*mu1+4*c1*k1*k2*mu2-16/3*c1*k1*mu2*mu1+4*c2*k2*k1*mu1-c2*k2*k1*mu2...
-16/3*c2*k2*mu2*mu1+8/3*k2*mu2*mu1;
ee1=2*k1*k2*mu2*mu1-4*c1*k1*k2*mu2*mu1+4*c2*k2*k1*mu1-4*c2*k2*k1*mu2*mu1;
m=1/2*(1/(c1/mu1+1/mu2-c1/mu2)+(c1*mu1+mu2-c1*mu2));
g=1;
tol=1e-06;
while (abs(g) > tol)
g=aa1*m^4+bb1*m^3+cc1*m^2+dd1*m+ee1;
m=m-g/(4*aa1*m^3+3*bb1*m^2+2*cc1*m+dd1);
nwhile=nwhile+1;
if(nwhile > 20)
tol=1e-05;
end
end
```

216

```
mu = m;
kappa=-4/3*mu+(k2+4/3*mu)*(k1+4/3*mu)/((1-c1)*(k1+4/3*mu)+c1*(k2+4/3*mu));
E = 9*(kappa*mu)/(3*kappa+mu);
v = E/(2*mu)-1;
end
```

Three Phase Model

```
% material propeties of each phase
e1=28;
e2=320;
v1=0.3;
v2=0.25;
mu1=e1/(2*(1+v1));
mu2=e2/(2*(1+v2));
kappa1=e1/(3*(1-2*v1));
kappa2=e2/(3*(1-2*v2));
% thickness of the graded region
h=1;
expon=1;
% relevant constants
eta1=(49-50*v1*v2)*(mu2/mu1-1)+35*(mu2/mu1)*(v2-2*v1)+35*(2*v2-v1);
eta2=5*v2*(mu2/mu1-8)+7*(mu2/mu1+4);
eta3=mu2/mu1*(8-10*v1)+(7-5*v1);
for j=1:expon
for i=0:0.01:1
% volume fraction
VF1 = 1-(i/h)^j;
VF2 = 1-VF1;
%
```

```
A = 8*(mu2/mu1-1)*(4-5*v1)*eta1*VF2∧(10/3)-2*(63*(mu2/mu1-1)*eta2...

+2*eta1*eta3)*VF2∧(7/3)+252*(mu2/mu1-1)*eta2*VF2∧(5/3)-50*...

( mu2/mu1-1)*(7-12*v1+8*v1∧2)*eta2*VF2+4*(7-10*v1)*eta2*eta3;

%

B = -2*(mu2/mu1-1)*(1-5*v1)*eta1*VF2∧(10/3)+2*(63*(mu2/mu1-1)*eta2...

+2*eta1*eta3)*VF2∧(7/3)-252*(mu2/mu1-1)*eta2*VF2∧(5/3)+75*...

(mu2/mu1-1)*(3-v1)*v1*eta2*VF2+3/2*(15*v1-7)*eta2*eta3;

%

C = 4*(mu2/mu1-1)*(5*v1-7)*eta1*VF2∧(10/3)-2*(63*(mu2/mu1-1)*eta2+...

2*eta1*eta3)*VF2∧(7/3)+252*(mu2/mu1-1)*eta2*VF2∧(5/3)+25*...

(mu2/mu1-1)*(v1∧2-7)*eta2*VF2-(7+5*v1)*eta2*eta3;

D=(B)∧2-A*C;

mu = (-B+D∧(0.5))/(A)*mu1;

kappa = kappa1+VF2*(kappa2-kappa1)/(1+VF1*(kappa2-kappa1)/...

(kappa1+4/3*mu1));

E=9*(kappa*mu)/(3*kappa+mu);

v=E/(2*mu)-1;

end

end



Mori-Tanaka Method

% material properties of each phase

e1=28;

e2=320;

v1=0.3;

v2=0.25;

mu1=e1/(2*(1+v1));

mu2=e2/(2*(1+v2));
```

```
kappa1=e1/(3*(1-2*v1));

kappa2=e2/(3*(1-2*v2));

% thickness of the graded region

h=1;

expon=1;

for j=1:expon

for i=0:0.01:1

VF1 = 1-(i/h)^j;

VF2 = 1-VF1;

mu = mu2+VF1*(mu1-mu2)*1/(1+(1-VF1)*(mu1-mu2)/(mu2+(mu2*...

(9*kappa2+8*mu2)/(6*(kappa2+2*mu2)))))

kappa = kappa2+VF1*(kappa1-kappa2)/(1+VF2*(kappa1-kappa2)...

/(kappa2+4/3*mu2));

E = 9*(kappa*mu)/(3*kappa+mu);

v = E/(2*mu)-1;

end

end
```

Differential Method

```
% material properties of each phase

e1=28;

e2=320;

v1=0.3;

v2=0.25;

m1=e1/(2*(1+v1));

m2=e2/(2*(1+v2));

k1=e1/(3*(1-2*v1));

k2=e2/(3*(1-2*v2));
```

```matlab
tlow = 0;

tup = 0.9999;

ylow = [m1, k1];

tspan=[tlow tup];

options=odeset('RelTol',1e-8,'AbsTol',[1e-8,1e-8]);

[t,y] = ode45('odequation', tspan ,ylow);

Esize = size(y);

E = zeros(Esize,1);

v = zeros(Esize,1);

for i = 1: Esize

E(i,1)= 9*y(i,1)*y(i,2)/(3*y(i,2)+y(i,1));

v(i,1)=(3*y(i,2)-2*y(i,1))/(2*(3*y(i,2)+y(i,1)));

end


% function called

function yp = odequation(t,y);

expon=1;

% thickness of the graded region

h=1;

yp = zeros(2,1);

e2=320;

v2=0.25;

m2=e2/(2*(1+v2));

k2=e2/(3*(1-2*v2));

yp(1)=1/(1-(t/h)^expon)*(m2-y(1))/(1+(m2-y(1))/(y(1)+(9*y(2)+8*y(1))*y(1))...
/(6*y(2)+12*y(1))))*expon*t^(expon-1)/h^expon;

yp(2) = -(y(2)-k2)/(1-(t/h)^expon)/(1+(k2-y(2))/(y(2)+4/3*y(1)))...
*expon*t^(expon-1)/h^expon;
```

A.2 Anisotropic elasticity

The generalized Hooke's law for stress-strain relationship is given by [95]

$$\varepsilon_i = a_{ij}\sigma_j, \quad a_{ij} = a_{ji} \ (i,j = 1,2,...,6) \tag{A.90}$$

where the compliance coefficients, a_{ij}, are contracted notations of the compliance tensor S_{ijkl} and

$$\varepsilon_1 = \varepsilon_{11}, \quad \varepsilon_2 = \varepsilon_{22}, \quad \varepsilon_3 = \varepsilon_{33}, \quad \varepsilon_4 = 2\varepsilon_{23}, \quad \varepsilon_5 = 2\varepsilon_{13}, \quad \varepsilon_6 = 2\varepsilon_{12}$$

$$\sigma_1 = \sigma_{11}, \quad \sigma_2 = \sigma_{22}, \quad \sigma_3 = \sigma_{33}, \quad \sigma_4 = \sigma_{23}, \quad \sigma_5 = \sigma_{13}, \quad \sigma_6 = \sigma_{12}. \tag{A.91}$$

For plane stress, the a_{ij} components of interest are

$$a_{ij} \ (i,j = 1,2,6) \tag{A.92}$$

and for plane strain, the a_{ij} components are exchanged with b_{ij} as follows:

$$b_{ij} = a_{ij} - \frac{a_{i3}a_{j3}}{a_{33}} \ (i,j = 1,2,6). \tag{A.93}$$

Two dimensional anisotropic elasticity problems can be formulated in terms of the analytic functions, $\phi_k(z_k)$, of the complex variable, $z_k = x_k + iy_k$ $(k = 1,2)$, $i = \sqrt{-1}$, where

$$x_k = x + \alpha_k y, \quad y_k = \beta_k y \ (k = 1,2). \tag{A.94}$$

The parameters α_k and β_k are the real and imaginary parts of $\mu_k = \alpha_k + i\beta_k$, which can be determined from the following characteristic equation [95]

$$a_{11}\mu^4 - 2a_{16}\mu^3 + (2a_{12} + a_{66})\mu^2 - 2a_{26}\mu + a_{22} = 0, \tag{A.95}$$

where the roots μ_k are always complex or purely imaginary in conjugate pairs as $\mu_1, \overline{\mu_1}; \mu_2, \overline{\mu_2}$.

A.3 Representative functions for SIFs

For orthotropic FGMs, the representative functions $\boldsymbol{f}(r^{1/2}, \theta, \boldsymbol{a}^{\text{tip}})$ in Eq. (3.1) are given by [131]:

$$f_1^I = \sqrt{2r/\pi}\,\text{Re}\left[\frac{1}{\mu_1^{\text{tip}} - \mu_2^{\text{tip}}}\left\{\mu_1^{\text{tip}}p_2\sqrt{\cos\theta + \mu_2^{\text{tip}}\sin\theta} - \mu_2^{\text{tip}}p_1\sqrt{\cos\theta + \mu_1^{\text{tip}}\sin\theta}\right\}\right],$$

$$f_1^{II} = \sqrt{2r/\pi}\,\text{Re}\left[\frac{1}{\mu_1^{\text{tip}} - \mu_2^{\text{tip}}}\left\{p_2\sqrt{\cos\theta + \mu_2^{\text{tip}}\sin\theta} - p_1\sqrt{\cos\theta + \mu_1^{\text{tip}}\sin\theta}\right\}\right],$$

$$f_2^I = \sqrt{2r/\pi}\,\text{Re}\left[\frac{1}{\mu_1^{\text{tip}} - \mu_2^{\text{tip}}}\left\{\mu_1^{\text{tip}}q_2\sqrt{\cos\theta + \mu_2^{\text{tip}}\sin\theta} - \mu_2^{\text{tip}}q_1\sqrt{\cos\theta + \mu_1^{\text{tip}}\sin\theta}\right\}\right],$$

$$f_2^{II} = \sqrt{2r/\pi}\,\text{Re}\left[\frac{1}{\mu_1^{\text{tip}} - \mu_2^{\text{tip}}}\left\{q_2\sqrt{\cos\theta + \mu_2^{\text{tip}}\sin\theta} - q_1\sqrt{\cos\theta + \mu_1^{\text{tip}}\sin\theta}\right\}\right],$$

where Re denotes the real part of the complex function, μ_1^{tip} and μ_2^{tip} denote crack-tip material parameters, which are obtained from Eq.(A.95) and taken for $\beta_k > 0$ $(k = 1, 2)$, and p_k and q_k are given by

$$p_k = a_{11}^{\text{tip}}(\mu_k^{\text{tip}})^2 + a_{12}^{\text{tip}} - a_{16}^{\text{tip}}\mu_k^{\text{tip}}, \qquad q_k = a_{12}^{\text{tip}}\mu_k^{\text{tip}} + \frac{a_{22}^{\text{tip}}}{\mu_k^{\text{tip}}} - a_{26}^{\text{tip}}, \qquad \text{(A.96)}$$

respectively.

The functions $g(r^{-1/2}, \theta, \boldsymbol{a}^{\text{tip}})$ in Eq. (3.3) are given by [131]:

$$g_{11}^I = \frac{1}{\sqrt{2\pi r}}\,\text{Re}\left[\frac{\mu_1^{\text{tip}}\mu_2^{\text{tip}}}{\mu_1^{\text{tip}} - \mu_2^{\text{tip}}}\left\{\frac{\mu_2^{\text{tip}}}{\sqrt{\cos\theta + \mu_2^{\text{tip}}\sin\theta}} - \frac{\mu_1^{\text{tip}}}{\sqrt{\cos\theta + \mu_1^{\text{tip}}\sin\theta}}\right\}\right]$$

$$g_{11}^{II} = \frac{1}{\sqrt{2\pi r}}\,\text{Re}\left[\frac{1}{\mu_1^{\text{tip}} - \mu_2^{\text{tip}}}\left\{\frac{(\mu_2^{\text{tip}})^2}{\sqrt{\cos\theta + \mu_2^{\text{tip}}\sin\theta}} - \frac{(\mu_1^{\text{tip}})^2}{\sqrt{\cos\theta + \mu_1^{\text{tip}}\sin\theta}}\right\}\right]$$

$$g_{22}^I = \frac{1}{\sqrt{2\pi r}}\,\text{Re}\left[\frac{1}{\mu_1^{\text{tip}} - \mu_2^{\text{tip}}}\left\{\frac{\mu_1^{\text{tip}}}{\sqrt{\cos\theta + \mu_2^{\text{tip}}\sin\theta}} - \frac{\mu_2^{\text{tip}}}{\sqrt{\cos\theta + \mu_1^{\text{tip}}\sin\theta}}\right\}\right]$$

$$g_{22}^{II} = \frac{1}{\sqrt{2\pi r}}\,\text{Re}\left[\frac{1}{\mu_1^{\text{tip}} - \mu_2^{\text{tip}}}\left\{\frac{1}{\sqrt{\cos\theta + \mu_2^{\text{tip}}\sin\theta}} - \frac{1}{\sqrt{\cos\theta + \mu_1^{\text{tip}}\sin\theta}}\right\}\right]$$

$$g_{12}^I = \frac{1}{\sqrt{2\pi r}}\,\text{Re}\left[\frac{\mu_1^{\text{tip}}\mu_2^{\text{tip}}}{\mu_1^{\text{tip}} - \mu_2^{\text{tip}}}\left\{\frac{1}{\sqrt{\cos\theta + \mu_1^{\text{tip}}\sin\theta}} - \frac{1}{\sqrt{\cos\theta + \mu_2^{\text{tip}}\sin\theta}}\right\}\right]$$

$$g_{12}^{II} = \frac{1}{\sqrt{2\pi r}}\,\text{Re}\left[\frac{1}{\mu_1^{\text{tip}} - \mu_2^{\text{tip}}}\left\{\frac{\mu_1^{\text{tip}}}{\sqrt{\cos\theta + \mu_1^{\text{tip}}\sin\theta}} - \frac{\mu_2^{\text{tip}}}{\sqrt{\cos\theta + \mu_2^{\text{tip}}\sin\theta}}\right\}\right] \qquad \text{(A.97)}$$

Notice that, in the above expressions, the graded material parameters are sampled at the crack tip.

For isotropic FGMs, the representative functions $f(r^{1/2}, \theta, a^{\text{tip}})$ for displacements in Eq. (3.1), and $g(r^{-1/2}, \theta, a^{\text{tip}})$ for stresses in Eq. (3.3) are given in many references (e.g. [33]). The graded material parameters are sampled at the crack tip.

A.4   Representative functions for T-stress

The presentation follows the Stroh formalism [137]. For orthotropic FGMs, the representative functions $t^u(\ln r, \theta, f, a^{\text{tip}})$ in Eq. (3.4) are given by [137]:

$$t_1^u = -\frac{h_1}{2\pi} \ln r - \frac{1}{2}\left(S_{11}h_1 + S_{12}h_2\right), \qquad t_2^u = -\frac{h_2}{2\pi} \ln r - \frac{1}{2}\left(S_{21}h_1 + S_{22}h_2\right). \qquad \text{(A.98)}$$

The parameters S_{ij} and h_i in Eq.(A.98) are the components in the 2×2 matrix $\boldsymbol{S}(\theta)$, and the 2×1 vector $\boldsymbol{h}$ as follows:

$$\boldsymbol{S}(\theta) = \frac{2}{\pi} \operatorname{Re}\left[\boldsymbol{A}\,\boldsymbol{C}(\theta)\,\boldsymbol{B}^T\right] = \begin{bmatrix} S_{11} & S_{12} \\ S_{21} & S_{22} \end{bmatrix},$$

$$\boldsymbol{h} = \boldsymbol{L}^{-1}\boldsymbol{f} = \left\{ \begin{array}{c} h_1 \\ h_2 \end{array} \right\}, \qquad \text{(A.99)}$$

where

$$\boldsymbol{A} = \begin{bmatrix} \lambda_1^{\text{tip}} p_1^{\text{tip}} & \lambda_2^{\text{tip}} p_2^{\text{tip}} \\ \lambda_1^{\text{tip}} q_1^{\text{tip}} & \lambda_2^{\text{tip}} q_2^{\text{tip}} \end{bmatrix}, \quad \boldsymbol{B} = \begin{bmatrix} -\lambda_1^{\text{tip}} \mu_1^{\text{tip}} & -\lambda_2^{\text{tip}} \mu_2^{\text{tip}} \\ \lambda_1^{\text{tip}} & \lambda_2^{\text{tip}} \end{bmatrix},$$

$$\boldsymbol{C}(\theta) = \begin{bmatrix} \ln s_1(\theta) & 0 \\ 0 & \ln s_2(\theta) \end{bmatrix}, \quad s_k(\theta) = \cos\theta + \mu_k^{\text{tip}} \sin\theta,$$

$$\boldsymbol{L}^{-1} = \operatorname{Re}\left[i\boldsymbol{A}\boldsymbol{B}^{-1}\right], \quad \boldsymbol{f} = [f, 0]^T, \qquad \text{(A.100)}$$

in which p_k^{tip} and q_k^{tip} ($k = 1, 2$) are given by Eq.(A.96), and λ_k^{tip} ($k = 1, 2$) is the normalization factor given by the expression

$$2(\lambda_k^{\text{tip}})^2(q_k^{\text{tip}}/\mu_k^{\text{tip}} - \mu_k^{\text{tip}} p_k^{\text{tip}}) = 1. \qquad \text{(A.101)}$$

The representative functions $t^s(r^{-1}, \theta, f, a^{\text{tip}})$ in Eq. (3.6) are given by [137]:

$$t_{11}^s = \sigma_{rr}^{aux} \cos^2 \theta, \qquad t_{22}^s = \sigma_{rr}^{aux} \sin^2 \theta, \quad t_{12}^s = \sigma_{rr}^{aux} \sin \theta \cos \theta, \qquad (\text{A.102})$$

where the auxiliary stresses are given by [137] ($k = 1, 2$):

$$\sigma_{rr}^{aux} = \frac{1}{2\pi r} n^T(\theta) N_3(\theta) h, \quad \sigma_{\theta\theta}^{aux} = \sigma_{r\theta}^{aux} = 0, \qquad (\text{A.103})$$

in which

$$n = [\cos \theta, \sin \theta]^T, \quad N_3(\theta) = 2 \text{ Re } [B \, P(\theta) \, B^T],$$

$$P(\theta) = \begin{bmatrix} \mu_1(\theta) & 0 \\ 0 & \mu_2(\theta) \end{bmatrix}, \quad \mu_k(\theta) = \frac{\mu_k^{\text{tip}} \cos \theta - \sin \theta}{\mu_k^{\text{tip}} \sin \theta + \cos \theta}. \qquad (\text{A.104})$$

For isotropic FGMs, the representative functions $t^u(\ln r, \theta, f, a^{\text{tip}})$ in Eq. (3.4) for displacements, and $t^s(r^{-1}, \theta, f, a^{\text{tip}})$ for stresses in Eq. (3.6) are given in many references (e.g. [136]) The graded material parameters are sampled at the crack tip.

A.5 Shape functions for four Gauss points of six-node triangular element

The shape functions for four Gauss points of a T6 element have a bilinear form given by

$$N(\xi, \eta) \;=\; a_1 + a_2 \xi + a_3 \eta + a_4 \xi \eta, \qquad (\text{A.105})$$

where ξ and η are triangular natural coordinates as shown in Figure A.7.
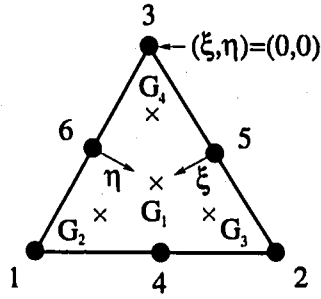
Figure A.7: Four-point Gaussian quadrature for a T6 element.

The locations of four Gauss points are given by

$$
\begin{aligned}
G_1(\xi_1, \eta_1) &\;\rightarrow\; \xi = \frac{1}{3}, \eta = \frac{1}{3}, \\
G_2(\xi_2, \eta_2) &\;\rightarrow\; \xi = \frac{3}{5}, \eta = \frac{1}{5}, \\
G_3(\xi_3, \eta_3) &\;\rightarrow\; \xi = \frac{1}{5}, \eta = \frac{3}{5}, \\
G_4(\xi_4, \eta_4) &\;\rightarrow\; \xi = \frac{1}{5}, \eta = \frac{1}{5}.
\end{aligned}
$$

In order to determine four unknowns in Eq.(A.105), one substitutes natural coordinates (ξ_j, η_j) corresponding to each Gauss point into Eq.(A.105) as follows:

$$
N_i(\xi_j, \eta_j) \;=\; a_1 + a_2\xi_j + a_3\eta_j + a_4\xi_j\eta_j \quad (i,j = 1,...,4), \tag{A.106}
$$

where

$$
N_i = 1.0 \quad \text{for } i = j
$$

$$
N_i = 0.0 \quad \text{for } i \neq j \tag{A.107}
$$

For each Gauss point, we have four system of equations as follows:

$$
\boldsymbol{n} = \boldsymbol{T a} \tag{A.108}
$$

225

where

$$n = [\delta_{1j} \ \delta_{2j} \ \delta_{3j} \ \delta_{4j}]^T,$$

$$T = \begin{bmatrix} 1 & \xi_1 & \eta_1 & \xi_1\eta_1 \\ 1 & \xi_2 & \eta_2 & \xi_2\eta_2 \\ 1 & \xi_3 & \eta_3 & \xi_3\eta_3 \\ 1 & \xi_4 & \eta_4 & \xi_4\eta_4 \end{bmatrix},$$

$$a = [a_1 \ a_2 \ a_3 \ a_4]^T. \tag{A.109}$$

Thus the unknown vector a is determined for each Gauss points as:

$$a = T^{-1}n. \tag{A.110}$$

Now the shape functions are given by

$$
\begin{aligned}
N_1 &= \frac{9}{4} - \frac{45}{4}\xi - \frac{45}{4}\eta + \frac{225}{4}\xi\eta, \\
N_2 &= -\frac{5}{4} + \frac{25}{4}\xi + \frac{15}{4}\eta - \frac{75}{4}\xi\eta, \\
N_3 &= -\frac{5}{4} + \frac{15}{4}\xi + \frac{25}{4}\eta - \frac{75}{4}\xi\eta, \\
N_4 &= \frac{5}{4} + \frac{5}{4}\xi + \frac{5}{4}\eta - \frac{75}{4}\xi\eta.
\end{aligned} \tag{A.111}
$$

References

[1] J. Abanto-Bueno and J. Lambros. Investigation of crack growth in functionally graded materials using digital image correlation. *Engineering Fracture Mechanics*, 69(14-16):1695–1711, 2002.

[2] J. Aboudi, S. M. Arnold, and M.-J. Pindera. Response of functionally graded composites to thermal gradients. *Composites Engineering*, 4(1):1–18, 1994.

[3] J. Aboudi, M.-J. Pindera, and S. M. Arnold. Elastic response of matal matrix composites with tailored microstructures to thermal gradients. *International Journal of Solids and Structures*, 31(10):1393–1428, 1994.

[4] J. M. Ambrico, E. E. Jones, and M. R. Begley. Cracking in thin multi-layers with finite width and periodic architectures. *International Journal of Solids and Structures*, 39(6):1443–1462, 2002.

[5] T. L. Anderson. *Fracture Mechanics: Fundamentals and Applications*. CRC Press LLC, Boca Raton, 1995.

[6] G. Anlas, J. Lambros, and M. H. Santare. Dominance of asymptotic crack tip fields in functionally graded materials. *International Journal of Fracture*, 115(2):193–204, 2002.

[7] G. Anlas, M. H. Santare, and J. Lambros. Numerical calculation of stress intensity factors in functionally graded materials. *International Journal of Fracture*, 104(2):131–143, 2000.

[8] G. Bao and H. Cai. Delamination cracking in functionally graded coating/metal substrate systems. *Acta Mechanica*, 45(3):1055–1066, 1997.

[9] G. Bao and L. Wang. Multiple cracking in functionally graded ceramic/metal coatings. *International Journal of Solids and Structures*, 32(19):2853–2871, 1995.

[10] K.-J. Bathe. *Finite element procedures*. Prentice-Hall, New Jersey, 1996.

[11] Y. Benveniste. A new approach to the application of Mori-Tanaka's theory in composite materials. *Mechanics of Materials*, 6(2):147–157, 1987.

[12] T. N. Bittencourt, P. A. Wawrzynek, and A. R. Ingraffea. Quasi-static simulation of crack propagation for 2D LEFM problems. *Engineering Fracture Mechanics*, 55(2):321–334, 1996.

[13] P. O. Bouchard, F. Bay, and Y. Chastel. Numerical modelling of crack propagation: automatic remeshing and comparison of different criteria. *Computer Methods in Applied Mechanics and Engineering*, 192(35-36):3887–3908, 2003.

[14] B. Budiansky. On the elastic moduli of some heterogeneous materials. *Journal of the Mechanics and Physics of Solids*, 13(4):223–227, 1965.

[15] B. Budiansky and J. R. Rice. Conservation laws and energy-release rates. *Journal of Applied Mechanics, Transactions ASME*, 40(1):201–203, 1973.

[16] G. E. Cardew, M. R. Goldthorpe, I. C. Howard, and A. P. Kfouri. On the elastic T-term. *Fundamentals of Deformation and Fracture: Eshelby Memorial Symposium*, 1985.

[17] R. D. Carpenter, W. W. Liang, G. H. Paulino, J. C. Gibeling, and Z. A. Munir. Fracture testing and analysis of a layered functionally graded Ti/TiB beam in 3-point bending. *Materials Science Forum*, 308-311:837–842, 1999.

[18] E. M. Carrillo-Heian, R. D. Carpenter, G. H. Paulino, J. C. Gibeling, and Z. A. Munir. Dense layered molybdenum disilicide-silicon carbide functionally graded composites formed by field-activated synthesis. *Journal of the American Ceramic Society*, 84(5):962–968, 2001.

[19] Y.-S. Chan, G. H. Paulino, and A. C. Fannjiang. The crack problem for nonhomogeneous materials under antiplane shear loading – A displacement based formulation. *International Journal of Solids and Structures*, 38(17):2989–3005, 2001.

[20] J. H. Chang and A. J. Chien. Evaluation of M-integral for anisotropic elastic media with multiple defects. *International Journal of Fracture*, 114(3):267–289, 2002.

[21] Y.-J. Chao and X. H. Zhang. Constraint effect in brittle fracture. In R. S. Piascik, J. C. Newman, and D.E. Dowling, editors, *Fatigue and Fracture Mechanics*, ASTM STP 1296, pages 41–60, Philadelphia, PA, 1997. American Society for Testing and Materials.

[22] C. S. Chen, R. Krause, R. G. Pettit, L. Banks-Sills, and A. R. Ingraffea. Numerical assessment of T-stress computation using a p-version finite element method. *International Journal of Fracture*, 107(2):177–199, 2001.

[23] J. Chen, L. Wu, and S. Du. A modified J integral for functionally graded materials. *Mechanics Research Communications*, 27(3):301–306, 2000.

[24] R. M. Christensen. *Mechanics of Composite Materials*. John Wiley, New York, 1979.

[25] R. M. Christensen and K. H. Lo. Solutions for effective shear properties in three phase sphere and cylinder models. *Journal of the Mechanics and Physics of Solids*, 27(4):315–330, 1979.

[26] R. D. Cook, D. S. Malkus, M. E. Plesha, and R. J. Witt. *Concepts and Applications of Finite Element Analysis*. (4th edition). John Wiley & Sons, Inc., New York, 2001.

[27] B. Cotterell and J. R. Rice. Slightly curved or kinked cracks. *International Journal of Fracture*, 16(2):155–169, 1980.

[28] F. Delale and F. Erdogan. The crack problem for a nonhomogeneous plane. *Journal of Applied Mechanics, Transactions ASME*, 50(3):609–614, 1983.

[29] F. Delale and F. Erdogan. On the mechanical modeling of an interfacial region in bonded half-planes. *Journal of Applied Mechanics, Transactions ASME*, 55(2):317–324, 1988.

[30] J. L. Desplat. Recent development on oxigenated thermionic energy converter - overview. In *Proceedings of the Fourth International Symposium on Functionally Gradient Materials*, Tsukuba City, Japan, 1996.

[31] J. Dolbow and M. Gosz. On the computation of mixed-mode stress intensity factors in functionally graded materials. *International Journal of Solids and Structures*, 39(9):2557–2574, 2002.

[32] Z.-Z. Du and J. W. Hancock. The effect of non-singular stresses on crack-tip constraint. *Journal of the Mechanics and Physics of Solids*, 39(3):555–567, 1991.

[33] J. Eftis, N. Subramonian, and H. Liebowitz. Crack border stress and displacement equations revisited. *Engineering Fracture Mechanics*, 9(1):189–210, 1977.

[34] J. W. Eischen. Fracture of non-homogeneous materials. *International Journal of Fracture*, 34(1):3–22, 1987.

[35] F. Erdogan. Fracture mechanics of functionally graded materials. *Composites Engineering*, 5(7):753–770, 1995.

[36] F. Erdogan and G. C. Sih. On the crack extension in plates under plane loading and transverse shear. *ASME Journal of Basic Engineering*, 85(4):519–527, 1963.

[37] F. Erdogan and B. H. Wu. Analysis of FGM specimens for fracture toughness testing. In J. B. Holt, M. Koizumi, T. Hirai, and Z. A. Munir, editors, *Proceedings of the Second International Symposium on Functionally Gradient Materials*, volume 34 of *Ceramic Transactions*, pages 39–46, Westerville, Ohio, 1993. The American Ceramic Society.

[38] F. Erdogan and B. H. Wu. Crack problems in FGM layers under thermal stresses. *Journal of Thermal Stresses*, 19(3):237–265, 1996.

[39] F. Erdogan and B. H. Wu. The surface crack problem for a plate with functionally graded properties. *Journal of Applied Mechanics, Transactions ASME*, 64(3):449–456, 1997.

[40] M. Finot and S. Suresh. Small and large deformation of thick and thin-film multi-layers: Effects of layer geometry, plasticity and compositional gradients. *Journal of the Mechanics and Physics od Solids*, 44(5):683–721, 1996.

[41] Y. Fukui, K. Takashima, and C. B. Ponton. Measurement of Young's modulus and internal friction of an *in situ* $Al - Al_3Ni$ functionally graded material. *Journal of Materials Science*, 29(9):2281–2288, 1994.

[42] J. Galvez, M. Elices, G. V. Guinea, and J. Planas. Crack trajectories under mixed mode and non-proportional loading. *International Journal of Fracture*, 81(2):171–193, 1996.

[43] H. Gao and C.-H. Chiu. Slightly curved or kinked cracks in anisotropic elastic solids. *International Journal of Solids and Structures*, 29(8):947–972, 1992.

[44] H. Getto and S. J. Ishihara. Development of the fire retardant door with functional gradient wood. In *Proceedings of the Fourth International Symposium on Functionally Gradient Materials*, Tsukuba City, Japan, 1996.

[45] A. E. Giannakopoulos, S. Suresh, M. Finot, and M. Olsson. Elastoplastic analysis of thermal cycling: layered materials with compositional gradients. *Acta Materialia*, 43(4):1335–1354, 1995.

[46] K. Golos and B. Wasiluk. Role of plastic zone in crack growth direction criterion under mixed mode loading. *International Journal of Fracture*, 102(4):341–353, 2000.

[47] M. Grujicic and Y. Zhang. Determination of effective elastic properties of functionally graded materials using Voronoi cell finite element method. *Materials Science and Engineering A – Structural Materials Properties, Microstructure and Processing*, 251(1-2):64–76, 1998.

[48] P. Gu and R. J. Asaro. Crack deflection in functionally graded materials. *International Journal of Solids and Structures*, 34(24):3085–3098, 1997.

[49] P. Gu and R. J. Asaro. Cracks in functionally graded materials. *International Journal of Solids and Structures*, 34(1):1–17, 1997.

[50] P. Gu, M. Dao, and R. J. Asaro. A simplified method for calculating the crack-tip field of functionally graded materials using the domain integral. *Journal of Applied Mechanics, Transactions ASME*, 34(1):1–17, 1997.

[51] A. S. Gullerud, K. C. Koppenhoefer, A. Roy, S. Roychowdhury, and R. H. Dodds Jr. *WARP3D-Release 13.11*. University of Illinois, UILU-ENG-95-2012, Urbana, Illinois, 2001.

[52] R. B. Haber and H. M. Koh. Explicit expressions for energy release rates using virtual crack extensions. *International Journal for Numerical Methods in Engineering*, 21(2):301–315, 1985.

[53] Z. Hashin and S. Shtrikman. A variational approach to the theory of the elastic behavior of multiphase materials. *Journal of the Mechanics and Physics of Solids*, 11(2):127–140, 1963.

[54] A. V. Hershey. The elasticity of an isotropic aggregate of anisotropic cubic crystals. *Journal of Applied Mechanics, Transactions ASME*, 21(2):236–240, 1954.

[55] Hibbitt, Karlson, and Sorensen. *ABAQUS/Standard User's Manual*. Hibbitt, Karlson,& Sorensen, inc., Vol. II, Pawtucket, RI, Version 6.1 (page 14.1.1-14), 2000.

[56] R. Hill. Continuum micro-mechanics of elastic-plastic polycrystals. *Journal of the Mechanics and Physics of Solids*, 13(2):89–101, 1965.

[57] R. Hill. A self-consistent mechanics of composite materials. *Journal of the Mechanics and Physics of Solids*, 13(4):213–222, 1965.

[58] T. Hirai. Functionally gradient materials and nanocomposites. In J. B. Holt, M. Koizumi, T. Hirai, and Z. A. Munir, editors, *Proceedings of the Second International Symposium on Functionally Gradient Materials*, volume 34 of *Ceramic Transactions*, pages 11–20, Westerville, Ohio, 1993. The American Ceramic Society.

[59] T. Hirano, J. Teraki, and Yamada T. On the design of functionally gradient materials. In M. Yamanouchi, M. Koizumi, T. Hirai, and I. Shiota, editors, *Proceedings of the First International Symposium on Functionally Gradient Materials*, pages 5–10, Sendai, Japan, 1990.

[60] T. Hirano, L. W. Whitlow, and M. Miyajima. Numerical analysis of efficiency improvement in functionally gradient thermoelectric materials. In J. B. Holt, M. Koizumi, T. Hirai, and Z. A. Munir, editors, *Proceedings of the Second International Symposium on Functionally Gradient Materials*, volume 34 of *Ceramic Transactions*, pages 23–30, Westerville, Ohio, 1993. The American Ceramic Society.

[61] T. Honein and G. Herrmann. Conservation laws in nonhomogeneous plane elastostatics. *Journal of the Mechanics and Physics of Solids*, 45(5):789–805, 1997.

[62] M. Hori and N. Vaikuntan. Rigorous formulation of crack path in two-dimensional elastic body. *Mechanics of Materials*, 26(1):1–14, 1997.

[63] Y. Huang and K. C. Hwang. A unified energy approach to a class of micromechanics models for microcracked solids. *Acta Mechanica Solida Sinica*, 8(2):111–120, 1995.

[64] Y. Huang, K. C. Hwang, K. X. Hu, and A. Chandra. A unified energy approach to a class of micromechanics models for composite materials. *Acta Mechanica Sinica*, 11(1):59–75, 1995.

[65] T. J. R. Hughes. *The finite element method: linear static and dynamic finite element analysis*. Prentice-Hall, New Jersey, 1987.

[66] M. A. Hussain, S. L. Pu, and J. Underwood. Strain energy release rate for a crack under combined mode I and mode II. In P. C. Paris and G. R. Irwin, editors, *Fracture Analysis*, ASTM STP 560, pages 2–28, Philadelphia, PA, 1993. American Society for Testing and Materials.

[67] T. Igari, A. Notomi, H. Tsunoda, K. Hida, T. Kotoh, and S. Kunishima. Material properties of functionally gradient material for fast breeder reactor. In M. Yamanouochi, M. Koizumi, T. Hirai, and I. Shiota, editors, *Proceedings of the First International Symposium on Functionally Gradient Materials*, pages 209–214, Sendai, Japan, 1990.

[68] Z.-H. Jin and R. C. Batra. Stress intensity relaxation at the tip of an edge crack in a functionally graded material subjected to a thermal shock. *Journal of Thermal Stresses*, 19(4):317–339, 1996.

[69] Z.-H. Jin and N. Noda. An internal crack parallel to the boundary of a nonhomogeneous half plane under thermal loading. *International Journal of Engineering Science*, 31(5):793–806, 1993.

[70] Z.-H. Jin and G. H. Paulino. Transient thermal stress analysis of an edge crack in a functionally graded material. *International Journal of Fracture*, 107(1):73–98, 2001.

[71] Z.-H. Jin, G. H. Paulino, and R. H. Dodds Jr. Finite element investigation of quasi-static crack growth in functionally graded materials using a novel cohesive zone fracture model. *Journal of Applied Mechanics, Transactions ASME*, 69(3):370–379, 2002.

[72] T. L. Becker Jr., R. M. Cannon, and R. O. Ritchie. Finite crack kinking and T-stresses in functionally graded materials. *International Journal of Solids and Structures*, 38(32-33):5545–5563, 2001.

[73] M. F. Kanninen and C. H. Popelar. *Advanced Fracture Mechanics*. Oxford University Press, New York, 1985.

[74] W. A. Kaysser and B. Ilschner. FGM research activities in Europe. *M.R.S. Bulletin*, 20(1):22–26, 1995.

[75] A. P. Kfouri. Some evaluations of the elastic T-term using Eshelby's method. *International Journal of Fracture*, 30(4):301–315, 1986.

[76] J.-H. Kim and G. H. Paulino. Finite element evaluation of mixed-mode stress intensity factors in functionally graded materials. *International Journal for Numerical Methods in Engineering*, 53(8):1903–1935, 2002.

[77] J.-H. Kim and G. H. Paulino. Isoparametric graded finite elements for nonhomogeneous isotropic and orthotropic materials. *Journal of Applied Mechanics, Transactions ASME*, 69(4):502–514, 2002.

[78] J.-H. Kim and G. H. Paulino. Mixed-mode fracture of orthotropic functionally graded materials using finite elements and the modified crack closure method. *Engineering Fracture Mechanics*, 69(14-16):1557–1586, 2002.

[79] J.-H. Kim and G. H. Paulino. An accurate scheme for mixed-mode fracture analysis of functionally graded materials using the interaction integral and micromechanics models. *International Journal for Numerical Methods in Engineering*, 58(10):1457–1497, 2003.

[80] J.-H. Kim and G. H. Paulino. The interaction integral for fracture of orthotropic functionally graded materials: Evaluation of stress intensity factors. *International Journal of Solids and Structures*, 40(15):3967–4001, 2003.

[81] J.-H. Kim and G. H. Paulino. Mixed-mode J-integral formulation and implementation using graded finite elements for fracture analysis of nonhomogeneous orthotropic materials. *Mechanics of Materials*, 35(1-2):107–128, 2003.

[82] J.-H. Kim and G. H. Paulino. T-stress, mixed-mode stress intensity factors, and crack initiation angles in functionally graded materials: A unified approach using the interaction integral method. *Computer Methods in Applied Mechanics and Engineering*, 192(11-12):1463–1494, 2003.

[83] J.-H. Kim and G. H. Paulino. On the Poisson's ratio effect on mixed-mode stress intensity factors ans T-stress in functionally graded materials. *International Journal of Computational Engineering Science*, 2003 (in press).

[84] J.-H. Kim and G. H. Paulino. Consistent formulations of the interaction integral method for fracture of functionally graded materials. (submitted for publication).

235

[85] J.-H. Kim and G. H. Paulino. T-stress in orthotropic functionally graded materials: Lekhnit-skii and Stroh formalisms. (submitted for publication).

[86] J. K. Knowles and E. Sternberg. On a class of conservation laws in linearized and finite elastostatics. *Archive for Rational Mechanics and Analysis*, 44(2):187–211, 1972.

[87] Y. Koike. Graded-index and single mode polymer optical fibers. In L. Y. Chiang, A.G. Garito, and D. J. Sandman, editors, *Electrical, Optical, and Magnetic Properties of Organic Solid State Materials*, volume 247, page 817, Materials Research Society Proceedings, Pittsburgh, PA, 1992.

[88] M. Koizumi. The concept of FGM. In J. B. Holt, M. Koizumi, T. Hirai, and Z. A. Munir, editors, *Proceedings of the Second International Symposium on Functionally Gradient Materials*, volume 34 of *Ceramic Transactions*, pages 3–10, Westerville, Ohio, 1993. The American Ceramic Society.

[89] N. Konda and F. Erdogan. The mixed mode crack problem in a nonhomogeneous elastic medium. *Engineering Fracture Mechanics*, 47(4):533–545, 1994.

[90] S. Krenk. On the elastic constants of plane orthotropic elasticity. *Journal of Composite Materials*, 13(2):108–116, 1979.

[91] J. Lambros, B. A. Cheeseman, and M. H. Santare. Experimental investigation of the quasi-static fracture of functionally graded materials. *International Journal of Solids and Structures*, 37(27):3715–3732, 2000.

[92] S. G. Larsson and A. J. Carlson. Influence of non-singular stress terms and specimen geometry on small-scale yielding at crack tips in elastic-plastic materials. *Journal of the Mechanics and Physics of Solids*, 21(4):263–277, 1973.

[93] Y.-D. Lee and F. Erdogan. Residual/thermal stresses in FGM and laminated thermal barrier coatings. *International Journal of Fracture*, 69(2):145–165, 1995.

[94] P. S. Leevers and J. C. D. Radon. Inherent stress biaxiality in various fracture specimen. *International Journal of Fracture*, 19(4):311–325, 1982.

236

[95] S. G. Lekhnitskii. *Anisotropic plates.* Gordon and Breach Science Publishers, New York, 1968.

[96] C. Y. Lin, Lin H. B. McShane, and R. D. Rawlings. Structure and properties of functionally gradient aluminium alloy 2124/SiC composites. *Materials Science and Technology,* 10(7):659–664, 1994.

[97] A. Maewal M. Dao, P. Gu and R. J. Asaro. A micromechanical study of residual stresses in functionally graded materials. *Acta Materialia,* 45(8):3265–3276, 1999.

[98] A. J. Markworth, K. S. Ramesh, and W. P. Parks Jr. Modelling studies applied to functionally graded materials. *Journal of Materials Science,* 30(9):2183–2193, 1995.

[99] P. R. Marur and H. V. Tippur. Numerical analysis of crack-tip fields in functionally graded materials with a crack normal to the elastic gradient. *International Journal of Solids and Structures,* 37(38):5353–5370, 2000.

[100] D. P. Miller and J. J. Lannutti. A model of structure optimization for a functionally graded materials. *Journal of Materials Research,* 8(8):2004–2013, 1993.

[101] R. J. Moon, M. Hoffman, J. Hilden, K. J. Bowman, K. P. Trumble, and J. Rodel. R-curve behavior in alumina-zirconia composites with repeating graded layers. *Engineering Fracture Mechanics,* 69(14-16):1647–1665, 2002.

[102] T. Mori and K. Tanaka. Average stress in matrix and average elastic energy of materials with misfitting inclusions. *Acta Materialia,* 21(5):571–574, 1973.

[103] N. I. Muskhelishvili. *Some Basic Problems of the Mathematical Theory of Elasticity.* Noordhoff Ltd., Holland, 1953.

[104] N. Noda and Z.-H. Jin. Thermal stress intensity factors for a crack in a strip of a functionally gradient material. *International Journal of Solids and Structures,* 30(8):1039–1056, 1993.

[105] N. P. O'Dowd, C. F. Shih, and R. H. Dodds Jr. The role of geometry and crack growth on constraint and implications for ductile/brittle fracture. In *Constraint Effects in Fracture Theory and Applications*, volume 2 of *ASTM STP 1244*, pages 134–159. American Society for Testing and Materials, 1995.

[106] H. Oonishi, T. Noda, S. Ito, A. Kohda, H. Yamamoto, and E. Tsuji. Effect of hydroxyapatite coating on bone growth into porous titanium alloy implants under loaded conditions. *Journal of Applied Biomaterials*, 5(1):23–27, 1994.

[107] T. Osaka, H. Matsubara, T. Homma, S. Mitamura, and K. Noda. Microstructural study of electroless-plated CoNiReP/NiMoP double-layered media for perpendicular magnetic recording. *Japanese Journal of Applied Physics*, 29(10):1939–1943, 1990.

[108] M. Ozturk and F. Erdogan. Mode I crack problem in an inhomogeneous orthotropic medium. *International Journal of Engineering Science*, 35(9):869–883, 1997.

[109] M. Ozturk and F. Erdogan. The mixed mode crack problem in an inhomogeneous orthotropic medium. *International Journal of Fracture*, 98(3-4):243–261, 1999.

[110] K. Palaniswamy and W. G. Knauss. On the problem of crack extension in brittle solids under general loading. In S. Nemat-Nasser, editor, *Mechanics Today*, volume 4, pages 87–148, Oxford, 1978. Pergamon Press.

[111] V. Parameswaran and A. Shukla. Asymptotic stress fields for stationary cracks along the gradient in functionally graded materials. *Journal of Applied Mechanics, Transactions ASME*, 69(3):240–243, 2002.

[112] G. H. Paulino and Z. Dong. A novel application of the singular integral equation approach to evaluate T-stress in functionally graded materials. (in preparation).

[113] G. H. Paulino, Z. H. Jin, and R. H. Dodds Jr. Failure of functionally graded materials. In B. Karihaloo and W. G. Knauss, editors, *Comprehensive Structural Integrity*, volume 2, Chapter 13. Elsevier Science, 2002.

[114] G. H. Paulino and J.-H. Kim. A new approach to compute T-stress in functionally graded materials using the interaction integral method. *Engineering Fracture Mechanics*, 2003, (in press).

[115] G. H. Paulino, I. F. M. Menezes, J. B. C. Neto, and L. F. Martha. A methodology for adaptive finite element analysis: towards an integrated computational environment. *Computational Mechanics*, 23(5-6):361–388, 1999.

[116] M. J. Pindera and P. Dunn. Evaluation of the higher-order theory for functionally graded materials via the finite element method. *Composites Part B – Engineering*, 28(1-2):109–119, 1997.

[117] B. N. Rao and S. Rahman. Mesh-free analysis of cracks in isotropic functionally graded materials. *Engineering Fracture Mechanics*, 70(1):1–27, 2003.

[118] T. Reiter and G. J. Dvorak. Micromechanical models for graded composite materials. *Journal of the Mechanics and Physics of Solids*, 45(8):1281–1302, 1997.

[119] T. Reiter and G. J. Dvorak. Micromechanical models for graded composite materials: II. thermomechanical loading. *Journal of the Mechanics and Physics of Solids*, 46(9):1655–1673, 1998.

[120] J. R. Rice. A path-independent integral and the approximate analysis of strain concentration by notches and cracks. *Journal of Applied Mechanics, Transactions ASME*, 35(2):379–386, 1968.

[121] D. Richardson and J. G. Goree. Experimental varification of a new two-parameter fracture model. In R. Chona, editor, *Fracture Mechanics: Twenty-third Symposium*, ASTM STP 1189, pages 738–751, Philadelphia, PA, 1993. American Society for Testing and Materials.

[122] R. Roscoe. The viscosity of suspensions of rigid spheres. *British Journal of Applied Physics*, 3:267–269, 1952.

[123] C.-E. Rousseau and H. V. Tippur. Compositionally graded materials with cracks normal to the elastic gradient. *Acta Materialia*, 48(16):4021–4033, 2000.

[124] S. Sampath, H. Herman, N. Shimoda, and T. Saito. Thermal spray processing of FGMs. *M.R.S. Bulletin*, 20(1):27–31, 1995.

[125] M. H. Santare and J. Lambros. Use of graded finite elements to model the behavior of nonhomogeneous materials. *Journal of Applied Mechanics, Transactions ASME*, 67(4):819–822, 2000.

[126] N. I. Shbeeb, W. K. Binienda, and K. L. Kreider. Analysis of the driving forces for multiple cracks in an infinite nonhomogeneous plate, Part I: Theoretical analysis. *Journal of Applied Mechanics, Transactions ASME*, 66(2):492–500, 1999.

[127] N. I. Shbeeb, W. K. Binienda, and K. L. Kreider. Analysis of the driving forces for multiple cracks in an infinite nonhomogeneous plate, Part II: Numerical solutions. *Journal of Applied Mechanics, Transactions ASME*, 66(2):501–506, 1999.

[128] Y.-L. Shen. Thermal expansion of metal-ceramic composites: a three-dimensional analysis. *Materials Science and Engineering A*, 252(2):269–275, 1998.

[129] A. H. Sherry, C. C. France, and M. R. Goldthorpe. Compendium of T-stress solutions for two and three dimensional cracked geometries. *Fatigue and Fracture of Engineering Materials and Structures*, 18(1):141–155, 1995.

[130] G. C. Sih. Strain energy density factor applied to mixed mode crack problems. *International Journal of Fracture*, 10(3):305–321, 1974.

[131] G. C. Sih, P. C. Paris, and G. R. Irwin. On cracks in rectilinearly anisotropic bodies. *International Journal of Fracture Mechanics*, 1(2):189–203, 1965.

[132] J. Sladek, V. Sladek, and P. Fedelinski. Contour integrals for mixed-mode crack analysis: effect of nonsingular terms. *Theoretical and Applied Fracture Mechanics*, 27(2):115–127, 1997.

[133] D. J. Smith, M. R. Ayatollahi, and M. J. Pavier. The role of T-stress in brittle fracture for linear elastic materials under mixed-mode loading. *Fatigue and Fracture of Engineering Materials and Structures*, 24(2):137–150, 2001.

240

[134] S. Suresh and A. Mortensen. *Fundamentals of Functionally Graded Materials.* IOM Communications Ltd, London, 1998.

[135] J. Tani and G. R. Liu. SH surface waves in functionally gradient piezoelectric plates. *JSME International Journal Series A (Mechanics and Material Engineering)*, 36(2):152–155, 1993.

[136] S. P. Timoshenko and J. N. Goodier. *Theory of Elasticity, 3rd Edition.* McGraw-Hill, New York, 1987.

[137] C. T. C. Ting. *Anisotropic Elasticity: Theory and Applications.* Oxford University Press, Oxford, 1996.

[138] Y. Ueda, K. Ikeda, T. Yao, and M. Aoki. Characteristics of brittle failure under general combined modes including those under bi-axial tensile loads. *Engineering Fracture Mechanics*, 18(6):1131–1158, 1983.

[139] L. J. Walpole. On the overall elastic moduli of composite materials. *ASME Journal of Applied Mechanics*, 17(4):235–251, 1969.

[140] S. S. Wang, H. T. Corten, and J. F. Yau. Mixed-mode crack analysis of rectilinear anisotropic solids using conservation laws of elasticity. *International Journal of Fracture*, 16(3):247–259, 1980.

[141] B. Wasiluk and K. Golos. Prediction of crack growth direction under plane stress for mixed-mode I and II loading. *Fatigue and Fracture of Engineering Materials and Structures*, 23(5):381–386, 2000.

[142] Y. Watanabe, Y. Nakamura, Y. Fukui, and K. Nakanishi. A magnetic-functionally graded material manufactured with deformation-induced martensitic transformation. *Journal of Materials Science Letters*, 12(5):326–328, 1993.

[143] F. Watari, A. Yokoyama, F. Saso, M. Uo, S. Ohkawa, and T. Kawasaki. EPMA elemental mapping of functionally graded dental implant in biocompatibility test. In *Proceedings of the Fourth International Symposium on Functionally Gradient Materials*, Tsukuba City, Japan, 1996.

[144] P. A. Wawrzynek. Interactive finite element analysis of fracture processes: an integrated approach. *M.S. Thesis, Cornell University*, 1987.

[145] P. A. Wawrzynek and A. R. Ingraffea. Discrete modeling of crack propagation: theoretical aspects and implementation issues in two and three dimensions. *Report 91-5, School of Civil Engineering and Environmental Engineering, Cornell University*, 1991.

[146] J. G. Williams and P. D. Ewing. Fracture under complex stress - the angled crack problem. *International Journal of Fracture*, 8(4):441-416, 1972.

[147] M. L. Williams. On the stress distribution at the base of a stationary crack. *Journal of Applied Mechanics, Transactions ASME*, 24(1):109-114, 1957.

[148] S. Yang and F. G. Yuan. Determination and representation of the stress coefficient terms by path-independent integrals in anisotropic cracked solids. *International Journal of Fracture*, 101(4):291-319, 2000.

[149] S. Yang and F. G. Yuan. Kinked crack in anisotropic bodies. *International Journal of Solids and Structures*, 37(45):6635-6682, 2000.

[150] J. F. Yau. Mixed-mode fracture analysis using a conservation integral. *PhD Thesis, Department of Theoretical and Applied Mechanics, University of Illinois at Urbana-Champaign*, 1979.

[151] J. F. Yau, S. S. Wang, and H. T. Corten. A mixed-mode crack analysis of isotropic solids using conservation laws of elasticity. *Journal of Applied Mechanics, Transactions ASME*, 47(2):335-341, 1980.

[152] H. Yin, L. Sun, and G. Paulino. Micromechanics-based elastic model for functionally graded composites with particle interactions. *7th United States National Congress on Computational Mechanics (USNCCM) Conference (United States Association for Computational Mechanics)*, 2003.

[153] J. Z. Zhu and O. C. Zienkiewicz. A posteriori error estimation and three-dimensional automatic mesh generation. *Finite Elements in Analysis and Design*, 25(1-2):167–184, 1997.

[154] J. R. Zuiker. Functionally graded materials: choice of micromechanics model and limitations in property variation. *Composites Engineering*, 5(7):807–819, 1995.

[155] J. R. Zuiker and G. J. Dvorak. Coupling in the mechanical response of functionally graded composite materials. *Mechanics and Materials for Electronic Packaging: Coupled Field Behavior in Materials, ASME New York*, 193:73–80, 1994.

[156] J. R. Zuiker and G. J. Dvorak. The effective properties of functionally graded composites – I. Extension of the Mori-Tanaka method to linearly varying fields. *Composites Engineering*, 4(1):19–35, 1994.

Vita

Jeong-Ho Kim was born in Korea, on Feburary 5, 1971. He received his B.S. degree in the Department of Architecture from Hanyang University of Seoul in 1996, and his M.S. degree in the Department of Civil and Environmental Engineering from University of Illinois at Urbana-Champaign in 2000. Upon the completion of his Ph.D, he will work as an assistant professor in the Department of Civil and Environmental Engineering at University of Connecticut at Storrs.